UNIVERSITY OF FRIBOURG / FACULTY OF SCIENCE

Department of Physics
University of Fribourg (Switzerland)

Synchrotron radiation based high–resolution grazing emission X–ray fluorescence

THESIS

presented to the Faculty of Science of the University of Fribourg (Switzerland)
in consideration for the award of the academic grade of *Doctor rerum naturalium*

by

Yves Kayser
from
Luxembourg

Thesis No: 1717
Editor: UniFr – UniPrint
Fribourg 2011

Accepted by the Faculty of Science of the University of Fribourg (Switzerland) upon the recommendation of

Prof. Dr. Christian Bernhard, Université de Fribourg (President of the jury)
Prof. Dr. Jean–Claude Dousse, Université de Fribourg (Thesis Supervisor)
Dr. Joanna Hoszowska, Université de Fribourg (Expert)
Dr. Burkhard Beckhoff, Physikalisch–Technische Bundesanstalt (External expert)

Fribourg, July 7th 2011

Thesis supervisor	Dean
Prof. Dr. Jean–Claude Dousse	Prof. Dr. Rolf Ingold

Contents

Abstract

Photo–induced surface–sensitive X–ray fluorescence measurements can be realized by different means. One can either irradiate the sample with a collimated primary X–ray beam at shallow incidence angles (0 to 2 degrees) relatively to the surface, or alternatively detect the X–ray fluorescence under well–defined shallow emission angles relatively to the sample surface. The first case corresponds to the Total Reflection X–ray fluorescence (TXRF) method, or the grazing incidence X–ray fluorescence (GIXRF) technique in the angle–dependent version, and the latter to the grazing emission X–ray fluorescence (GEXRF) technique. The principle of these methods is either to confine the X–ray fluorescence production to a surface–near region (on a nanometer scale) or to detect only the X–ray fluorescence emitted by surface–near atoms. In both geometries the probed depth region, which extends from the sample surface into the bulk, changes significantly with the angle and varies from a few nm to several hundred nm.

The physical principles of TXRF, GIXRF and GEXRF will be thoroughly presented. The requirements on the experimental setup for the realization of grazing incidence or grazing emission conditions, as well as their main differences, will be discussed. From a purely physical point of view the grazing incidence and the grazing emission geometry can be treated equivalently because of the principle of microscopic reversibility. Thus, their application domains are similar. In particular, the variation of the probed depth region with the angle predestines these methods for non–destructive depth–profiling experiments. The depth distribution of the atoms is assessed from the dependence of the X–ray fluorescence intensity on the angle. In the present thesis, GEXRF depth–profiling measurements for different ion–implanted Si and Ge wafers with different implantation energies and fluences will be reported. The motivation for carrying out depth–profiling measurements and the description of existing methods will be presented. Calculations of the X–ray fluorescence intensity dependence on the grazing emission angle re-

ported in review articles of H.P. Urbach und P.K. de Bokx will also be summarized.

The experiments were carried out by means of the von Hámos crystal X–ray spectrometer of the University of Fribourg installed at the European Synchrotron Radiation Facility (ESRF) ID21 beam line. Both the spectrometer and the beam line will be presented in detail. The realization of the grazing emission conditions in the von Hámos geometry will be explained. In the experiments, profit was made from the high resolution of the wavelength–dispersive detection setup and the advantages offered by synchrotron radiation. In addition, a focusing polycapillary half–lens was installed in the spectrometer for micro–focused experiments permitting a local characterization of the sample. The necessary modifications, operational requirements and equipment for a successful implementation of the polycapillary optics in the von Hámos spectrometer will be presented.

In principle, the extraction of the depth concentration distribution of the implanted ions from the angular intensity profile of an X–ray fluorescence line measured by means of the presented experimental setup can be realized with different approaches. However, those based on purely theoretical concepts, discussed in detail, did not provide satisfactory results because of experimental intensity fluctuations (Poisson noise). Conversely, adopting the dopant depth distributions calculated with the SRIM (Stopping and Range of Ions in Matter) code, well–defined distribution functions for the implanted dopant atoms could be assumed and implemented in the fit of the angular intensity profiles to assess the dopant depth distribution. This approach provided accurate results in good agreement with theoretical expectations. In addition, an algorithm for the extraction of the dopant depth distribution without *a priori* knowledge has been developed. Its application to real data and its limits will be discussed. For few samples, comparative measurements with GIXRF and secondary ion mass spectrometry (SIMS) were performed. The retrieved depth profiles were found to be in good agreement with the depth profiles obtained with GEXRF. In summary, the synchrotron radiation based high–resolution GEXRF technique presented in this thesis, which can be optionally combined with focusing optics for the primary X–ray beam, is a powerful tool for extracting dopant depth profiles of ion–implanted samples.

Résumé

Des expériences par fluorescence X sensibles à la région près de la surface de l'échantillon peuvent être réalisées de différentes manières. Une possibilité, connue sous les noms de TXRF (Total Reflection X–ray Fluorescence – fluorescence X par réflexion totale) ou GIXRF (Grazing Incidence X–ray Fluorescence – fluorescence X sous incidence rasante) consiste à irradier l'échantillon avec un faisceau de rayons X collimé sous des angles d'incidence très petits (entre 0 et 2 degrés). Une autre alternative, dénommée GEXRF (Grazing Emission X–ray Fluorescence – Fluorescence X en émission rasante) est de mesurer la fluorescence X sous des angles d'émission très petits et bien définis. Le principe de base est soit de confiner la production de la fluorescence X à une région proche de la surface (sur une échelle nanométrique), soit de détecter uniquement la fluorescence X émise par des atomes situés près de la surface. Dans les deux géométries, la région étudiée s'étend de la surface de l'échantillon jusqu'à une profondeur variant entre quelques nanomètres et quelques centaines de nanomètres selon l'angle d'incidence ou d'émission.

Les principes physiques sur lesquels se basent les méthodes TXRF, GIXRF et GEXRF, les exigences imposées à l'instrumentation expérimentale ainsi que les principales différences entre les trois méthodes seront discutés en détail. D'un point de vue physique, l'incidence et l'émission sous angles rasants peuvent être traitées de manière équivalente à cause du principe de réversibilité microscopique. Les domaines d'application étudiés sont donc similaires. En particulier, la variation de la profondeur étudiée en fonction de l'angle d'incidence ou d'émission prédestine ces techniques à la mesure non destructive de la distribution d'implants dans la profondeur de l'échantillon. Dans cette thèse de doctorat, les profils d'implantation de différents ions introduits par implantation ionique avec différentes énergies et différentes doses dans des échantillons de Si et de Ge ont été déterminés au moyen de la méthode GEXRF où la dépendance de l'intensité de la fluorescence émise par les atomes implantés est mesurée en fonction de l'angle d'émission. La motivation qui

nous a conduit à réaliser de telles mesures ainsi que les méthodes expérimentales alternatives existantes seront discutées. Un résumé du modèle théorique développé par H.P. Urbach et P.K. de Bokx pour calculer la variation de l'intensité de la fluorescence en fonction de l'angle d'émission sera également présenté.

Les mesures ont été réalisées en haute résolution avec le spectromètre à cristal incurvé von Hámos de Fribourg, lequel a été installé sur la ligne ID21 de l'ESRF (European Synchrotron Radiation Facility). Le spectromètre, sa géométrie, la réalisation des conditions d'émission rasante ainsi que la ligne de faisceau seront présentés en détail. Les mesures ont pu être réalisées grâce aux avantages offerts par le rayonnement synchrotronique et la haute résolution du spectromètre. En plus une optique polycapillaire focalisante a été installée à l'intérieur du spectromètre pour réaliser des mesures avec un faisceau d'une taille latérale micrométrique ce qui a permis une caractérisation locale de l'échantillon. Les modifications du spectromètre requises pour l'installation du polycapillaire, les exigences pour l'alignement de ce dernier et l'instrumentation nécessaire seront expliquées.

L'extraction des profils d'implantation des ions à partir de la dépendance angulaire de l'intensité de la fluorescence X, mesurée à l'aide du dispositif expérimental mentionné ci–dessus, peut être réalisée de différentes manières. Des approches basées sur la théorie seront présentées bien que celles–ci ne délivrent pas des résultats satisfaisants à cause des fluctuations d'intensité expérimentale. Alternativement, en se basant sur des calculs effectués à l'aide du code SRIM (Stopping and Range of Ions in Matter), une distribution bien définie peut être supposée pour reproduire les mesures et retrouver ainsi la distribution en profondeur des dopants implantés. Cette approche a donné de bons résultats en comparaison avec les attentes théoriques. De plus un algorithme n'utilisant aucune connaissance *a priori* de la distribution en profondeur des ions mis à part un profil en forme en cloche a été développé. Son application aux mesures et ses limites théoriques seront discutées. Pour certains échantillons des mesures comparatives avec les méthodes GIXRF et SIMS (secondary ion mass spectrometry – spectrométrie de masse à ionisation secondaire) ont donné des résultats en bon accord avec les mesures GEXRF. Les résultats de cette thèse montrent que la technique GEXRF à haute résolution utilisant le rayonnement synchrotronique, avec l'option d'utilisation d'une optique focalisante, est un outil puissant pour la détermination non destructive des profils en profondeur de dopants introduits par implantation ionique.

Zusammenfassung

Photoinduzierte Röntgenfluoreszenzanalyse kann zur Oberflächenanalyse von Proben eingesetzt werden. Zwei Möglichkeiten hierzu sind die Anstrahlung der Probe mit einem Röntgenstrahl unter streifenden Einfallswinkeln bezüglich der Probenoberfläche und die Beobachtung der Fluoreszenzstrahlung unter streifenden Ausfallswinkeln. Im ersten Fall ist von Totalreflexions-Röntgenfluoreszenzanalyse (TXRF – Total Reflection X–ray fluorescence) oder Röntgenfluoreszenzanalyse unter streifendem Einfall (GIXRF – Grazing Incidence X–ray Fluorescence) die Rede, im zweiten Fall von Röntgenfluoreszenzanalyse unter streifendem Ausfall (GEXRF – Grazing Emission X–ray Fluorescence). Die dahinter stehende Idee ist entweder die Erzeugung der Röntgenfluoreszenz auf eine oberflächennahe Schicht (auf einer Nanometerskala) zu begrenzen oder nur die Fluoreszenzstrahlung von oberflächennahen Atomen zu detektieren. In beiden Fällen ändert sich die untersuchte Probentiefe, die sich von der Oberfläche in die Probe hinein erstreckt, mit dem streifenden Winkel und kann je nach Winkel zwischen ein paar Nanometer oder mehreren hundert Nanometer variieren.

Die physikalischen Grundlagen von TXRF, GIXRF and GEXRF werden ausführlich diskutiert. Die Anforderungen an die Messapparatur um streifende Einfallswinkel oder streifende Ausfallwinkel zu erzeugen werden erörtert, sowie die Unterschiede zwischen beiden Messgeometrien. Von einem rein physikalischen Standpunkt können beide Messgeometrien, wegen des Prinzips der mikroskopischen Reversibilität, als äquivalent betrachtet werden. Dem zu Folge sind sich die Anwendungsgebiete der Verfahren ähnlich. Insbesondere die Abhängigkeit der erprobten Tiefe vom Winkel prädestiniert die beiden Messmethoden für nicht destruktive Tiefenprofilmessungen. Die Verteilung der Atome, die die Fluoreszenzstrahlung emittieren, kann von der Winkelabhängigkeit der Intensität der Fluoreszenzstrahlung abgeleitet werden. In der vorliegenden Dissertation wurden Tiefenprofilmessungen mit Hilfe der GEXRF Geometrie für ionenimplantierte Si and Ge Proben vor-

genommen. Die Wichtigkeit von Tiefenprofilmessungen wird hervorgehoben und bestehende Alternativen werden diskutiert. Eine Zusammenfassung der von H.P. Urbach und P.K. de Bokx publizierten Berechnungen der Winkelabhängigkeit der Intensität der Fluoreszenzstrahlung wird ebenfalls dargestellt.

Die Messungen der Winkelabhängigkeit der Fluoreszenzstrahlung wurden mit Hilfe des von Hámos Kristallspektometers der Universität Fribourg an der Strahllinie ID21 im ESRF (European Synchrotron Radiation Facility) vorgenommen. Das Spektrometer, dessen Geometrie, die Definition von streifenden Ausfallwinkeln in dieser Geometrie, und die Strahllinie werden vorgestellt. Die hohe Energieauflösung sowie die Synchrotronstrahlung boten einzigartige Vorteile für die Durchführung der Messungen. Zusätzlich wurde eine mikrofokussierende Polykapillaroptik im Spektrometer installiert um eine lokale Charakterisierung der Probe zu ermöglichen. Die notwendigen Änderungen am Spektrometer, die Anforderungen an die korrekte Ausrichtung der Polykapillaroptik, sowie die erforderliche Ausrüstung diesbezüglich werden visualisiert.

Die Rekonstruktion der Tiefenprofile der implantierten Atome kann aus der, mit Hilfe der eben erwähnten Messapparatur, beobachteten Winkelabhängigkeit der Intensität der Fluoreszenzstrahlung mit unterschiedlichen Ansätzen verfolgt werden. Auf theoretischen Konzepten basierende Ansätze werden präsentiert, sie liefern allerdings keine zufriedenstellenden Resultate. Anhand der Berechnungen der Tiefenprofile mit Hilfe des SRIM (Stopping and Range of Ions in Matter) Programms, konnte die Tiefenverteilung der implantierten Atome aus der Winkelabhängigkeit der Fluoreszenzstrahlungsintensität konstruiert werden. Es zeigte sich eine gute Übereinstimmung mit den theoretischen Erwartungen. Zusätzlich wurde ein Algorithmus entwickelt, der es erlaubt die Tiefenverteilung der implantierten Atome ohne *a priori* Annahmen aus den Messungen zu extrahieren. Die Anwendung des Algorithmus auf experimentelle Daten und die Validität der erhaltenen Resultate werden diskutiert. Darüber hinaus wurden für einige Proben komplementäre Messungen mit Hilfe von GIXRF und Sekundärionen–Massenspektrometrie (SIMS) vorgenommen. Die erhaltenen Tiefenprofile entsprachen den GEXRF Messungen. Die in dieser Dissertation vorgestellte, auf hoher Energieauflösung und Synchrotronstrahlung basierende, GEXRF–Technik (mit der Möglichkeit eine fokussierende Polykapillaroptik zu nutzen) ermöglicht die Durchführung von präzisen, nicht destruktive Tiefenprofilmessungen von ionenimplantierten Proben.

Chapter I

Introduction

X–rays, which have a wavelength between the wavelengths of UV radiation and gamma rays, were discovered in 1895 by W.C. Röntgen [1], a discovery for which he was awarded the Nobel prize in 1901, and are nowadays widely used for analytical aims in physics, chemistry, biology, archeology, geology and medicine of course. Indeed methods based on X–ray excitation and detection offer, due to the soft interaction of X–rays with materials in comparison with ion excitation, the advantage of non-consumptive analysis while at the same time requiring little sample preparation. In comparison to other analytical techniques an operation under atmospheric pressure can be envisaged for hard X–rays. The combination of these advantages allows to integrate X–ray based analytical setups as an automatized, routine control in manufacturing processes.

X–ray analytical methods where X–rays are used in the detection channel are either based on X–ray scattering or X–ray fluorescence. Other analytical methods may use X–rays only in the excitation channel, like it is the case in Auger electron spectroscopy (AES) and X–ray photoelectron spectroscopy (XPS).

In X–ray scattering techniques, an X–ray beam is incident on the sample and the scattered radiation is measured as a function of the incidence angle, the scattering angle, the energy (elastic or inelastic scattering) and sometimes the polarization. Scattering experiments allow to deduce structural information from crystalline, powder (polycrystalline) or liquid samples. In this perspective X–rays are optimal since their wavelength is comparable to interatomic distances. For example X–ray diffraction (XRD) experiments enabled J. Watson and F. Crick in 1953 to determine the DNA structure [2].

X–ray fluorescence, on the other side, is based on the excitation and detection of X–rays. The X–ray emission process can either be induced by particles (electrons, protons, ions) or by X–rays, resp. gamma rays, provided there is enough energy to excite the electrons in the atomic shells surrounding the nucleus. During the following de–excitation process, the excitation energy can be emitted in the form of an Auger electron or a fluorescence X–ray photon. The energy of both the Auger electron and the emitted X–ray photon, which is measured in X–ray fluorescence experiments, is characteristic for the considered element. Consequently, if the electron involved in the de–excitation process originates from a valence shell, X–ray fluorescence experiments are essentially used when the (quantitative) elemental or chemical analysis are the main goals.

However, if the intent is to realize surface–sensitive X–ray fluorescence measurements, the quite large penetration depths of the primary X–rays used to excite the fluorescence radiation are cumbersome (Fig. I.1). Alternatively particles could

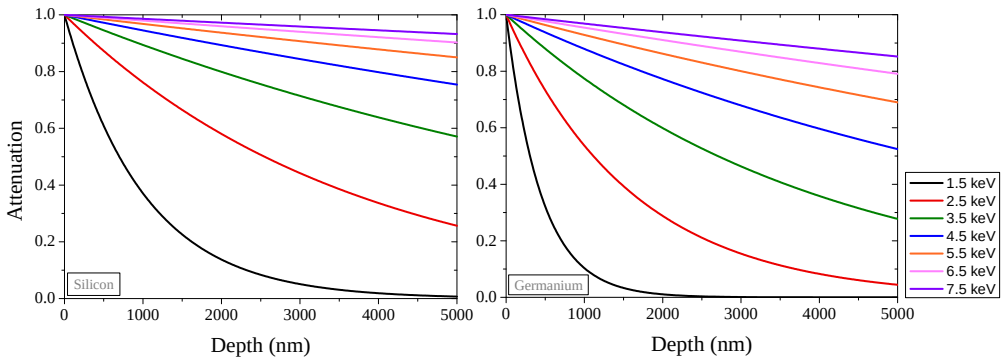

Figure I.1: Illustration of the intensity decay for X–rays penetrating Si respectively Ge bulk samples at normal incidence. The X–ray beams penetrate quite deeply into the bulk, making surface–sensitive measurements (in the nanometer regime) difficult if not impossible due to the large background contribution (Compton scattering, Rayleigh scattering, X–ray fluorescence) from the bulk.

be used to excite the X–ray fluorescence since their penetration depths into the sample are much shorter. However, particle induced X–ray emissions require a high–vacuum setup to avoid the absorption of the particles in air and result in noisier X–ray spectra. Indeed particles have compared to X–ray photons a larger probability to multiply ionize atoms, which makes the quantitative interpretation

of the spectra more difficult due to the many satellite lines. In addition a quite noisy background radiation is induced due to the particle Bremsstrahlung produced in the bulk target. Fluorescence radiation induced by photons on the other hand provides cleaner experimental spectra which is especially useful in the case of micro- and trace analysis. The realization of surface–sensitive measurements is also possible by either adjusting the angle of incidence of the primary photon beam or the emission angle of the fluorescence radiation.

Chapter II

Total Reflection X–ray Fluorescence

Usually the efficiency of surface analysis (or interface analysis of multilayered samples) by means of X–ray probing is limited by the rather large penetration of the incident primary X–rays into the sample. The surface–near region is not efficiently excited with respect to the bulk. The excited fluorescence X–ray signal originates from the whole excited sample region and therefore the signal from the surface (or interface) region may be hidden in the bulk fluorescence signal or background (due to elastic scattering, detector noise and photoelectron Bremsstrahlung) if the X–ray energy of the surface elements is not located in a clean, i.e., free of any other signals, region of the X–ray spectrum.

One possibility to improve the surface analytical capabilities is to enhance the excitation of the atoms at the surface with respect to the excitation of bulk atoms. This can be done by creating an X–ray standing wave–pattern resulting from the coherent superposition of two plane waves on the surface of the bulk sample. To this end one can employ the X–ray standing waves (XSW) technique (Fig. II.1) or the total reflection of X–rays (Fig. II.2) as used in the total reflection X–ray fluorescence (TXRF) method.

II.1 X–ray standing wave technique

The XSW technique has been pioneered by B.W. Batterman [3] who used it to trace interstitial impurities in crystalline samples. The bulk sample is a perfect crystal or a multilayer and the standing wave–pattern results from the interfer-

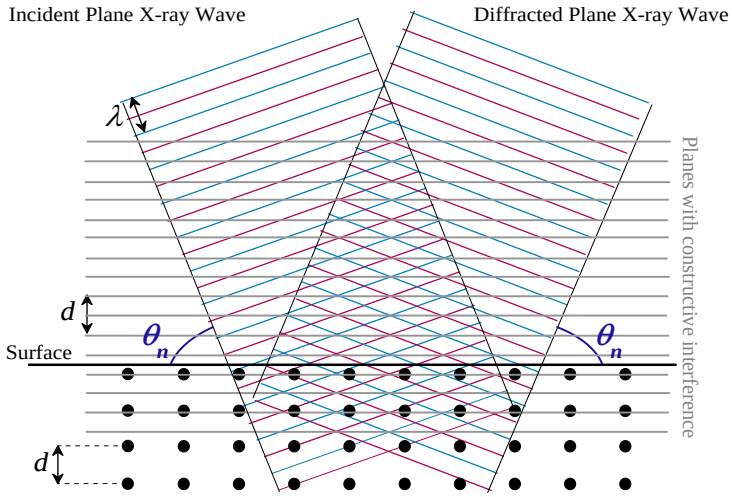

Figure II.1: X–ray standing wavefield created by the interference of an incident and a Bragg–diffracted (section IV.2.1) plane wave of wavelength λ around the surface region of a Bragg diffraction crystal. The maximum and minimum amplitudes of the plane waves are colored in blue, resp. in red. The planes in which constructive interferences take place are parallel to the Miller planes of the crystal and the periodicity is connected to the crystal lattice spacing.

ence of the incident X–ray beam with the Bragg diffracted beam (Fig. II.1). The condition for Bragg diffraction is discussed in paragraph IV.2.1, illustrated in Fig. IV.4 and mathematically described in Eq. IV.1 [1]. The theoretical description for the standing wave–pattern due to the coherent superposition of the incident and diffracted beams is based on the dynamical diffraction theory. The standing wave–pattern is characterized by regions with constructive, respectively destructive, interference. The interference regions are parallel to the crystal Miller planes. In regions with constructive interference, the initial amplitude of the plane waves is doubled. The probability to excite fluorescence X–rays is increased compared to a situation where no interference effects take place, favoring thus the detection of X–rays emitted from the parts where constructive interference occurs. In regions with destructive interference the probability of photoelectric absorption is drastically reduced. By the different incidence angles around the Bragg angle, the

[1] Note that the Bragg law is for the constructive interference of plane X–ray waves diffracted at different Miller planes of the crystal. The waves considered in this type of interference propagate therefore in the same direction in contrast to the waves creating the standing wavefield–pattern. The Bragg law assumes that phase differences between the diffracted waves are only due to different pathlengths, the phase shift upon the coherent scattering at the atoms of the Miller planes having a constant value.

standing wave–pattern is altered and accordingly the regions with constructive or destructive interference are displaced. This allows in principle to obtain spatial information on the distribution of the target element. This technique can also be combined with X–ray diffraction.

In the perspective of surface analysis, a drawback of the XSW technique is the extension of the standing wave–pattern which is formed both above and below the sample surface. A contribution from the bulk sample in the experimental X–ray spectrum is still present. If the focus of the experiment is surface analysis, a standing wave–pattern which is present only above the surface would be preferable since then only contributions from the region of interest would be present in the measured X–ray spectrum. In this perspective the penetration of the incident X–rays into the sample should be minimized. The total external reflection of X–rays on a smooth sample surface does not allow an X–ray photon to penetrate deeply into the sample, while at the same time a standing wave–pattern is created on top of the sample surface due to the interference of the incident and reflected X–ray beams (Fig. II.2).

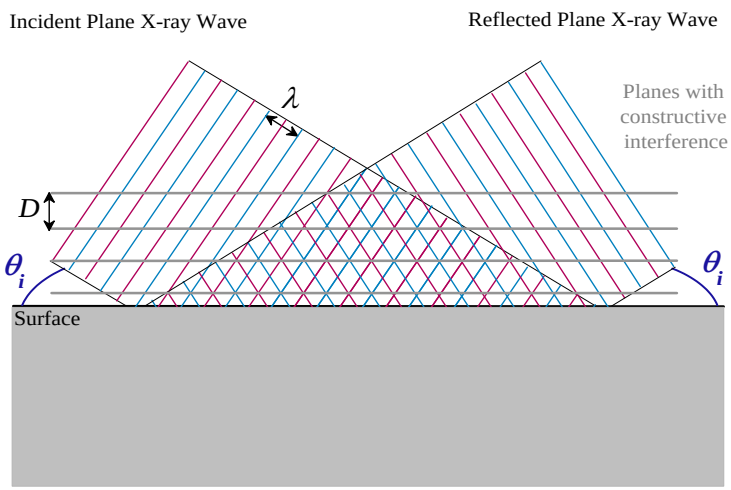

Figure II.2: X–ray standing wavefield created by the interference of an incident and a totally reflected (section II.2) X–ray plane wave of wavelength λ. The maximum and minimum amplitudes of the plane waves are again colored in blue, resp. in red. The planes in which constructive interference takes place are parallel to the sample surface. The periodicity varies with the incidence angle θ_i and is larger than in the case of an X–ray standing wave–pattern created by Bragg diffraction (section II.5).

II.2 Total external reflection of X–rays

As X–rays are electromagnetic waves, refraction (transmission and reflection) of X–rays at the interface between different media takes place. The TXRF method is based on the total external (to the bulk sample) reflection of the incident X–ray beam, meaning that the reflected beam has an intensity nearly equal to the one of the incident beam and no refracted beam penetrates deep into the sample. A.H. Compton was the first to report in 1923 on total reflection of X–rays from solid samples [4], whereas the first theoretical formalism on the basis of dispersion theory was established by L.G. Paratt in 1954 [5] to discuss surface properties of solids.

In order to observe total reflection of X–rays (or light in general) at the interface of two media, two conditions need to be satisfied:

1. The refractive index n_1 of the medium in which the X–ray beam is initially propagating needs to be larger than the refractive index n_2 of the medium onto which the beam is incident. The second medium should be optically less dense.

2. The X–ray beam should be incident on the interface at angles θ_i below the critical angle for total reflection.

Both conditions can be derived from Snell's law (also known as Snell–Descartes law) which can be deduced from the continuity condition for the incident, reflected and refracted electromagnetic waves at the interface requiring that the temporal and spatial evolution of the three waves shall be identical at the interface,

$$n_1 \times \cos\theta_i = n_2 \times \cos\theta_t. \tag{II.1}$$

In the case where $n_1 > n_2$ with an X–ray beam incident from the medium with refractive index n_1 on the medium with refractive index n_2, i.e., in a situation corresponding to the first condition for total reflection, the refraction angle θ_t needs to be smaller than θ_i in order for Eq. II.1 to be verified. This means that upon penetration into the second medium with refractive index n_2 the X–ray beam is refracted towards the interface of the two media (Fig. II.3). Accordingly there exists a minimum angle θ_i for which $\theta_t = 0°$, meaning that the refracted X–ray beam propagates along the surface in medium 2. This angle is called the critical angle for total reflection $\theta_c = \arccos(n_2/n_1)$, the incident beam cannot be further

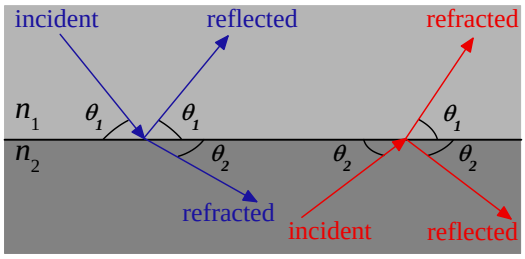

Figure II.3: At the interface between two media of refractive indexes n_1 and n_2, with $n_2 < n_1$ in the present example, light beams in general and X–ray beams in particular are partially refracted (transmitted) and partially reflected. The reflection angle is equal to the incidence angle θ_1 on the interface while the refraction angle θ_2 and thus the deviation of the refracted beam is fixed by Snell's law (Eq. II.1).

refracted towards the interface boundary for incidence angles θ_i smaller than θ_c (section II.3). Indeed only an evanescent, exponentially damped wave, propagating along the surface penetrates into the second medium. The short, vertical penetration range is due to energy and momentum conservation. The incident beam will be reflected, the reflection angle θ_r being identical to the incidence angle θ_i (Fig. II.3) because of the continuity condition at the interface. This justifies the second condition for total reflection. The incident and reflected beam will superpose coherently above the region where the incident beam hits the sample surface, creating a standing X–ray wave–pattern (Fig. II.2).

The total external reflection of X–rays not only improves the excitation efficiency for fluorescence radiation of the near–surface region like the XSW technique does but prevents in addition any fluorescence excitation of the bulk, provided the incidence angle θ_i is below the critical angle for total external reflection θ_c (see Fig. II.4). For larger incidence angles θ_i, the primary X–ray radiation can penetrate into the sample, but due to the shallow incidence angles, the X–ray absorption is quite pronounced in the depth direction (factor $\sin\theta_i$), limiting the depth region which is effectively excited to very narrow regions (see Fig. II.4 and Fig. I.1 for comparison).

For $n_1 < n_2$ no total reflection can occur, since the refracted beam will be refracted away from the interface of the two media and will therefore penetrate into the medium with refractive index n_2, independently of the incidence angle θ_i (Fig. II.3).

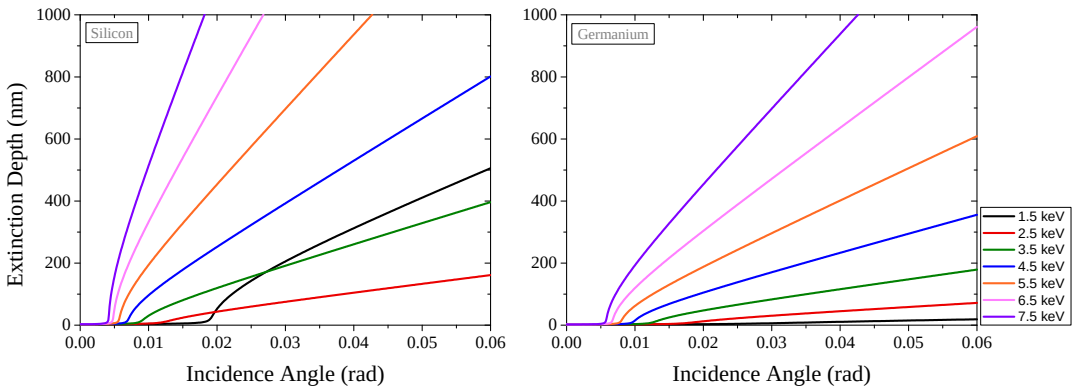

Figure II.4: Plot of the extinction depth as a function of the incidence angle θ_i for different primary beam energies in Si and Ge. The extinction depth corresponds to the perpendicular distance from the surface after which the intensity has been attenuated by a factor e^{-1}. The extinction depth depends strongly on the incidence angle θ_i: below the critical angle θ_c (marked by a steep step in the variation of the extinction depth) only a shallow surface layer (about 3–5 nm) is penetrated, whereas for larger incidence angles the primary X–rays penetrate deeper into the sample. However, in comparison to Fig. I.1, the extinction depth is much narrower for grazing incidence angles.

II.3 Critical angle for total external reflection

Since the refractive index n_1 of vacuum is one, the condition for total external reflection of X–rays incident on the sample with refractive index n_2 can be rewritten

$$\cos\theta_c = n_2/n_1 = n_2. \tag{II.2}$$

The refractive index of solid samples in the X–ray domain is a complex quantity, $n_2 = 1 - \delta_2 + i\beta_2$, the refractive index decrement δ_2 and the absorption index β_2 being positive quantities related to the scattering and absorption properties [6],

$$\delta_2 = \frac{N_\mathrm{A}}{2\pi} \times r_e \times \frac{\rho_2}{A_2} \times f_2(\lambda_i) \times \lambda_i^2, \tag{II.3}$$

$$\beta_2 = \frac{\mu_2(\lambda_i)}{4\pi} \times \rho_2 \times \lambda_i. \tag{II.4}$$

Here λ_i represents the wavelength of the incident X–rays, $N_\mathrm{A} = 6.022 \times 10^{23}$ the Avogadro's number, $r_e = 2.818 \times 10^{-3}$ Å the electron radius (or equivalently the X–ray scattering amplitude per electron), ρ_2 the mass density of the scattering sample, A_2 the molar mass of the sample, $\mu_2(\lambda_i)$ the total mass absorption coefficient of the sample's element and $f_2 = f_2(0) + f_2^*(\lambda_i)$ the real part of the atomic scattering factor, where $f_2(0)$ corresponds to the atomic forward scattering factor, being approximately equal to the atomic number Z_2 of the sample's element

(the difference being given by a small relativistic correction [7]) and $f_2^*(\lambda_i)$ to a correction factor that is essential in the X–ray wavelength domain below the absorption edges of the sample's element. In formulas II.3 and II.4 a homogeneous monoelemental sample was assumed but the formulas can also be applied if the scattering factor f_2 is known for the considered compound, the other factors being in principle calculable with a weighted linear combination of the corresponding elemental factors. The weights are given by the relative elemental concentration. The ratio $N_\mathrm{A}\,\rho_2/A_2$ corresponds to the atomic density, which can be related with $f_2(0)$ to the electronic density, the electrons being the X–ray scatterers.

The order of magnitude of δ_2 and β_2 varies between 10^{-3} and 10^{-6}. The real part of the refractive index n_2 is thus really close to one, implying that θ_c is very small. Representing the cosine function by the first terms of a Taylor series one obtains:

$$\begin{aligned} n_2 &= \cos\theta_c \approx 1 - \frac{\theta_c^2}{2} \\ \Rightarrow \theta_c &\approx \sqrt{2\times\delta_2} \approx \frac{\lambda_i}{\sqrt{\pi}} \times \sqrt{N_\mathrm{A}\times r_e \times \frac{\rho_2\times Z_2}{A_2}}\,. \end{aligned} \tag{II.5}$$

The latter approximation is for X–ray wavelengths shorter than wavelengths corresponding to the absorption edges of the sample's element. Given the order of magnitude of δ_2, the critical angle θ_c for total external reflection is of the order of 1° or smaller. It depends on the sample's element and the wavelength of the incident X–rays and tends to decrease for heavier elements and higher X–ray energies.

In order for total external reflection to happen, i.e., the reflection occurs on the vacuum (or air) side of the vacuum (resp. air) – sample interface for a bulk sample, the refractive index of the sample (the second medium) should be smaller than one, the refractive index associated to vacuum (resp. air). This premise is valid for solid samples in the wavelength domain of X–rays, as explained in [6] and [8] with the following arguments. The X–ray frequency is of the order of the binding frequency of the atomic electrons. In the derivation of the refractive index n in the Lorentz theory, the electrons are assumed to be quasi–elastically–bound and forced to oscillations by the incident primary X–rays. Upon this the electrons radiate with a phase–difference and by superposition of both radiations the phase velocity v of the primary beam is altered to values larger than c, the speed of light. Hence the refractive index $n = c/v$ is modified to values smaller than one

by a quantity δ. This is not in contradiction with the relativity theory, since the group velocity, i.e., the speed at which the signal is transported, does not exceed c.

The refraction angle is a complex number and can also be calculated with Eq. II.1 with the small angle approximation for the cosine functions,

$$\theta_t = \sqrt{\frac{\theta_i^2 - 2 \times \delta_2 + 2i \times \beta_2}{1 - \delta_2 + i\beta_2}} \tag{II.6}$$

For visible light, only total internal reflection, on the sample side of the air–sample interface, can occur since in this wavelength region the refractive index of a solid sample is always larger than one.

II.4 Characterization of the TXRF standing wave–pattern

The sample surface is supposed to be perfectly smooth on the nanometer scale. The X–ray standing wave–pattern is formed on top of the sample surface by the coherent superposition of the incident X–ray beam $\vec{E_1}(\vec{r}, t)$ with the one reflected by the sample surface $\vec{E_2}(\vec{r}, t)$,

$$\begin{aligned} \vec{E}(\vec{r}, t) &= \vec{E_1}(\vec{r}, t) + \vec{E_2}(\vec{r}, t) \\ &= \vec{E_0} \times \exp i(\omega t - \vec{k} \cdot \vec{r}) + \vec{E_0^R} \times \exp i(\omega t - \vec{k^R} \cdot \vec{r} + \Delta\phi^R), \end{aligned} \tag{II.7}$$

where E_0^R is the amplitude of the reflected beam and E_0 the amplitude of the incident beam, $\vec{k}$ the wavevector with norm $k = 2\pi/\lambda_i = k^R$ and $\Delta\phi^R$ the phase difference between the incident and the reflected plane X–ray wave due to scattering. The transmitted plane wave is defined similarly to the incident and reflected plane waves,

$$\vec{E_3}(\vec{r}, t) = \vec{E_0^T} \times \exp i(\omega t - \vec{k^T} \cdot \vec{r} + \Delta\phi^T), \tag{II.8}$$

the norm of the transmitted wavevector being $k^T = n_2 \times 2\pi/\lambda_i$. The reflectivity R and transmittivity T are defined as

$$R = \left|\frac{E_0^R}{E_0}\right|^2 \quad \text{and} \quad T = \left|\frac{E_0^T}{E_0}\right|^2. \tag{II.9}$$

Assuming a reflectivity R equal to 1, i.e., total reflection, and requiring the spatial and temporal evolution of the incident and the sum of the refracted and transmitted vectors to be identical at the surface, the wavevectors $\vec{k}$ and $\vec{k^R}$ are collinear

and the total electromagnetic vector $\vec{E}(\vec{r},t)$ resulting from the superposition will be equal to

$$\vec{E}(\vec{r},t) = \vec{E_0}\cos\left(\frac{(\vec{k}-\vec{k^R})\cdot\vec{r}}{2}+\frac{\Delta\phi^R}{2}\right)\times\exp i(\omega t-\frac{(\vec{k}+\vec{k^R})\cdot\vec{r}}{2}+\frac{\Delta\phi^R}{2})\text{(II.10)}$$

Choosing a coordinate system with the z axis perpendicular to the surface and pointing out from it, $z = 0$ corresponding to the sample surface which lies thus in the xy–plane, and assuming the incident wavevector $\vec{k}$ to be confined in the xz–plane, Eq. II.10 gives for a plane wave incident at the angle θ_i relative to the surface

$$\vec{E}(\vec{r},t) = \vec{E_0}\cos\left(k\sin\theta_i\times z+\frac{\Delta\phi^R}{2}\right)\times\exp i(\omega t-k\cos\theta_i\times x+\frac{\Delta\phi^R}{2}).\quad\text{(II.11)}$$

This result corresponds to a wavefield moving along the x–direction but presenting standing waves in the z–direction. Parallel to the surface there are nodal and anti–nodal lines with zero or maximum amplitude, respectively, meaning that the cosine function has either the value zero or unity. The period, or spacing, of the nodal or anti–nodal lines is given by the periodicity of the cosine function and is equal to $\lambda_i/2\sin\theta_i$. The intensity in the general case where the reflectivity is not one is given in [9]

$$I(\theta_i,z) = |E_0|^2\times\left(1+R+2\sqrt{R}\times\cos\left(\arccos(\frac{2\theta_i^2}{\theta_c^2}-1)-\frac{4\pi z\sin\theta_i}{\lambda_i}\right)\right).\text{(II.12)}$$

The maximum and minimum values of $I(\theta_i,z)$ define the anti–nodal and nodal lines, respectively.

Below the surface the intensity is exponentially damped due to X–ray absorption, the beam propagating along the direction defined by θ_t (Eq. II.6). The surface ($z = 0$) intensity is defined by Eq. II.12 since the intensity varies continuously [6].

II.5 Standing wave–patterns of TXRF and XSW

Both Bragg diffraction used in the XSW technique and total external reflection of X–rays used in the TXRF method can be employed to create standing X–ray wavefields of monochromatic, coherent X–ray beams propagating in different directions. As it has been mentioned, in the first case the coherent scattering of X–rays at the atoms of the different crystal planes is used, while in the second

case the total external reflection of X–rays at a perfectly smooth vacuum–sample interface is employed. Therefore a few differences result in the properties of the standing X–ray wave–pattern. The first one concerns the samples. For the XSW technique only crystals are used, whereas for the TXRF technique any sample with a smooth (on the nanometer scale), homogeneous and sharp vacuum–sample interface is conceivable. However, samples with low–Z elements are preferred since they offer larger critical angles θ_c and are therefore less demanding in the angular alignment to achieve total external reflection conditions.

Another difference is the period between regions with constructive interference in the X–ray standing wave–pattern. For a standing wave–pattern created by means of the XSW technique, the period is determined by the lattice spacing between the Miller planes of the crystal and is therefore of the order of a few Ångström. When the TXRF method is used, the period is a strong function of the incidence angle θ_i and, referring to Eq. II.11, varies as [9]

$$D = \frac{\lambda_i}{2 \sin \theta_i} \,. \tag{II.13}$$

The periodicity can also be geometrically deduced from Fig. II.2. As a consequence, the period in the standing wave–pattern is much longer in the latter case due to the small angles of incidence θ_i. Thus, standing wave–patterns created by means of total external reflection are more suitable for the analysis of impurities in layers thicker than a few Ångström. Indeed there will be no ambiguity due to the very short period of a standing wave–pattern created by means of Bragg diffraction [9], which allows nevertheless to very accurately localize adsorbate atoms on crystal surfaces [10,11]. In the TXRF case the period of the standing wave–pattern will vary from infinity at 0° incidence angle to

$$D_{\text{crit.}} = \frac{\lambda_i}{2 \sin \theta_c} \approx \frac{\lambda_i}{2\theta_c} \approx \frac{\lambda_i}{2\sqrt{2\delta_2}} = \frac{\sqrt{\pi}}{2} \times \sqrt{\frac{A_2}{N_\text{A} \times r_e \times \rho_2 \times Z_2}} \tag{II.14}$$

at the critical angle θ_c. Note that the latter value is independent of the incident X–ray wavelength λ_i and depends solely on the reflecting sample.

The boundary condition at the vacuum–sample interface implies that in the case of total reflection the phase shift between the incident wave and the reflected wave varies from π to zero if the incidence angle θ_i varies from 0° to θ_c. This means that at 0° the nodes of the wave–pattern lie on the sample surface and at the

critical angle θ_c the antinodes. The nodes correspond to the regions with destructive interference where the phase difference between the incident and reflected (or diffracted) beam corresponds to an odd multiple of π. Equivalently, in the antinodes the phase difference is an even multiple of π and constructive interference occurs. At the antinodes, the amplitude of the total wavevector (i.e., the sum of the incident and reflected wavevectors) is doubled and the intensity is multiplied by four (see Eq. II.12, assuming a reflectivity of 100%).

In the Bragg diffraction case, the conditions to fix the phase of the diffracted beam are more complex [10]. However, an angular scan through the Bragg region, i.e., the region in the vicinity of the Bragg angle, corresponds to a phase shift of π or equivalently to a shift of the nodal and anti–nodal lines by half of the lattice spacing d (into the crystal if the scan is performed from smaller to larger incidence angles). For the smallest angle the nodal lines and for the largest angle the anti–nodal lines are on the diffracting Miller planes. The nodal and anti–nodal lines present not only a periodicity corresponding to the crystal lattice spacing d but they are also parallel to the crystal Miller planes. Outside the Bragg region, the modulation of the wavefield is lost as the intensity of the diffracted beam decreases strongly [12]. In the TXRF case these lines are parallel to the surface. For both techniques the standing X–ray wave–pattern can be altered by an angular adjustment of the monochromatic incident X–ray beam: in the XSW case it is shifted, in the TXRF case it is compressed (when D decreases) or decompressed (when D increases).

The bulk background contribution to the experimental result is lower if the standing wave–pattern is created by TXRF than if it is produced by Bragg diffraction. On one side there is the peak reflectivity which can approach 100% in the total reflection case for perfect metallic mirrors but is usually lower for Bragg crystals. On the other side, there are geometrical considerations. In the TXRF approach, the evanescent wave propagation along the sample surface affects a narrower region than in a Bragg crystal irradiated at the Bragg angle. Nevertheless in both cases, the background contributions can be drastically reduced by tuning the wavelength λ_i of the incident X–ray beam above the absorption edge wavelengths of the bulk atoms (if the latter are below the absorption edges of interest for the experiment). The surface regions over which the standing wave–patterns extend vary inversely with the incidence angle θ_i and are thus larger in the total reflection regime for

identical beam widths. However, the X–ray source coherence lengths have also a major impact on the extension of the standing wave–pattern, especially in the height direction (along the z–axis) [13, 14].

II.6 TXRF instrumentation

The geometry of a TXRF setup corresponds to a special configuration of an energy–dispersive X–ray fluorescence (EDXRF) setup [15], the difference being the standing X–ray wave–pattern created in front of the sample. While for EDXRF the beam intensity in front of the sample surface has a constant value, it is characterized by local oscillations in the TXRF case (see Eq. II.12). The oscillations vary between zero and four times the intensity of the incident beam for a perfectly reflecting surface. Thus, in comparison to EDXRF, the fluorescence signal of particles above the surface is considerably enhanced since the probability for a photoelectric absorption is correspondingly locally enhanced. At the same time the background contribution is drastically reduced. Indeed, for typical TXRF incidence angles θ_i below the critical angle θ_c, only an evanescent wave penetrates a few nanometers into the sample (Fig. II.4), while in a standard EDXRF setup the primary beam penetrates up to a few micrometers into the sample (Fig. I.1). As a consequence a TXRF setup presents a drastically improved signal–to–background ratio compared to EDXRF.

Since TXRF is a special case of EDXRF, the instrumentation for measurements is similar, except that there are a few special requirements on the primary beam and the sample surface. Basically the setup for TXRF measurements consists of an X–ray source, a beam modulation unit, the sample with its holder and an energy–dispersive detector [6, 16–18] (Fig. II.5). In the choice of the setup components presented hereafter a difference needs to be made, depending on the purpose of the measurement [6].

1. If, for example, the aim is to check the quantitative elemental composition of grains or residues on top of a reflecting surface, measurements at a single, fixed incidence angle θ_i below the critical angle θ_c will be sufficient. Usually an incidence angle θ_i of about 71% of the critical angle θ_c is chosen. This incidence angle is called the isoradiant angle in [19].

2. If the goal is to assess, besides the elemental information, the structural,

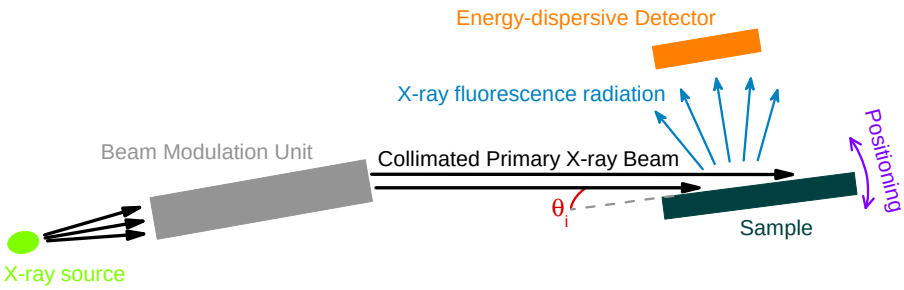

Figure II.5: Schematic view of the main components of a TXRF–based setup: the X–ray source which can be an X–ray tube or a synchrotron light source, the beam modulation unit for geometrical (and monochromatic) refinement of the X–ray beam, the sample, which in GIXRF setups can be oriented relatively to the beam, and the energy–dispersive detector for the measurement of the fluorescence X–rays. Details can be found in the text.

in–depth distribution of (buried) layers, for example, then the fluorescence intensity needs to be recorded at different incidence angles θ_i (below and also above the critical angle θ_c). Here a monochromatic incidence beam is required to avoid to blur the correlation between the standing wave–pattern and the local distribution of the fluorescence atoms.

These experimental requirements affect especially the beam preparation and sample positioning system. Experimental setups optimized for the first type of experiment are called TXRF setups, while for the second type of experiment they are called grazing incidence X–ray fluorescence (GIXRF) setups.

The X–ray source

The X–ray source may be a high power, fine focus X–ray tube with a fixed or rotating anode or a synchrotron radiation beam line. Only these two types of X–ray sources provide high enough intensities to realize measurements in a reasonable time interval. A synchrotron radiation beam offers the additional advantages of energy–tunability, monochromaticity, linearly polarization and low divergence. This reduces the requirements on the beam modulation unit.

The beam modulation unit

After the source the spatial shape and spectral distribution need to be refined. The beam incident on the target should be indeed a few micrometer high, the height being the vertical direction with respect to the propagation direction. For

reasons of angular resolution of the incidence angle, the beam divergence in the vertical direction should be very low. The width may be a few millimeter up to one centimeter and is mainly limited by the detector window's dimensions for easier quantification. A first refinement of the geometrical beam shape can be realized with collimator slits or metallic edges acting as diaphragms.

The refinement of the spectral distribution when an X–ray tube is used depends on the aforementioned experimental purposes. In the case of elemental quantification, it is sufficient to remove the high–energy part of the continuous Bremsstrahlung. Indeed Eq. II.5 shows that the critical angle θ_c depends inversely on the X–ray energy. Consequently total reflection conditions are more difficult to realize for high X–ray energies. Since the photoelectric cross–section diminishes also with the energy and as the high–energy part of the continuous Bremsstrahlung spectrum contains only a small fraction of X–ray photons (Fig. II.6), it is removed from the incident beam by a low–pass filter. The low–pass filter can be a either

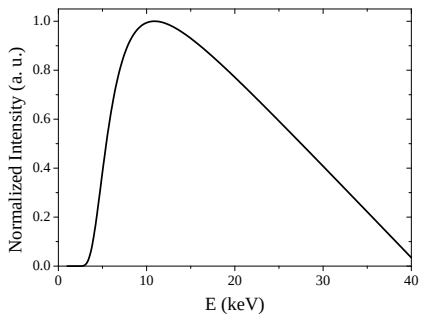

Figure II.6: Theoretical example for the continuous Bremsstrahlung distribution of an X–ray tube. In this example a W anode, a voltage of 40 kV and a 150 μm thick Be window were chosen. The characteristic lines (Lα at 8.398 keV, Lβ at 9.672 keV and Mα at 1.775 keV) of the anode are omitted.

metallic mirror or a perfect crystal or glass upon which the geometrically refined beam is incident at a grazing angle, called the cut–off angle θ_{cut} which depends on the selected cut–off energy E_{cut} (Eq. II.5). X–ray photons with a higher energy than the cut–off energy E_{cut} are not totally reflected and thus removed from the beam by absorption in the low–pass filter. To diminish the divergence of the beam and sharpen the cut–off in its spectral distribution, the beam may be multiply reflected, at the expense of a lower intensity. If the experimental purpose is the assessment of the elemental spatial distribution by a scan of the incidence angle θ_i, the spectral distribution needs to be adjusted by a monochromator to produce a monochromatic beam. For X–ray tubes this means that the characteristic flu-

orescence lines of the X–ray tube anode are to be used since the latter provide the highest X–ray intensities. For synchrotron radiation the choice of the primary X–ray energy is far less restricted. Different setup configurations or categories to modulate the beam are mentioned in [17]. In any setup it is essential that a (monochromatic) low–divergence beam is produced by the beam modulation unit.

The sample and its positioning

The incidence angle θ_i of the beam is controlled by positioning the sample adequately. The specific requirements on the sample positioning system depend on the experimental purpose. For elemental quantification with a laboratory X–ray tube and a fixed beam modulator unit where a single measurement at a fixed incidence angle is sufficient, the sample may simply be pressed against a reference holder to adjust the incidence angle θ_i. Otherwise a 5–axis motorized sample positioning system with 3 translational and 2 rotational (around the axes of the surface) displacement directions is necessary. The incidence angle θ_i needs to be known precisely and varied accurately. Geometrical effects due to the varying incidence angle are discussed in [20].

The reflecting surface on which the residues or grains are disposed, respectively the (layered) sample surface, have also to meet some requirements. Ideally it should be characterized by a high reflectivity R (to reduce the scattered background radiation), a very low roughness and the absence of waviness within the irradiated area in order to meet the requirement of being optically flat and smooth and presenting a sharp, plane vacuum (air) – sample boundary (section II.4). The requirements of sharp interface boundaries hold also for the layers of a layered sample; in addition the boundaries should be parallel to the surface so that the properties do not vary in a plane parallel to the surface. The effects of rough surfaces or layer interfaces in the grazing incidence geometry are widely discussed in literature and introduced in theory [21–28]. In the case of trace analysis with a typical TXRF setup, the carrier of the residues or grains should also be free of impurities and resist to cleaning with acids. Different types of glass carriers or pure crystals may assume the role of a carrier. At the same time the residue or grain size should be sufficiently small to not disturb the X–ray standing wave–pattern created on top of the reflecting surface [29].

The X–ray fluorescence detector

The excited X–ray fluorescence signal is detected by an energy–dispersive detector mounted close (about one centimeter) to the sample surface. The small distance between the detector and the sample surface ensures a large solid angle of detection and thus an efficient X–ray fluorescence signal detection, permitting to reduce the counting time. Different orientations of the detector with respect to the sample surface have been compared in [30] to find the best configuration. The use of a synchrotron radiation beam permits to reduce the background related to scattering. Aligning the sample surface along the linear polarization vector of the synchrotron beam diminishes indeed the scattered X–ray intensity in the detector direction [31]. Energy–dispersive detector present also the advantage of simultaneous multi–elemental detection, even if they suffer from a lower efficiency for X–rays emitted by low–Z elements. In this energy range the energy resolution, of about 130 eV for the best detectors, and escape peaks may be also troublesome.

The sample–detector assembly can be operated in air, a huge advantage with respect to other surface–analytical techniques. To reduce the absorption, a He environment may be advantageous. To further diminish the absorption effects, the whole setup can be placed in vacuum. This allows to use windowless detectors for a better detection of the X–ray fluorescence signal emitted by low–Z elements.

Developments

The different parts of TXRF setups have profited over the years from on–going technical developments and improvements. Profit was made of X–ray tubes with increased intensities and more efficient X–ray optics until physical limits were reached [32]. Detectors with improved signal–to–background ratios and better resolutions were made available. The advent of synchrotron radiation sources provided very intense X–ray sources. However, the increased source intensity results not only in an increased X–ray fluorescence intensity but also an increased background radiation from the sample with the risk to overload the detector. Detectors supporting high count rates, i.e., detectors with very low dead and shaping time are thus necessary to profit from the increased source intensity, the alternative being a decrease of the solid angle of detection. Silicon drift detectors (SDD), supporting count rates of up to 10^6 counts per second have nowadays replaced the Si(Li) detectors if a very bright X–ray source is used [16].

Different designs for the beam modulator unit were tested [33–35] and the use of polycapillary optics in the collimation direction [36], respectively the focusing direction, together with slits [37], was proposed instead. More details on polycapillary optics can be found in section IV.3.1.

II.7 Applications of TXRF

The TXRF experimental conditions at glancing incidence angles below the critical angle θ_c are characterized by a surface reflectivity close to 100% and a penetration depth of a few nanometers in the in–depth direction of the sample. Thus the main applications of the TXRF method are the surface and near-surface analysis of samples. Compared to standard X–Ray fluorescence (XRF) measurements, TXRF experiments profit from the significantly improved sensitivity, due to the more efficient excitation and drastically reduced background, for elemental detection at the sample surface region while preserving at the same time the advantages of being non–destructive, applicable to a wide range of materials and not very time consuming [15]. Another good point for TXRF compared to some other trace analysis methods is the possibility to regroup the different components in a compact laboratory spectrometer. This promoted the use of TXRF setups.

Elemental micro- and trace–analysis

One of the main applications of TXRF is (quantitative) micro- and trace–element analysis. TXRF was already used in this perspective in the late 1980's [38,39] and then promoted in the early 1990's as an efficient tool in this domain [40]. The quantification is realized by adding a well-known quantity of a reference element to the sample, in order to assess the detection efficiency; afterwards the different detected elements can be quantified with respect to the reference [13], the broad linear range of 3–4 orders of magnitude of the detectors being advantageous [16]. A drawback is that the sample mass needs to be known. Sampling techniques for TXRF are reported in [41]. Usually a small sample amount is deposited (either in the form of small grains or a droplet which is dried before the experiment) on a reflecting surface, the reflector, and irradiated at a fixed incidence angle θ_i below the critical angle θ_c determined by the reflector and the (shortest) wavelength λ_i of the incident X–rays. The experimental purposes are twofold, either the quantitative el-

emental composition of a sample or the presence of contaminants in or on a sample has to be assessed. In this perspective TXRF is used in a wide range of domains: in medicine for the analysis of human blood, blood serum or human hair [42–45] and the analysis of human tissues [46–50], in pharmacy to analyze drugs [51,52], in petrochemistry [53,54], in food science to detect harmful elements or to assess the environmental influences [55–60], in biology [61], in life sciences [62], in forensic sciences [63], in soil analysis and environmental sciences [64–67], in the analysis of materials used at nuclear plants [68], in archeology [69–72], in cultural heritage studies [73–76] and in the study of ancient artworks and historical objects [29].

Especially in the latter domains the micro- and trace–analytical capabilities prove to be useful. Indeed minute sample amounts are sufficient for the analytical purposes and the acquisition of reliable results. An overview of the sample preparation methods is presented in [13], where it is shown that special care is necessary for the homogenization of the sample. The advantage is that the object of study remains almost unaltered and is thus preserved. The sample does not need to be displaced, nor does the detection setup. Thus the analysis is completely non–destructive, the representativeness of the results obtained with very small sample pieces compared to the object of study remaining, however, questionable in some cases.

Surface contamination control

The most successful micro- and trace–analysis application with regard to industrial applications is, however, the detection of contaminants on semiconductor wafers which are detrimental to the functioning of the devices to be produced [77]. The aims are to sort out contaminated wafers before further processing, to trace the contamination sources and to survey the cleanliness of the different production processes of a semiconductor device [78]. The possibility of automatized analysis (sample preparation, measurement and data analysis), in–line of the production chain between two different processing steps, and the relatively facile control of the technical elements of a TXRF setup together with an easy data management make it a widely used industrial monitoring tool [32]. TXRF setups are operated in many cleanrooms to support further developments. A requirement is however, that the TXRF sample holder provides enough space to load and orientate adequately the wafers which have presently a diameter of 300 millimeters and 450 millimeters in the near future. The continuing trend of decreasing devices sizes

increases the demands on the contamination control in terms of detection limits down to ultra–trace levels (about 10^8 atoms/cm^2 or femtogram amounts with pre–concentration techniques) nowadays. The "International Technology Roadmap for Semiconductors" (ITRS) consortium publishes regularly roadmaps for semiconductors (developments, perspectives, monitoring and future requirements). In this perspective, synchrotron radiation sources helped to match the industrial requirements regarding the detection limits, especially for low–Z elements where X–rays of 1–2 keV are advantageous. X–ray tubes cannot be used efficiently in this energy domain. Since their spectral output shows the highest intensities for larger energies, alternative X–ray sources are necessary.

The trace contaminations on the Si surfaces to be tracked are either metallic elements [19, 79, 80] or low–Z elements [30, 31, 81–84]. The difficulty for observing low–Z contaminants is given by the background originating from the bulk Si of the wafer. Even if the strong Si–Kα peak is not excited by choosing an X–ray energy below the K absorption edge (either with an energy–tunable X–ray source or by selecting the W–Mα line of an X–ray tube with a W anode), the resonant Raman scattering (RRS) from Si [85] is overlapping with the Kα–line of elements lighter than Si [86]. The poorer efficiency of the detector for low X–ray energies and their limited resolution are not helpful in this perspective. The detection efficiency can be improved by placing the whole TXRF setup in a vacuum chamber: window–less X–ray tubes (for a more efficient excitation of the low–Z elements) or detectors with either very thin Be windows or without window (to diminish the absorption of the fluorescent X–rays) can then be used. Organic contaminants, which are even lighter than the low–Z elements discussed so far, have been traced by combining TXRF with the near edge X–ray absorption fine structure (NEXAFS) technique, looking at the absorption edges of different organic compounds [87].

To further enhance the sensitivity to surface contaminants, TXRF can be combined with vapor phase decomposition (VPD), a pre–concentration technique [16, 19, 32, 88, 89]. The idea is to collect the contaminants dispersed over the whole surface at a single surface spot which is then irradiated by the X–ray source to perform the TXRF measurements. The principle is to etch the native silicon surface oxide layer away with a high purity hydrofluoric acid and to collect afterwards the contaminants by scanning the wafer with a microliter droplet of a water–based solution. Finally the droplet is dried and the residue deposited on the wafer sur-

face constitutes the sample. Due to the risk of loosing parts of the sample by evaporation or inhomogeneous residue deposition, the drying process is the most critical step. The order of magnitude of the improvement factor offered by the VPD pre–concentration technique in terms of detection limits is given by the ratio of the wafer size to the irradiated spot size seen by the detector, assuming an initially homogeneous distribution of the contaminants over the wafer surface and that the whole residue is irradiated during the experiment. Improvement factors of two to three orders of magnitude are reported in [19,31], depending on the wafer diameter (100 – 300 millimeters in diameter) and the area irradiated on the sample seen by the detector (about 0.5 cm^2). On the other side any spatial information on the initial position of the contaminants is lost, only the integrated amount of surface contamination being detected by the combined VPD–TXRF method [31].

If mapping capabilities are required, which help to track and eliminate the contamination source in a production process, the TXRF setups have to be partially modified. A rough mapping of the surface contaminants is obtained with the Sweeping–TXRF method [88, 90, 91]. The sample is moved gradually in the plane of its surface, the incident beam and the detector being kept fixed in space. The result is that the wafer surface is subdivided into different regions, for each region a TXRF spectrum is measured. The sum of the different spectra will give the integrated surface contamination and the individual spectra allow to localize the contaminants on a rough scale, the scale size being given by the intercept of the region seen by the detector and the region irradiated by the incident beam. The detection limits are, however, worse than those obtained with VPD–TXRF.

The quantification of the contaminants is usually realized by adding an internal reference standard. At the Physikalisch–Technische Bundesanstalt (PTB) in Berlin, the quantification is realized in a reference–free manner by an exact calibration of the instrumentation and an approach based on the knowledge of the atomic fundamental parameters [92]. This allows circumventing problems related to deviations from the expected linear response between the contaminant concentration and the X–ray fluorescence intensity when an external standard is used for quantification. A quantification attempt with solely theoretical calculations is presented in [93].

Depth–profiling

Besides the wafer surface, it is also possible to analyze the in–depth direction, i.e., to perform depth–profiling of ion implanted Si wafers by means of TXRF. Ion implantation is used to dope the semiconductor wafer with atoms in order to alter its physical properties in a controlled manner for the realization of different applications. Two approaches for depth–profiling by means of TXRF are used: TXRF combined with etching or GIXRF (see section II.6). A single TXRF measurement at a single incidence angle does not permit to retrieve structural information so that either sequential TXRF measurements of different sample regions have to be performed or the dependence of the X–ray fluorescence intensity on the incidence angle θ_i has to be measured. In the first approach, promoted by R. Klockenkämper et al., either the previously oxidized sample surface is etched chemically with an acid droplet and subsequently the residue of the dried droplet, placed on a reflector, as well as the freshly oxidized surface are analyzed by means of TXRF [94–96] or the sample surface is etched by ion sputtering with a subsequent TXRF analysis of the etched surface [97, 98]. Note that after an ion sputtering etching process the sample surface is still smooth and flat enough to be analyzed by TXRF. If chemical etching is applied, it is assumed that only the Si atoms are oxidized and that they are completely oxidized. The last assumption is necessary for quantification reasons. Before and after each etching step the Si wafer is weighted in order to deduce the etched quantity (differential weighing). The depth–resolution is of the order of one nanometer and it depends on the amount of etched material. It varies also with the ratio of bulk wafer atoms and implanted atoms present at the surface and the penetration depth of the evanescent wave. A comparison of the depth–profiling results obtained by the combination wet–chemical etching and TXRF together with the depth–profiles obtained from different other depth–profiling techniques can be found in [99].

GIXRF, the second TXRF–based method for depth–profiling is based on the fact that the penetration depth of the incident X–ray beam depends significantly on the incidence angle θ_i (see Fig. II.4), which makes accessible different depth regions by varying the incidence angle θ_i. Thus the number of implanted atoms which can be excited by the incident beam and accordingly the X–ray fluorescence intensity varies with the incidence angle θ_i. The dependence of each dopant's X–ray fluorescence line on the incidence angle θ_i contains thus information on the distribution

of the implanted atoms in the depth–direction of the sample. This approach for depth–profiling of ion–implanted samples has been used in [100, 101] and more recently in [102] and in [103] in combination with SIMS for ultra–shallow implantation profiles in Si. The depth–profile of the implanted ions may be retrieved by inverse modeling: starting from a reasonable assumption on the depth–profile, the standing wave–pattern and the primary beam penetration into the sample is simulated and the expected fluorescence intensity at the different incidence angles is calculated and compared to the experimental angular intensity profile in order to improve the initial assumption and converge to a final result [19]. From the point of view of calculations, the recursive algorithm presented in [5] for the calculation of the angular intensity profiles $I(\theta_i)$ is more difficult to apply to the inverse problem, i.e., the characterization of the structural elemental distribution from the observed angular intensity dependence. GIXRF was also used for the analysis of implanted solar wind particles, the sensitivity of the technique proving to be useful to distinguish the ions collected during the NASA mission from the terrestrial surface contamination caused by the landing crash [104].

GIXRF allows also depth–profiling measurements of other types of samples, multilayers or thin films deposited on a surface [5, 35, 105–107]. The thickness and the density of the films as well as the elemental amount or quantity of deposited material are assessed. For layers and thin films having a refractive index n_l superior to the refractive index of the underlying substrate n_s, a standing wave–pattern is created inside the sample leading to a enhanced excitation efficiency of the layer atoms. Note that the critical angle allows to deduce the density of the surface layer (Eq. II.5). However, the physical properties of a thin film differ significantly from the bulk properties [108] and the surface roughness of the substrate on which the films is deposited should be known [27]. Actually, in most cases the assumption of homogeneous and discrete layers is made in the data analysis, but the physical sample needs to satisfy this condition for a reliable interpretation. Depth–profiling of thin films has also been realized by means of TXRF combined with sputter–etching [109–112].

Finally TXRF and GIXRF can be applied to a wide range of samples to determine their elemental composition as well as their near–surface structure. While TXRF provides (quantitative) elemental information, GIXRF measurements permit to distinguish between different types of surface depositions or types of sam-

ples: bulk samples, (buried) layers, multilayers, implanted samples, residual grains. The modulation of the X–ray standing wave–pattern above the sample surface for incidence angles θ_i varying below the critical angle for total external reflection θ_c and the increasing penetration depth for increasing incidence angles θ_i above the critical angle θ_c influence significantly the detected X–ray fluorescence intensity. The evolution of the intensity with the incidence angle θ_i differs with the type of sample. Grains, particles or residues on top of a reflecting surface are the most efficiently excited for incidence angles θ_i below the critical angle θ_c while (buried) layers and implanted samples are the most efficiently excited around the critical angle. Consequently the highest fluorescence intensity is observed below the critical angle θ_c for residues, particles and grains and around or above the critical angle θ_c for other samples. This difference allows already to distinguish qualitatively between different samples independently of the element. In [19] it is proposed, based on a similar discussion, to distinguish between a particle- and a layer–like surface structure by simply comparing the X–ray fluorescence intensity of a sample at two different incidence angles θ_i below the critical angle. On the other hand the angular intensity profile of a bulk sample is characterized by an increasing intensity once the incidence angle θ_i has passed the value of the critical angle θ_c. GIXRF is thus an efficient and versatile surface analytical tool.

Chapter III

Grazing Emission X–ray Fluorescence

An alternative to or rather a variant of TXRF, resp. GIXRF, for surface–sensitive analysis by X–ray fluorescence detection is grazing emission X–ray fluorescence (GEXRF). The basic idea is to switch from an angle–dependent excitation process under grazing incidence conditions to the detection of the angular dependent X–ray fluorescence intensity under grazing emission conditions. In GEXRF the X–ray fluorescence radiation is detected at angles that are similar to the incidence angles of the primary X–ray beam in GIXRF setups. In a GEXRF setup the primary beam for X–ray fluorescence excitation is in principle perpendicular to the sample surface, as was the detection direction in a GIXRF setup. Thus, a GEXRF setup is sometimes called an inverted GIXRF setup since the paths for excitation and detection of X–ray fluorescence are exchanged between the two geometries. Actually, the two setups are not only similar but also equivalent from a physical point of view.

III.1 Principle of microscopic reversibility

The grazing emission geometry was first introduced and compared to the grazing incidence geometry in 1983 by R.S. Becker, J.A. Golovchenko and J.R. Patel [113]. In the latter geometry, as discussed previously, total external reflection and an evanescent wave propagating into the (optically less dense) sample are observed. By varying the incidence angle θ_i the strength of the evanescent wave varies due to the varying penetration depth (kinematical factor) and the changing standing wave–pattern (dynamical factor). For continuity reasons the intensity of the

evanescent wave has to be equal to the one of the standing wave at the surface interface. Below the critical angle of incidence θ_c, the incident beam is expelled from the target by the reflection but there is also a non–negligible chance for absorption due to the evanescent wave propagating along the sample surface. In this angular range the evanescent wave has to match at the interface the external conditions described by the interference of the incident and the reflected X–ray beam. As explained previously, the standing wave–pattern created by the incident and totally external reflected X–ray beam presents nodal and anti–nodal lines parallel to the surface. At 0° incidence the wave–pattern presents a nodal line at the surface interface which changes gradually into an anti–nodal line as the incidence angle varies from 0° to the critical angle θ_c.

In the grazing emission geometry, no external standing wave–pattern is created due to incidence angles far above the critical angle for total reflection. Only a fraction of a percent of the primary beam is reflected at the surface, the major part penetrates into the bulk sample. This is the first major difference with GIXRF where only the near surface region is excited by the primary X–ray beam. In GEXRF, however, for sufficiently small observation angles θ_e relatively to the surface only the X–ray fluorescence emitted by surface–near atoms is observable. Indeed X–rays emitted from atoms located far from the interface, are considered as plane waves which are refracted and reflected at the boundary interface(s) according to the Fresnel laws. At the sample vacuum interface, the fluorescence X–rays propagate from an optically less dense into an optically denser medium. Accordingly the fluorescence X–rays are refracted away from the interface (see discussion and equations in section II.2). The consequence is that for a range of observation angles between 0° and the critical angle θ_c relatively to the sample surface no fluorescence X–rays emitted from the bulk atoms can be detected. This angular range is indeed simply inaccessible for X–ray radiation (fluorescence and scattered X–rays) produced far from the surface. This results in a considerably enhanced surface sensitivity as the contribution of the bulk atoms to the detected intensity is suppressed and explains why GEXRF is also a surface–sensitive XRF technique. Note that the critical angle θ_c (Eq. II.5) referred to in a grazing emission setup is defined relatively to the wavelength λ_e of the fluorescence X–rays and not to the one of the primary X–rays (λ_i) as in grazing incidence setups. The X–ray fluorescence radiation emitted by near–surface atoms is described at the interface by spherical waves. A Fourier decomposition of the latter shows that the correspond-

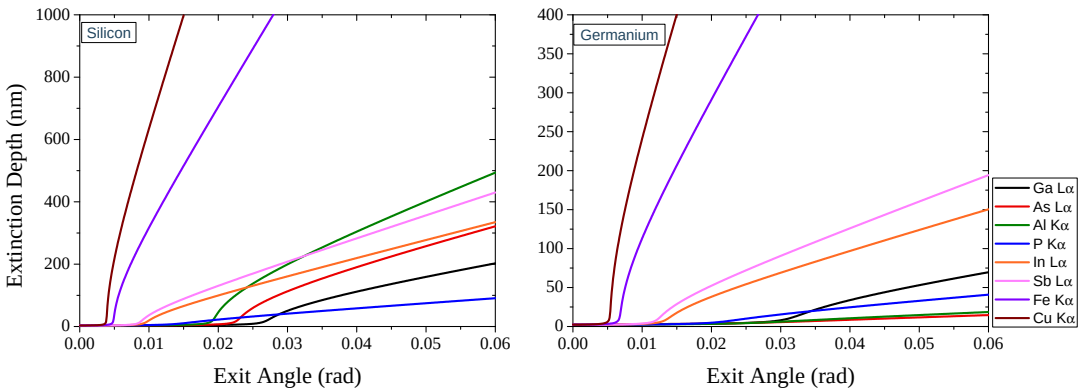

Figure III.1: Plot of the extinction depth as a function of the emission angle θ_e for different dopant X–ray fluorescence lines in Si and Ge wafers. The extinction depth shows at which vertical distance from the wafer surface the fluorescence atoms, whose signal is attenuated by a factor e^{-1} upon emission in the direction θ_e relatively to the surface, are located. It gives an estimate of the sample depth at which implanted dopants still contribute in a significant way to the production of the measured X-ray fluorescence signal. In the grazing emission geometry, the extinction depth depends on the emission angle θ_e, the fluorescence wavelength λ_e and the wafer. Comparable extinction depths as for the grazing incidence geometry (Fig. II.4) are observed.

ing evanescent wave has a non–negligible amplitude [8]. Thus grazing emission is characterized by the excitation of an internal evanescent wave, equivalently to the evanescent wave in grazing incidence.

A comment should be made if the GEXRF measurements concern residues, grains or particles on top of a reflecting surface. For the mentioned types of samples the grazing emission geometry does not profit from a standing wave–pattern which enhances the probability for fluorescence excitation as does the grazing incidence geometry. Nevertheless grazing emission setups also show an enhanced sensitivity with respect to standard XRF for these types of samples. The reason is that there is more than one detection path. Indeed either the fluorescence X–rays can be emitted directly towards the detector or the second possibility for detection is via a reflection on the optically smooth and flat substrate surface (see Fig. III.2). Thus, for emission angles θ_e below the critical angle θ_c the probability for detection is doubled. The same argument holds for thin layers and films on a substrate if the refractive index of the substrate n_s is smaller than the refractive index of the layer n_l. This is the same condition as the one for the creation of a standing wave–pattern inside a thin film or layer. Considering a fluorescence X–ray source

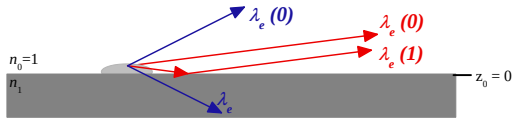

Figure III.2: For an emission angle θ_e (defined relatively to a line parallel to the substrate surface) smaller than the critical angle θ_c (red paths in the figure), there are two possible detection paths due to the reflection on the substrate surface. Once the emission angle θ_e is above the critical angle θ_c (blue paths in the figure), only the X–rays directly emitted towards the detector contribute to the measured fluorescence since X–rays are no longer reflected at the surface and penetrate into the bulk.

at height z above the reflecting substrate surface, the path difference between the direct detection path and the one with a single reflection is $2 \times z \sin\theta_e$. Depending on the emission angle θ_e and thus the length difference between the two detection paths, the fluorescence X–rays can interfere constructively or destructively. Constructive or destructive interferences will not only occur for fluorescence X–ray sources at the considered height z, but simultaneously also for fluorescence X–ray sources at other, precise heights. This leads to the creation of interference planes parallel to the sample surface, the position of the planes depending on the emission angle θ_e. The period in the height direction of the interference pattern created by the coherently emitting sources is similar to the one corresponding to the nodal and anti–nodal lines in the grazing incidence geometry (Eq. II.13),

$$D = \frac{\lambda_e}{2\sin\theta_e} \tag{III.1}$$

except that in the grazing emission geometry the fluorescence X–ray wavelength λ_e and the emission angle θ_e are to be considered.

Due to the inverted experimental setup and because the same physical principles are valid for the two geometries, grazing incidence and grazing emission are closely related to each other. This can be further explained by the principles of microscopic reversibility and reciprocity: if grazing incidence and grazing emission experiments were performed with the same wavelength λ, the distributions of the atoms contributing to the observed fluorescence yields would be identical [113]. However, the wavelengths λ of interest cannot be identical. Since the wavelength λ_i of the X–rays used to excite the samples is always smaller than the one (λ_e) of the fluorescence X–rays ($\lambda_i < \lambda_e$), the critical angle θ_c will be smaller in the grazing incidence geometry than in the grazing emission geometry. The angular scale

is thus changed. The depth distribution of the atoms contributing to the measured fluorescence yield will also differ due to the slightly different absorption coefficients.

Mathematically the reciprocity theorem can be formulated as follows. Two sufficiently small radiating dipoles at two distinct positions, $\vec{r_1}$ and $\vec{r_2}$, and with moments $\vec{P_1}$ and $\vec{P_2}$, respectively, satisfy the reciprocity law if

$$\vec{E_1}(\vec{r_2}) \cdot \vec{P_2} = \vec{E_2}(\vec{r_1}) \cdot \vec{P_1} \tag{III.2}$$

where $\vec{E_k}(\vec{r_l})$ is the electric field created at the position $\vec{r_l}$ by the radiating source located at $\vec{r_k}$ [114]. As shown by Eq. III.2, an exchange of the source and detection position will not affect the result. Reciprocity for sound waves and EM waves goes back to Rayleigh, Stokes, Lorentz and Helmholtz. A more recent review concerning reciprocity in optics can be found in [115] together with a discussion for stratified media and multilayer stacks.

III.2 GEXRF setup

In GEXRF setups (Fig. III.3), components of the GIXRF setup can be retrieved, which, considering the reciprocal equivalence, is not surprising. However there are a few distinctions. The primary X–ray beam can be produced by an X–ray tube or a synchrotron radiation source as in GIXRF setups. However, an electron gun [116] or a particle accelerator [117, 118] can also be envisaged. A laser plasma source was also investigated [119]. Thus GEXRF setups are not solely limited to X–ray sources but other sources for the excitation of the X–ray fluorescence radiation can also be chosen. GEXRF setups are indeed less restrictive towards the exact production process of the fluorescence radiation since the experimental results depend on the refraction of the fluorescence X–rays and not on the reflection of the primary X–rays at the sharp sample interfaces. Therefore in GEXRF setups one speaks more generally about an excitation source rather than about an X–ray source. The independence of GEXRF on the excitation source allows to acquire for one sample different data sets without changes in the experimental setup by realizing measurements with different fluorescence lines [8].

Consequently a beam modulation unit between the excitation source and the sample is not absolutely necessary. Indeed neither the spatial nor the spectral distribution of the beam produced by the excitation source needs to be modified, except

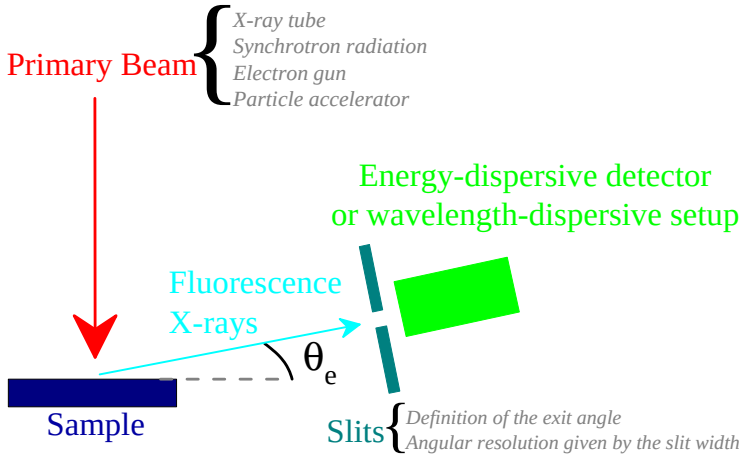

Figure III.3: Illustration of the grazing emission geometry and the main components of the latter. The X–ray fluorescence production can be realized in different ways. The definition of the emission angle θ_e requires a collimation of the fluorescence X–rays. A detailed description can be found in the text.

if the background is to be improved. This offers the possibility to use collimated and microfocused beams to realize surface mapping applications with a resolution of a few tens of micrometers [120]. With the sweeping–TXRF technique mapping applications can also be realized with the grazing incidence geometry, but the spatial resolution is much broader (section II.7).

The requirements on the sample surface and the sample positioning system are for grazing emission setups the same as for grazing incidence setups (section II.6). The only difference is that in the grazing emission geometry, it is not the angle of incidence θ_i of the primary beam which is controlled but the emission angle θ_e. The emission angle θ_e needs to be as well–defined and controlled as is the incidence angle θ_i in the grazing incidence geometry. Sometimes cooled sample stages are used to prevent thermal deformation. The control and the variation of the emission angle θ_e is usually realized by rotating the sample but it can also be realized by moving the detection system as will be explained below. The definition of the emission angle is usually realized by an adjustable (double) slit collimator system placed in front of the detection system. The opening of the slits, their separating distance as well as the separation distance to the irradiated sample system define the angular resolution of the system. Reported angular resolutions are of the order of mrad or lower [8, 14]. In addition, in each setup a compromise between angular resolution and detection sensitivity has to be made depending on the main exper-

imental purposes (trace–element control or structural surface characterization).

The detection system for the fluorescence X–rays can be an energy–dispersive or a wavelength–dispersive system[1], contrarily to grazing incidence systems where usually only energy–dispersive systems are used with some exceptions where combinations with wavelength–dispersive setups were studied [32]. Since in the grazing incidence geometry the beam modulation system reduces the effectively used X–ray intensity to a fraction of the total X–ray intensity emitted by the X–ray source, a detection system with a high solid angle for detection is used for compensation. In the grazing emission geometry the full intensity emitted by the excitation source can in principle be used for the production of the X–ray fluorescence. This is an advantage, but the fluorescence X–ray radiation has then to be collimated in order to define the emission angle θ_e, which leads to low solid angles of detection, a main disadvantage of GEXRF setups. The collimation of the fluorescence radiation is realized automatically in wavelength–dispersive detection setups, the insertion of slits for a further collimation being only necessary if the angular resolution has to be refined. This offers the possibility to profit from the advantages of wavelength–dispersive setups without being too much penalized by the small solid angle characterizing wavelength–dispersive instruments.

The main advantages offered by wavelength–dispersive setups are their energy resolution and good background rejection capabilities, which considerably increases the sensitivity towards low–Z elements by a better separation of their fluorescence lines from other X–ray lines and an improved signal–to–background ratio. This compensates the lower detection efficiency which is due to the somewhat smaller solid angle for detection. The low–Z sensitivity was one the main motivations to develop wavelength–dispersive GEXRF spectrometers [121] as a complement to the grazing incidence setups used for metallic contamination control. A greater sensitivity to chemical states (when measuring X–ray emission lines where a valence shell is involved in the atomic decay process) and a good separation of the many L–lines of mid–Z elements and / or M–lines of heavy elements can also

[1]For geometries with a vertical focusing, grazing emission geometries can be realized quite straightforward as will be shown in this thesis. For a horizontal focusing geometry, a modification of the geometry and a position–sensitive detector would be required. In the latter case a the angular dependent intensity profile could possibly be acquired at once, while in the former case it has to be measured sequentially.

be achieved with wavelength–dispersive detection setups. The main idea of a wavelength–dispersive detection setup is to separate the fluorescence X–rays by their wavelength λ_e with a dispersion device which deviates the X–rays to the detector. Depending on the detector (position–sensitive detection or not), either a single X–ray energy corresponding to the wavelength λ_e is measured by the detector or an energy range, which is, however, much narrower than in energy–dispersive detectors. Thus, wavelength–dispersive setups are not suitable for the elemental determination of an unknown sample since the alignment of the dispersion device and the detector depend on the wavelength λ_e of the X–rays which are to be measured. In GEXRF measurements a single fluorescence line of wavelength λ_e is usually measured, so that it is in principle not necessary to cover a broad energy–range (for background–free conditions).

Energy–dispersive detection setups can also be used in combination with grazing emission setups at the expense of the advantages offered by wavelength–dispersive detection. The solid angle for detection will not be significantly increased, but the intensity profile of multiple X–ray fluorescence lines of different elements can be recorded simultaneously (and not sequentially as with a wavelength–dispersive detector). By controlling the position of a light–weighed detector and moving it on a circle centered on the irradiated spot on the sample surface, the emission angle θ_e can also be varied [14], the incidence angle of the primary beam on the sample being kept constant throughout the experiment. In this case, the requirements on the angular control and accuracy are valid for the detector positioning and no more for the sample positioning.

In the grazing emission geometry, the double collimator slit system and / or the dispersive device (grating or crystal of the wavelength–dispersive detection setup) is the equivalent of the beam modulation unit in a grazing incidence setup. Spectrometers using the grazing emission geometry were particularly developed in the late 1990's [121–123].

The combination of grazing incidence and grazing emission geometries has also been realized [27, 124–128]. Either the dependence of the X–ray fluorescence intensity on the incidence angle can be measured for different emission angles or vice–versa. Due to the collimation of the incident and emitted X–ray radiation, the detection efficiency of these setups is reduced. Thus, they were not used for

trace analysis but only for thin film analysis, the chemical conditions and roughness issues at the surface and the interfaces between two layers being analyzed together with the film density and thickness. The main motivation for this type of setup is the very low background. A further motivation is that the control of the incidence and the emission angle, and consequently the observation depth due to the refraction and absorption processes of the incident and emitted X–rays, allows to obtain more information on the sample's structure due to the many data sets which can be acquired. As in the standard grazing emission geometry, the data sets can be further extended by realizing measurements for different fluorescence lines. In addition the excitation and the detection process focus both on the near–surface region. Alternatively the grazing incidence X–ray beam can be replaced by an electron beam for the excitation of the X–ray fluorescence. Electrons do not penetrate much further than the near–surface region and thus the X–ray fluorescence production would also be limited to the near–surface region, i.e., a region comparable to the extinction depth of the grazing emission geometry at large exit angles θ_e.

It can also be mentioned that in [127] the dependence of the X–ray fluorescence intensity on the grazing emission angle was assessed with a simple imaging plate without a slit collimator system in front. This allowed to acquire the X–ray fluorescence intensity dependence on the grazing emission measurement in a single measurement and not in a series of sequential measurements as with the setups presented so far. In the grazing incidence geometry there is no alternative to point–by–point measurements due to the nature of the definition of the incidence angle. The disadvantage of X–ray detection with an imaging plate is that there is no energy discrimination at all: different elements cannot be distinguished and background events not rejected.

III.3 GEXRF applications

GEXRF setups are used for similar applications as TXRF and GIXRF setups which is not surprising since both techniques are based on the refraction of X–rays. Thus the application domains for the GEXRF method are the same, with identical motivations, as those presented in section II.7 for TXRF and GIXRF, the advantages offered by the grazing incidence geometry being preserved. The

first applications concerned the characterization of Ag monolayer adsorbates on Si [129] and depth–profiling of As implants in Si [128].

In the domain of micro- and trace–analysis the GEXRF method has been applied for tracing Na, Zn and Pb [130], resp. Si [131] in an organic matrix, metals in drinking water [132], low–Z elements on Si surfaces [8, 133] or in marine aerosols [134] and metallic contaminants on Si surfaces [135, 136]. GEXRF was further used for the analysis of pigments of an artwork in cultural heritage [137] and the determination of the weight of polymers deposited on a Si substrate [138]. Tap water analysis by means of GEXRF together with a review of the necessary sample preparation for trace analysis of liquid samples, i.e. the reflecting carrier and the droplet deposition, is discussed in [139]. Similarly to the grazing incidence geometry, a measurement at a single emission angle θ_e is sufficient for trace–analysis. An emission angle of 71% of the critical angle θ_c as for TXRF setups (section II.6) is proposed in [140]. For spatial information, however, the intensity dependence on the emission angle θ_e has to be measured. For trace analysis special substrates with a periodic structure were proposed to enhance the sensitivity [141]. Detection limits similar to [120] or one order order of magnitude lower [14] than the detection limits achieved with TXRF based setups were reported. On a theoretical basis similar detection limits are expected [142], the lower detection efficiency of GEXRF setups being expected to be partially compensated by their better signal–to–background ratio with respect to TXRF and GIXRF setups. An experimental comparison between TXRF and GEXRF with plate beamguide devices showed, however, that for most elements TXRF presents better detection limits, the difference being of up to one order of magnitude. The VPD pre–concentration technique allows in principle to improve the sensitivity of a GEXRF setup more than the sensitivity of a TXRF or GIXRF setup since in a GEXRF setup the irradiated area of the sample surface is smaller than in TXRF or GIXRF setups [120, 133]. If the residue of the droplet fits the irradiated area in a GEXRF setup, the enhancement factor for a GEXRF setup is larger than for grazing incidence setups according to the arguments presented in section II.7,.

The quantification issues with GEXRF setups are also discussed in literature [140, 143]. For low–Z elements the calibration curves for quantification (intensity versus sample amount) are not absolutely linear. If this problem can be dealt with by choosing carefully the calibration standard, the fact that the sample ma-

trix considerably influences the results is a more serious problem [139]. Sample inhomogeneities are to be avoided due to the larger pathlength of the fluorescence X–rays in the grazing emission geometry compared to the pathlength of the incident X–ray beam in the grazing incidence geometry at a comparable angle. Indeed the sample structure will considerably influence the X–ray fluorescence intensity due to the high mass attenuation coefficients for low–energy X–rays. The elemental composition and density (lateral and vertical) distribution need to be known beforehand in order to perform quantification calculations with a model sample which is as close as possible to the real sample. One solution consists in observing the elastic and inelastic scattering peaks, since their intensity also depends on the matrix [143]. This allows to obtain more information on the sample. A shift of the critical angle θ_c depending on the sample surface was observed [144]. Since this shift depends on the surface or interface density ρ (Eq. II.5), it can be used in the quantification. The shift of the critical angle θ_c indicates a gradual transition from a particle– to a layer–like structure on the surface: it is the surface of the layer and no longer the surface of the carrier or substrate which determines the critical angle θ_c For particles, the size or thickness affects also the slope of the quantification curves [140]. Of course the surface roughness also affects the experimental results since the reflection coefficient of the particle–carrier interface with air is directly influenced. Thus, many physical parameters need to be accurately known in order to realize a reliable quantification.

The GEXRF technique is also used to a great extent for thin–film and layer analysis of metallic elements or alloys [8, 144–153] in order to study surface oxidation, growth processes or simply the density and thickness of the deposited films. The sensitivity of wavelength–dispersive detection setups towards elemental chemical states is essential for some of the applications. The GEXRF method shows a good potential for layer characterization and for process control, the layer density being the control parameter. To obtain besides the elemental information also structural information on the thin films, the X–ray fluorescence intensity dependence on the emission angle θ_e has to be measured. The oscillations observed in the angular intensity profile of the Cr-Kα line of Cr/Au/Cr layers deposited on quartz glass were interpreted as an experimental evidence of the reciprocity theorem (section III.1) [153]. The oscillations are due to constructive interferences (section III.1). A rather original application was realized in [154]: the intensity of the Ni-Kα line of a Ni layer deposited on a thick Pt layer was enhanced by sandwiching it with

C layers. The angular intensity profile was found to depend strongly on the thickness of the C layers. In principle this method could thus also be reversed to detect indirectly low–Z layers (Fig. III.4).

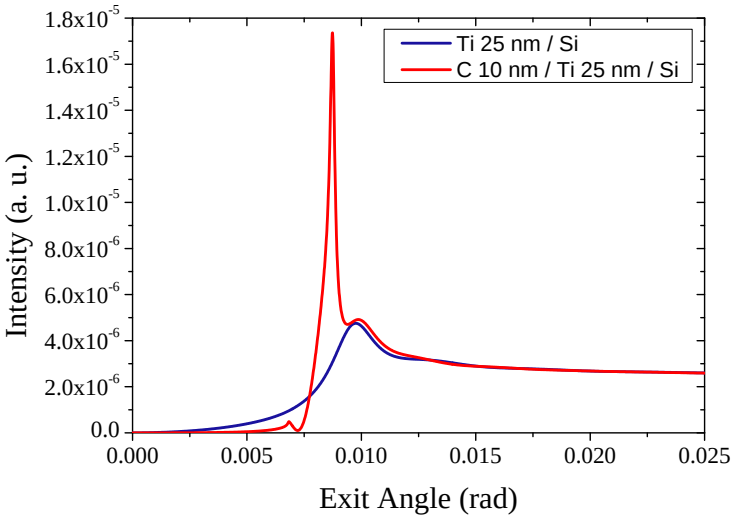

Figure III.4: The presence of a thin C layer below a Ti layer strongly influences the angular intensity profile $I(\theta_e)$ of the Ti Kα–line.

In section III.2 it was mentioned that the grazing emission geometry is favorable for mapping applications. This was realized with micrometer–resolution in [120] with a collimated synchrotron beam and in [155–157, 168] with a polycapillary optics mounted in front of an X–ray tube. Together with depth–profiling, this offers the possibility for 3D measurements with a good spatial resolution [158].

Experimental depth–profiling of implanted ions in a wafer by means of GEXRF has been less addressed in literature. This application has been realized in the present thesis (chapters V and VI) and has been partially presented in [159].

Particles and aerosols deposited on a surface or thin films on top of a substrate have also been analyzed with a GEXRF setup combined with electron excitation for the characteristic fluorescence X–ray radiation [117, 160–164], thus limiting fluorescence excitation to the near–surface region, or with particle induced X–ray emission (PIXE) [117, 118]. For the latter case the sensitivity enhancement for the near–surface region with respect to standard XRF has also been shown [118]. In the following chapter, however, only photon–induced X–ray fluorescence will be considered.

For the sake of completeness it should also be mentioned that both the grazing incidence and the grazing emission geometries can be combined with other X–ray analytical techniques like absorption (with grazing incidence [39, 165–167] and grazing emission [168–170]) and diffraction (with grazing incidence [171, 172] and grazing emission [150]) to realize more specific applications like the assessment of the nearest–neighbor configurations. Note that in the grazing incidence geometry the critical angle θ_c varies with the incident beam energy, while it does not in the grazing emission geometry.

III.4 Intensity Calculations

In this section the angular dependence of an X–ray fluorescence line of wavelength λ_e on the emission angle θ_e will be calculated. The angular dependence of the intensity in the grazing emission geometry could be calculated by using the reciprocity theorem III.1 to derive the angular profile from calculations made in the grazing incidence geometry [114]. Another approach would consist to use a matrix formalism to profit from the mathematical properties of the Hessenberg matrix for simulating the propagation of an electromagnetic wave through a stratified medium [173–175]. On the other side H.P. Urbach and P.K. de Bokx presented an approach to calculate the angular intensity profile by considering directly the radiating X–ray fluorescence sources distributed in the sample and calculate for each emission angle θ_e their individual contributions to the detected X–ray fluorescence intensity [114, 176]. In this approach, the total X–ray fluorescence intensity for the emission angle θ_e is obtained by summing the contribution of all the radiating sources. Physical phenomena influencing the X–ray fluorescence intensity are directly taken into account, thus the final formula for the angular intensity distribution $I(\theta_e)$ of X–rays of wavelength λ_e is more transparent in terms of physical processes than other calculations. This is useful when the inverse process is addressed, the characterization of a sample starting from experimental angular intensity profiles $I(\theta_e)$. The approach of H.P. Urbach and P.K. de Bokx for calculating the angular intensity profile $I(\theta_e)$ is presented in more details hereafter.

III.4.1 Theoretical derivation

A sample with N homogeneous layers with refractive index n_j $(j = 1, ..., N)$ is assumed, the interfaces being sharp (flat and smooth on a nanometer scale) and

parallel to each other (see Fig. III.5). A Cartesian coordinate system (x,y,z) is

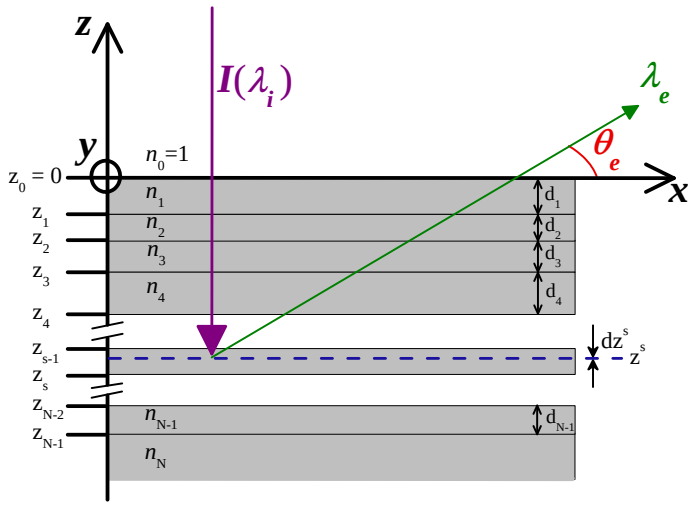

Figure III.5: In the derivation of the general formula for the angular intensity profile $I(\theta_e)$, a sample of N homogeneous layers is assumed, each being characterized by its refractive index n_j and its interface positions z_{j-1} and z_j on the z–axis ($j = 1, ..., N$). The N–th layer corresponds to the substrate. First an X–ray fluorescence source at the vertical position z^s contained within the depth region dz^s is considered.

chosen, the xy–plane is parallel to the sample interfaces and $z = 0$ is the sample–vacuum interface with the z–axis pointing upwards. The vacuum, corresponding to the upper–half space ($z > 0$), is characterized by the index 0 in the following calculations, the first layer by the index 1 and so on, the N–th layer being the substrate. The remaining lower half–space ($z < z_N$) corresponds to the substrate. The layers 1 to $N-1$ have thicknesses $d_j = z_{j-1} - z_j$ ($j = 1, ..., N-1$), z_j being the z–coordinate of the interface between the layer with index j and index $j+1$. Each layer is characterized by its refractive index $n_j = 1-\delta_j+i\beta_j$ (see Eqs. II.3 and II.4).

To determine the intensity in the emission direction θ_e of a fluorescence line of wavelength λ_e of atoms of an element labeled X placed in layer s at depth z^s from the surface, one should first compute the efficiency of the excitation process. The wavelength λ_e corresponds to the transition of a bound electron from the upper electronic subshell B to the lower subshell A in an atom of element X after a hole was created in subshell A. For the excitation of the fluorescence radiation only X–ray beams will be considered here, a calculation based on electron excitation can be found in [177]. The efficiency of the excitation process depends upon the intensity (number of incident primary photons per second) and spectral distribu-

tion of the primary X–ray beam $I_i(\lambda_i)$, the incidence angle θ_i relatively to the sample surface (θ_i being a macroscopic angle so that reflection and deviations due to refraction at any interface can be neglected), the X–ray absorption $\mu_k(\lambda_i)$ in the k layers of density ρ_k above the layer s as well as inside the layer s of density ρ_s (to the depth z^s) and finally the photo–electric cross–section $\sigma_s^{X,A}(\lambda_i)$ of the electronic subshell A of element X in layer s. In addition the probability $\omega_{X,A} \times P_{B\to A}$ has to be considered, $\omega_{X,A}$ being the fluorescence factor of subshell A of element X and $P_{B\to A}$ the probability that among the possible electronic transitions to fill the hole created in subshell A the transition $B \to A$ will take place. In certain cases the Coster–Kronig yields need also to be considered in the probability $P_{B\to A}$. Finally the fluorescence power of a source placed in layer s at depth z^s within the depth region $\mathrm{d}z^s$ in terms of number of photons per second is given by

$$\begin{aligned} p_s(z^s) = & \omega_{X,A} \times P_{B\to A} \times \\ & \int_{\lambda_i<\lambda_{X,A}} \Bigg[I_i(\lambda_i) \\ & \times \exp\left(-\sum_{k=1}^{s-1} \mu_k(\lambda_i)\rho_k \frac{d_k}{\sin\theta_i} - \mu_s(\lambda_i)\rho_s \frac{z_{s-1}-z^s}{\sin\theta_i} \right) \\ & \times \sigma_s^{X,A}(\lambda_i)\rho_s \frac{\mathrm{d}z^s}{\sin\theta_i} \Bigg] \mathrm{d}\lambda_i \end{aligned} \tag{III.3}$$

where $\lambda_{X,A}$ is the absorption edge of subshell A.

If the incident X–ray beam is monochromatic (wavelength λ_0), the incident intensity is described by a delta function $I_i(\lambda_i) = I_i \times \delta(\lambda_i - \lambda_0)$. When a layer l ($l = 1, ..., s$) is not monoelemental but a homogeneous mixture of different elements, the product $\mu_l(\lambda_i)\rho_l$ is given by the weighted sum of the corresponding product of each element, the weight being given by the relative mass concentration. In the case where $l = s$ also the photo–electric cross-section $\sigma_s^{X,A}(\lambda_i)$ has to be multiplied by the relative mass concentration of element X in layer s.

In the case of multielemental samples, it is possible that the fluorescence X–ray radiation is produced for different elements. If one of the fluorescence lines has a shorter wavelength than the absorption edge $\lambda_{X,A}$, the intensity of this fluorescence line will also contribute to the intensity of the fluorescence line of wavelength λ_e for which the angular intensity profile $I(\theta_e)$ is calculated. This is called secondary fluorescence and can also be taken into account in the calculation of $I(\theta_e)$. In this perspective, first the fluorescence power of all fluorescence lines with a shorter

wavelength than $\lambda_{X,A}$ has to be calculated by means of Eq. III.3, then their field strength at the position z^s where the source s is positioned has to be calculated by taking into account only the absorption of the intermediate sample material. Again reflection and refraction at interfaces will be neglected since the X–rays considered for secondary X–ray fluorescence production will in general not be incident at grazing angles on the interface. The exact formalism together with the modified function $p_s(z^s)$ can be found in [114]. For all the samples considered in chapters V and VI, no secondary fluorescence needs to be considered.

Once the radiated fluorescence power $p_s(z^s)$ of the source located in layer s and placed at depth z^s is known, the electric field $\vec{E}$ produced by the source in the upper half–space ($z > 0$) has to be calculated, $|\vec{E}|^2$ being equal to the intensity of the fluorescence X–rays of wavelength λ_e. Only the electric field component E parallel to the interfaces is considered. This component satisfies

$$\text{inside layer } j \neq s \quad k^2 n_j^2 E + \Delta E = 0 \tag{III.4}$$

$$\text{inside layer } j = s \quad k^2 n_s^2 E + \Delta E = -\sqrt{4\pi p_s(z^s)}\delta(\vec{r} - \vec{r_s}) \tag{III.5}$$

where $\vec{r_s} = (x^s, y^s, z^s)$ is the position vector of the point source and $k = 2\pi/\lambda_e$ the norm of the wavevector corresponding to the emitted fluorescence X–rays. At the interfaces, the electric field component E and its derivative $\delta E/\delta z$ are required to be continuous. A Fourier decomposition with respect to the coordinates x and y reduces the above system to a set of differential equations which can be solved for the different layers,

$$\begin{aligned}\hat{E}(k_x, k_y, z) =& A_j(k_x, k_y) \exp -ik_z^j z + B_j(k_x, k_y) \exp ik_z^j z \\ & - \frac{\delta(j-s)}{\pi}\sqrt{\frac{p_s(z^s)}{4\pi}} \times \left(H(z - z^s) - \frac{1}{2}\right) \\ & \times \frac{\sin(k_z^s(z - z^s))}{k_z^s} \exp\left(-ik_x x^s - ik_y y^s\right)\end{aligned} \tag{III.6}$$

where $\hat{E}(k_x, k_y, z)$ is the Fourier transform of $E(x, y, z)$ for the components x and y, $H(z)$ the Heaviside function ($H(z) = 1$ for $z > 0$, $H(z) = 0$ for $z < 0$), $\delta(j - s)$ equals 1 for $j = s$ respectively 0 if $j \neq s$ and k_x, k_y and k_z^j are the components of $n_j\vec{k}$. For $j \neq s$, $\hat{E}$ is the sum of two plane waves propagating downwards, respectively upwards. Knowing the amplitude A_0 of the downwards propagating wave in the layer $j = 0$ and B_N of the upwards propagating wave in the layer $j = N$, a numerically stable recursive algorithm can be developed, which is valid

for the propagating and evanescent waves, to calculate $\hat{E}(k_x, k_, z)$ in the different layers, independently of their thickness. In the experimental situation $|E|^2$ will be measured in the upper half–space $z > 0$ for a fluorescence source radiating with power $p_s(z^s)$ located inside the sample, i.e., $z < 0$ or equivalently $s \geq 1$. In this case $A_0(k_x, k_y) = 0$, the source being in a lower layer, and only $B_0(k_x, k_y)$ needs to be calculated. The detailed description can be found in [176]. Only the final result from [176] will be reproduced here,

$$\hat{E}(k_x, k_y, z) = (\prod_{j=0}^{s-1} |t_j^{\uparrow}|) \times \sqrt{\frac{p_s(z^s)}{4\pi}} \times \frac{i}{2\pi k_z^s} \times (\chi_{\text{even}} + \chi_{\text{odd}}) \times \tag{III.7}$$
$$\exp\left(-i(k_x x^s + k_y y^s) + ik_z^s(z_{s-1} - z^s) + i\sum_{j=1}^{s-1} k_z^j d_j + ik_z^0(z - z_0)\right)$$

where $k_z^j = \sqrt{n_j^2 k - k_x^2 - k_y^2} = k\sqrt{n_j^2 - \cos^2\theta_e}$, χ_{even} and χ_{odd} corresponds to X–rays which have undergone an even respectively odd number of reflections. $t_j^{\uparrow}$ is the transmission coefficient of X–rays at the interface z_j between the layers j and $j+1$, the X–rays being incident from the side of the layer $j+1$ (Fig. III.6). The arrow indicates thus the propagation direction after the refraction of the X–ray at the interface. Similarly the transmission coefficient $t_j^{\downarrow}$ would correspond to the transmission coefficient of X–rays being incident on the interface at z_j from the side of layer j, the arrow again indicating the propagation direction after the refraction process. Equivalently $r_j^{\uparrow}$ and $r_j^{\downarrow}$ stand for the reflection coefficients of X–rays being incident on the interface at z_j from the side of the layer j, respectively $j+1$, and propagating after the refraction upwards respectively downwards (the vertical component of the propagating X–rays being opposite to the one of the incident X–rays) (Fig. III.6). The definitions of the transmission and reflection coefficients as well as the relationships between the coefficients can be found in the following equations,

$$r_j^{\downarrow} = \frac{k_z^{j+1} - k_z^j}{k_z^{j+1} + k_z^j} = -r_j^{\uparrow}, \tag{III.8}$$

$$t_j^{\uparrow} = 1 - r_j^{\uparrow} = \frac{2k_z^{j+1}}{k_z^{j+1} + k_z^j}, \tag{III.9}$$

$$\text{and} \quad t_j^{\downarrow} = 1 - r_j^{\downarrow} = \frac{2k_z^j}{k_z^{j+1} + k_z^j} = \frac{k_z^j}{k_z j + 1} t_j^{\uparrow}. \tag{III.10}$$

The coefficients χ_{even} and χ_{odd} are defined as follows

$$\chi_{\text{even}} = \frac{1}{\prod_{j=1}^{s}\left[1 - r_{j-1}^{\downarrow} R_j^{\uparrow} \exp\left(2ik_z^j d_j\right)\right]}, \tag{III.11}$$

$$\text{and} \quad \chi_{\text{odd}} = \frac{R_s^{\uparrow} \exp\left(2ik_z^s(z^s - z_s)\right)}{\prod_{j=1}^{s}\left[1 - r_{j-1}^{\downarrow} R_j^{\uparrow} \exp\left(2ik_z^j d_j\right)\right]} \tag{III.12}$$

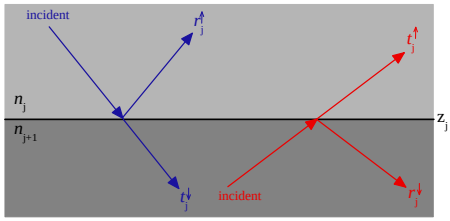

Figure III.6: Definition of the reflection and transmission coefficients in the grazing emission intensity calculation.

with $R_j^{\uparrow}$ accounting for reflections on all the interfaces below the interface at z_j. The coefficients $R_j^{\uparrow}$ can be obtained in the mentioned recursive algorithm,

$$\text{for } 0 \leq j < N-1: \qquad R_j^{\uparrow} = \frac{r_j^{\uparrow} + R_{j+1}^{\uparrow} \exp\left(2ik_z^{j+1} d_{j+1}\right)}{1 + r_j^{\uparrow} R_{j+1}^{\uparrow} \exp\left(2ik_z^{j+1} d_{j+1}\right)}, \tag{III.13}$$

$$\text{and for } j = N-1: \quad R_{N-1}^{\uparrow} = r_{N-1}^{\uparrow}. \tag{III.14}$$

The electric field in the upper half space corresponding to the X–rays emitted by a source located at (x^s, y^s, z^s) in the layer s (i.e., $z_{s-1} \leq z^s \leq z_s$) in the lower half–space, is obtained by an inverse Fourier transformation of $\hat{E}(k_x, k_y, z)$ for the x and y components

$$E(x, y, z) = \int\int \hat{E}(k_x, k_y, z) \exp\left(ik_x x + ik_y y\right) \mathrm{d}k_x \mathrm{d}k_y. \tag{III.15}$$

By inserting Eqs. III.9, III.11, III.12, III.13, III.14 into Eq. III.7 which itself is inserted into Eq. III.15 and using a stationary phase method to solve the integrals on k_x and k_y, $E(x, y, z)$ can be approximated by an analytical expression with a simplification given by Eq. III.10 (for details see [176]). Finally $|E(x, y, z)|^2$ will be proportional to the intensity emitted by the source located at (x^s, y^s, z^s) per solid angle above the sample ($z > 0$), the intensity being modulated by the fluorescence power (Eq. III.3). By integrating over all possible source positions inside the layer s, the lateral positions being delimited approximately by the area irradiated by the primary beam of intensity $I_i(\lambda_i)$ and the vertical positions by the layer interfaces at z_{s-1} and z_s, the total fluorescence intensity in counts per second per solid angle is obtained,

$$\begin{aligned} I(\theta_e) = A_i \times \Big(\prod_{j=0}^{s-1} |t_j^{\downarrow}|^2\Big) \times \int_{z_s}^{z_{s-1}} \Bigg[& \frac{p_s(z^s)}{4\pi} \\ & \times \exp\left(-2\sum_{j=1}^{s-1} \mathrm{Im}(k_z^j) d_j - 2\mathrm{Im}(k_z^s)(z_{s-1} - z^s)\right) \\ & \times \left|\chi_{\text{even}} + \chi_{\text{odd}}\right|^2 \Bigg] \mathrm{d}z^s. \end{aligned} \tag{III.16}$$

In this equation the product of the transmission coefficients $|t_j^{\downarrow}|^2$, which is called the transmission factor, stands for the change in the field strength upon transmission through the different interfaces above the layer s, the exponential factor accounts for the X–ray absorption of the fluorescence radiation of wavelength λ_e on the path from the source position towards the sample surface, while the interferences due to multiple reflections (together with X–ray absorption) are incorporated in the term $|\chi_{\text{even}} + \chi_{\text{odd}}|^2$. These interferences between X–rays transmitted directly through the different interfaces and X–rays reflected at some interface(s) are only observable at grazing emission angles θ_e. Examples for angular intensity profiles $I(\theta_e)$ calculated for a periodic multilayer sample and a sample with two layers can be seen in Fig. III.7.

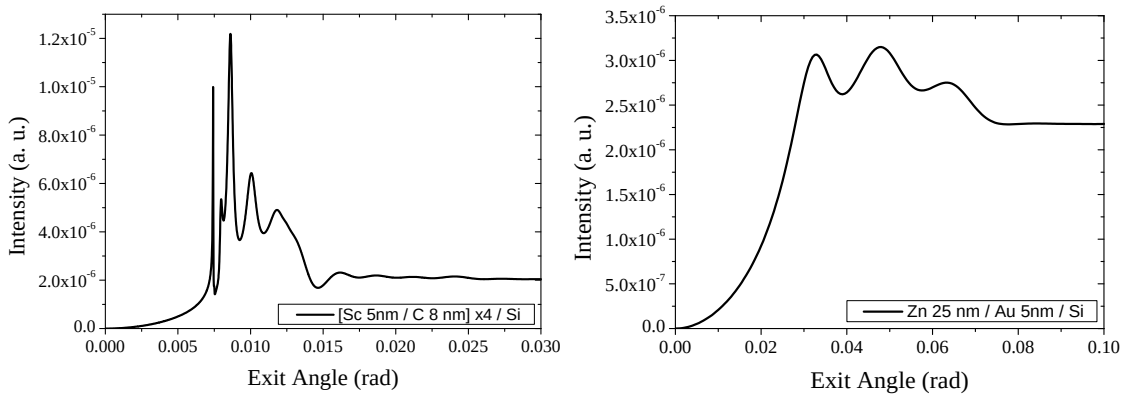

Figure III.7: Calculated angular intensity profiles $I(\theta_e)$ of the Zn Lα–line for a 25 nm Zn layer on the top of a 5 nm Au layer covering a Si substrate (right side) and the Sc Kα–line for a periodic multilayer consisting of 4 periods of 2 alternating layers (left side). The 2 layers were a Sc layer of 5 nm on the top of a C layer of 8 nm, the substrate being Cr.

If the fluorescent X–rays are incident on an interface at z_{j-1} $(j = 1, ..., s)$ at an angle θ below the critical angle θ_c^j, the imaginary part of k_z^j, equal to $k\text{Im}(\sqrt{n_j^2 - \cos\theta^2})$, is large. Hence the fluorescent X–rays will be evanescent in the z direction inside layer j. Correspondingly the detected intensity will be very small, except if the X–ray fluorescence source is very close to the sample surface at $z = z_0$.

The polarization direction of the X–rays has been considered implicitly as negligible in the calculation since the relative difference in the reflectivity at an interface is of the order of the relative difference of the refractive index of the two adjacent layers.

If the radiated fluorescence power is independent of the depth z ($p_s(z) = p_s$), which is a valid assumption for thin layers irradiated vertically by an X–ray beam, the integral in Eq. III.16 can be calculated explicitly,

$$\begin{aligned} I(\theta_e) =& A_i \times (\prod_{j=0}^{s-1} |t_j^{\downarrow}|^2) \times \left[\frac{p_s}{4\pi} \times \frac{1 - \exp\left(-2\mathrm{Im}(k_z^s)d_s\right)}{2\mathrm{Im}(k_z^s)d_s} \times \exp\left(-2\sum_{j=1}^{s-1} \mathrm{Im}(k_z^j)d_j\right) \right. \\ & \left. \times \frac{1 + \left|R_s^{\uparrow}\right|^2 \exp\left(-2\mathrm{Im}(k_z^s)d_s\right) + \Psi(\theta_e)}{\prod_{j=1}^{s} \left|1 - r_{j-1}^{\downarrow} R_j^{\uparrow} \exp\left(2ik_z^j d_j\right)\right|^2} \right] \end{aligned} \tag{III.17}$$

where $\Psi(\theta_e)$ represents the interference between the fluorescence X–rays emitted directly towards the detector and the fluorescence X–rays reflected by the layers situated below the considered layer s,

$$\begin{aligned} \Psi(\theta_e) =& \frac{2\,\mathrm{Im}(k_z^s)d_s \exp\left(2\,\mathrm{Im}(k_z^s)d_s\right)}{1 - \exp\left(2\,\mathrm{Im}(k_z^s)d_s\right)} \times 2\,\mathrm{Re}\left(R_s^{\uparrow} \exp\left(i\mathrm{Re}k_z^s d_s\right)\right) \\ & \times \frac{\sin\left(\mathrm{Re}k_z^s d_s\right)}{\mathrm{Re}k_z^s d_s}\,. \end{aligned} \tag{III.18}$$

Extensions of formula III.16 to account for instrumental factors broadening the angular resolution are also discussed in [114, 176].

III.4.2 Examples

For illustration the reduced forms of Eq. III.16 for a single layer on the top of a substrate, a substrate below a single layer, an implanted sample and a particle–like coverage on the top of a substrate will be presented here below.

If the fluorescence X–ray radiation of wavelength λ_e emanates from a single layer on top of a substrate, this comes up to set $s = 1$ and $N = 2$ in Eq. III.16, which is thus reduced to

$$\begin{aligned} I(\theta_e) =& A_i \times |t_0^{\downarrow}|^2 \times \int_{z_1}^{z_0} \left[\frac{p_1(z)}{4\pi} \times \exp\left(-2\mathrm{Im}(k_z^1)(z_0 - z)\right) \times \right. \\ & \left. \left| \frac{1 + r_1^{\uparrow} \exp\left(2ik_z^1(z - z_1)\right)}{1 - r_0^{\downarrow} r_1^{\uparrow} \exp\left(2ik_z^1 d_1\right)} \right|^2 \right] \mathrm{d}z\,. \end{aligned} \tag{III.19}$$

Only the part of the layer above the considered source depth in the integration contributes to the absorption process, the single interface which needs to be considered for transmission is the one between the vacuum and the layer at $z = z_0$ and

reflection processes can occur at the interfaces between the layer and the vacuum above or the substrate below the layer at $z = z_0$ and $z = z_1$ respectively. In Fig. III.8 the angular intensity profile of a Si layer of 30 nm on the top of a Cu substrate is shown. Interference fringes can be observed above the critical angle of Si for the

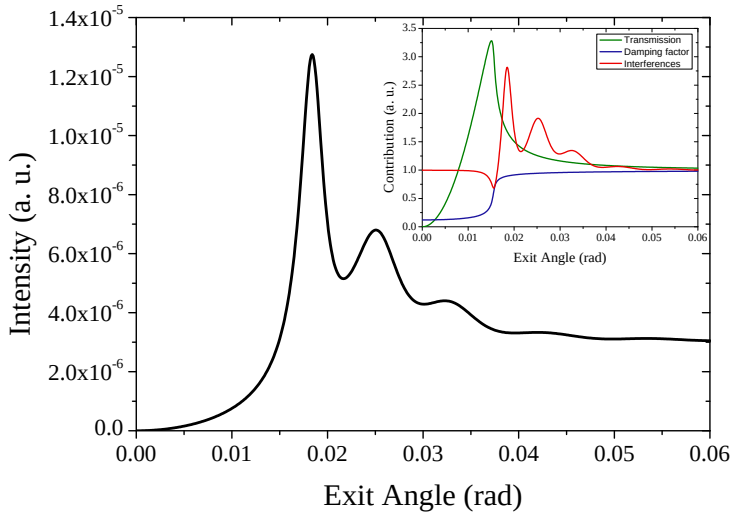

Figure III.8: Calculated angular intensity profile for the Si Kα–line of a 30 nm Si layer on the top of a Cu substrate. In the region between the critical angles of Si and Cu for the Si Kα–line strong oscillations can be observed due to interference of the directly transmitted and the multiply reflected fluorescence X–rays.

Si Kα–line and the critical angle of Cu for the Si Kα–line which is larger due to the smaller refractive index ($n_{\mathrm{Si}}(\mathrm{Si\ K}\alpha) > n_{\mathrm{Cu}}(\mathrm{Si\ K}\alpha)$). Neither the transmission factor $|t_0^{\downarrow}|^2$ nor the exponential absorption factor can account for the interference fringe pattern. Thus the interferences between the direct X–ray detection path and detection paths containing reflection(s) are responsible for the fringes in Fig. III.8. The damping of the oscillations is due to a decreasing reflection coefficient and not to the absorption. The fringe period allows to deduce the layer thickness [114].

The insertion of a thin Au layer between the Si and Cu layers allows to further enhance the oscillations due to the even larger critical angle of Au for the Si–Kα line (Fig. III.9) and an increased reflection coefficient.

Starting from a single X–ray source, due to the different possible detection paths for the X–ray fluorescence because of multiple reflections (Fig. III.10), constructive as well as destructive interferences can occur (see section III.1). The depth period for a fixed emission angle θ_e for constructive interference between the direct

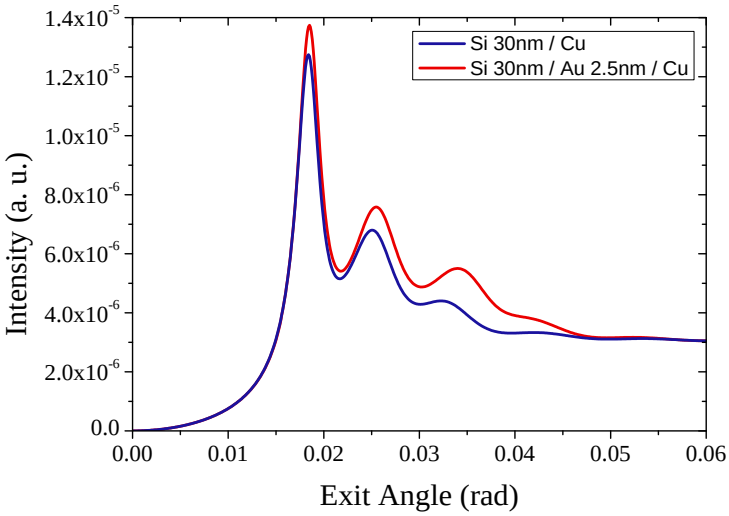

Figure III.9: The interference fringes are more pronounced if a highly reflecting Au layer is deposed before the Si layer on the top of the Cu substrate.

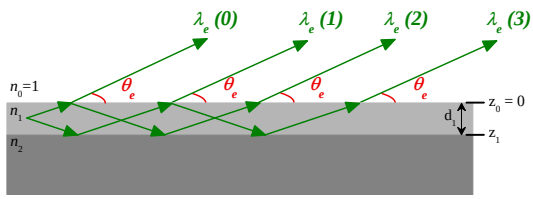

Figure III.10: For a given exit angle θ_e, reflections on the vacuum–layer and layer–substrate interfaces result in different possible paths for the detection of the X–rays of wavelength λ_e. The number in parentheses indicates the number of reflections undergone by X–rays following this path.

detection path and the one containing a single reflection on the layer–substrate interface is given in Eq. III.1. However, the integration over the layer depth will cancel in general the interference between these two detection paths since all possible source depths are accounted for. Consequently the interference fringe pattern in Figs. III.8 and III.9 is due to multiple reflections, the total number of reflections being even. For example if the detection path where the fluorescence X–ray is first reflected at the vacuum–layer interface and afterwards at the layer–substrate interface is selected, the path difference with the direct detection path is $2d_1/\sin\theta_e$ independently of the source position (Fig. III.11). If this path difference corresponds to an entire multiple of the wavelength λ_e, the X–rays following the two detection paths will interfere constructively. Due to the independence on the depth position for this type of constructive interferences, it will also be conserved when summing up the different source contributions to $I(\theta_e)$ by integrating from z_1 to z_0.

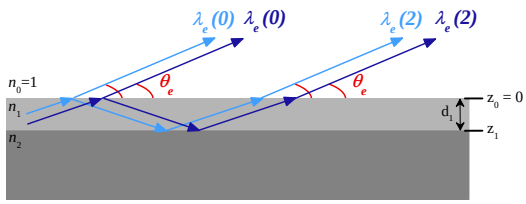

Figure III.11: The length difference in the detection path is independent of the depth position of the X–ray source only for the X–rays which are directly transmitted and those which are reflected an even number of times.

In contrast to the example chosen above, almost no fringes are visible for a layer with a refractive index larger than the one of the substrate for the fluorescence wavelength λ_e of interest. Fig. III.12 shows the angular intensity profile $I(\theta_e)$ of the V Kα–line for V layers of different thicknesses on the top of a Si substrate. The possible interferences are damped by the evanescent wave and are thus not or

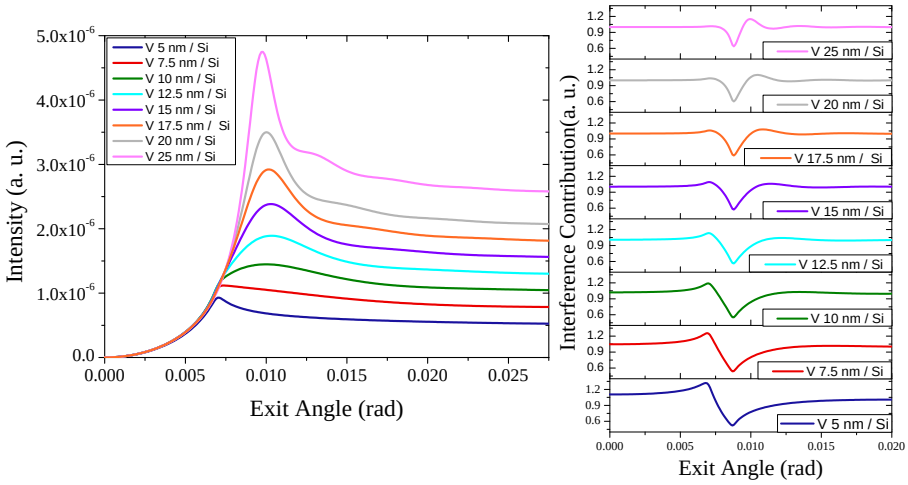

Figure III.12: Angular intensity profile of the V Kα–line emitted from V layers with different thicknesses on the top of a Si substrate (left panel). Interferences are hardly visible. Their contribution to the measured intensity is also shown (right panel). The transmission factor for the vacuum–V layer interface does not depend on the layer thickness, while the damping factor is more pronounced for increasing layer thicknesses.

only hardly visible in the total angular intensity profile $I(\theta_e)$.

For emission angles θ_e far above the critical angle the X–ray fluorescence intensity depends only upon the sample amount (which increases with the layer thickness)

(Fig. III.12). Note that the critical angle in the angular intensity profiles θ_e depends on the density ρ, whereas visible interference fringes allow to deduce the layer thickness. All these pieces of information have to be combined in the experimental characterization of a layer sitting on the top of a substrate.

The angular intensity profile of the substrate below a single layer is obtained by setting $s = 2$ and $N = 2$, with z_2 being the back–end of the sample ($z_2 \to -\infty$) and $R_2^{\uparrow} = 0$ since there is no interface below the substrate to reflect X–rays,

$$I(\theta_e) = A_i \times |t_0^{\downarrow} t_1^{\downarrow}|^2 \times \int_{z_2}^{z_1} \left[\frac{p_2(z)}{4\pi} \times \exp\left(-2\mathrm{Im}(k_z^1)d_1 - 2\mathrm{Im}(k_z^2)(z_1 - z)\right) \times \left| \frac{1}{1 - r_0^{\downarrow} r_1^{\uparrow} \exp\left(2ik_z^1 d_1\right)} \right|^2 \right] \mathrm{d}z \,. \tag{III.20}$$

There are two interfaces, at $z = z_1$ and $z = z_0$ where the field strength is modulated upon transition and where reflection processes can occur. The absorption of the fluorescence intensity in the layer has to be considered in addition to the absorption by the substrate atoms above the considered source depth. X–rays incident on the layer–substrate interface from the substrate side do not contribute to the calculated intensity if reflected. Multiple reflections need only to be considered when the first reflection occurs at the vacuum–layer interface and the second one at the layer–substrate interface, the X–rays being incident from the layer side of the interface. So only an even number of reflections can contribute to the angular intensity profile $I(\theta_e)$. For illustration the substrate intensity profiles $I(\theta_e)$ of the Fe Kα–line from the Fe bulk covered by a 35 nm Mg, respectively a 10 nm Ag layer is shown in Fig. III.13. The critical angle of Mg for the Fe Kα–line is smaller than the critical angle of Fe, while the critical angle of Ag for this fluorescence line is larger than the one of Fe. This results in a shift of the apparent critical angle in the angular profile. In the first case slight oscillations are perceptible. For comparison the angular intensity profile $I(\theta_e)$ of the Fe Kα–line for an uncovered Fe bulk sample is shown in Fig. III.14.

Indeed, setting d_1 to 0, $t_0^{\downarrow}$ to 1 and $r_1^{\uparrow}$ to 0 gives the formula for the angular intensity profile $I(\theta_e)$ of a simple bulk sample (Fig III.14). Only the transmission at the vacuum–sample interface and absorption processes need to be considered (inset of Fig. III.14).

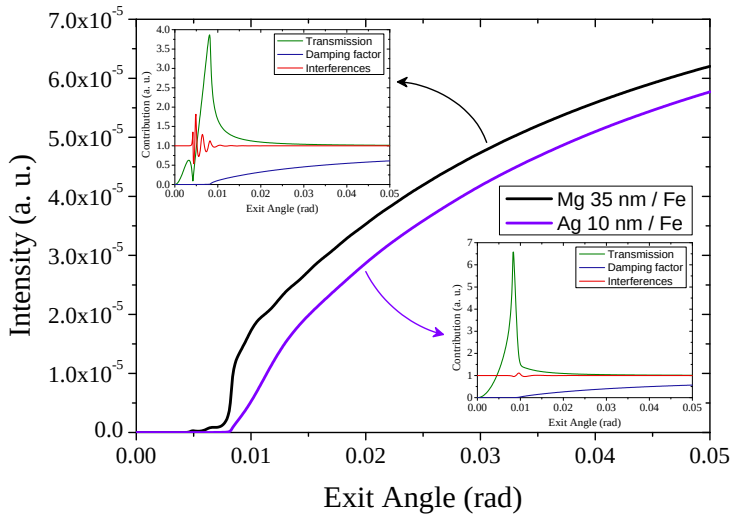

Figure III.13: Calculated angular intensity profiles for the Fe Kα–line emitted from a Fe bulk below a 35 nm Mg layer, resp. a 10 nm Ag layer. Either oscillations or a stronger damping of the Fe Kα fluorescence intensity are observed depending on the value of the critical angle of the layer for the Fe Kα–line (see text).

The same holds for an ion–implanted substrate,

$$I(\theta_e) = A_i \times (|t_0^{\downarrow}|^2) \times \int_{z_1}^{z_0} \left[\frac{p(z)}{4\pi} \times f(z) \times \exp\left(-2\mathrm{Im}(k_z)(z_0 - z)\right) \right] \mathrm{d}z \,, \quad \text{(III.21)}$$

where $f(z)$ corresponds to the relative concentration distribution in the depth–direction of the implanted ions, respectively the substrate, depending on whether the angular intensity profile $I(\theta_e)$ is calculated for a fluorescence line of the implanted element or the substrate element. Note that for transparency reasons $f(z)$ has been extracted here from the fluorescence power $p(z)$ (Eq. III.3). For low–implantation concentrations the latter is calculated by assuming that the attenuation of the incident radiation is equal to the one of the bulk substrate, but for the factors $\omega_{X,A}$, $P_{B\to A}$ and $\sigma_s^{X,A}\rho_s$ the values corresponding to the implanted element have to be considered. This approximation is usually justified for low implantation doses. For the same argument the refractive index n_1 is considered to be constant in the depth–direction and is determined by the bulk and the fluorescence wavelength λ_e. The angular profiles of ion–implanted samples and the inverse problem (retrieve the ion depth–distribution $f(z)$ from a measured angular profile $I(\theta_e)$) will be discussed in chapter VI. Examples of angular intensity profiles for different group III and group V elements implanted at 1 keV into a Si wafer are given in Fig. III.15.

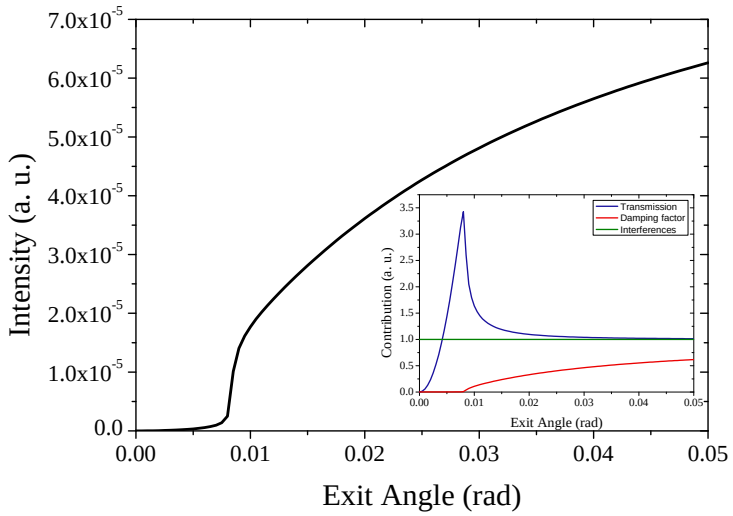

Figure III.14: Calculated angular intensity profile for the Fe Kα–line emitted from a Fe bulk sample. The inset shows the contributions from the different factors in Eq. III.16. For exit angles above the critical angle θ_e the intensity increases drastically.

For the sake of completeness, the case of a low–concentration particle distribution on the top of a reflecting surface will be considered. The model of a thin, low–concentration layer can be assumed where $p(z)$ is constant and proportional to the particle concentration. Thus the integral in Eq. III.16 can be calculated and the angular profile can be obtained from Eq. III.17, assuming that the X–ray fluorescence sources are all distributed at the substrate–vacuum interface at $z = z_0$ (on the vacuum side of the interface) and do not form an optical interface due to their low concentration ($s = 1$, $N = 1$, $|t_0^{\downarrow}| = 1$ and $|r_0^{\downarrow}| = 0$),

$$I(\theta_e) = A_i \times \frac{p}{4\pi} \times \frac{1 - \exp\left(-2\mathrm{Im}(k_z)d\right)}{2\mathrm{Im}(k_z)d} \times \left[1 + |r_1^{\uparrow}|^2 \exp\left(-2\mathrm{Im}(k_z)d\right) + \Psi(\theta_e)\right] , \qquad \text{(III.22)}$$

where $\Psi(\theta_e)$ is given by Eq. III.18 and $k_z = k\sqrt{n_0^2 - \cos^2\theta_e} = k \sin\theta_e$ since the refractive index of vacuum n_0 is one. Further approximations to simplify $I(\theta_e)$ (e.g., the non–consideration of the absorption effects inside the particles) can be found for small and large particle sizes d (on the nanometer–scale) in [140]. For illustration the particle–like angular intensity profiles for different elements deposited on a Si wafer is represented in Fig. III.16. Since the substrate material is the same for all profiles, the dependence of the critical angle θ_c on the X–ray fluorescence wavelength λ_e is clearly visible. Once the emission angle θ_e exceeds the critical angle for total reflection θ_c, the intensity in the angular profile remains approximately constant since interference effects are no longer possible, the X–rays

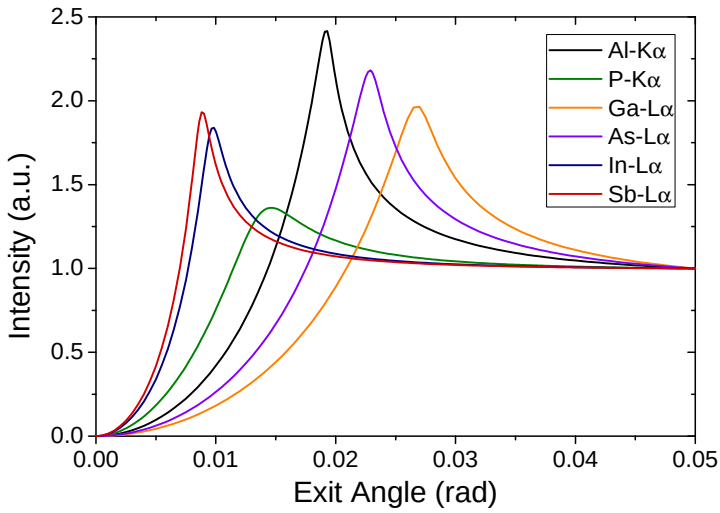

Figure III.15: Calculated angular intensity profiles for different group III and group V dopants implanted at 1 keV into Si. The position of the maximum intensity depends on the fluorescence wavelength λ_e, whereas the maximum intensity itself is influenced by the absorption of the fluorescence X–rays in the Si matrix.

being not reflected any more by the substrate at these exit angles (Fig. III.2).

Based on Eq. III.16 a Mathematica program has been written to calculate the angular intensity profiles $I(\theta_e)$ of bulk, (multi-)layered, periodically layered and implanted samples in a freely selectable angular range. Any elemental combination with $3 \leq Z \leq 92$ can be considered for the sample and for each element different diagram fluorescence lines can be used to calculate $I(\theta_e)$. The layer and bulk thicknesses can be chosen, too. For implanted samples, the implantation profile can either be introduced by selecting a Gaussian function and entering the width and center of the Gaussian curve or by loading the output of a SRIM (Stopping and Range of Ions in Matter) [178] calculation. The latter option offers also the possibility to calculate angular intensity profiles of layered, implanted samples. All the theoretical angular profiles $I(\theta_e)$ throughout this thesis were calculated with this program, the fluorescence power $p_s(z^s)$ being approximated by a constant. In Fig. III.17, where the attenuation of the primary beam at the extinction depth corresponding to the respective emission angles (see Fig. III.1) is shown, it can be seen that the error made when using a constant fluorescence power is not too large. Further extensions of the program could be the insertion of Eq. III.22 for dilute monolayers on a reflecting substrate and the use of a more realistic fluorescence power $p(z)$ (Eq. III.3). The possibility to perform calculations for samples

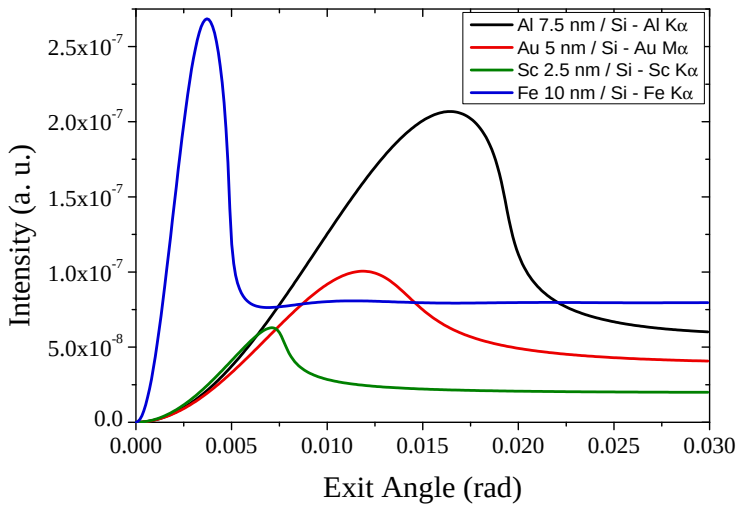

Figure III.16: Examples for particle–like profiles for different elements of different thicknesses deposited on top of a Si substrate. For emission angles θ_e smaller than the critical angle for total external reflection θ_c, the enhanced X–ray fluorescence intensity is the result of the interference between a the directly emitted X–rays and the X–rays reflected at the substrate surface.

with homogeneously mixed layers or layers with compound materials for which the relevant physical constants are known as well as the simulation of counting statistics or angular resolution (by convolution of $I(\theta_e)$ with a Gaussian) could also be envisaged.

So far the surface or interface roughness has not been considered, the interfaces being considered to be smooth and flat. Rough surfaces are in general described by four parameters: the root-mean square σ of the fluctuations in the depth direction, the coherence length of σ (the distance after which σ does not change any more), the Hurst parameter which indicates the frequency of low–amplitude depth oscillations (the jaggedness) and the fractal dimension of the surface. Surface roughness affects the reflection and transmission coefficients [25], the diffuse scattering being enhanced. If the coherence length and the roughness are small, the corrected reflection and transmission coefficients can be written as

$$r_j^{\uparrow} = \frac{k_z^j - k_z^{j+1}}{k_z^j + k_z^{j+1}} \times \exp\left(-2k_z^j k_z^{j+1}\sigma^2\right), \tag{III.23}$$

$$t_j^{\downarrow} = \frac{2k_z^j}{k_z^j + k_z^{j+1}2} \times \exp\left((k_z^j - k_z^{j+1})\sigma^2/2\right). \tag{III.24}$$

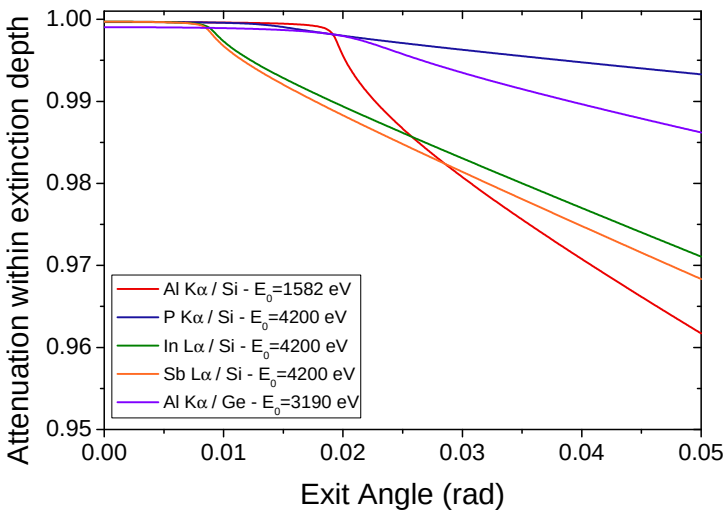

Figure III.17: Calculated attenuation of the primary beam at the extinction depth of the respective emission angle (Fig. III.1). The calculations were performed for the beam energies used in the measurements for the excitation of the different fluorescence lines (see section V.3).

If the coherence length is large, the following relations should be used

$$r_j^{\uparrow} = \frac{k_z^j - k_z^{j+1}}{k_z^j + k_z^{j+1}} \times \exp\left(-(k_z^j + k_z^{j+1})^2\sigma^2/2\right), \tag{III.25}$$

$$t_j^{\downarrow} = \frac{2k_z^j}{k_z^j + k_z^{j+1}2} \times \exp\left(-(k_z^j - k_z^{j+1})^2\sigma^2/2\right). \tag{III.26}$$

However, results provided by the above relations are only approximately correct, some second order processes which are expected to influence the reflection and transmission coefficients [24] being not accounted for. For intermediate cases an approach for calculating the correction coefficient can be found in [23]. Other approaches to take into account interface roughness subdivide the interface region into a stack of many layers with varying indexes of refraction due to the varying density caused by the intermixing between the 2 adjacent layers.

Chapter IV

Experimental Setup

The presented grazing emission experiments were realized at the beam line ID21 of the European Synchrotron Radiation Facility (ESRF) in Grenoble, France. The high–resolution von Hámos curved crystal X–ray spectrometer of the University of Fribourg [179] was transported to and installed at the mentioned beam line to realize synchrotron radiation based high–resolution grazing emission measurements. The beam line itself as well as the spectrometer will be described in this chapter. It will be shown how grazing emission conditions with the crystal spectrometer can be fulfilled. In addition, by installing a polycapillary focusing optics inside the spectrometer, microfocused measurements were realized. This installation needed some modifications of the spectrometer target chamber.

IV.1 ESRF ID21 beam line

The ESRF (Fig. IV.1) is besides the SPring-8 facility in Japan and the Advanced Photon Source in the USA one of the three largest third generation synchrotron light sources. Its construction began in 1988, the commissioning in 1994 and its forty beam lines were fully operable in 1998. Third generations synchrotron sources are characterized by a high brilliance and low emittance which are both inherent with the introduction of new, versatile insertion devices (wigglers and undulators) in the straight sections of the electrons storage ring. The brightness, energy bandwidth, polarization, coherence and size of the beam can be controlled if desired. The ESRF electron storage ring is operated at an energy of 6 GeV and the maximum current is about 200 mA.

The ID21 beam line can effectively deliver photon beams with energies ranging

Figure IV.1: View on the ESRF storage ring and the Control Room (courtesy ESRF).

between 1 keV and 7.2 keV. To minimize the absorption of the produced X–rays the beam line is operated at ultra high vacuum which allows to connect the beam line in a windowless way to the storage ring, reducing thus further absorption effects. For the production of the primary beams three different insertion devices are available in the 4.8 m long straight storage ring section, one wiggler and two different undulators. Their characteristics are displayed in Table IV.1. While the linear wiggler and linear undulator produce a linearly polarized primary beam, the helical undulator delivers a full circularly polarized primary beam for energies between 3.4 and 6.6 keV. For energies lower than 3.4 keV, the polarization level is still above 80%. The source has a size of 47 mm in the horizontal direction and 12 mm in the vertical direction. The divergences range between 82 – 92 mrad and 12 – 44 mrad in the horizontal, respectivley vertical direction, and decrease with the photon energy.

Table IV.1: Parameters of the insertion devices at the ESRF ID21 beam line.

Parameters	Linear Wiggler	Linear Undulator	Helical Undulator
Period [mm]	80	42	52
Number of Poles	20	38	59
Length [m]	1.60	1.53	1.60
B_0 [T]	0.80	0.54	0.88 (B_{0x}) / 0.99 (B_{0y})
K_{max}	5.9	2.1	1.21 (K_x) / 1.83 (K_y)
P_{max} [kW]	4.6	2.0	0.8

The white beam produced by the selected source is incident, through primary slits with a 5×12 mm^2 aperture, on a fixed exit double mirror system in the lead-shielded *optics hutch*. The incidence or cut–off angles can be tuned from about 5 mrad to 20 mrad. Mirrors with Rh, Si or Ni coatings are available. The mirrors are efficient low–pass filters which allow to work without lead shielding downstream of the primary beam, reducing thus the construction costs of the beam line and facilitating the access to the experimental components. Indeed the maximum integrated power is reduced from 700 W down to 50 W and 90% of the unwanted radiation is already removed from the beam by the first mirror. The best achievable harmonic rejection factor is better than 10^{-3} for any energy between 1 keV and 6 keV while the total transmission is still above 70%. After the mirrors, the primary beam, now called pink beam, passes in a fixed direction successively through a Bremsstrahlung stop and a collimator with a 5×5 mm^2 aperture into the *optics cabin*.

In the *optics cabin* the beam can be further conditioned and collimated by pre–focusing optics (beam steering multilayer, channel–cut monochromator, focusing mirrors, plane–grating monochromator) in order to filter and clean the beam. The beam steering multilayer consists of a carousel where several multilayers (currently Ni and Si mirrors and a NiB_4C multilayer with variable spacing) are mounted, in order to cover a large energy range. The *optics cabin* serves also to split the beam between the infrared microscopy section and the X–ray microscopy section. Consequently the deflection angle of this monochromator is quite large (5.5°). The inherent power reduction realized with these components of the beam line allows a stable operation of the focusing optics (Kirkpatrick-Baez mirrors system, zone plate or polycapillary optics) installed in the scanning X–ray microscope (SXM) chamber which is placed in the *experimental cabin*. A wavelength–dispersive spectrometer is also connected to the SXM chamber for X–ray measurements with a high counting statistics and a high resolution [180]. However, for the presented measurements no focusing optics was used and the von Hámos spectrometer was installed downstream of the SXM chamber to which it was connected with a 1.8 m long evacuated pipe.

At the entrance of the *experimental cabin*, a fixed exit double crystal monochromator (DCM) from Kohzu is installed, which allows energy scans with negligibly small displacements or deviations of the beam. It is generally used for energies

above 2 keV. It can be equipped either with two Si (111) mirrors for measurements requiring a high energy resolution (relative factor 10^{-4}) or a NiB_4C multilayer optics for experiments requiring rather a high photon flux at a moderate energy resolution (relative factor 10^{-3}–10^{-2}).

Above information on the ID21 beam line was taken from the ESRF website[1].

IV.2 Von Hámos spectrometer

For the grazing emission measurements the high–resolution von Hámos curved crystal X–ray spectrometer of the University of Fribourg [179] was transported from Fribourg to Grenoble and installed downstream of the SXM chamber in the *experimental cabin* of the ESRF ID21 beam line (Fig. IV.2). The geometry and the design of the spectrometer will be explained in this section.

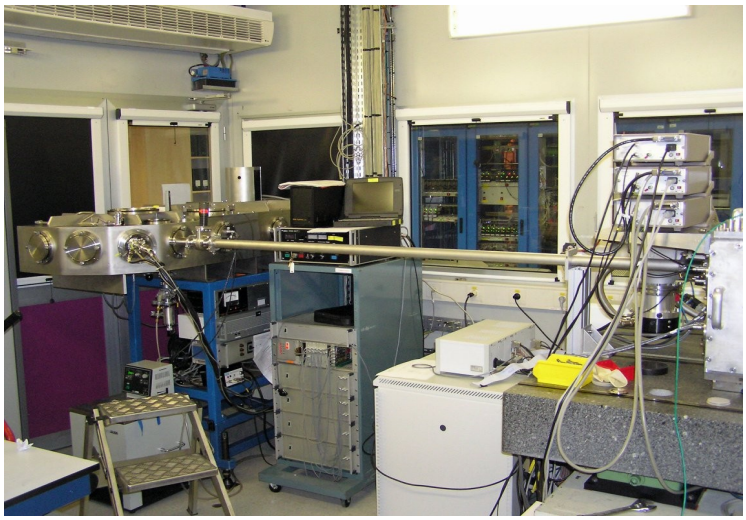

Figure IV.2: Picture of the high–resolution von Hámos X–ray crystal spectrometer of the University of Fribourg installed at the ID21 beamline of the ESRF, Grenoble. The spectrometer, on the left side, is connected to the ID21 beam line via an evacuated pipe.

IV.2.1 Von Hámos geometry

The basic concept of the spectrometer was introduced in 1933 by L. von Hámos [181]. The design is based on a reflection type geometry. It comprises an effective

[1] `http://www.esrf.eu/UsersAndScience/Experiments/Imaging/ID21/`

X–ray source, a cylindrically curved crystal whose axis of curvature lies in the dispersion plane (resulting in a focusing in the non–dispersive, or vertical, plane and an enhancement of the collection efficiency) and a position sensitive detector (Fig. IV.3). The source and detector are placed on the curvature axis of the cylindrically bent diffraction crystal (radius of curvature R).

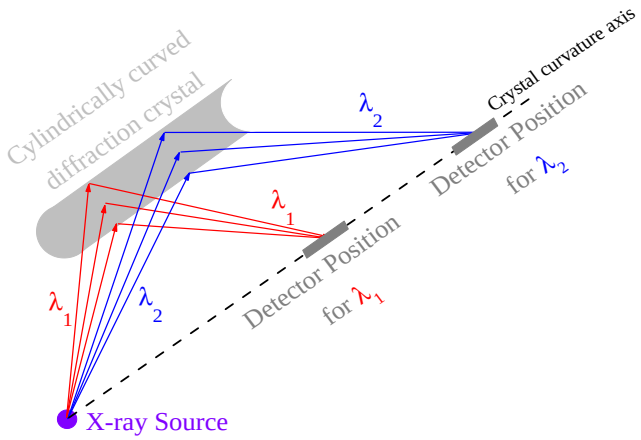

Figure IV.3: Illustration of the von Hámos geometry.

From the source, X–rays are emitted in all directions, in particular towards the diffraction crystal which is represented as a set of regularly spaced atoms organized in Miller planes separated by only a few Ångstroms (similar to the wavelength λ of the X–rays). The X–rays can be subject to an elastic scattering on the Miller planes: if the path difference between the X–rays diffracted on different crystal planes corresponds to an integer number of the X–ray wavelength λ, the diffracted X–rays will interfere constructively (Fig. IV.4). Otherwise there will be destructive interference. This is known as Bragg's law [182],

$$n \times \lambda = 2d \times \sin\theta_n, \tag{IV.1}$$

where n is an integer number and stands for the diffraction order, d corresponds to the crystal lattice spacing (the distance between two Miller planes) and θ_n to the Bragg angle of the n-th diffraction order. For crystal planes parallel to the surface, the Bragg angle corresponds to the incidence and exit angle on the Miller planes. For each wavelength λ there exits a set of Bragg angles where the condition for constructive interference is verified.

The Bragg law can also be expressed in terms of X–ray energy,

$$E[keV] = h\nu = \frac{h \times c}{\lambda} = \frac{h \times c \times n}{2d \times \sin\theta_n} \overset{\text{Eq. } IV.1}{=} \frac{12.3984[\text{keV} \cdot \text{Å}] \times n}{2d[\text{Å}] \times \sin\theta_n}, \tag{IV.2}$$

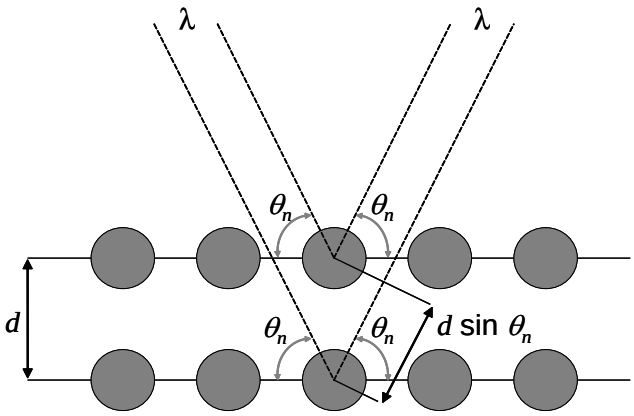

Figure IV.4: Illustration of the Bragg diffraction (Miller planes are supposed here to parallel to the crystal surface).

Due to the Bragg law, if X–rays of wavelength λ are to be detected the positions of the crystal and the detector are fixed relatively to the source. If the Miller planes are parallel to the crystal surface and therefore to the axis of curvature of the crystal, two conditions need to be fulfilled:

1. The crystal, which can be moved on an axis parallel to the curvature axis, needs to be positioned so that the X–rays are incident at an angle where the Bragg condition is verified.

2. The detector, which can be moved on the curvature axis, has to be placed in order that the crystal is on the bisection of the line segment sustained by the source and the detector. In other words, the source–to–crystal and the crystal–to–detector distances need to be identical.

The geometrical constraints are illustrated in Fig. IV.5. Since the source and the detector are placed on the curvature axis of the crystal, the distance between the axes on which the diffraction crystal and the detector are moved corresponds to the curvature radius R of the crystal. Therefore the source–to–crystal and the crystal–to–detector distances correspond to $R \sin \theta_n$, θ_n being determined by the X–ray wavelength λ. The position of the crystal on its axis of displacement is equal to $R \cot \theta_n$, the zero position of the axis being defined by the perpendicular projection of the source position. Correspondingly the detector position on its displacement axis is equal to $2 \times R \cot \theta_n$, the source itself defining the zero position of this axis. The consequence it that this setup is not suitable for elemental tracing of an unknown sample since the position of the components cannot be fixed

beforehand due to the unknown X–ray wavelength(s).

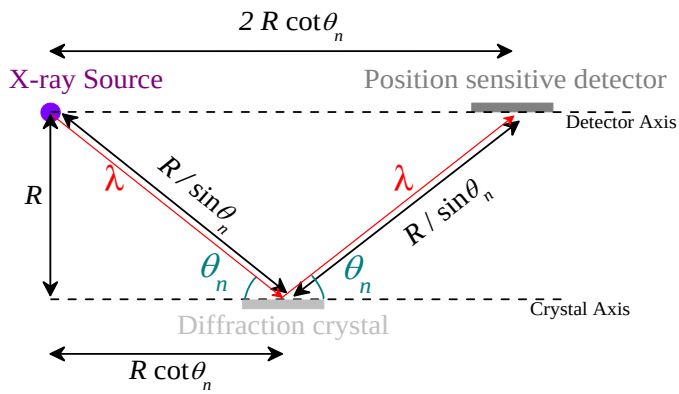

Figure IV.5: Top view on the von Hámos geometry to illustrate the geometrical constraints.

For a fixed position of the crystal and detector, experimental data are collected over a certain energy range which varies with the Bragg angle (Fig. IV.6). Since this region is scanned at once, the measurements are faster than with spectrometers based on point by point scanning methods. This partially compensates the lower collection efficiency, due to the small solid angle of detection of wavelength–dispersive instruments compared to energy–dispersive detectors. The energy range which is covered in the von Hámos geometry is limited by either the crystal or detector length on the dispersion axis, depending on whether the half of the crystal length is smaller then the detector length or not. In Fig. IV.6 the covered energy range is limited by the detector length.

The main advantages of wavelength–dispersive setups are the high background rejection and the high energy resolution.

Due to the Bragg condition, most of the background events are eliminated by the diffraction crystal and are not refracted towards the detector. Therefore the acquired X–ray spectra are in general clean. Remaining background events are mainly due to the electronic noise of the detector, X–rays scattered towards the detector and cosmic events. The background related to the noise of the detector is removed by subtracting a so–called background frame from each acquired image. A further diminution of the background is performed by sorting the events by means of energy discrimination.

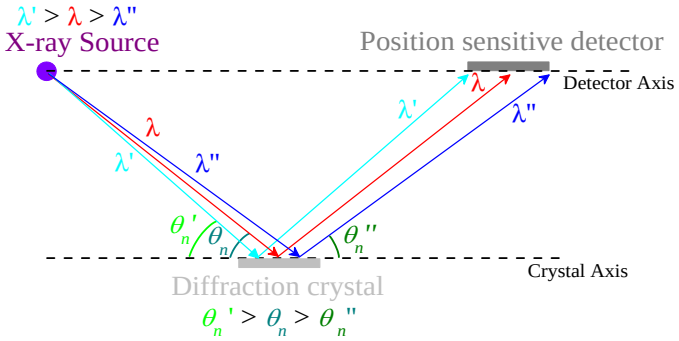

Figure IV.6: The von Hámos geometry allows covering a certain energy range at a fixed position of its components.

The relative energy resolution of the spectrometer can be deduced from Eq. IV.2,

$$\begin{aligned} \Delta E &= \frac{h \times c}{2d} \times \frac{-1}{\sin^2\theta_n} \times \cos\theta_n \times \Delta\theta_n \\ \Rightarrow \frac{\Delta E}{E} &\overset{\text{Eq. } IV.2}{=} \cot\theta_n \times \Delta\theta_n. \end{aligned} \tag{IV.3}$$

The relative energy resolution $\Delta E/E$ depends thus on the Bragg angle θ_n and the angular resolution $\Delta\theta_n$ and improves for increasing θ_n and decreasing $\Delta\theta_n$. For infinitely small source widths $\Delta\theta_n$ is determined by the Darwin width of the diffraction crystal which is of the order of μrad for pure crystals. If, however, the source has a width Δy in the direction perpendicular to the emission of the X–rays with wavelength λ, the angular resolution will depend mainly on the source width. Indeed the Bragg law will be valid in a region with extension $\Delta x = \Delta y/\sin\theta_n$ on the axis of the diffraction crystal (Fig. IV.7). Recalling that the crystal position is given by $x = R\cot\theta_n$, the angular resolution due to the finite source width can be obtained from the differential,

$$\Delta\theta_n = \left|\frac{-\Delta x \times sin^2\theta_n}{R}\right| = \frac{\Delta y \times \sin\theta_n}{R}. \tag{IV.4}$$

The relative energy resolution of the spectrometer can then be deduced from Eq. IV.3 by inserting Eq. IV.4,

$$\frac{\Delta E}{E} = \frac{\Delta y \times \cos\theta_n}{R}. \tag{IV.5}$$

It becomes apparent that the relative energy resolution improves with decreasing source widths Δy and increasing curvature radius R and Bragg angle θ_n. A large

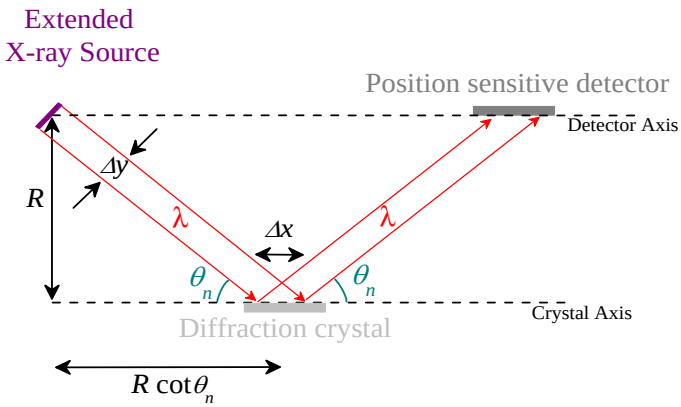

Figure IV.7: An extended X–ray sources broadens the angular resolution.

curvature radius R or a small source width Δy are inherent, however, with a decreasing collection efficiency. Therefore a compromise between a higher luminosity and a poorer energy resolution needs to be made.

IV.2.2 Technical details

The presented spectrometer concept was realized inside a $180 \times 60 \times 24.5$ cm^3 stainless steel chamber (Fig. IV.2). The curvature radius R of the crystal was chosen to 25.4 cm. The X–ray source is represented by a rectangular slit placed on the detector axis, labeled DET. It consists of two juxtaposed Ta pieces, one being movable, which are 0.3 mm thick, 10 mm high and whose separating distance Δy can be adjusted from 0 to 0.8 mm depending on whether a high energy resolution or a larger luminosity is desired. Typically a slit width Δy of 0.2 mm is chosen, resulting in a relative energy resolution $\Delta E/E$ of the order of 5×10^{-4}. The edges of the slit are sharpened to avoid Compton scattering into the detection part of the spectrometer.

The real X–ray source, the target exposed to ionizing radiation (X–rays, electrons, ions) and emitting fluorescence X–rays, is mounted behind the slit. It emits X–ray radiation in all directions, in particular through the slit, which represents the (virtual) source of the von Hámos geometry, onto the diffraction crystal placed on the crystal axis (CRY). The incidence direction on the crystal surface is defined by the Bragg condition (Eq. IV.1); this fixes the crystal position (section IV.2.1) and the target position relatively to the slit. Since the slit aperture is quite narrow, the target position needs to be tuned accordingly (Fig. IV.8). To allow for

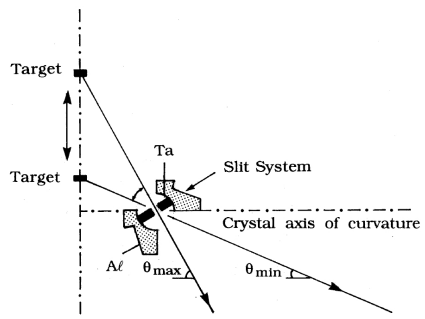

Figure IV.8: Depending on the Bragg angle θ_n, and thus the fluorescence X–ray energy, the target position needs to be adjusted relatively to the slit in order to be placed on the direction sustained by the crystal and the slit.

this adjustment, the target holder carriage is driven by a stepping motor with a minimum increment of 2.5 μm, in the direction perpendicular to the crystal and detector axes (CRY and DET), on an axis labeled TAF. The target holder itself consists of a motorized carousel on which four to six targets can be mounted simultaneously, depending on the used holder. The targets are mounted on the back side of the carousel (seen from the direction of the incident ionizing radiation) in order to ensure a sample mounting which is independent of the sample thickness from the point of view of sample positioning. This allows switching between targets without opening the spectrometer. In addition the target holder can be moved by stepping motors on an axis labeled TAT parallel to the crystal and detector axes with a minimum step of 2.5 μm and rotated relatively to the incident ionizing radiation around a vertical axis, labeled TAL, passing through the surface of the sample exposed to the incident ionizing radiation and being perpendicular to the TAF and DET axes. On each of these three axes, inductive proximity detectors are placed at the ends to interrupt the movement if necessary. At the same time the proximity detectors serve as spatial reference positions and allow a calibration of the position. The different axes are illustrated in Fig. IV.9. All the motors are remotely controlled via an electronic rack with controllers connected to a PC.

The rotation stage (TAL) allows to control the incidence angle of the ionizing radiation and the emission angle of the emitted X–rays. The emission angle is defined by the Bragg angle corresponding to the wavelength of the measured X–rays and the employed crystal as it can be deduced from Eq. IV.1. The accuracy of the rotational movement is 0.00225° which meets the requirements for measurements based on grazing emission. A more detailed description of the grazing emission

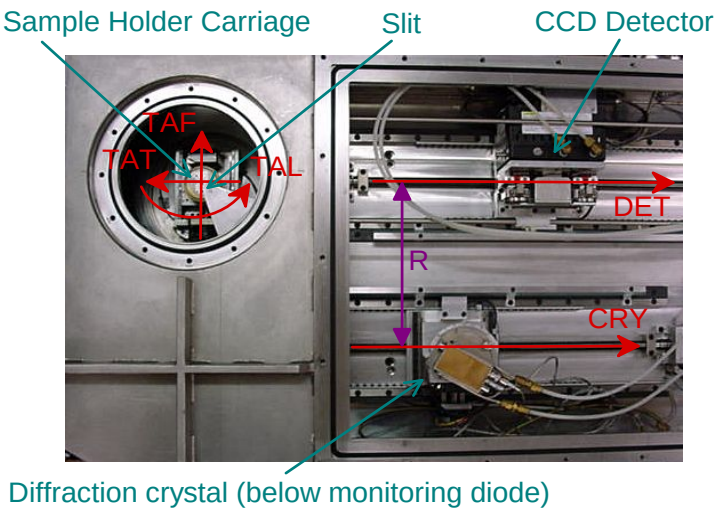

Figure IV.9: Picture of the main components of the Fribourg von Hámos spectrometer. The motion axes of the different axes are also shown. The synchrotron radiation beam is is parallel to the TAF axis if the spectrometer is correctly aligned at the ESRF ID21 beam line.

measurements performed with the von Hámos spectrometer can be found in sections IV.2.3 and V.3.

The movement (TAF) of the target holder perpendicular to the crystal (CRY) and detector (DET) axes implies, in order to have a well–defined source width for the von Hámos geometry that the slit needs to be rotated when the target is displaced. This rotation around a perpendicular axis passing through the center of the slit is realized mechanically. A rod connects the target holder carriage to the slit–rotation system and ensures an automatic alignment of the slit for any displacement of the target.

The spectrometer chamber is equipped with four circular ports, all centered on the dispersion plane of the spectrometer (Fig. IV.2). The ports allow the connection to a synchrotron or ion accelerator beam line or the installation of an electron gun. Through the ports it is thus possible to irradiate the sample at angles varying between 0° and 90° in 30° steps relatively to the crystal (CRY) and detector (DET) axes. Alternatively a side–window X–ray tube can be mounted directly in front of the samples through a flange on the top the spectrometer. The X–ray tube can be oriented freely. To minimize background radiation during the experiment, a Al–Cu–Pb shielding separates the part of the spectrometer where the target is moved and irradiated from the part with the detection setup (crystal and detec-

tor), the single shielding hole between the two parts being due to the rectangular slit.

At the ESRF ID21 beam line, the incident photon beam enters the spectrometer chamber perpendicularly to the crystal (CRY) and detector (DET) axes. The spectrometer is positioned relatively to the beam which is fixed in space. The beam should hit the vertical sample at the height of the dispersion plane and on the TAL axis around which the sample can be turned. These requirements on the beam for the insertion direction and the incidence position with respect to the sample define the position of the spectrometer chamber relatively to the incident synchrotron X–ray beam.

The crystal and detector are also mobile, as required by the von Hámos geometry. A Schneeberger linear rail system allows a very precise positioning of the carriages on which the crystal support, respectively the detector, are installed. The carriages are both moved by means of a hardened stainless steel screw which itself is driven by a remotely controlled stepping motor (400 steps per turn) and a bronze nut fixed at the bottom of the carriage. The screw–nut system was manufactured without any play. The screws have a diameter of 16 mm and a length of 69 cm (crystal axis) and 99 cm (detector axis), respectively. The DET axis limits thus the usable range for measurements. The tow screws have a 2 mm thread, which gives for every step of the driving motor a 5 μm displacement of the crystal or detector. At both ends of the two rails, inductive proximity detectors, which serve as absolute position references, stop the carriages automatically. For the detector axis the distance between the rectangular slit and the two sensors are 28 cm and 112 cm, respectively. Considering the crystal radius of curvature R of 25.4 cm, this allows covering an angular range from 24.4° to 61.1°. The motion system for the crystal and the detector is mounted on a separate 25 mm thick aluminum plate, fixed to the bottom of the chamber, to minimize any distortion of the tracks caused by possible deformations of the vacuum chamber.

The crystals are glued on Al blocks which have been milled on one side to have the concave cylindrical shape with the required curvature radius. The crystal surface is in principle 10 cm high and 5 cm wide in the dispersion direction. The large height provides a higher luminosity. To correct for possible focusing errors the crystal support can also be moved perpendicularly to the crystal axis. The

available crystals are listed in Table IV.2 together with their orientation and their lattice $2d$ spacing. For each crystal the energy range covered in the first diffraction order is also quoted.

Table IV.2: Available diffraction crystals for the von Hámos spectrometer of Fribourg.

Crystal	Orientation	Lattice spacing [Å]	Energy range in 1st order [keV]
TlAP	001	25.772	0.544 – 1.178
ADP	101	10.642	1.317 – 2.853
SiO_2	$1\bar{1}0$	8.5096	1.647 – 3.568
LiF	200	4.0280	3.480 –7.538
Ge	220	4.000	3.504 – 7.591
Si	220	3.8410	3.649 – 7.849
SiO_2	$2\bar{2}3$	2.7500	5.097 – 11.041
LiF	420	1.8010	7.782 – 16.859

The detector used for the presented GEXRF experiments is a two–dimensional back–illuminated coupled charge device (CCD) which has been characterized in [183]. A CCD can be described as an array of capacitors which collect the electron–hole pairs created in Si by the incident X–rays (one per 3.65 eV). A light–tight environment is a prerequisite. Thus a CCD allows, after the subtraction of a previously recorded background image, a position–dependent analysis of the energy of the incident X–ray photons with a good background rejection capability. W.S. Boyle and G.E. Smith were awarded the physics Nobel prize in 2009 for the invention in 1969 of the CCD as the first successful imaging technology using a digital sensor. The CCD which was used for the GEXRF measurements is 2.68 cm long (in the dispersion direction) and 0.80 cm high and consists of 1340 $\times$ 400 pixels, each pixel having a size of 20 $\times$ 20 μm^2. The effectively used crystal width for the X–ray detection is therefore limited to 1.34 cm (see Fig. IV.6). The detector's horizontal dimension defines the energy bandwidth (i.e., the covered energy region) during the measurement. Depending on the measured X–ray energy and the position of the components, the bandwidth varies approximately between 30 eV and 330 eV. As for the crystal, the vertical extension of the CCD permits to increase the luminosity. For the read–out and digitalization of the CCD signal, the ST–133 controller from Roper Scientific is used. The read–out speed is 1 MHz, the reading and successive cleaning of a complete CCD frame takes thus about half a second. A shutter (Fig. IV.10), consisting of a 0.5 mm thick stainless steel

plate superimposed on a 1.5 mm thick aluminum plate, is placed in front of the CCD. During the read–out sequence the shutter is closed. The shutter closing

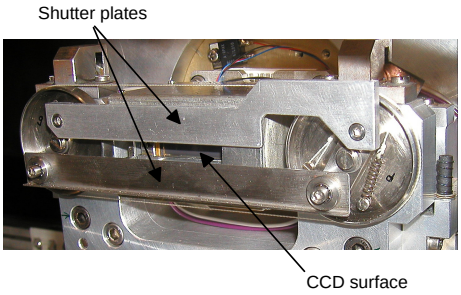

Figure IV.10: Picture of the shutter installed in front of the position–sensitive CCD X–ray detector. The shutter is in the open position which reveals the CCD surface, i.e. the acquisition position.

takes about 200 ms. The exposure time of the CCD can be freely controlled but is in principle chosen between one and five seconds, depending on the incident X–ray intensity. To limit the dark charge, which is a thermally induced build–up of charges in the CCD array during the exposure time and which introduces some statistical noise, the CCD chip is cooled down to -45° by a cold finger mounted on two–stage Peltier element which is itself coupled to a water cooling circuit. These low temperatures require the CCD to be placed in a dry and clean environment to prevent any deposition on the CCD surface. As a consequence the measurements have all to be performed in vacuum.

Two vacuum pumps are used to evacuate the spectrometer chamber: a two–stage rotary pump and a turbo–molecular pump. The first pump has an exhaust power of almost 10 liters per second and can reach a final pressure of the order of 10^{-2} mbar. The second pump has an exhaust power of 900 liters per second and the final pressure which can be obtained in the spectrometer chamber is about 10^{-7} mbar. The turbo–molecular pump is air–cooled and its final rotation speed is 27000 rpm. The two pumps are complementary to each other. The rotary pump first creates a pre–vacuum, then the turbo–molecular pump is switched on. Indeed at atmospheric pressure the efficiency of the turbo–molecular pump is reduced due to friction with air. The heat created by excessive friction could damage the turbo–molecular pump. Therefore, when opening the spectrometer chamber, the pump first needs to slow down before the spectrometer chamber is filled with nitrogen until the atmospheric pressure is reached. The spectrometer chamber is reinforced

by 20 mm thick ribs on the top and bottom parts to prevent a deformation of the walls due to the pressure difference between the inside and the outside of the spectrometer.

IV.2.3 Realization of grazing emission conditions

One condition for the achievement of grazing emission conditions in the von Hámos geometry is to detect the fluorescence X–ray radiation of wavelength λ_e under a single, well–defined angle relatively to the sample surface. In other terms, the emission direction for X–ray detection has to be well–defined so that the flat and smooth sample surface can be oriented adequately relatively to the detection direction. In the von Hámos spectrometer, the detection direction is defined by the Bragg condition (see section IV.2.1, the relevant parameters being the fluorescence X–ray wavelength λ_e, the lattice spacing d of the diffraction crystal and the diffraction order n). Indeed the Bragg condition (Eq. IV.1) implies that only those X–rays which are incident at the Bragg angle θ_n relatively to the diffraction crystal surface are diffracted towards the CCD detector. Thus, in the von Hámos spectrometer the detection direction for fluorescence X–rays of wavelength λ_e is precisely defined (by the Bragg angle θ_n relatively to the crystal axis CRY) and grazing emission conditions can be straightforwardly fulfilled. Indeed it is sufficient to turn the flat target surface, mounted perpendicularly to the spectrometer's dispersion plane which contains also the incidence direction of the primary beam, close enough to the detection direction defined by the Bragg angle θ_n. In this configuration, as shown in Fig. IV.11, a fixed target position corresponds to a fixed grazing emission angle θ_e and angular X–ray fluorescence intensity scans $I(\theta_e)$ are realized by recording the intensity of the selected X-ray fluorescence line of wavelength λ_e at different angular positions of the target.

The experimental definition of the emission angle θ_e needs, however, additional care. Indeed, due to the target mounting, the exit angle is only controlled on a relative scale and not on an absolute scale. A reference position is thus needed to associate to the different target angular positions the corresponding emission angles. For implanted or thin–layered samples the calibration of the angular scale is realized with the critical angle of an X–ray fluorescence line of the substrate. In this case the critical angle is supposed to be identical to the one of a pure bulk sample. For sufficiently low implantation doses, respectively thin layers, this

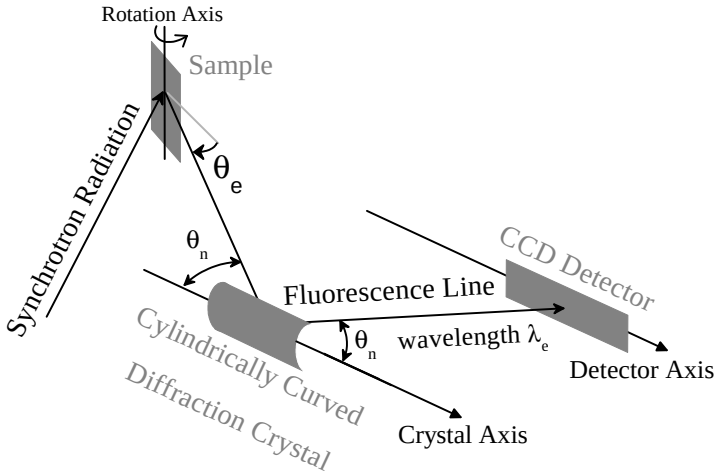

Figure IV.11: Grazing emission conditions are realized by turning the flat sample surface, irradiated by the synchrotron radiation beam, close to the emission direction defined by the diffraction crystal and the fluorescence wavelength λ_e.

condition is verified. A sufficiently low implantation dose means that the optical properties of the bulk substrate are not altered. For the presented measurements this condition was satisfied. Further details about the calibration of the emission angle θ_e will be given in section V.3 of the experimental part (chapter V).

Moreover in the experiment the slit of the spectrometer can be completely opened. Since the crystal itself sees the target only as a line-like source of width $\Delta y = W_i \times \sin\theta_e$, W_i being the irradiated sample width in the spectrometer's dispersion plane, the angular resolution can be approximated from Eq. IV.4,

$$\Delta\theta = \frac{W_i \sin\theta_e \times \sin\theta_n}{R + S\tan\theta_n} \tag{IV.6}$$

where $S = 2.5$ cm corresponds to the distance between the slit and the sample TAF translation axis which is parallel to the incoming beam. Assuming that the beam has a width $W_B = 1$ mm, the irradiated width W_i on the sample turned to a grazing emission angle is approximately equal to $W_B/\cos\theta_n$ and thus $\Delta\theta$ is of the order of 10^{-1} mrad for the largest experimental emission angles θ_e used in our measurements. The contribution of the crystal Darwin width can thus be neglected. This angular resolution is sufficient, GEXRF angular resolutions reported in the literature being typically of the order of mrad [8,168]. A refinement by slits is not necessary. This simplifies also the experiment since no beam profile effects due to narrow slits have to be considered. The slit-less geometry results in addition in an

increased intensity since the whole irradiated surface of the sample contributes to the measured fluorescence.

However, in the von Hámos geometry, the position sensitive CCD detector covers a given range of diffraction angles. Since the exit angle is defined with respect to the Bragg angle, for a fixed target angular position the exit angle varies on the CCD along the dispersion direction. This contributes also to the angular resolution of the grazing emission experiment, even if this contribution is attenuated by the intensity distribution of the measured fluorescence X–ray line. In order to acquire grazing emission intensity profiles $I(\theta_e)$ with a proper angular resolution an area of interest is defined on the CCD in both the horizontal and vertical directions of the dispersion plane. The horizontal restriction is centered on the maximum peak intensity of the measured X–ray fluorescence line. Only X–rays detected within the area of interest are taken into account in the angular intensity profile $I(\theta_e)$. The vertical restriction is necessary for two reasons, first the so–called "'Banana effect"' due to the cylindrically curved diffraction crystal (see Fig. IV.12) and second the target mounting. Indeed the angular resolution can be spoiled if the target is not mounted exactly at 90° with respect to the dispersion plane since the emission angle varies then in the vertical direction due to the fixed emission direction. In the selection of the area of interest a compromise between intensity and angular resolution has thus to be done.

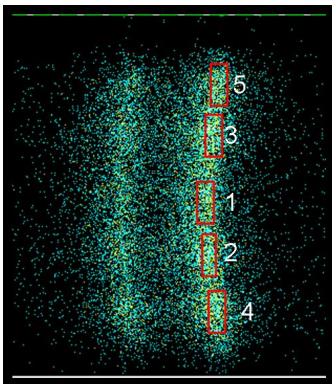

Figure IV.12: Illustration of the "Banana shape" affecting the 2D CCD images. The depicted 2D image corresponds to the the acquisition of a Cr–Kα doublet. The effect is due to the cylindrically curved diffraction crystal and, depending on the crystal and detector positions, is more or less pronounced.

IV.3 High–resolution microfocused GEXRF

In section III.2, the feasibility of microfocused GEXRF was mentioned, i.e. the combination of grazing emission conditions with a microfocused primary X–ray beam. Due to the geometry of the grazing incidence setups, this is not possible for TXRF and GIXRF setups as the primary beam is spread over the sample surface. A polycapillary optics was installed in front of the sample inside the von Hámos spectrometer. The realization of this project required some modifications on the mechanical parts of the target positioning system and the installation of additional components to allow for a correct positioning and alignment of the polycapillary optics. Note that the focusing optics devices available on the ID21 beam line could not be used due to the too large distance between them and the sample.

IV.3.1 Polycapillary optics

Based on monocapillary tubes which were used from the 1960's on to guide X–rays, the polycapillary optics, developed by Kumakhov about 30 years later [184], has been in the last 20 years a study field on its own. The working principle of both types of capillary optics is to collect and redirect X–rays by means of hollow glass capillary tube(s), the steering of the X–rays in each individual polycapillary channel being realized by multiple total external reflections (section II.2) on the inner glass wall of the gently curved capillary. Glass is used because of its high–reflectivity for X–rays allowing thus for a quite efficient deflection of the X–rays. As indicated by the name, a polycapillary optics is formed by an array of many thin–walled capillaries pointing all to the same, common point, the focal point, at one end for half–lenses and at both ends for full–lenses. First polycapillary optics devices contained about 10^3 capillaries, actual polycapillary optics consists of 10^5 (or more) individual capillaries. The large number of individual capillaries allows for an efficient X–ray collection. Initially the capillaries were individually supported by a metallic grid, but nowadays they are fused together into a single bundle and drawn to the desired shape (monolithic design) [185]. The fusing and pulling process allowed to considerably decrease the size and increase the X–ray energy acceptance of the polycapillary optics while simplifying the production [186]. Presently tapered polycapillary optics are frequently used. In this kind of polycapillary optics the diameter of the individual capillaries changes along the length direction, the tapering of the capillaries allowing to optimize the X–ray transmis-

sion while still preserving total reflection conditions on the capillary walls [185,186].

Polycapillary optics can be either used for focusing or for collimating purposes, depending on its orientation with respect to the propagating X–rays. In the latter case divergent X–ray radiation originating from a small source at the focal point in front of the polycapillary entrance is collected and deflected in order to form a parallel X–ray beam at the exit of the polycapillary optics, while in the first case the X–ray radiation is redirected towards a focal point behind the polycapillary optics [187] to produce a high–density X–ray flux. The X–ray radiation can be either emanating from a point source, then a full polycapillary lens needs to be used, or it can be an X–ray beam (usually a parallel beam but parts of a divergent beam can also be considered), in which case a polycapillary half–lens is used, as in the collimating orientation. Both, focusing and collimating polycapillary optics, are used in micro–XRF, X-ray Absorption Near Edge Structure (XANES) and XRD experiments to realize measurements with micrometer resolution, to reduce the collection time, resp. to lower the local detection limit, or to increase the solid angle of detection (since collimating polycapillary optics can be positioned closer to the sample than detectors) [185, 186, 188, 189]. The combined use of a focusing polycapillary on the X–ray excitation path and a collimating polycapillary on the detection path, arranged in the confocal geometry, allows to define small sample volumes to which the detection setup is sensitive and thus to realize 3D–measurements on a micrometer scale [190]. Different possible arrangements of polycapillary optics in X–ray analysis measurements are resumed in [191]. In PIXE measurements, collimating polycapillary optics are reported to be placed on the X–ray detection path in order to shield the detector from scattered particles [188]. Similarly X–ray scattering rejection can also be realized with a polycapillary optics [187].

The advantages offered by polycapillary optics with respect to other focusing X–ray optics devices, like X–ray mirrors or crystals, Bragg–Fresnel or compound lenses and Fresnel zone–plates, are to offer at the same time a compact size for the optics device, a large spatial acceptance of the incoming X–ray beam and a broad usable energy range [192]. Other X–ray optics devices allow the production of submicron X–ray spots but are at the same time only usable for monochromatic X–ray radiation while polycapillary optics accept and transmit polychromatic X–ray radiation. The size and position of the focal spot produced by polycapillary optics do not de-

pend markedly on the size and position of the X–ray source along the polycapillary length axis [192]. The focal spot position does not depend neither on the energy of the X–ray radiation [188] but the latter my influence the focal spot size [188,192].

The size of the collimated beam, respectively the focal spot size in the case of a focusing polycapillary optics can be measured by wire or knife edge scans or alternatively with a position–sensitive detector [188]. In [186] a theoretical approximation is reported for the focal spot size S: $S = 2 \times \text{focal distance} \times \theta_c + d$, where θ_c is the critical angle for total external reflection and d the diameter of an individual capillary. The divergence at the exit of a polycapillary optics can be estimated by a simple geometrical argument to be twice the critical angle θ_c.

Besides the focal spot size, polycapillary optics are characterized by their input and / or output focal distance(s) (10^{-3}–10^{-2}m), transmission (0.1–0.6) and gain (5×10^1–10^3; for focusing polycapillary optics only). The theoretical upper limit for the transmission is given by the area ratio of the individual entrance apertures to the polycapillary entrance aperture. In general these characteristics vary since for each individual application the design of the polycapillary (length, diameter and radius of curvature of the capillaries; entrance and exit apertures) has to be adapted. The transmission is the ratio of the X–ray intensity at the exit to the X–ray intensity at the entrance of the polycapillary, while the gain is the transmission multiplied by the ratio of the sample areas irradiated without and with the polycapillary optics in the beam. Thus the gain corresponds to the increase in the X–ray photon density. Due to the gain, pinhole or slit collimation cannot compete with polycapillary optics for the micrometer–size X–ray spots.

Since the transport of the X–rays inside the polycapillary optics is realized by total reflection of X–rays, the diameter and radius of curvature of the capillaries need to be chosen adequately in order that X–rays are incident at angles smaller than the critical angle θ_c (Eq II.5) for total reflection on the inner wall of the capillary. This defines some constraints on the radius of curvature R and the diameter d of the individual capillaries which should be sufficiently large, respectively small [187] (Fig IV.13). In order for the incidence angle on the polycapillary optics wall to be of the order of one degree (like the critical angle θ_c), the diameter d should be of the order of microns and the curvature radius R of the order of m. From Fig. IV.13 it can be derived, by making use of the small angle approximation

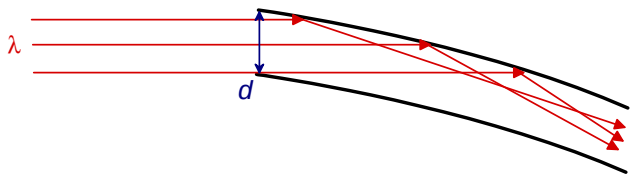

Figure IV.13: Illustration of the constraints imposed by the total reflection conditions on the diameter d and the curvature of a single polycapillary channel. If X–rays hit the channel wall at an angle larger than the critical angle for total external reflection, they will depending on their energy be absorbed or pass through the wall. In the latter case a halo will appear around the focal spot. To efficiently deflect the incident X–rays the maximum channel diameter d and the minimum radius of curvature are limited.

for the cosine function and assuming $d/R << 1$, that the largest possible incidence angle θ_{M} for fixed R and d is

$$\cos\theta_{\mathrm{M}} = \frac{R}{R+d} \Rightarrow 1 - \frac{\theta_{\mathrm{M}}^2}{2} \approx \frac{1}{1+d/R} \approx 1 - \frac{d}{R} \Rightarrow \theta_{\mathrm{M}} \approx \sqrt{\frac{2d}{R}}\,. \tag{IV.7}$$

As the critical angle θ_c depends inversely on the X–ray energy, the transmission through the polycapillary optics begins to fall off with increasing X–ray energies once the critical angle θ_c starts to be smaller than the largest possible acceptance angle θ_{M}. This limits in some extent the X–ray energy for which a specific polycapillary optics can be used [193] but allows also to use polycapillary optics as low–pass filters to get rid of harmonics at synchrotron radiation sources or to remove the high–energy part of an X–ray tube spectrum. Another limiting factor is the penetration of harder X–rays through the capillary walls, the lower energy limit being given by the X–ray absorption at the entrance and exit windows of the polycapillary optics [186, 192] and also by the length of the polycapillary optics. Most polycapillary optics are used in an energy domain of 1–40 keV [189].

A theoretical description of the polycapillary X–ray full-lens is given in [194], while [195] provides a recent review on the different polycapillary optics parameters, the applications of X–ray polycapillary optics (also at synchrotron radiation facilities) as well as theoretical simulations, realized either by Monte Carlo simulations or ray–tracing (to assess experimental effects, like capillary wall roughness for example).

IV.3.2 Installation of a polycapillary optics in the von Hámos spectrometer

A polycapillary focusing half–lens was mounted inside the von Hámos spectrometer in the perspective of microfocused GEXRF experiments. Due to the limited space inside the spectrometer, a polycapillary optics represented the single possible solution. The compact size of the device and its relatively easy manipulation are the main advantages. The polycapillary half–lens was manufactured by X–ray Optical Systems (XOS).

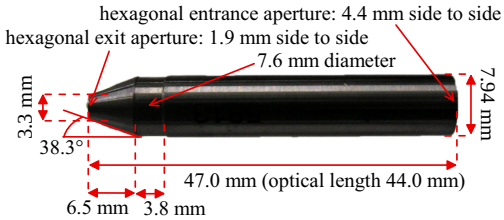

Figure IV.14: Picture of the polycapillary focusing half–lens. The dimensions are indicated in the Figure. The output focal distance was 8 mm and the focal spot size 50 μm.

The main characteristics of the employed polycapillary half–lens are displayed in Fig. IV.14. It is contained in a steel housing (outer diameter 7.94 mm) to protect the extremities of the optics from any contact. Therefore the optical length (44 mm) is shorter than the length of the housing (47 mm). The side–to–side distance of the hexagonal optics entry and exit are 4.4 mm and 1.9 mm, respectively. Thus the primary beam at the ID21 beam line transmitted through a pinhole of 2 mm in diameter can be fully captured while still some tolerance for beam displacements is offered. The output focal distance (from the polycapillary optics exit window to the focal point) has been chosen to 8 mm, the focal spot size to 50 μm. These parameters influenced the design of the polycapillary optics which was optimized for X–ray energies from 2 to 8 keV. The transmission for these energies was calculated and compared to experimental results (Fig. IV.15). Experimentally the polycapillary transmission was determined in two ways. First the intensity of the incident synchrotron radiation beam waas measured using a photodiode with and without polycapillary optics. The photodiode was then replaced by P–implanted Si and Ge wafers. The fluorescence intensity of P Kα– and Ge Lα–lines was measured by means of the von Hámos spectrometer, again with and without polycapillary

optics. The photodiode measurements were performed wit a single beam energy (4.2 keV), those with the spectrometer at two beam energies (3.19 keV and 4.2 keV). As shown in Fig. IV.15 (left part), partly inconsistent results were obtained. No definitive explanation was found so far for the observed discrepancies. The uncertainty of the result obtained with the diode is larger because of the precision of the read–out electronics. The sensitivity of the polycapillary optics alignment is also shown in Fig. IV.15, the standard deviation of the transmission curve in the horizontal and vertical directions being 0.12° and 0.10°.

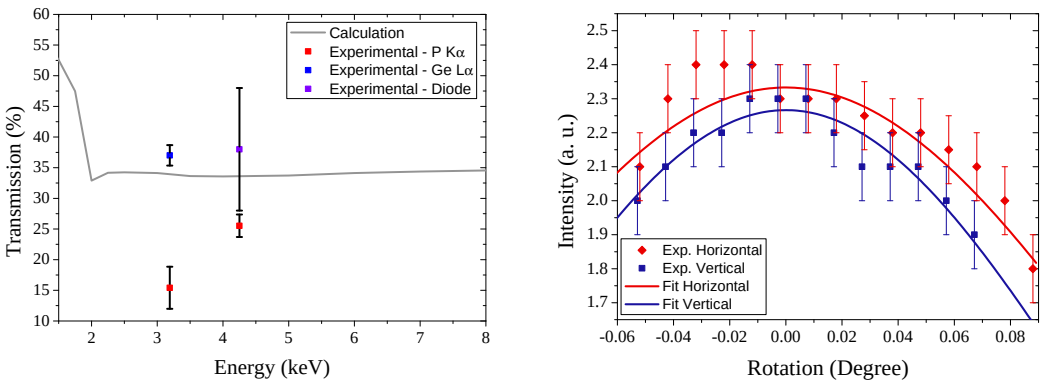

Figure IV.15: The sensitivity of the angular alignment of the polycapillary optics is shown on the right side, while on the left side the theoretical and experimental maximum transmission as a function of the energy are shown. For 1.5 keV the manufacturer ensured a transmission above 30% and a focal spot size smaller than 45 μm.

The polycapillary optics is hold by an aluminum arm (Fig. IV.18) which itself is screwed on a vacuum compatible and motorized 5–axis positioning stage (Figs. IV.16, IV.17 and IV.18) produced by SmarAct and delivered by FerroVac. The

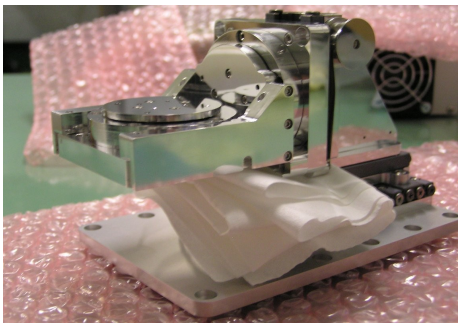

Figure IV.16: Picture of the 5–axis positioning stage.

positioning stage is composed of 3 transversal translation axes (X,Y and Z) and 2 rotation axes (Θ and Φ) and could be installed inside the spectrometer chamber

because of its compact size. The order of magnitude of the positional increments can be chosen freely from 10^{-9} to 10^{-2} meters for the translational axes, and from 10^{-6} to 1 degrees for the rotation axes. The minimal increments are in both cases 3 orders of magnitude below the precision needed for the positioning of the polycapillary optics, so that an accurate alignment was ensured. Among the translational axes, two (X and Z) are perpendicular to the incident primary beam direction, one (the X–axis) being contained in the spectrometer's dispersion plane. These two axes serve to position the polycapillary optics relatively to the primary beam. The third translational axis (Y) is parallel to the primary beam, and thus the TAF axis, and is needed to adjust the distance between the polycapillary optics output and the sample surface. This distance corresponds to the output focal distance so that the focal spot is coincident with the sample surface. Furthermore it is important that the focal spot lies not only on the sample surface but also on the sample's axis of rotation (TAL) which allows the adjustment of the grazing emission angle θ_e and passes through the sample's surface. If the primary beam is incident on the TAL axis, its position will not change on the sample surface when the emission angle θ_e is changed. The same holds for the focused primary beam. If the focal spot is not on the TAL axis, the detected X–ray fluorescence signal will not remain within the same area on the CCD surface throughout an angular scan of the fluorescence intensity under grazing emission conditions. This would make the definition of the area of interest in the CCD surface ambiguous (see section IV.2.3).

The two rotation axes (Θ and Φ around the Z and X axes, respectively) of the positioning stage are both perpendicular to the primary beam, one (Φ) being contained in the spectrometer's dispersion plane, the second (Θ) being transversal to it (Fig. IV.17). The distance along the Y–axis between the polycapillary entrance and the rotation axes (Θ and Φ) is approximately 8 cm. The two rotation axes (Θ and Φ) serve for the proper orientation of the polycapillary axis relatively to the beam in order to maximize the transmission of the primary beam. Indeed, as it has been explained in section IV.3.1, the collimated primary beam is guided by multiple total reflections on the inner side of the individual capillary glass walls through the optics. This makes crucial the angular alignment of the polycapillary axis relatively to the primary beam direction crucial.

The angular alignment of the polycapillary optics should be preceded by a cor-

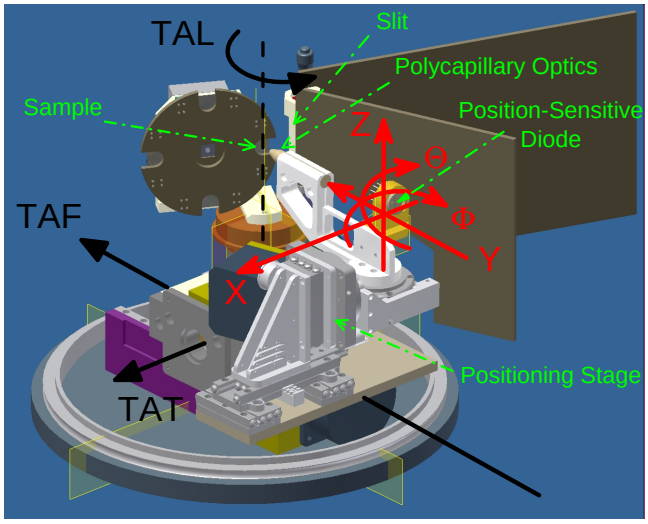

Figure IV.17: Illustration of the additional pieces which needed to be installed in order to manipulate the polycapillary optics and ensure its alignment relative to the synchrotron radiation beam, which has to be incident along the Y–axis. The whole positioning stage has to move with the sample stage along the TAF–axis, but be independent of the TAT–axis in order to keep the possibility for surface scans. The position–sensitive diode is necessary to retrieve the synchrotron radiation beam inside the spectrometer chamber and position the polycapillary optics accordingly.

rect positioning relative to the primary X–ray beam and followed by a proper adjustment of the distance between the polycapillary optics output and the sample surface to the focal output distance. In other words the polycapillary optics needs first to be inserted into the beam with the help of the two translation axes X and Z. In this perspective a position–sensitive X–ray photodiode (Fig. IV.19) was installed next to the polycapillary entrance by screwing the aluminum photodiode holder on the aluminum arm holding the polycapillary optics (Figs. IV.17 and IV.23). The holder and the arm were separated by a Milar foil for reasons of electric isolation of the position–sensitive X–ray photodiode from the electrically grounded positioning stage. The center of the polycapillary entrance aperture and the one of the position–sensitive photodiode are at the same vertical level and they are separated horizontally by exactly 14 mm. Thus, by assessing the primary beam position inside the spectrometer with the photodiode mounted besides the polycapillary optics entrance, the position of the polycapillary half–lens relatively to the primary X–ray beam is known. A simple displacement along the X–translation axis is sufficient to capture the X–ray beam with the polycapillary half–lens. The range of this axis ($\approx$ 40 mm) is sufficient to move the polycapillary optics and the

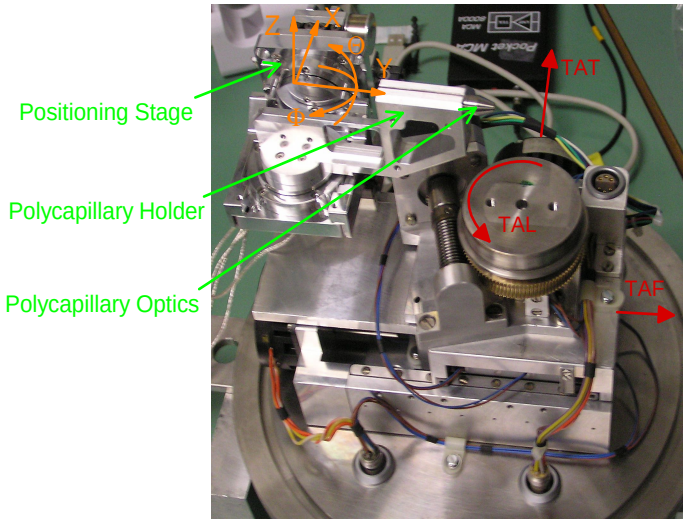

Figure IV.18: Photograph of the mounted polycapillary optics and the installed positioning module. The positioning module is only connected to the TAF axis and independent of the TAT and TAL ones.

position–sensitive X–ray photodiode out of the beam and perform measurements with the full primary X–ray beam as delivered by the ID21 beam line.

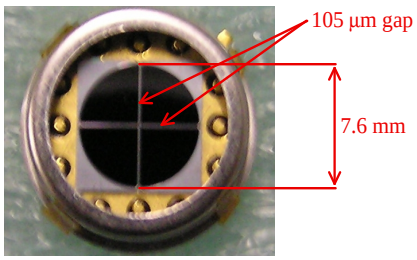

Figure IV.19: Photograph of one of the position–sensitive diodes. The dimensions are indicated in the Figure.

The position–sensitive X–ray photodiode (Fig. IV.19) was provided by the International Radiation Detectors (IRD) Incorporation. It consists of four quadrants which form a circle of 7.6 mm in diameter. Two neighboring quadrants are separated by a gap of 105 μm. The photodiode was oriented so that the separating axes of the quadrants were parallel to the X and Z axes of the positioning stage. These photodiodes were specially developed for X–ray detection with high photon fluxes like those of synchrotron beam lines. They are characterized by their robustness against radiation, their long–term stability as well as their dynamic range of 8 orders of magnitude. To prevent the deterioration of the stability of the

Si photodiode due to the UV radiation generated in the SiO_2 window protecting the photodiode, the detector window was replaced by a platinum silicide one. The amplifier and read–out (Fig. IV.21) electronic devices were provided by OnTrak.

Once the polycapillary half–lens is inserted in the primary beam, it needs to be orientated with the help of the two rotation motors of the positioning stage relatively to the incidence direction in order to optimize the X–ray intensity transmission through the polycapillary. The transmitted intensity is surveyed by a second position–sensitive diode, identical to the first one and placed at the position of the sample holder carousel. The center of the position–sensitive photodiode is identical to the position of the spot which should be irradiated on the sample subject to the measurement, i.e., the interception of the sample's rotation axis (TAL) and the spectrometer's dispersion plane defined by the TAF and CRY (or DET) axes. The diode allows not only to observe the transmitted beam intensity but also its relative spatial position later on on the sample. For this purpose the distance between the polycapillary optics exit and the photodiode should not deviate too much from the focal output distance. Note that this second position–sensitive photodiode was also used to position the spectrometer chamber correctly with respect to the primary beam. However, since the photodiodes were not calibrated in intensity and due to the gap between the quadrants the transmission through the polycapillary optics cold not be quantified accurately using the two photodiodes.

For the final orientation of the polycapillary optics relative to the primary X–ray beam, first the horizontal rotational orientation is optimized, then the vertical rotational orientation and finally the horizontal one may be checked again. The polycapillary optics position on the X and Z axes may need to be slightly corrected due to the fact that, because of the holding arm, the polycapillary optics aperture is not positioned on the axes around which the rotational movements are executed. The length of the holding arm was, however, dictated by spatial constraints. The stepping motors of the TAF and especially the TAL axis did not allow to place the positioning stage closer to the samples and thus to use a shorter holding arm.

The final adjustment step, once the transmission of the primary beam through the polycapillary has been optimized, is to adjust the distance between the polycapillary optics tip and the sample surface. For this purpose the position-sensitive photodiode used to survey the transmission is replaced by the sample holder on

which one of the four sample positions on the carousel is occupied by a fluorescence screen coated onto a polished aluminum plate (Fig. IV.20). The fluorescence screen was produced and deposited on the polished aluminum plates by Proxitronic Detector Systems. Its material composition was Gd_2O_2S:Tb and it is characterized by a green color light emission, the decay time of the emission being 2.6 milliseconds from 100% intensity down to 1%. The fluorescence screen thickness was 4 μm and the finest grain size was used. The latter choices were dictated by the enhancement of the spatial resolution of the emission, increasing dimensions resulting in larger fluorescence spots upon irradiation.

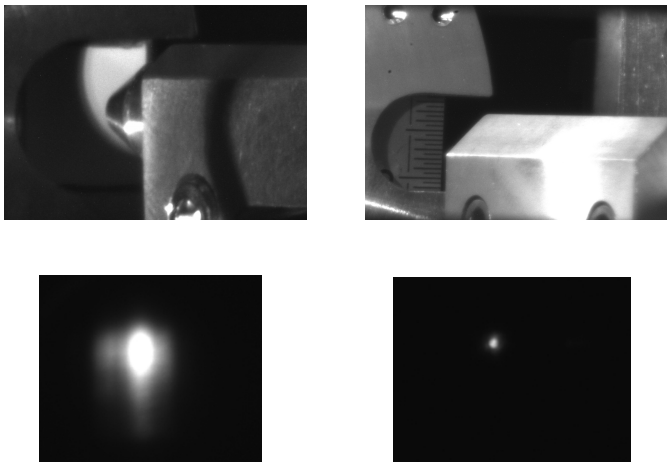

Figure IV.20: Pictures taken with the videosystem. On the top pictures, an outtake of the full field of view (right side) and a zoomed perspective are shown when the fluorescence screen was installed (left side). In both pictures the polycapillary optics in the aluminum holder can be seen. On the bottom pictures, a comparison of the irradiated spot sizes on the fluorescence screen without (left side) and with the aligned polycapillary optics in the beam (right side) is made. The view angle of the videosystem was 30° with respect to the primary synchrotron radiation beam direction.

The fluorescence screen allowed to observe qualitatively the spot size produced by the polycapillary optics (Fig. IV.20). Moving the polycapillary optics along the Y–axis (parallel to the TAF axis of the spectrometer) towards or away from the fluorescence screen changes the area illuminated on the screen. The separation distance to the sample can thus easily be tuned to the focal output distance. At this point the polycapillary optics is finally correctly aligned on the beam and the sample. A simple rotation of the carousel to switch from the fluorescence screen to

a sample allows to bring a sample surface into the focused primary X–ray beam. Indeed the mounting of the fluorescence screen and the samples on the back of the carousel ensures that upon a rotation of the carousel to switch from the fluorescence screen to a sample (or from one sample to an other) the distance between the polycapillary optics exit and the irradiated surface will not change (apart from the thickness of the fluorescence screen). The fluorescence screen, however, tends to deteriorate with time if exposed too long to an intense X–ray radiation.

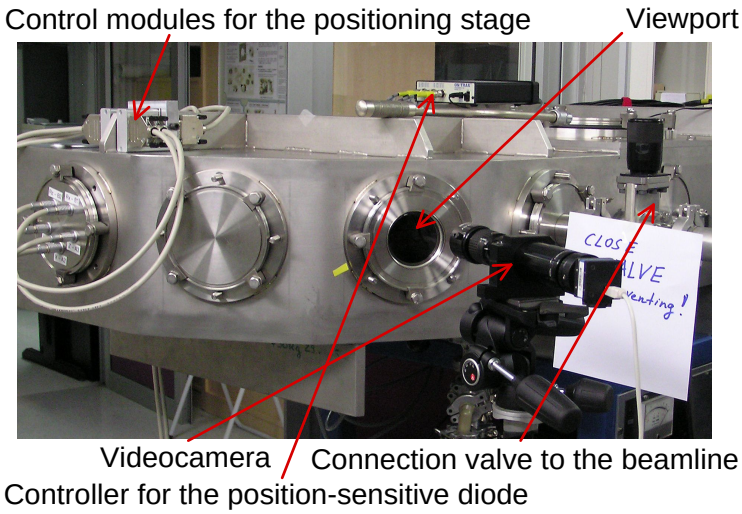

Figure IV.21: Photograph of the equipment installed outside the von Hámos spectrometer and needed for the control of the positioning of the polycapillary optics. A comparison with Fig. IV.2 shows the increased complexity of the operation of the experimental measurements.

The spot produced by the polycapillary optics on the fluorescence screen was directly observed through a viewport by a videocamera system installed on a tripod outside the spectrometer chamber (Fig. IV.21). The system was produced by Navitar and delivered by VIDEAL. The observation distance was 45 cm which made the requirements on the optics installed in front of the camera quite demanding (Fig. IV.22). During the experimental measurements the viewport was covered to avoid that any light enters the spectrometer chamber and produces background signals in the CCD detector.

The videosystem and the fluorescence screen allowed also a qualitative survey of the rotational orientation of the polycapillary optics and hence of the primary beam X–ray transmission by observing the luminosity and size of the spot on the fluorescence screen.

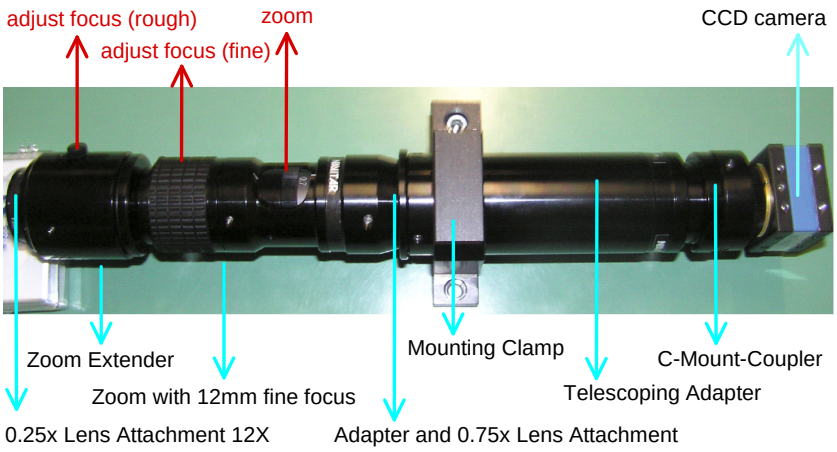

Figure IV.22: Photograph of the assembled videocamera system.

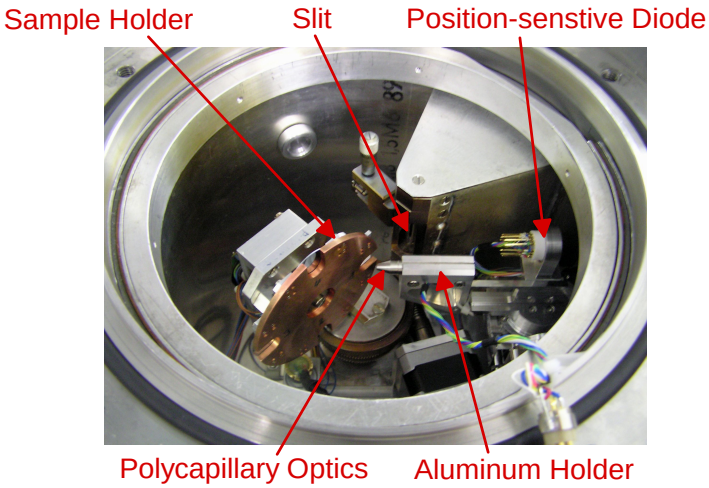

Figure IV.23: Photograph of the polycapillary optics installed inside the von Hámos spectrometer, showing the restriction in space.

The von Hámos geometry of the spectrometer requires that the sample needs to be positioned adequately on the spectrometer's TAF axis with respect to the (open) slit system (Fig. IV.23) in order that the measured fluorescence X–rays of wavelength λ_e can hit the diffraction crystal at the Bragg angle (Eq. IV.1; section IV.2.2). In order to avoid that the distance between the polycapillary optics output and the sample surface had to be adjusted for each position to the output focal distance, the positioning stage was connected for convenience and security reasons to the carrier of the sample holder so that it was moved together with the sample holder along the TAF axis. This was quite challenging since the positioning stage and the two other axes for the adjustment of the sample holder, the TAT and TAL axes, should still be independent from each other. The motivation was to

preserve the lateral surface mapping and of course the angular scanning capabilities. Therefore it was necessary that the sample could be moved along respectively around these axes while the position of the polycapillary optics remaining unaltered. Since in the construction of the sample carrier system, the two spectrometer axes TAT and TAL are superimposed on the TAF axis, these requirements made some mechanical modifications necessary when the positioning stage was installed. Also a new fixation system was designed to be able to easily install or remove the positioning stage. To minimize vibrations on the positioning stage when moving the carriage of the sample support together with the positioning stage along the TAF axis, the speed of the corresponding stepping motor was reduced.

The choice of the focal output distance to 8 mm was also guided by space constraints. The samples should indeed not touch the polycapillary exit when rotated to grazing emission angles. Since the vertical rotation axis passes through the middle of the 12 mm wide sample and because the measurement positions correspond to angles between the sample surface and the polycapillary axis of up to 60°, some free space between the polycapillary exit and the samples was really needed. Similarly the polycapillary exit should not intercept the detection path of the fluorescence X–rays.

Chapter V

Experimental

The presented depth–profiling measurements were performed with the synchrotron radiation based high–resolution based GEXRF setup presented in chapter IV. The experiments were carried out at the ID21 beam line at the ESRF in Grenoble, France, employing the von Hámos–type bent crystal spectrometer of the University of Fribourg which was transported to the ESRF and installed downstream the SXM chamber of the ID21 beam line (see section IV.1). Two sets of samples were investigated, namely, Al–implanted Si wafers and P–, In–, and Sb– implanted Si and Ge (only P–implantations) wafers. For the latter a polycapillary optics was used to focus the primary synchrotron X–ray beam.

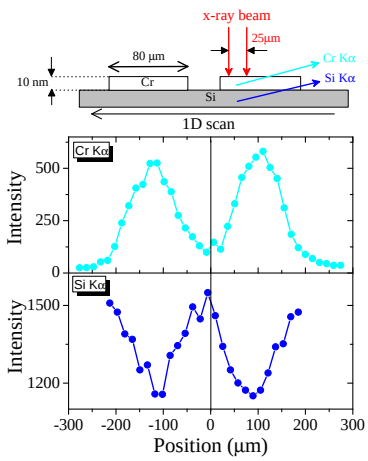

Figure V.1: Lateral surface scan of a Si surface covered by Cr strips with a micrometer resolution beam realized with the von Hámos spectrometer at the ESRF ID21 beam line.

In the following the importance of depth–profiling measurements with nanometer resolution will be emphasized. The nanometer resolution is especially important

with regards to actual applications of ion–implanted samples where the focus lies especially in the semiconductor industry on lower implantation energies and thus shallower implantation profiles. In this domain, as it will be shown, depth–profiling by means of GEXRF presents an attractive alternative to existing depth–profiling techniques since it can fully profit from intense synchrotron radiation beams and the advantages offered by wavelength–dispersive detection setups to perform non–destructive sample analysis. In addition lateral 2D–scanning capabilities are offered [120] (see Fig. V.1). So far, mostly implantations in Si wafers have been studied, but with respect to future applications in the semiconductor industry and solar cells doped Ge wafers are also of interest.

V.1 Motivation for depth–profiling experiments

The production of semiconductor–based devices, e.g., transistors or diodes, reposes on a reliable doping of the semiconductor wafers. The semiconductor material to be doped is in general Si, an element of group IV of the periodic table, but Ge or group III/V compounds can also be envisaged. The doping of Si is necessary to alter its physical and electrical properties in order to realize specific applications. In the doping process, in general group III (acceptors) and group V (donors) elements are introduced in a controlled way in the Si matrix to produce for example p–n junctions.

The doping of the Si wafer can be realized with different approaches, like diffusion and implantation. In doping by diffusion, the Si wafer is exposed to a high–temperature environment containing the dopant atoms. The latter will diffuse into areas with a lower dopant atom concentration, i.e. into the semiconductor wafer. Even if several wafers can be treated simultaneously, ensuring thus a high wafer throughput, dopant diffusion has been replaced by ion implantation.

Indeed the method of choice to dope semiconductors is nowadays ion implantation as it presents the best control over the relevant parameters for the final distribution (laterally and in the depth direction) of the dopants, a great flexibility (possible material combinations, sequential doping of the same wafer) as well as an excellent reproducibility [196]. The usefulness of ion implantation was first discussed by W. Shockley in the early 1950's [197] to improve the performance and characteristics

and facilitate the construction of semiconductor transistors. For his efforts in this domain he was awarded the Nobel prize in 1956. Ion implantation started to be widely used about twenty years later for doping semiconductor devices and thus modifying the electrical properties of selected areas by bombarding these areas with specific ions. Today it is one of the techniques of choice when it comes to alter the physical, chemical or electrical near surface properties of a material.

As a material engineering technique, ion implantation is not only used in the semiconductor domain but, since it can be applied to a wide range of materials, also in the domain of surface finishing, for example to strengthen tool steel [198,199] or to improve the war resistance of joint prosthetic material [200, 201] by implantation of N ions. The wear, friction and corrosion properties of surfaces can be improved by ion implantation. For steel tools the difficulties with respect to other coating techniques are the shape of the tool, and thus the varying orientation with respect to the incident ion beam, and the inability to treat very large areas in a reasonable time [199]. The advantages offered by ion implantation are the facts that it is not a high–temperature treatment, that a delamination of the treated surface is impossible and that the object size is not altered. In addition ion implantation is a very clean technique, which explains also partially its success in the semiconductor world where the produced devices are very sensitive to any contamination.

The main parameters for the implantation process are on one hand the ions used for implantation and the wafer to be implanted, and on the other hand the implantation energy (in keV) and fluence (in atoms/cm^2) [196]. For a given ion–target combination, the latter two parameters determine the mean penetration range (or centroid position), the width of the concentration distribution (Fig. V.2) and the ion concentration level in the depth direction inside the implanted sample. If the implantation energy is chosen low enough, only the near–surface region is altered. The distribution of the implanted ions is characterized by a maximum concentration peak (which may be above the limit for solid solubility) at the mean penetration range and diffusion tails on both sides of the concentration peak. In the implantation process the ions are extracted from the source and accelerated by electric fields towards the target. To implant larger lateral areas either the target sample or the beam have to be moved. Upon target impact, the ions start to gradually lose their kinetic energy during collisions with electrons and nuclei in the sample until they come to rest. Due to the random distribution of the collisions

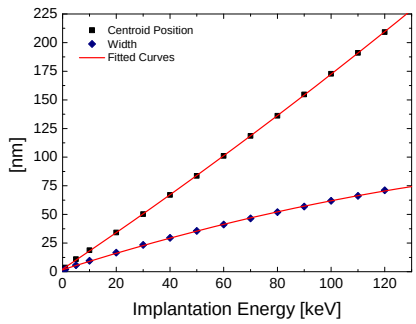

Figure V.2: Illustration of how the centroid position for maximum concentration and the standard deviation of the distribution of Al ions implanted into Si depends (in theory) on the implantation energy.

the ions do not all stop at the same distance from the sample surface. For heavy ions or low energies, nuclear stopping (elastic collision between the implanted ions and the substrate atoms) dominates, while for light ions or high energies, electronic stopping (excitation of the electrons and ionization of the substrate atoms) prevails.

When doping semiconductor wafers by means of ion implantation, the implantation process is inherent with the creation of defects (interstitials and vacancies) in the crystal structure of the Si wafers. In order to repair these defects, which can also affect the final dopant distribution, the implanted Si wafers are annealed, i.e., thermally treated to provide a sufficient activation energy in order to induce defect migration. The redistribution of the atoms reduces the damage. However, annealing is also responsible for a further diffusion (transient enhanced diffusion) of the dopants and therefore an extension of the implanted region, in particular in the depth direction. In this perspective annealing techniques are still an active research area, different annealing procedures (rapid thermal annealing, spike annealing, laser annealing) being tested in order to minimize diffusion. Besides diffusion during annealing, channeling is also responsible for the propagation of implanted ions to larger depths than expected. Channeling means that the implanted ions propagate along the crystallographic directions, the number of collisions with substrate atoms being thus reduced. This effect can, however, be avoided by pre–amorphization of the Si wafer before implanting it. A further aspect which may affect the dopant profile as well as the effectively retained dose is sputtering of substrate atoms by the implanted dopants. The most critical aspect remains, however, the diffusion of the implanted ions since the diffusion determines

the depth region affected by the implantation process.

Indeed, the advances made over the last decade in the semiconductor industry are essentially due to the miniaturization of devices. Currently the smallest commercially available devices are based on the 32 nm manufacturing process, and for reasons of device-scaling, smaller device sizes require shallower dopant distributions. Decreasing feature sizes offer the chance to further enhance the device speed and to design more and more complex integrated circuits (IC) leading nowadays to ultra large scale integrated circuits (ULSI) with more than a billion transistors. Moreover the production cost per device unit and the power consumption decrease with the device size. However, in order to keep the aspect ratio of the devices constant, this down-scaling implies shorter channels and therefore increased leakage currents, strongly limiting the device performance. This short-channel effect can be suppressed by designing devices based on USJ (ultra-shallow junctions) with junction depths of several tens of nanometers. In order to produce the required shallow dopant profiles, the implantation energies are decreased to a few keV since this is the parameter which determines the projected range of the final dopant distribution. However, the diffusion of the ions sets a second limit to the smallest achievable junction depth. Alternatively, for a fixed implantation energy, shallower profiles can be produced in a Ge matrix compared to a Si matrix, due to the higher Ge density. Decreasing implantation energies, however, reduces the efficiency of the implantation process: due to space-charge effects the beam current is limited, resulting in longer production times. Implantation doping at low energies may economically not be suitable for reasons of wafer throughput. Alternatives to ultra low energy (ULE) ion implantation combined with rapid thermal annealing (RTA) for efficiently doping to shallow depths in a controlled way are plasma ion immersion implantation [202] which suffers less from heating and charging effects on the sample while high doping doses can be achieved and cluster ion implantation [203] which profits from the decreased charge density of the implanted molecules but produces more damage. Tilting the wafer with respect to the incident ion beam during the implantation allows also to dope narrower depth areas [204]. A further alternative is gas cluster infusion [205].

Besides the study of new doping techniques, alternatives to Si as the semiconductor material of choice are also considered. In this perspective Ge draws again an increased interest [206]. As a semiconductor material Ge was for a long time

considered to be inferior to Si. Indeed Ge presents a smaller band gap, thus a lower junction breakdown voltage and a higher sensitivity to short–channel effects. In addition, the lack of a stable oxide needed to passivate the surface and act as an etch protector hampered the industrial use of Ge [207]. On the other hand, Ge presents attractive electrical and chemical properties (ability to deposit high-k gate dielectrics, high mobility of electrons and holes) which allow the realization of faster chips and smaller transistors than with Si–based semiconductors [207–209]. The main problem up to now is the diffusion of P in Ge which made it impossible to introduce large–scale transistors on the basis of Ge.

Independently of the doping technique and the chosen material combination, an accurate experimental assessment of the dopant depth concentration profile is needed in order to support further progress in the semiconductor industry. The profiling of narrow junctions is quite challenging but necessary to survey the manufacturing processes and assist in further developments. Indeed, progresses in order to realize a reliable and precise characterization of dopant distributions in semiconductor materials, for example ultra shallow junctions in metal oxide semiconductor field effect transistors (MOSFET), are needed in order to follow the trend of shrinking down device sizes to some nanometers. Channeling and diffusion make a theoretical prediction of the dopant distribution difficult, novel and improved diagnostic tools for the experimental depth–profiling of dopants in semiconductor materials and the determination of the retained dose are essential for further developments in the semiconductor technology.

V.2 Current methods for depth–profiling

For the experimental determination of the dopant concentration profiles, several well established methods exist for depth–profiling which have each their advantages and drawbacks.

The most common and widely used depth–profiling technique is secondary ion mass spectroscopy (SIMS) [210]. In SIMS the surface is sputtered by an incident ion beam (the ions being used for analysis not doping) and the sputtered ions are mass–analyzed. Usually the latter analysis is realized with a mass spectrometer after the extraction of the ions. In time–of–flight (TOF) SIMS [211] a pulsed

sputtering ion beam is used and the time after each pulse until the individual ions are detected is considered. Heavier ions of a given energy need more time to arrive to the detector than light ions of the same energy. Knowing the sputtering rate, i.e., the sample thickness removed by sputtering per unit of time, the detected sputtered ions can be associated to a depth, depending on the time at which they are detected after the measurement has started. SIMS is very precise but struggles with the characterization of the depth and concentration distribution of dopants located within the first few nanometers below the surface. Despite recent progresses [212,213], like decreasing the energy of the sputtering ions or using different types of sputtering ions, SIMS suffers from the formation of a transient region. Thus, until an equilibrium regime between the implanted and sputtered ion yields is established, SIMS delivers unreliable results in terms of quantification and reconstruction of the dopant concentration profile. The possible presence of an oxidized surface aggravates this problem. Therefore SIMS, which is usually a very precise depth–profiling technique, has difficulties to fully characterize narrow depth distributions located within the first 10–15 nanometers below the surface. In [103], the problem with the transient region was circumvented by combining results obtained by means of GIXRF and SIMS, the depth profile obtained by means of GIXRF being used to correct the depth scale of the result obtained from the SIMS measurement of the corresponding sample. Besides the mentioned drawbacks, SIMS is also a destructive depth–profiling technique and a lateral mapping is only possible on a rough scale.

In Rutherford backscattering (RBS) [214] and, the related technique, medium energy ion scattering (MEIS) [215], an incident monoenergetic ion beam is incident on the sample and the number and energy of backscattered projectiles from the near–surface region are measured with the aim to determine the quantitative structural composition of this sample area. Both techniques are non–destructive but RBS might not have the proper depth resolution, the resolution being of the order of some nanometers. Although high resolution RBS and MEIS do have the proper depth resolution, they both suffer from their low efficiency for light elements and low mass resolution for heavy elements. In addition the lateral resolution is again poor.

Techniques based on electrons [216] like Auger electron spectroscopy (AES) or X–ray photoelectron spectroscopy (XPS) are quite surface–sensitive. Both tech-

niques rely on the excitation of atoms and the measurement of electrons emitted from the sample surface. In AES the Auger electrons emitted as a result of the radiationless de–excitation of an ionized atom are measured, while in XPS the photoelectrons are detected. In both methods, the kinetic energy of the electron depends strongly on the element and the electronic shell from which the electron emitted. Due to the low mean penetration range of electrons, they are confined to the surface so that depth–profiling measurements cannot be realized for distributions of dopants implanted at higher energies. Combinations with surface sputtering have been realized in order to increase the accessible depth region. Further, despite the surface–sensitivity an absolute quantification of the implanted dose is quite difficult if not impossible.

PIXE based depth–profiling (by varying the incident proton energy or the detection angle of the induced X–ray emission) is characterized by a poor depth–resolution and can only be successfully applied to study some specific samples [217].

On the other hand GIXRF and GEXRF do not suffer from the mentioned drawbacks, like the destruction of the analyzed sample or the need to work in a high–vacuum environment for particle–based methods, and are sensitive enough to detect trace amounts of impurities on or inside wafers [102, 140]. Quantification problems have been discussed for GEXRF in [140, 143] and for XRF applied to implanted samples in [218]. Depth–profiling of implanted dopants by means of GIXRF and GEXRF is possible because of the diffraction of the emitted fluorescence X-rays at the flat, polished sample surfaces. By tuning the incidence angle θ_i, respectively the exit angle θ_e, the accessible region for measurements with GIXRF and GEXRF can be changed from few nanometers to hundreds of nanometers.

For implantation energies in the keV–range, the typical ion penetration ranges are on the scale of several tens of nanometers to at most hundreds of nanometers, i.e. on a submicrometer scale, and are thus well adapted for the GIXRF and GEXRF techniques, due to their surface–sensitivity. Because of the refraction of the X–rays at the vacuum–sample interface, only the X–ray intensity from atoms very close to the surface (typically 3–5 nm; Figs II.4 and III.1) is detected at incidence, respectively, emission angles below the critical angle θ_c. Above the critical angle, the depth region contributing to the measured X–ray intensity starts to increase. It will extend from the sample surface towards larger depths, the ex-

tension in the depth–direction increasing with the incidence angle θ_i respectively the emission angle θ_e. However, the grazing incidence angles imply long incidence paths whereas the grazing emission angles imply long emission paths within the sample. This results in a large sensitivity to the sample matrix and a limited depth region which effectively contributes to the detected X–ray fluorescence intensity to several hundreds of nanometers, the primary X–rays being strongly attenuated in the depth direction respectively the fluorescence X–rays emitted by atoms located at larger depths being mostly absorbed. However, because of the wide range of accessible depth regions (2–3 orders of magnitude by increasing sufficiently the incidence, respectively, the emission angle) these methods can be applied, with regard to the sample composition, to a broader range of ion-implanted samples compared to SIMS, AES, or XPS. Also, depending on the realized application, the implantation dose can differ by several orders of magnitude, but the linearity in the intensity response of X–ray detectors provides enough flexibility.

GIXRF and GEXRF present thus an interesting alternative to the already known methods of depth–profiling. In addition, as shown in [95], TXRF combined with chemical etching can be also used for depth–profiling but, in this case, the advantage of non-destructibility is lost. Consequently, as it will be shown in the discussion of the experimental results, the depth distribution of implanted ions can be reconstructed by means of GEXRF by measuring the intensity dependence of an X–ray emission line from the implanted species on the grazing exit angle defined relatively to the flat target surface. In Fig. V.3 the theoretical concentration distributions of P ions implanted at different energies into Si are shown (upper left panel), the mean penetration depth and the width of the distribution depending on the implantation energy (upper right panel). The expected angular intensity curves for the P Kα–line depend directly on the P distribution (lower left panel); the knowledge of the extinction depth for the P Kα–line (Fig. III.1) allowing to estimate up to which emission angle θ_e the angular intensity profiles should be measured so that all of the implanted ions are within the extinction depth (lower right panel). This may be interesting for high implantation energies to estimate which angular range should be covered. The latter should anyhow exceed something like two times the critical angle θ_c. GEXRF has thus the potential to extend the accessibility of depth–profiling techniques towards dopant distributions on a nanometer scale.

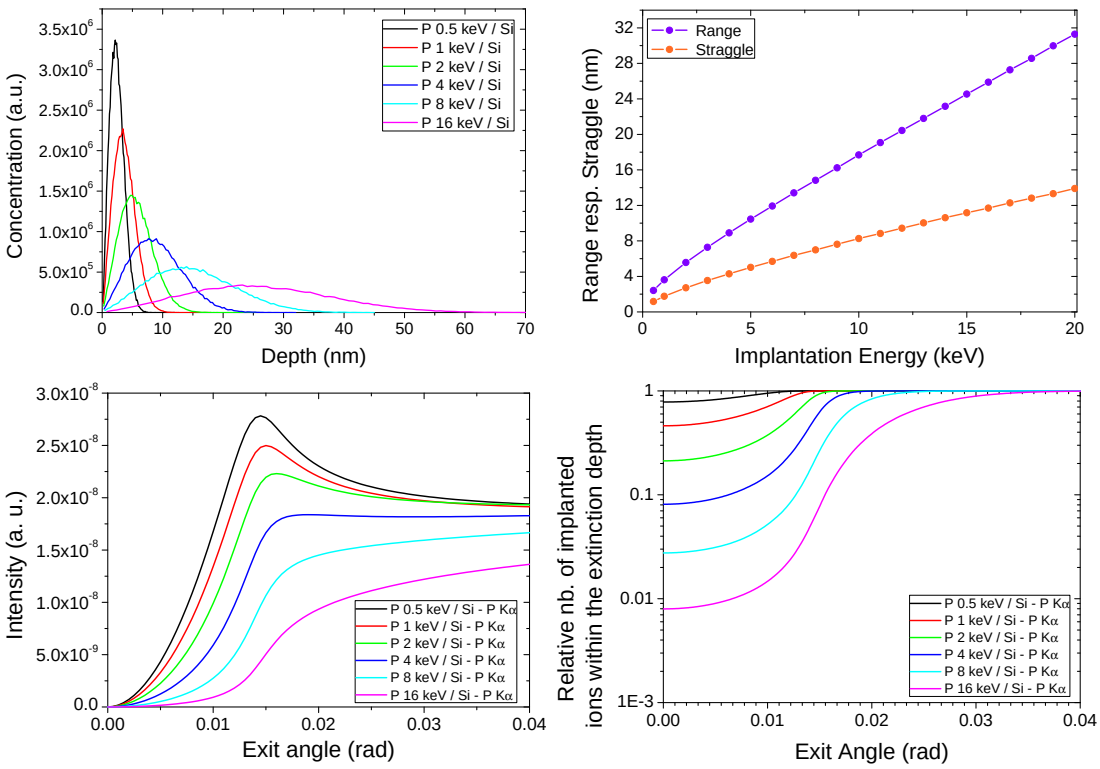

Figure V.3: Study of the case of low–energy P–implantations into Si. The expected depth distributions depend on the implantation energies (upper panel). Note that all of the calculated dopant distribution curves have the same area and contain thus the same number of ions. The dopant distribution influences significantly the angular intensity profile (lower left panel) and the number of implanted ions contained within the extinction depth varies with the exit angle θ_e (lower right panel) since for larger exit angles the extinction depth increases (Fig. III.1).

The realization of depth–profiling measurements without *a priori* assumptions on the dopant distribution allows also to study diffusion processes, the understanding of which is extremely important with regard to applications. In addition, it supports simulations of dopant distributions resulting from ion implantation procedures. It will be shown that from the angular intensity profile $I(\theta_e)$ obtained by means of GEXRF, the dopant depth distribution can be extracted with and without *a priori* knowledge on the shape of the distribution.

V.3 Experimental Conditions and Measurements

The experiments for the Al–implanted Si wafers and the P–, In– and Sb–implanted Si and Ge wafers were realized in two different runs at the ESRF. The different

components of the setup were described in chapter IV.

V.3.1 Al–implanted Si wafers

For the measurement of the Al–implanted Si wafers the primary X–ray beam was delivered by a wiggler and monochromatized by two Ni/B_4C multilayers. Higher–order harmonics were rejected by means of two Si mirrors tilted at an angle of 12 mrad with respect to the incident primary beam. The beam size was defined by a pinhole with a diameter of 2 mm. The beam energy resolution was about 6 eV for the two selected primary X–ray beam energies, namely 1.582 keV for the detection of the Al-Kα line and 2.000 keV for the Si-Kα line, both energies being just above the absorption edge of the considered X–ray fluorescence lines. The primary beam photon flux was about 5×10^{10} respectively 2×10^{11} photons per second for the mentioned energies. The choice of the excitation energy for the Al Kα fluorescence line was guided by several considerations. At the excitation energy of 1.582 keV, in addition to the suppression of the strong Si Kα fluorescence line and an increase of the photoelectric absorption cross–section, a considerable background reduction could be achieved. A possible overlap of the K X–ray resonant Raman scattering (RRS) of the Si L-shell [85] with the Al Kα fluorescence line that could affect the detection limit of Al impurities in or on Si wafers was avoided [120, 133]. As the position of the Raman structure cut–off $E_{\mathrm{R,\,L}}$ for the L–shell depends directly on the primary beam energy E_{B},

$$E_{\mathrm{R,\,L}} = E_{\mathrm{Si\ K\alpha}} - \Delta, \text{ where } \Delta = E_{\mathrm{B}} - E_{\mathrm{Si\ K\text{–}edge}} < 0\,, \tag{V.1}$$

an adequate tuning of the primary X–ray beam energy allowed avoiding this overlap. At a beam energy of E_{B} of 1585.6 eV, the cut–off energy of the Raman structure E_{R} is identical to the energy of the Al Kα fluorescence line (1486.7 eV). By choosing a primary beam energy between 1559.6 eV (the Al K–edge) and 1585.6 eV, the Si RRS–KL (resonant Raman scattering) could be separated from the Al Kα fluorescence line and the elastic peak did not overlap with the Al Kα–line (Fig V.4). Note that this separation which could be achieved thanks to the high resolution of the von Hámos spectrometer would not have been possible with an energy–dispersive detection setup. Finally, the remaining background overlapping with the Al Kα line was found to arise only from the weak Si RRS–KM and the intrinsic noise of the CCD detector (about 2.5×10^{-4} counts per second). The background conditions for the measurements with the Al–implanted samples are

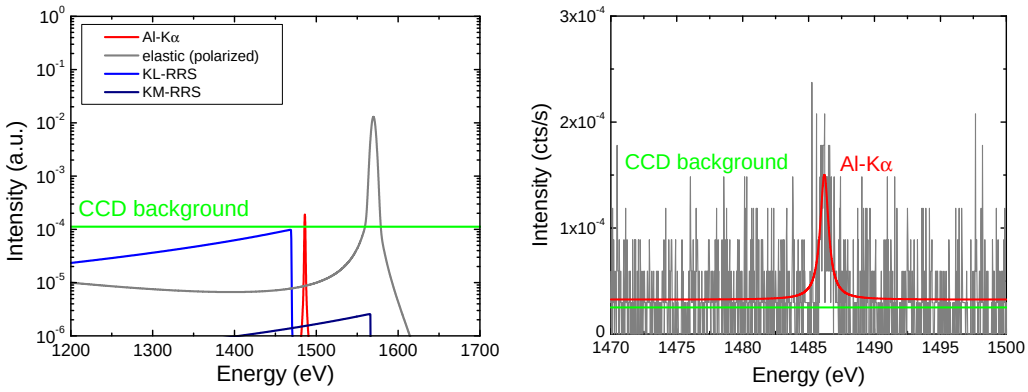

Figure V.4: Shown are the expected background contributions (left side) and the experimentally observed background on a clean Si wafer (right side). The choice of the primary beam energy and the high–resolution of the detection setup allows separating the Si RRS from the Al Kα–line. With a less good energy resolution the Si–RRS and the Al Kα signals would broaden (the area remaining constant) and overlap, worsening the detection limits. The optimized background conditions allowed to observe the Al signal from impurities on a supposedly clean Si wafer.

illustrated in Fig. V.5. With these optimized background conditions, a direct detection limit of 4×10^{12} atoms/cm^2 could be reached for the detection of Al impurities on the surface of Si wafers [133]. Note that the combination of primary beam energy tunability and high energy resolution detection is very helpful if it comes to extracting the signal from a trace element of atomic number Z located in (or on) a bulk material with atomic number $Z + 1$ [219].

For higher Z impurities in (or on) a Si wafer, the Si RRS is not present and direct detection limits of 10^{12} atoms/cm^2 or better could be achieved with the present setup, except for heavy elements [120] (Fig. V.6). These detection limits are below the technologically relevant implantation doses ranging currently from about 10^{15} atoms/cm^2 down to 10^{14} atoms/cm^2 and below.

For the detection of the Al Kα, respectively Si Kα fluorescence lines, the spectrometer was equipped with the cylindrically curved ADP (101) crystal ($2d = 10.642$ Å, curvature radius $R = 25.4$ cm, see table IV.2) and the back-illuminated position-sensitive CCD (Coupled Charge Device) camera (1340×400 pixels of 20×20 μm^2, read–out speed of 1 MHZ, see section IV.2.2).

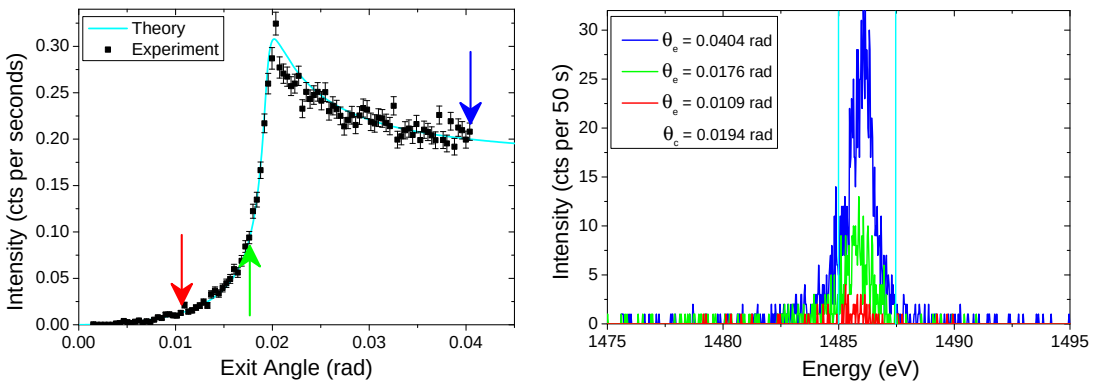

Figure V.5: The choice of the beam energy of 1582.2 eV (see text for details) allowed to perform the measurements of the intensity dependence on the exit angle at very clean background conditions. The background conditions are shown for three different exit angles, once below, once in the vicinity and once above the exit angle. The light blue bars indicate the region of interest selected on the CCD.

The Al and Si Kα X–ray lines were measured as a function of the exit angle by means of an automated acquisition system. The measurements of the Al Kα–line were performed in two successive scans consisting of 100 different angular positions with a step of 0.0225° (except for the sample implanted at 1 keV for which 156 points spaced by 0.01125° were acquired, plus 20 points for the largest exit angles spaced by 0.0225°) and an acquisition time of 50 seconds for each step. The stability and reproducibility of the experimental setup were checked by comparing the two scans. For each sample, an excellent agreement was found. The Si Kα fluorescence X–ray line was measured at 40 different points separated by 0.05625° with a collecting time of 20 seconds per point. The angular profiles for Si were needed for calibration purposes. Indeed, as it has been stated in section IV.2.1, the exit angle can be controlled only on a relative scale and in order to know the exit angle on an absolute scale, a reference position is needed. In our case this reference position corresponds to the critical angle $\theta_{c,\mathrm{Si}}$ of the Si Kα–line of the considered implanted Si sample. The corresponding sample position is extracted from a Gaussian fit of the derivative of the measured angular intensity curve for the Si Kα–line (Fig. V.7).

Here, however, special care is necessary because the formula given by Eq. II.5 is only a reasonable approximation of the critical angle if the energy of interest, i.e. in the present case the energy of the fluorescence line is far enough from the

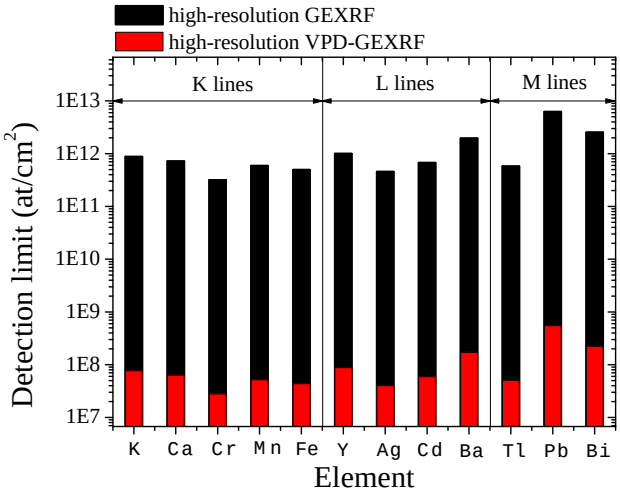

Figure V.6: Detection limits achieved with the synchrotron radiation based high–resolution GEXRF setup.

absorption edge. This limitation becomes apparent when comparing the critical angles calculated by means of Eq. II.5 to the values furnished by the Center for X–ray Optics (CXRO)[1] (see Fig. V.8). For the critical angles of the fluorescence lines (Si–Kα for Si and Ge–Lα) used for the calibration of the angular scale, this limitation may be not too severe, but for the depth–profiling calculations for some fluorescence lines this difference has to be considered and the exact values provided by CXRO are recommended.

Once this reference position is known, the offset of the angular scale and consequently the absolute exit angle can be determined for each position of the investigated sample. The critical angle $\theta_{c,\mathrm{Si}}$ of the Si Kα–line for the implanted samples was assumed to be the same as the one corresponding to the bulk Si. This assumption can be justified by the fact that the investigated samples are implanted at too low doses to induce significant changes in the refractive index (Fig. V.10). Actually such changes, if any, are expected for the lowest implantation energies since then the samples have the highest peak concentrations of Al. In addition for these samples a considerable part of the implanted ions are located close, i.e., within the extinction depth for exit angles below the critical angle $\theta_{c,\mathrm{Si}}$, to the surface where the emitted fluorescence X–rays are diffracted. For the sample implanted at an energy of 1 keV, considering the energy of the Si Kα–line, the estimated maximum relative change with respect to bulk Si of the real part of the refractive index (the

[1] `http://henke.lbl.gov/optical_constants/`

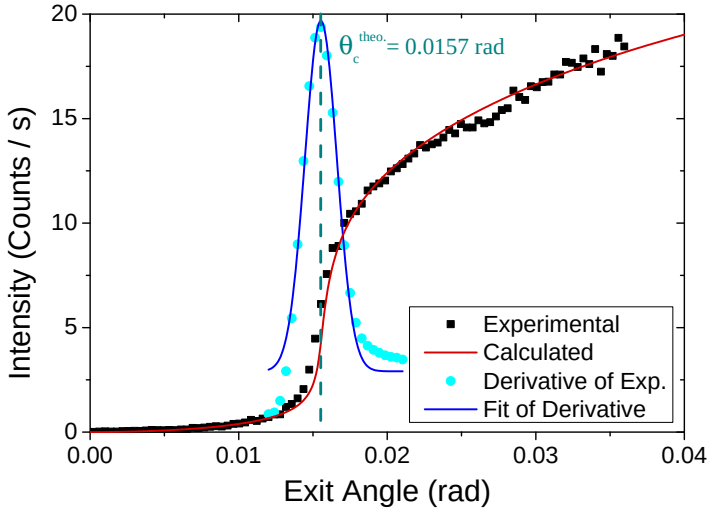

Figure V.7: Calibration of the exit angle θ_e with the angular intensity profile of a bulk fluorescence line, namely the Si Kα. The derivative of the angular intensity profile yields the position of the critical angle.

part describing the scattering properties) is of the order of 10^{-6}, whereas for the imaginary part (describing the absorption properties) the relative change is about 4%. Calculations of the Si Kα angular intensity revealed no difference for bulk Si and ion–implanted Si. It can be noted that the changes are small not only because the concentration of Al in the investigated samples is low, but also because the elements corresponding to the dopant and the wafer lie close together in the periodic table.

Nine different Al–implanted Si samples were analyzed, corresponding to implantation energies of 1, 5, 10, 15, 20, 25, 30, 50 and 100 keV. Each implantation was realized at room temperature and 90° incidence to the surface with a fluence of 10^{16} atoms/cm^2 into clean 0.2 mm-thick Si (100) wafers. The implantations with energies between 1 keV and 25 keV were realized at the Ion Beam Physics and Materials Research Institute at the Forschungszentrum Dresden–Rossendorf in Germany, whereas the other samples were prepared at the Institute of Electronic Materials Technology in Warsaw, Poland.

V.3.2 P–, In– and Sb–implanted Si wafers and P–implanted Ge wafers

For the second set of wafers, the depth–profiling measurements were realized by means of micro–focused GEXRF. To this end, a polycapillary focusing half–lens

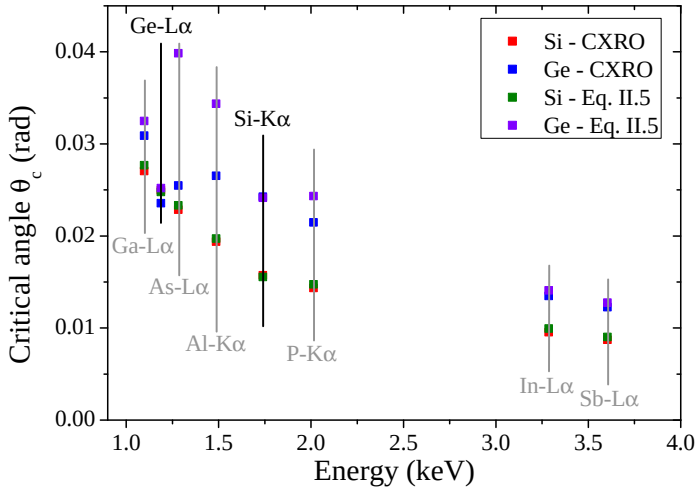

Figure V.8: Comparison of the calculated critical angles to the values furnished by the Center for X–ray Optics (CXRO) for Si and Ge substrates.

was inserted in the primary X–ray beam. The alignment of the polycapillary optics was described in section IV.3.2. This setup allowed to study the dopant depth profile locally and to perform a lateral surface scan with micrometer resolution to study the homogeneity of the implanted dose. A 3D–scan of the surface–near region of a sample is thus conceivable.

The primary X–ray beam was delivered by the two undulators of the ID21 beam line and the size of the 3×3 mm^2 beam was defined by two pairs of slits. The full beam was thus intercepted by the polycapillary entrance aperture of 4.4 mm in diameter. The simultaneous use of two undulators resulted in fluxes as high as 3.5×10^{13} and 2.4×10^{13} photons per second for the two selected primary beam energies. The experimental measurements with the P–, In– and Sb–implanted Si wafers were performed at an energy of 4240 eV (just above the L_3 absorption edge of Sb), whereas an energy of 3190 eV was selected for the measurements with the P–implanted Ge wafer. To avoid primary X–ray beam position instabilities, due for example to changes of the thermal load on the optical components, and thus the necessity to realign the polycapillary half–lens, only two X–ray beam energies were used. The monochromatization of the primary beam was realized with two Ni/B_4C multilayers, while the higher order harmonics were rejected by Ni mirrors tilted to 7.25 mrad with respect to the incident primary beam. The K– respectively L–absorption edges of the implanted P, In and Sb dopants being all above the K absorption edge of Si, the background contribution of the strong Si Kα fluorescence lines was thus unavoidable. The high–resolution detection with the

von Hámos spectrometer permits, however, to separate accurately the different fluorescence signals. This was of prime importance for the P–implanted Si wafers, the P Kα–line (2013.7 eV) being separated by only 274 eV from the Si Kα–line (1739.9 eV).

Note, however, that the choice of the X–ray beam energy to ensure a high photon flux did not allow to acquire the angular profiles for the Lα–lines of Ga (1097.9 eV) and As (1282.0 eV) dopants. The reason was probably the Bremsstrahlung of the photoelectrons from the bulk Si or Ge atoms which induced a quite intense background in the low energy region (see Fig. V.9). The maximum energy of the Bremsstrahlung corresponds to the difference between the primary beam energy and the binding energy of the electrons creating the Bremsstrahlung. Since the Bremsstrahlung intensity decreases with the X–ray energy, the photoelectron Bremsstrahlung background did not affect the measurements of the In and Sb Lα–lines, and only to a small content the measurements of the P Kα and Si Kα–lines. Because of the Z–dependence of the Bremsstrahlung intensity and the lower L–absorption edge of Ge with respect to the K absorption edge of Si, the primary beam energy was decreased from 4240 eV to 3190 eV for the measurements with the P–implanted Ge wafers. The primary photon beam flux decreased by about 30%, but it was still high enough.

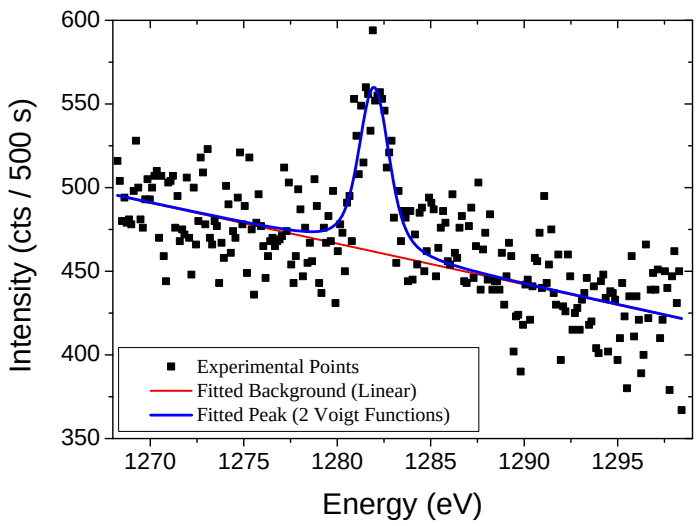

Figure V.9: The photoelectron–induced background at the beam energy of 3.19 keV made it impossible to measure the angular dependence profile for the As Lα–line.

The P Kα, In Lα, Sb Lα and Si Kα fluorescence X–ray lines of the P–, In– respec-

tively Sb–implanted Si wafers were diffracted by means of the cylindrically curved ADP (101) crystal ($2d = 10.642$ Å, curvature radius $R = 25.4$ cm, see table IV.2) in first order for the P Kα and Si Kα–lines, and in second order for the In Lα and Sb Lα–lines. The energy discrimination of the CCD allowed to well separate the Lα–lines diffracted in second order from the tails of the Si Kα line diffracted in first order which were partially overlapping with the dopant fluorescence lines. For the P–implanted Ge wafers the cylindrically curved TlAP ($2d = 25.772$ Å, curvature radius $R = 25.4$ cm, see table IV.2) was employed in second order for the Ge Lα–line and the P Kα–line. The diffracted X–rays were detected by means of the back-illuminated position-sensitive CCD (Coupled Charge Device) camera (1340×400 pixels of 20×20 μm^2, read–out speed of 1 MHZ) described in section IV.2.2.

The emission angles were calibrated for each sample by means of the critical angles $\theta_{c,\mathrm{Si}}$ or $\theta_{c,\mathrm{Ge}}$ for the Si Kα–line emitted by the bulk Si wafer or the Ge Lα–line of the bulk Ge wafer, respectively. For the present ion–implanted samples it was assumed, like for the Al–implanted Si wafers, that the implanted dopants did not affect noticeably the refractive index of the implanted wafers with respect to a pure bulk sample (Fig. V.10). The angular intensity profiles $I(\theta_e)$ were measured at 100 different exit angles θ_e for 50 seconds per angle for the P Kα–line (for both the P–implanted Si and Ge wafers), at 60 different exit angles for 150 seconds per point for the In and Sb Lα–lines, and 50 different exit angles for 20, respectively 30 seconds for the Si Kα and Ge Lα–lines. The points in the angular X–ray fluorescence intensity scans were separated by 0.0225° for the dopants (P Kα, In Lα and Sb Lα–lines), respectively by 0.0450° for the signal from the bulk (Si Kα and Ge Lα–lines).

The undoped Si and Ge crystal wafers were delivered by Siltronix. The crystal orientation of the wafers was (100), the thickness 500 μm and the wafers were polished on a single side. The doping of the wafers by ion implantation was realized at the Ion Beam Physics and Materials Research Institute at the Forschungszentrum Dresden–Rossendorf in Germany, the implantation direction being perpendicular to the wafer surface. The In and Sb ions were implanted at energies of respectively 1, 2 and 4 keV, the implantation fluence being 5×10^{14} atoms/cm^2, while the P ions were implanted at a fluence of 5×10^{15} atoms/cm^2 at energies of 1, 2, 4, 6 and 8 keV, respectively.

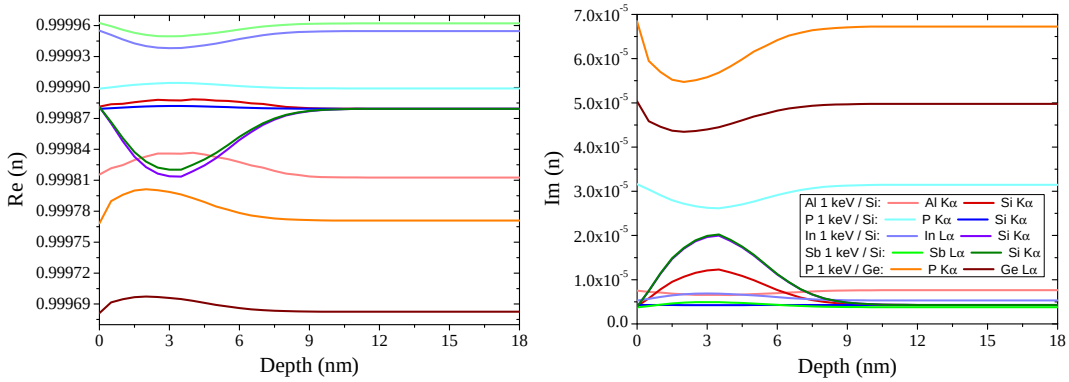

Figure V.10: Calculated change in the refractive index (real part on the left side, imaginary part on the right side) of the ion–implanted Si and Ge wafers. The calculations have been realized for the lowest implantation energies, since for these samples the largest changes are expected due to the highest dopant peak concentrations. The largest variation of the real part of the refractive index is expected for the P Kα–line of the P–implanted Ge wafers and the Si Kα–line of the In– and Sb–implanted Si wafers. In the latter case the angular calibration by means of the Si Kα–line may be affected. However, calculations of the angular intensity profiles of the Si Kα–line for pure and implanted samples indicated no change.

The experimental conditions for the different samples are summarized in Table V.1.

Table V.1: Summary of the experimental conditions for the different samples. The indicated values for the photon flux ϕ correspond to the unfocused primary X–ray beam of energy E_0. The primary beam was produced by a wiggler for the Al–implanted samples and two undulators for the other ones. The implantation fluences were 10^{16} atoms/cm^2 for the Al ions, 5×10^{15} atoms/cm^2 for the P ions and 5×10^{14} atoms/cm^2 for the In and Sb ions. For all of the measurements a back–illuminated CCD of 1340×400 pixels of 20×20 μm^2 was used for the X–ray detection.

Sample	X–ray Lines	E_0 [keV]	ϕ [ph/s]	Focusing	Crystal	Order
Al / Si	Al Kα; Si Kα	1.582; 2.000	5×10^{10};2×10^{11}	No	ADP	n=1
P / Si	P Kα; Si Kα	4.200	3.5×10^{13}	Yes	ADP	n=1
In / Si	In Lα; Si Kα	4.200	3.5×10^{13}	Yes	ADP	n=2; n=1
Sb / Si	Sb Lα; Si Kα	4.200	3.5×10^{13}	Yes	ADP	n=2; n=1
P / Ge	P Kα; Ge Lα	3.190	2.4×10^{13}	Yes	TlAP	n=2

Chapter VI

Results and Discussion

The depth–profiling capabilities of the presented synchrotron radiation–based high-resolution GEXRF method are discussed for different ion–implanted samples.

VI.1 General Considerations

The angular intensity profile $I(\theta_e)$ can by calculated with Eq. VI.1 (for details see section III.4.1),

$$I(\theta_e) = |t_0^{\downarrow}|^2 \times \int_{z_1}^{z_0} \left[f(z) \times \exp\left(-2\mathrm{Im}(k_z)(z_0 - z)\right)\right] \mathrm{d}z \,. \tag{VI.1}$$

where θ_e represents the exit angle, $f(z)$ the depth distribution of the implanted ions and $|t_0|^2$ stands for the transmission factor of the emitted x-rays at the sample-vacuum interface. The exponential term in Eq. VI.1 accounts for the absorption of the X–rays, $k_z = 2\pi/\lambda_e \times \sqrt{n_1^2 - \cos^2\theta_e}$, where n_1 is the complex refractive index of the substrate and is assumed to be constant because of the low implantation doses, z_0 and z_1 are the coordinates of the front and rear surfaces of the sample, the z–axis being perpendicular to the irradiated side of the sample. Multiple reflections can be neglected since, since in contrast to layer-like samples, there are no sharp interfaces inside the ion–implanted wafers. Refraction phenomena for X–rays take only place at the vacuum–sample interface. The aim of the experiment is to retrieve, starting from the measured angular intensity profile $I(\theta_e)$ of an X–ray fluorescence line of wavelength λ_e, the concentration distribution $f(z)$ in the depth–direction of the emitting atoms (Fig. VI.1). This is called the inverse problem.

Below the critical angle θ_c, which according to Eq. II.5 depends on the substrate

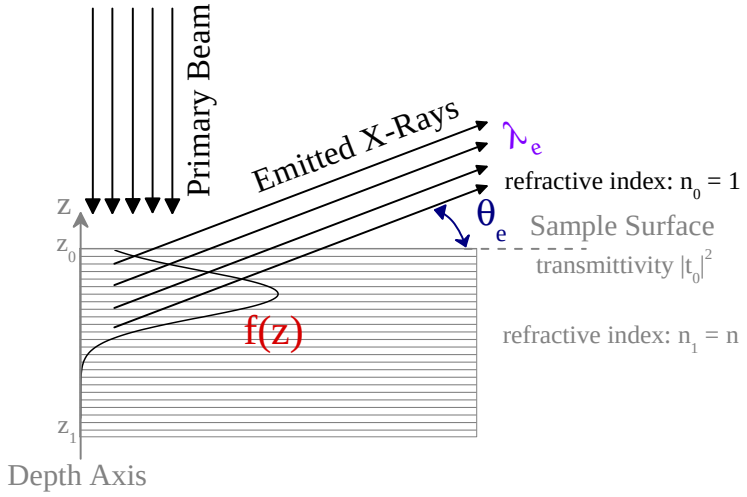

Figure VI.1: Illustration of the inverse problem: the depth distribution $f(z)$ of implanted ions is to be assessed from the dependence of the fluorescence radiation of wavelength λ_e on the emission angle θ_e.

and the X–ray fluorescence wavelength of interest λ_e, a higher surface–to–bulk ratio for the X–ray intensity is observed. The contributing depth region is only a few nanometers (3–5 nm) wide. For exit angles θ_e larger than the critical angle of total reflection θ_c, the detection setup becomes sensitive to X–rays emitted deeper inside the target (Fig. III.1). In this angular range the accessible depth region is limited by the self–absorption of the emitted X–rays: due to the grazing emission angles the exit path of the emitted X–rays is quite large and varies with the inverse sine of the exit angle. Different exit angles provide thus information from different depth regions allowing in principle to reconstruct the distribution of the emitting atoms.

The measured angular intensity profiles of a fluorescence X–ray line of the implanted dopant atoms can be first compared to theoretical calculations. In this perspective, calculations of the different distributions $f(z)$ for different implantation energies and different dopant–substrate combinations were performed by means of the SRIM [178] program which is a Monte Carlo simulation of the implantation process taking into account different physical effects[1]. SRIM calculations, however, neglect sputtering at the surface which can lead to a distortion or broadening of the profile because the effects of preceding ions are not taken into account. Each ion in the calculation is treated as if it was the first ion to be implanted. The obtained theoretical dopant distributions can then used in Eq

[1] `http://www.srim.org/`

VI.1 to calculate the corresponding theoretical angular profiles $I(\theta_e)$.

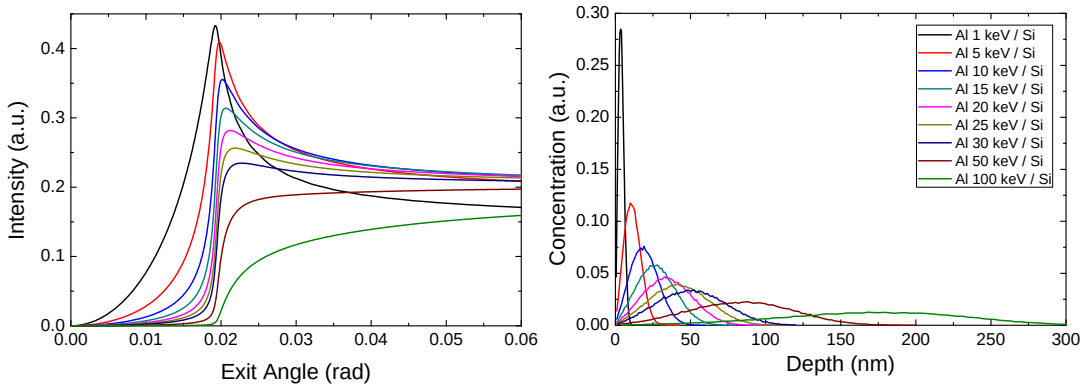

Figure VI.2: Calculated Al Kα angular intensity profiles $I(\theta_e)$ for Si wafers implanted at different energies with Al ions. The angular intensity profiles $I(\theta_e)$ are directly related to and depend sensitively on the dopant depth distribution (calculated with SRIM), indicating the feasibility of depth–profiling measurements by means of GEXRF.

As one can infer from Figs. VI.2 and VI.3, where the calculated profiles of the Al Kα–line from Al–implanted Si wafers respectively the As Lα–line from As–implanted Si wafers are compared, the angular profiles change gradually with the depth distribution of the implanted ions. Fig. VI.2 shows that a wide range of implantation energies can be covered, while Fig. VI.3 shows the sensitivity of the GEXRF setup to dopant concentration profiles which differ by only few nanometers. For low implantation energies, most implanted ions are located close to the surface, which explains the observed increase of the intensity at exit angles already below the critical angle. The extinction length below the critical angle (see Fig. III.1) is about 3 nm. In addition, it can be observed that the observed critical angle θ_c of the dopant fluorescence line shifts slightly towards larger values with increasing implantation energies and approaches the theoretical value for the Al Kα–line, respectively the As Lα–line, emitted from pure Si. Since the critical angle depends on the density ρ of the sample (Eq II.5), this shift illustrates how the number of implanted ions in the surface vicinity diminishes with increasing implantation energy. The intensity for exit angles θ_e much larger than the critical angle θ_c depends mainly on the implantation dose. A good agreement between the experimental and theoretical profiles was observed. It should thus be possible to extract from the measured angular dependence of the intensity of a fluorescence line $I(\theta_e)$ of a dopant X–ray fluorescence line the depth distribution $f(z)$ of the

implanted ions. This task is however not trivial since the depth distribution has to be assessed from an angular–dependent measurement. A simple differentiation with respect to z of Eq. VI.1 will not solve the problem.

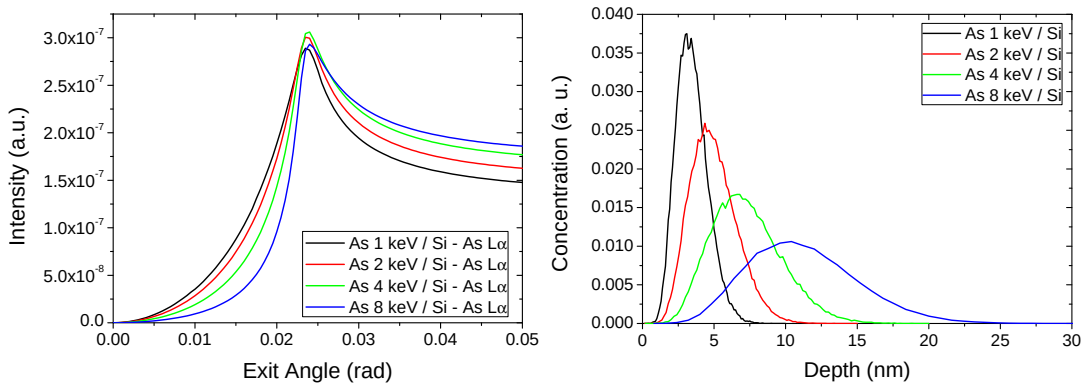

Figure VI.3: Calculated As Lα angular intensity profiles $I(\theta_e)$ for Si wafers implanted at different energies with As ions. The Lα–line (1.282 keV) rather than the more intense Kα–line (10.508 keV) has been chosen because of the inverse dependence of the critical angle on the fluorescence X–ray energy (Eq. II.5 and Fig. III.1). For the Kα–line the requirements on the angular accuracy would be much more severe.

To determine $f(z)$, the depth distribution of the implanted ions, the experimental angular profiles can be fitted using equation Eq. VI.1. The SRIM calculations for a given ion–substrate combination for different implantation energies may suggest the use of a certain analytical curve for $f(z)$ in the fitting procedure. For example for Al implantations in Si, the use of a Gaussian to fit the angular profiles seems to be adequate, the center and the width of the Gaussian being the free parameters of the fit. For other ion–implanted samples less symmetric functions $f(z)$ may be preferable. Alternatively, existing tables and functions [220–223] can be used to adjust the function $f(z)$ in order to fit the angular intensity profile $I(\theta_e)$. Alternatively Eq. VI.1 can also be inverted on a theoretical basis in order to determine $f(z)$ without assuming *a priori* a given function.

VI.2 Theoretical Inversions

From Eq. VI.1 it can be deduced that the measured X–ray fluorescence intensity of a dopant for a given emission angle θ_e depends linearly on the concentration distribution through an integral equation. In particular, the dopant concentra-

tion distribution is contained in $f(z)$, the dopant depth distribution. Isolating $f(z)$ in Eq. VI.1 would thus allow to assess the dopant depth concentration of an ion–implanted sample, the only necessary input being the angular intensity profile $I(\theta_e)$ of the fluorescence X–rays and the refractive index of the ion–implanted wafer which depends on the bulk wafer and the wavelength λ_e of the fluorescence X–rays. Thus, in principle, the inversion of Eq. VI.1 would provide the opportunity to discuss the limits of GEXRF, and hence optimize the GEXRF setups, for depth–profiling applications with regard to different dopant–sample combinations and the different implantation energies and the resulting dopant concentration distributions $f(z)$ [8].

The general inversion of Eq. VI.1 is, however, even in the simple case of ion–implanted samples where the refractive index and the angular intensity profile $I(\theta_e)$ are known, a severely ill–posed problem [176]. Even if the concentration depth distribution $f(z)$ and the angular intensity profile $I(\theta_e)$ are uniquely related to each other, the problem remains ill–posed and a direct inversion of the equation system obtained from a discretization of the emission angles θ_e and the depth positions z is expected to be highly unstable because of experimental and numerical errors [8].

VI.2.1 The truncated Laplace transform and Tykhonov's regularization method

The alternative is to turn to regularization methods as proposed in [224] specifically for GEXRF measurements. First the similarity of Eq. VI.1 with a truncated Laplace transform has to be remarked. Setting

$$p = 2\mathrm{Im}(k_z) = 2\pi/\lambda_e \times \sqrt{n_1^2 - \cos^2\theta_e}\,, \tag{VI.2}$$

$$F(p) = \frac{I(\theta_e)}{|t_0^{\downarrow}|^2}\,, \tag{VI.3}$$

$$z_0 = 0 \text{ and } z_1 \to +\infty\,, \tag{VI.4}$$

and inverting the orientation of the z–axis (the bulk wafer is supposed to be infinitely thick for X–rays), one obtains

$$\begin{aligned} I(\theta_e) &= |t_0^{\downarrow}|^2 \times \int_{z_1}^{z_0} \left[f(z) \times \exp\left(-2\mathrm{Im}(k_z)(z_0 - z)\right)\right] \mathrm{d}z \\ \Rightarrow F(p) &= \int_0^{+\infty} \left[f(z) \times \exp\left(-pz\right)\right] \mathrm{d}z\,. \end{aligned} \tag{VI.5}$$

The function $F(p)$ corresponds to the truncated Laplace transform of $f(z)$ which implies that $f(z)$ is uniquely determined by the values of $F(p)$ on any subset on the positive real axis with at least one accumulation point [224]. However, since the measurements are performed for a finite angular range of exit angles θ_e, the range of p–values for which an experimental value $F(p)$ exists is also finite. The availability of data on only a finite p–interval enhances the instability of the explicit inversion [8]. This limitation on a finite p–interval is of physical nature and cannot be circumvented in the experiment, the minimum value for p being obtained if $\theta_e = \pi/2$ ($p_{\min} = 2\beta$, remembering that $n = 1 - \delta + i\beta$), i.e., not for a grazing emission angle, and the maximum for $\theta_e = 0$ ($p_{\max} = 2k_z\sqrt{n^2 - 1} \approx 2\sqrt{2}k\sqrt{-\delta + i\beta}$, neglecting second order terms). The values of $F(p)$ (Fig VI.4) need thus to be extrapolated on the entire positive p–axis in order to invert Eq. VI.5.

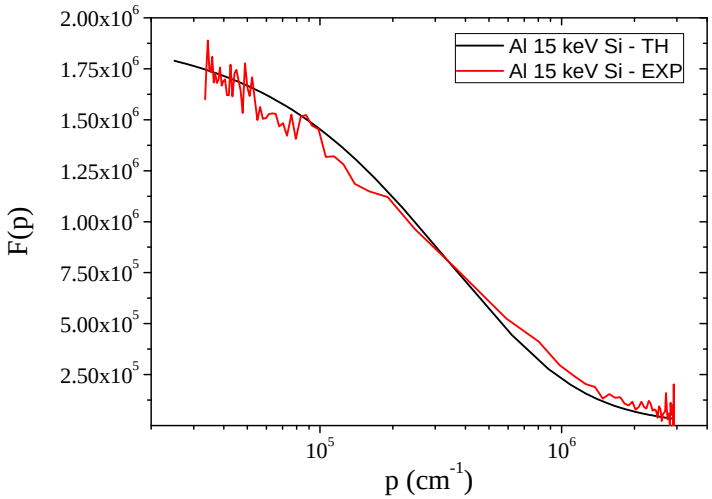

Figure VI.4: Theoretical and experimental intensity profiles in the p–space. Due to oscillations, the extrapolation on the entire positive axis is difficult.

The extrapolation is, however, not straightforward since noise is clearly visible for small and large p–values for experimental data (see Fig. VI.4 for theoretical and experimentally obtained $F(p)$). In Ref. [224] it is proposed to extrapolate $F(p)$ by means of the following expression

$$\sum_{k=1}^{N} \frac{a_k}{p^k} \tag{VI.6}$$

for large, p values and by means of

$$\sum_{k=1}^{M} \frac{(-1)^k |b_k|}{p^k} \tag{VI.7}$$

for small p–values. In both cases a (weighted) least–squares problem with respect to the values of $F(p)$ has to be solved to obtain the parameters a_k respectively b_k. For noisy data small extrapolation orders (N and M), not larger than 3 or 4, should be chosen [224, 225].

Once the extrapolation has been performed, the properties of the Laplace transform operator can be used to invert Eq. VI.5. This operator is symmetric, bounded, injective but not compact [224]. The spectral decomposition on the interval $[-\sqrt{\pi}, \sqrt{\pi}]$ (the spectral range) gives an orthogonal system of eigenvectors,

$$g_\lambda(p) = \frac{1}{|\lambda|(\pi^2 - \lambda^4)^{\frac{1}{4}}} \left(\Gamma(\frac{1}{2} + it)^{\frac{1}{2}} \frac{p^{-\frac{1}{2}-it}}{\sqrt{2\pi}} + \mathrm{Sign}(\lambda)\Gamma(\frac{1}{2} - it)^{\frac{1}{2}} \frac{p^{-\frac{1}{2}+it}}{\sqrt{2\pi}} \right), \quad \text{(VI.8)}$$

where $t = \mathrm{arccosh}(\pi/\lambda^2)/\pi$ for $\lambda \neq 0$, and Γ corresponds to the Gamma function. However, the inverse Laplace transform operator, defined on the basis of the eigenvectors g_λ, is unbounded (since $\lambda = 0$ is contained in the spectral range of the Laplace transform operator) and discontinuous which makes the inversion an ill–posed problem [224]. The instability of the inversion is determined by the scalar product (Fig. VI.5),

$$(F, g_\lambda) = \int_0^{+\infty} [F(p)\, g_\lambda^*(p)]\, \mathrm{d}p, \quad \text{(VI.9)}$$

which should be exponentially decaying with t. This poses a severe demand on the functional F which can not be satisfied for experimental, noisy data because of the strongly oscillating eigenfunctions [224].
Therefore, based on Tykhonov's regularization method, only an approximation $f_\rho^\epsilon(z)$ of $f(z)$ can be calculated,

$$f_\rho^\epsilon(p) = \int_{-\sqrt{\pi}}^{\sqrt{\pi}} \left[\frac{\lambda}{\rho + \lambda^2} (F^\epsilon, g_\lambda) g_\lambda \right] \mathrm{d}\lambda \quad \text{(VI.10)}$$

$$= 2\mathrm{Re} \int_0^{+\infty} \left[\frac{\cosh(\pi t)\Gamma(\frac{1}{2} + it)}{\pi + \rho\cosh(\pi t)} (F^\epsilon, \frac{p^{-\frac{1}{2}+it}}{\sqrt{2\pi}}) \frac{p^{-\frac{1}{2}-it}}{\sqrt{2\pi}} \right] \mathrm{d}t\,, \quad \text{(VI.11)}$$

where $F^\epsilon(p)$ has been extracted from the extrapolated measurements $F(p)$ with an error satisfying $||F - F^\epsilon|| = \epsilon$, F and F^ϵ being functionals of the Laplace transform operator. The choice of the regularization parameter ρ depends on the error level ϵ, and the noise in the experimental measurement will make $f_\rho^\epsilon(z)$ inaccurate if the regularization parameter ρ is chosen too small. At the same time ρ should not be chosen too large, in order to obtain a reasonable approximation

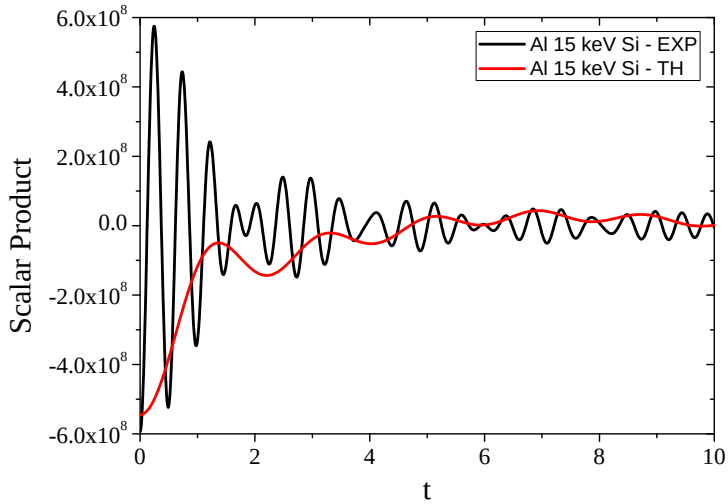

Figure VI.5: Calculated scalar product for theoretical and experimental data for a restricted domain on the t–axis. The experimental noise induces strong oscillations which extend over the whole t–axis.

of $f(z)$ [225]. The choice of the regularization parameter ρ can be either made with Morozov's discrepancy principle or generalized cross–validation (GCV) [224]. The latter presents the advantage that no estimation of the experimental error is needed, the regularization parameter ρ being found by minimization of (see [224] for further details)

$$q(\rho) = \frac{\rho}{4\arctan\sqrt{\frac{\pi}{\rho}}} \int_{\sqrt{\pi}}^{\sqrt{\pi}} \left[\frac{|(F^{\epsilon}, g_{\lambda})|^2}{(\rho + \lambda^2)^2} \right] \mathrm{d}\lambda \,. \tag{VI.12}$$

The function $q(\rho)$ shows also a great sensitivity on the experimental noise, only for low noise levels a minimum for $q(\rho)$ for a finite value ρ can be found [224]. Without noise $q(\rho)$ is minimum for $\rho = 0$, with too high noise levels $q(\rho)$ is monotonically decreasing.

This inversion method has been successfully applied to simulated data, without and with statistically added noise, in Refs. [8, 224]. The sensitivity of the approximation $f_{\rho}^{\epsilon}(z)$ on noise requires all the integrals to be computed analytically in order to minimize any numerical error, the functions for which no analytical value is available being interpolated linearly [224]. However, the simulated noise levels were only of the order of 1%, thus really low. For the presented experimental measurements such low noise levels were not obtained, Tykhonov's regularization method could not be applied successfully[2]. However, simulations and the appli-

[2]Personal comment: An application on experimentally obtained data could not be found.

cation of Tykhonov's regularization method on the simulated data can be used in the view of preparing experiments in order to know how many experimental points are necessary and which measurement time for each point is required for a succesful inversion of the truncated Laplace transform. In addition, the depth distributions of shallow, peaked as well as deeply implanted dopant concentration profiles are more difficult to reconstruct because of either a narrower p–range and an increased weight on eigenvectors (Eq. VI.8) corresponding to small eigenvalues λ or an increased X–ray absorption [224, 225].

VI.2.2 The maximum–entropy method

An alternative to the inversion of the truncated Laplace transform is the maximum–entropy method which has been adopted to determine dopant–concentration profiles by GEXRF measurements [225]. The maximum–entropy method leads to a convex constrained optimization problem with a unique solution which converges to the exact depth concentration profile $f(z)$ provided that the noise levels are reduced and the number of data points is increased. In the maximum–entropy method it is first necessary to assume a finite sample depth T which should be sufficiently large to contain all the implanted dopants. Whether the choice for T was reasonable can be seen in the returned result. Supposing that the angular intensity profile $I(\theta_e) = |t_0|^2 \times F(p)$ was measured at R different exit angles $(\theta_{e,1}, ..., \theta_{e,R})$, corresponding each to a point in the p–space (Eq. VI.2), and that the interval $[0, T]$ on the z–axis (pointing into the sample) has been discretized into $Q + 1$ points $(z_0, ..., z_Q)$, the maximum–entropy problem resumes to minimize [225]

$$\frac{T}{Q+1} \sum_{j=0}^{Q} f(z_j) \times \log f(z_j) \tag{VI.13}$$

under the constraints

$$f(z_j) \geq 0 \; \forall j \, , \tag{VI.14}$$

$$\frac{T}{Q+1} \sum_{j=0}^{Q} f(z_j) = 1 \, , \tag{VI.15}$$

$$\frac{1}{R} \sum_{k=1}^{R} \omega_k | \sum_{j=0}^{Q} f(z_j) \exp\left(-p_k z_j\right) - F(p_k)|^2 \leq \sigma \, , \tag{VI.16}$$

with ω_k being a normalized ($\sum_{k=1}^{R} \omega_k = 1$) balancing factor to put more weight on points with a smaller relative error (i.e., with good statistics) and the regularization parameter $\sigma > 0$ being equal to the weighted squared sum of the (estimated)

absolute errors on the different $F(p_k)$ $(k = 1, ..., R)$.

For sufficiently large σ, the optimization problem has a unique solution due to the convex character of the minimization problem. As characterized in Eq. VI.13, a flat depth distribution $f(z)$ is considered at the beginning of the optimization problem, i.e., all the different depths (points $z_0, ..., z_Q$) have the same concentration of fluorescence atoms. If some *a priori* assumption about the depth distribution $f(z)$ can be made, this assumption $h_a(z)$ can be inserted in the optimization problem, Eq. VI.13 is modified and the following function has to be minimized [225]

$$\frac{T}{Q+1}\sum_{j=0}^{Q} f(z_j) \times \log\frac{f(z_j)}{h_a(z_j)} + h_a(z_j) - f(z_j)\,, \tag{VI.17}$$

the constraints being unchanged.

Like Tykhonov's regularization method, the maximum–entropy method can be used in the view of experiment preparation.

Note that, as it has already been mentioned, the inversion of the Laplace transform, respectively the successful application of the maximum entropy method, are only possible for low–concentration dopants, meaning that the ion–implantation dose should be low enough to not alter the refractive index of the bulk wafer. Otherwise, the dependence of the angular intensity profile $I(\theta_e)$ on the concentration would be non–linear because of the depth–dependent refractive index.

The maximum–entropy method could only be satisfactorily applied to experimental data of the Al–, P–, In– and Sb–implanted wafers in the case where some *a priori* knowledge was incorporated into the minimization problem (Eq. VI.17), the function $h_a(z)$ being obtained from the fit of the corresponding SRIM profile. In some cases it was necessary to smoothen the angular profile in order to reduce the Poisson noise. In Fig. VI.6, the theoretical and experimental inversions are shown. However, the inversion with *a priori* knowledge seems to stick to the input function $h_a(z)$ which is not very convenient since a good knowledge on the dopant depth distribution is necessary for a successful inversion of Eq. VI.1. The returned depth concentration distributions are strongly oscillating (Fig. VI.6). In addition the result may sometimes be influenced by the number of points on the grid of the p–space and the extension of the depth region which needs to be inserted beforehand.

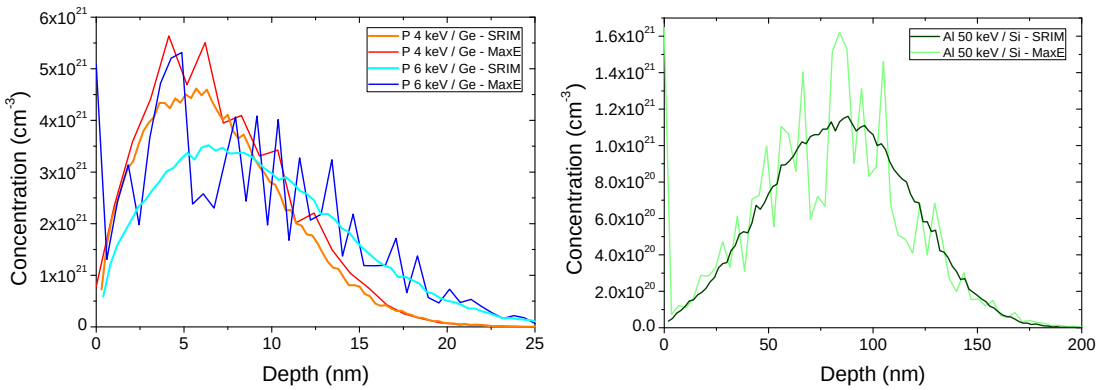

Figure VI.6: Dopant concentration profiles obtained by means of the maximum–entropy method. The left panel shows the application of the inversion method to theoretical angular intensity profiles (i.e., without statistical noise), and on the right panel to an experimental angular intensity profile. In both cases strongly oscillating functions are obtained.

VI.3 Fitting with a Gaussian

As already mentioned, the depth profiles can also be assessed by employing a more direct approach, starting from Eq. VI.1. Since the shape of the implanted ion distribution (Gaussian, Pearson IV, half-joined Gaussian,...) [223] can be more or less known from calculations of the dopant distribution for different implantation energies, an analytical function $f(z)$ was first assumed to fit the experimental angular profiles with Eq. VI.1. In the simplest case a Gaussian can be chosen with the center and width as free parameters in the fit. Indeed, for the Al–implanted and partially for the In– and Sb–implanted Si wafers, the theoretical depth profiles were found to be well fitted by Gaussian functions. The quality of the fits was not improved significantly when using Pearson IV distributions. Furthermore, as the skewness and the kurtosis of the Pearson IV distributions were close to 0, respectively 3, Gaussian distributions could be safely used since for these values of the skewness and the kurtosis, Pearson IV and Gaussian distributions are identical. Last but not least, Gaussian functions presented the advantage that the fits could be performed with two free parameters, whereas for fits using Pearson IV functions four free parameters would have been needed. Note also that for a Gaussian distribution which is symmetric, the position of the peak and the mean value of the implantation depth of the ions, the so-called projected range, are identical. It should also be mentioned that for technologically relevant, annealed samples, where the ions have diffused during the thermal treatment following the implan-

tation, a different function $f(z)$ needs to be used to represent the overall dopant profile. Indeed, the SRIM calculations for P–implantations into Si and Ge wafers, showed an asymmetric bell–shaped curve. Since the center values when fitting the SRIM output with a Gaussian or with a Pearson IV distribution did not vary by more than 0.5 nm, attempts with a Gaussian distribution to fit the corresponding angular intensity curves $I(\theta_e)$ were made in order to see if at least the centroid position and the approximate width of the dopant depth profile could be assessed.

The output of a fit for a given experimental angular profile was found to depend on the initial values chosen for the center and the width of the Gaussian distribution, probably because of local minima in the least-squares fitting procedure. To elude this dependence, for each sample the angular profile was fitted 1000 times, each individual fit using different, randomly scattered initial values for the center and the width of the assumed distribution. The returned values of each individual least-squares fit for the angular profile of a given sample were found to be distributed quite symmetrically in narrow regions whose center correspond to results with the best χ_r^2 for the fit of the experimental angular intensity profile $I(\theta_e)$. In order to get a single result the mean of all returned values for the center respectively the width of the assumed Gaussian distribution was thus taken as the final result, the standard deviation of the retrieved values during the fitting procedure allowing to estimate the precision of the fit. The results of this procedure are listed in Table VI.1, and from Fig. VI.7 it can be seen that the choice of a Gaussian distribution was justified for the Al–implanted Si wafers. In addition, the evolution with the number of fits of the correlation coefficient between the experimental angular profile and the profile calculated with the mean values of the realized fits was considered. After 40 to 50 fits the coefficient was already converging to the final value and did not change markedly afterwards, thus indicating that the presented fitting procedure is already approaching its final result.

In Table VI.1, the experimental results for the depth distribution of the implanted ions are compared to the theoretical values obtained from fitting the depth distributions calculated by using the SRIM code with a Gaussian (coefficient of determination superior to 0.99, except for the P–implanted Ge wafer). The peak position for the sample implanted with an energy of 1 keV is less precise since the standard deviation is quite large with respect to the average value obtained by the fitting procedure. A graphical comparison for some of the samples is also presented in

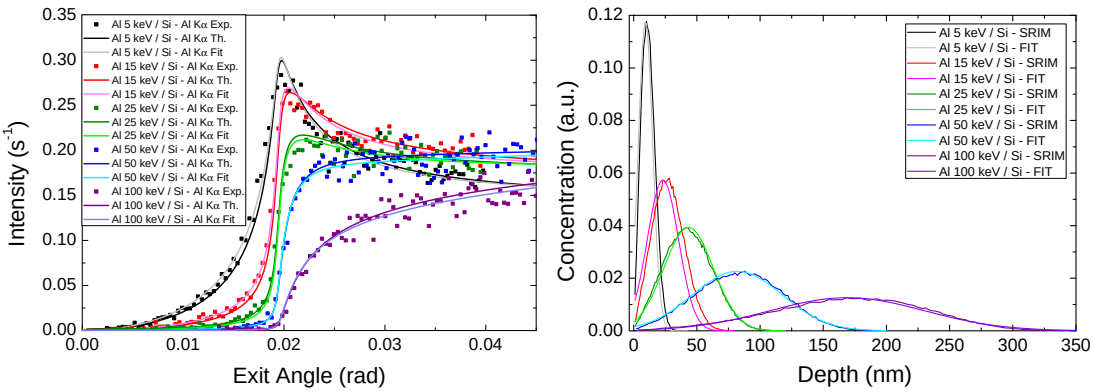

Figure VI.7: Results of the fitting procedure for Al–implanted Si wafers. As shown a Gaussian distribution as the depth concentration function provides very good fits (left side) and dopant depth distribution functions comparable to the SRIM calculations (right side, see also Table VI.1).

Figs. VI.7 and VI.8. For the Al–implanted samples it can be observed that in most cases the theoretical values for the center of the distribution are slightly larger than the experimental values. These shifts may be due to the uncertainties of the parameters used in the fits and in the SRIM calculations. They may be also related to the sample preparation. Nevertheless, both sets of data are quite close showing that the presented high–resolution grazing emission setup is able to distinguish accurately between samples implanted with different energies. It can be stated that the experimentally deduced shapes of the Al ion depth distributions agree with the calculated ones except for the small systematic shifts of the peak positions (see Fig. VI.7). The strong dependence of the angular profile on the implanted ion distribution and the small values of the standard deviation indicate that the presented high–resolution grazing emission setup leads to precise results of the implanted ion depth profiles, provided a reasonable a priori assumption about the depth profile shape is made.

Assuming that the dependence between the mean penetration range of the ions and the implantation energy from the SRIM dataset is correct (Fig. V.2), the mean peak positions deduced from the experimental data allow to estimate the implantation energy. The obtained values were found to be within 10% of the nominal implantation energy for all samples except the one implanted with an energy of 1 keV. Conversely the fits could also be realized with a single fitting parameter, the implantion energy. Then however, the possible concentration distributions are fixed and the different possible depth distributions cannot be accounted for. Con-

Table VI.1: Values of the experimentally extracted depth profiles. C stands for the center and W for the width (both in units of nm) of the distribution. σ is the standard deviation of all the values returned by the different fits and $\sigma_{C_{\mathrm{Fit}}}$ and $\sigma_{W_{\mathrm{Fit}}}$ stand for the standard deviation of the distribution of the results returned by the fits for the considered samples. The experimental results are also compared to the values of a Gaussian fit of the distribution calculated with the SRIM software.

Sample	C_{SRIM}	C_{Fit}	$\sigma_{C_{\mathrm{Fit}}}$	W_{SRIM}	W_{Fit}	$\sigma_{W_{\mathrm{Fit}}}$
Al 1 keV / Si	3.65	4.01	0.49	1.92	1.92	0.03
Al 5 keV / Si	10.9	9.34	0.15	5.73	5.67	0.03
Al 10 keV / Si	18.7	18.3	0.22	9.57	9.53	0.03
Al 15 keV / Si	26.1	23.1	0.22	12.6	12.4	0.03
Al 20 keV / Si	34.2	32.7	0.37	16.6	16.5	0.03
Al 25 keV / Si	42.3	43.4	0.41	19.5	19.6	0.06
Al 30 keV / Si	50.2	56.8	0.56	23.4	24.1	0.07
Al 50 keV / Si	83.7	82.1	0.38	35.6	35.3	0.06
Al 100 keV / Si	173	169	0.67	62.0	61.0	0.17
In 1 keV / Si	3.82	4.25	1.28	0.91	1.24	0.19
In 2 keV / Si	5.23	5.76	1.32	1.33	1.57	0.15
In 4 keV / Si	7.33	9.34	1.18	1.97	2.67	0.20
Sb 1 keV / Si	3.89	6.00	2.64	0.90	1.32	0.17
Sb 2 keV / Si	5.32	7.02	2.14	1.32	1.62	0.17
Sb 4 keV / Si	7.41	11.2	1.8	1.94	2.93	0.21
P 1 keV / Si	3.44	6.52	1.11	1.84	2.08	0.18
P 2 keV / Si	5.27	6.89	0.75	2.82	2.64	0.20
P 4 keV / Si	8.44	9.54	0.21	4.48	6.07	0.49
P 6 keV / Si	11.3	13.0	0.3	5.97	7.84	0.61
P 8 keV / Si	14.1	15.6	0.1	7.35	12.2	1.2
P 1 keV / Ge	2.11	7.10	0.33	1.65	2.64	1.12
P 2 keV / Ge	3.69	5.55	0.47	2.87	2.68	0.50
P 4 keV / Ge	5.87	6.08	0.70	4.45	4.88	5.11
P 6 keV / Ge	7.81	4.25	1.10	5.86	3.81	7.01
P 8 keV / Ge	9.66	2.03	1.44	7.19	9.43	6.15

sidering the widths of the implanted dopant distributions for the Al–implanted samples, an excellent agreement between the theoretical and experimental results was found. The results are consistent within 0.3 nm for all samples except for the one implanted with 100 keV ions. For this sample, the X–ray absorption in Si is more pronounced and the real shape of the implantation profile is a bit distorted

towards larger depths as it is usual for increasing implantation energies.

However, the In–, Sb–, and P–implanted Si samples do not present the same excellent agreement between results obtained from the fitting procedure and the SRIM calculations. The retrieved peak concentration positions are larger than those indicated by the SRIM calculations and the quite large standard deviation (up to 30%) of the obtained results indicates a larger relative uncertainty then for the Al–implanted Si wafers. Only for the In– and Sb–implanted Si samples with energies of 1 and 2 keV is the predicted value within the standard deviation of the results obtained by the fits. For the P–implanted Si wafers the difference between the theoretical and experimental values is comparable or smaller but the $\sigma_{C_{\mathrm{Fit}}}$ are smaller. The widths of the retrieved concentration distributions are also larger than the theoretical values, thus the experimentally obtained distributions are broader than the theoretical ones. The standard deviation of the results returned by the individual fits for a given sample is for the widths up to 10%. The uncertainty for the widths is thus smaller than for the center of the assumed Gaussian distribution. Because of the low implantation energies, X–ray absorption should not significantly influence the results. It seems rather that either the real distribution of the dopant distribution is different from the theoretical one or, because of the low implantation energies, there is a noticeable concentration of dopant atoms close to the surface which could influence the angular scattering of the fluorescence X–rays from the dopant atoms and the bulk. This would, however, contradict the assumption that the refractive index for implanted wafers is unchanged for the bulk wafer for the wavelength of interest λ_e. Furhter investigations are necessary. In addition, the SRIM calculations point also out that a symmetric function for $f(z)$ may not be the best choice. To take this into account, fits with two joined half-Gaussian distributions were also realized VI.4.

The results for the P–implanted Ge wafers are more than intriguing. Indeed, the value returned by the fitting procedure for the center of the assumed Gaussian distribution decreases with the implantation energy. The standard deviation $\sigma_{C_{\mathrm{Fit}}}$ can not be taken into account to explain this trend. This is contrary to what is expected from the SRIM calculations. The obtained widths agree within the standard deviation of the results returned by the individual fits with the theoretical values. Possibly the light P ions have diffused in the Ge matrix V.1, but a more detailed analysis is necessary. For the other samples diffusion effects should not

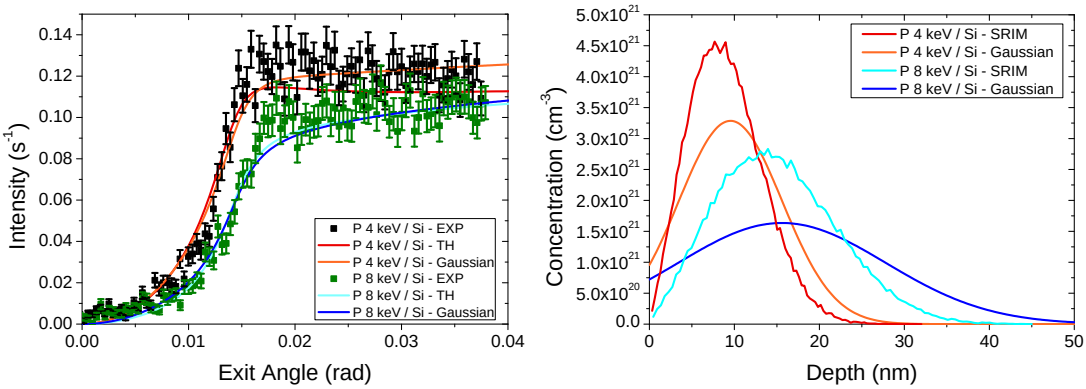

Figure VI.8: Fits of the experimental angular profiles of P–implanted Si wafers. A Gaussian distribution as the depth concentration function provides reasonable fits of the angular intensity profiles. However, the dopant depth distribution functions are markedly different from the SRIM calculations (see also Table VI.1).

be thus pronounced since the implanted ions are comparable in weight or much heavier than the atoms of the Si matrix.

VI.4 Fitting with joined half–Gaussian distributions

In order to verify that the use of a Gaussian for $f(z)$ was the best choice, the angular intensity profiles can also be fitted with an asymmetric depth distribution. Two joined half-Gaussian functions, i.e., a Gaussian distribution where the widths on the left and right side of the center are allowed to be different, are used instead of the standard Gaussian distribution. Thus, asymmetric dopant concentration distributions are allowed for, widening the set of possible samples where the GEXRF depth–profiling approach can be applied to.

The results of the fits of the angular profiles with Gaussian and joined half–Gaussian curves are listed in Table VI.2 and examples of angular intensity profile fits with joined half–Gaussian distributions are shown in Fig. VI.9 (left side) together with a comparison of the obtained results with the corresponding SRIM calculations.

For the Al–implanted Si wafers, the central positions of the peaks are for almost all the samples in an excellent agreement with the positions found with the simple

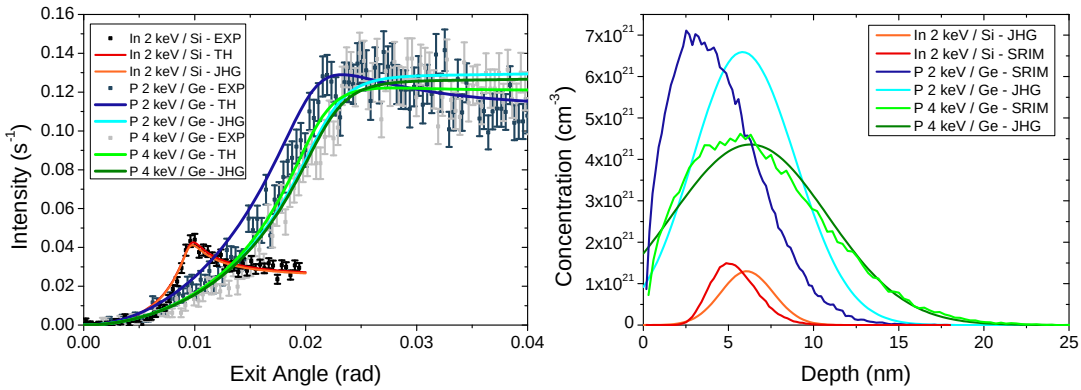

Figure VI.9: Examples of fitting P Kα angular profiles from P–implanted Ge wafers, respectively In Lα angular profiles from In–implanted Si wafers with a joined half–Gaussian depth distribution function. Especially the regions below the respective critical angles are better reproduced by the fit than by the calculated angular intensity profiles. On the right side the retrieved depth distributions are compared to calculated ones (SRIM): the concentration profiles returned by the fitting procedure are broader and the peak concentration is located slightly deeper in the sample.

Gaussian distribution. The widths for the joined half-Gaussian distributions differ by about 1% or less and are very close to the widths of the simple Gaussians. Except for the samples implanted at 1 and 100 keV, the widths of the first half-Gaussian are larger than the widths of the second one. In all but one case the widths of the second half-Gaussian correspond to the widths of the simple Gaussian distributions. The surface concentrations obtained with joined half-Gaussians are thus slightly larger. The fits of the angular profiles are of the same quality for both types of distributions showing that the initial choice of a symmetric distribution suggested by theory was well founded.

For the P–, In– and Sb–implanted Si wafers, where less symmetric depth distributions are expected, the final fit of the angular intensity profile was slightly improved (which is not surprising since more parameters in the fits were used). The returned results for the central peak position are in good agreement with the values obtained when fitting with a simple Gaussian and the standard deviation of the individual results are comparable. The central peak values vary around the central peak positions obtained with the single Gaussian. The same holds for the width of the second half–Gaussian (which extends from the dopant concentration peak into the bulk), the widths being identical or smaller than the widths of the

Table VI.2: Comparison of the experimentally extracted depth distributions using Gaussian and joined half-Gaussian functions. Again C stands for the center, W for the width, both in units of nm. The index 1 for the width of the joined half-Gaussian represents the depth region extending from the surface to the center, the index 2 indicates the further depth region. The values in parentheses stand for the standard deviation σ of the results retrieved by the described fitting procedures.

Sample	C_{Gauss}	$C_{\text{Half–Gauss}}$	W_{Gauss}	$W_{1,\text{Half–Gauss}}$	$W_{2,\text{Half–Gauss}}$
Al 1 keV / Si	4.01 (0.49)	4.44 (0.73)	1.92 (0.03)	1.9 (0.7)	1.96 (0.10)
Al 5 keV / Si	9.34 (0.15)	9.32 (0.13)	5.67 (0.03)	5.7 (2.0)	5.67 (0.03)
Al 10 keV / Si	18.3 (0.2)	18.3 (0.2)	9.53 (0.03)	9.9 (3.2)	9.53 (0.03)
Al 15 keV / Si	23.1 (0.2)	23.1 (0.2)	12.38 (0.03)	12.5 (4.3)	12.4 (0.03)
Al 20 keV / Si	32.7 (0.4)	32.7 (0.3)	16.51 (0.03)	17.0 (6.1)	16.5 (0.03)
Al 25 keV / Si	43.4 (0.4)	43.4 (0.4)	19.6 (0.1)	19.8 (6.9)	19.6 (0.1)
Al 30 keV / Si	56.8 (0.6)	56.8 (0.4)	24.1 (0.1)	24.2 (8.3)	24.1 (0.1)
Al 50 keV / Si	82.1 (0.4)	82.1 (0.5)	35.3 (0.1)	36.1 (12.3)	35.3 (0.1)
Al 100 keV / Si	169.0 (0.7)	169.0 (0.5)	61.0 (0.2)	60.2 (20.6)	61.0 (0.1)
In 1 keV / Si	4.25 (1.28)	4.28 (1.23)	1.24 (0.19)	1.19 (0.43)	1.24 (0.11)
In 2 keV / Si	5.76 (1.32)	5.67 (1.29)	1.57 (0.15)	1.52 (0.52)	1.55 (0.15)
In 4 keV / Si	9.34 (1.18)	9.28 (1.15)	2.67 (0.20)	2.53 (0.88)	2.66 (0.20)
Sb 1 keV / Si	6.00 (2.64)	5.94 (2.65)	1.32 (0.17)	1.19 (0.41)	1.31 (0.17)
Sb 2 keV / Si	7.02 (2.14)	6.94 (2.06)	1.62 (0.17)	1.52 (0.51)	1.61 (0.17)
Sb 4 keV / Si	11.2 (1.8)	12.0 (1.8)	2.93 (0.21)	2.50 (0.89)	2.82 (0.22)
P 1 keV / Si	6.52 (1.11)	6.58 (1.10)	2.08 (0.18)	1.82 (0.47)	2.08 (0.18)
P 2 keV / Si	6.79 (0.75)	6.89 (0.75)	2.64 (0.20)	2.38 (0.62)	2.65 (0.21)
P 4 keV / Si	9.54 (0.21)	9.52 (0.37)	6.07 (0.49)	5.98 (1.57)	6.06 (0.48)
P 6 keV / Si	13.0 (0.3)	13.0 (0.3)	7.84 (0.61)	7.50 (1.99)	7.82 (0.63)
P 8 keV / Si	15.6 (0.13)	15.6 (0.1)	12.2 (1.2)	11.8 (3.1)	12.1 (1.1)
P 1 keV / Ge	7.10 (0.33)	7.10 (0.48)	2.64 (1.12)	1.65 (0.32)	2.33 (0.93)
P 2 keV / Ge	5.55 (0.47)	5.82 (0.40)	2.68 (0.50)	2.93 (0.54)	3.12 (0.64)
P 4 keV / Ge	6.08 (0.70)	6.30 (0.14)	4.88 (5.11)	4.63 (0.84)	4.52 (0.41)
P 6 keV / Ge	4.25 (1.10)	4.98 (0.35)	3.81 (7.01)	5.80 (1.05)	5.57 (0.70)
P 8 keV / Ge	2.03 (1.44)	1.80 (0.10)	9.43 (6.15)	7.19 (1.32)	7.14 (0.74)

single Gaussian distribution. The width of the first half–Gaussian are smaller, leading to lower surface concentration values (as expected from the SRIM calculations). The standard deviation of this fitting parameter is also larger, about 30%. This indicates that the depth profiles of the Gaussian were slightly too broad. In general, the results obtianed with the simple Gaussian distribution are confirmed,

the shape of the obtained depth distributions being slightly refined.

For the P–implanted Ge wafers similar conclusions can be drawn except for the samples implanted at 2 and 6 keV for which the widths are estimated to be (much) broader than in the case where the fitting procedure was performed with a single Gaussian distribution. For some samples the relative uncertainties on the central peak positions are reduced with respect to the fit with a single Gaussian.

VI.5 Fitting without *a priori* knowledge

In an alternative approach the depth distributions of the implanted ions were extracted without *a priori* knowledge of their shape (Fig. VI.10). To this end, a triangular shape with regularly spaced points was first adopted to fit the experimental angular profiles. The aim was to determine the approximate depth region of the dopant distribution and its maximum concentration. A triangular shape seemed to be reasonable since in general implanted ions show (asymmetric) bell-shaped distributions. Actually, different pyramid–like polygonal shapes resulted in comparable final results, so that it can be assumed that the choice of the initial shape is not too crucial. Indeed in the next step an asymmetry of the triangular shape is allowed for in order to improve the fit of the angular intensity profile $I(\theta_e)$: the left and right sides of the triangular shape are allowed to shift within the range of the depth resolution (given by the division of the depth range over which the triangle extends and the number of points in the triangular distribution) and the concentration values are simultaneously allowed to be varied.

Finally the depth coordinates z_i and the concentration values $f(z_i)$ $(i = 1, ..., p)$ of the p points of the initial triangular distribution were allowed to vary within certain square boundary limits to further improve the fit of the experimental angular profile (Fig. VI.10). The boundary limits are fixed on the depth axis by the depth resolution (obtained from the depth region over which the triangular distribution extends and the number of points p) and on the concentration axis by the initial concentration value and the slope of the original triangular distribution. Points with a larger concentration value were thus permitted to be varied on a larger scale. The smoothened spline interpolation of the obtained set of point coordinates (z_i, $f(z_i)$) was used as an input for the next step in an iteration pro-

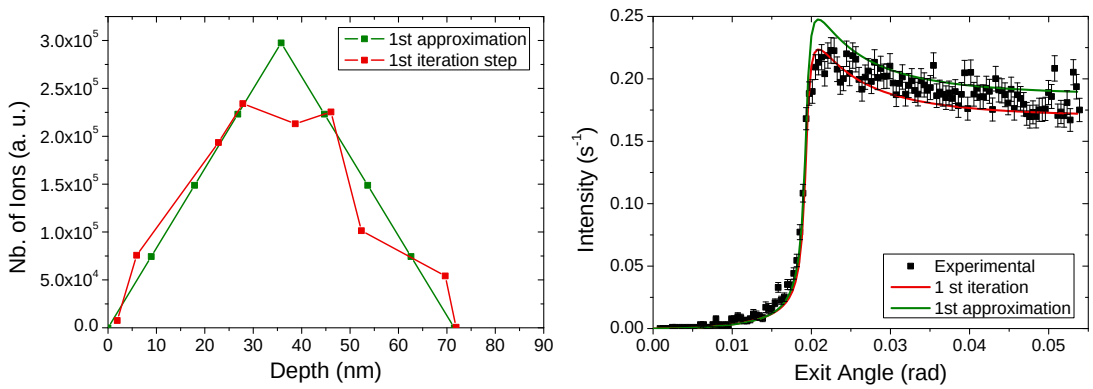

Figure VI.10: Illustration of the first steps of the approach to fit the angular intensity profiles without *a priori* knowledge. The Si wafer implanted with Al ions at 20 keV was chosen to illustrate this fitting approach. The triangular shape allows to get a first idea about the rough dopant depth distribution and the variation within boundary boxes of the points allows to refine the fit of the angular intensity profiles.

cess. The smoothening is necessary to attenuate too strong oscillations on the depth distribution curve. In each iteration step the depth resolution was improved by fitting the experimental angular profile with an increased number of equidistant points p in the depth distribution curve returned by the preceding iteration step. The depth coordinates z_i and the concentration values $N(z_i)$ of the initially regularly spaced points were allowed to vary within given limits defined by the starting values for the coordinates of each point and its immediate neighbors as explained previously. After each iteration step neighboring points lying close to each other (compared to the depth resolution of the actual iteration step) were replaced by a single point and, depending on the concentration value for the last point at $(z_p, f(z_p))$ with respect to the maximum concentration value of the p point coordinates, it was verified whether an additional point had to be added to the tail of the distribution propagating into the sample. This iteration process was stopped when the desired depth resolution was obtained or the precision of the obtained point coordinates could not be improved further by the calculation program. It can be seen in Fig. VI.11 that for the Si wafer implanted with Al ions of 25 keV this approach provides a result comparable to the SRIM calculations. In comparison to the fits with a Gaussian (section VI.3) or joined half–Gaussian distributions (section VI.4), however, a more asymmetric shape is obtained.

The limits of this approach were also tested with theoretical angular intensity

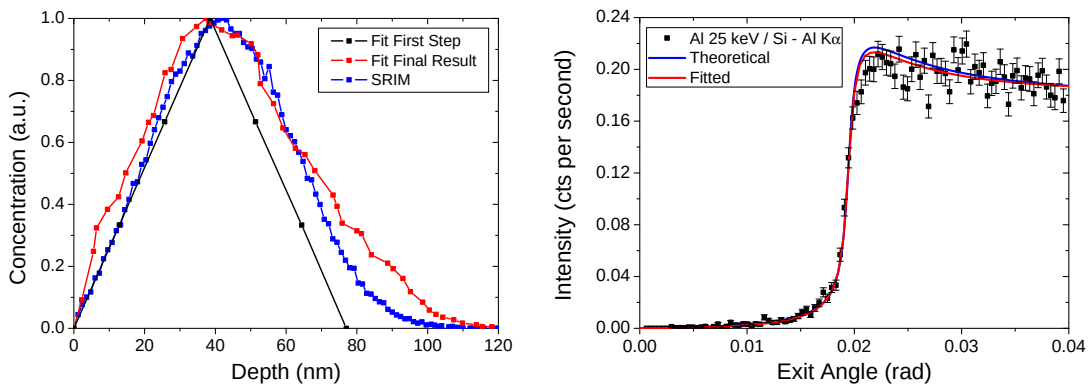

Figure VI.11: Illustration of the final dopant concentration distribution obtained when fitting the angular intensity profile without *a priori* knowledge. The angular intensity profile is well fitted (right side), the shape being slightly better reproduced by the present approach than by the theoretical curve. The dopant depth distributions for the two curves are shown together with the initial triangular distribution of the fitting procedure on the left side.

profiles to see if dopant concentration distributions similar to the SRIM calculations (used as an input to calculate the angular intensity profiles) are obtained. For the P–implanted Si wafers (Fig. VI.12), the agreement with the theoretical depth distribution is quite good, the peak positions are quite close to each other and the overall shapes are similar. The tails of the extracted depth distributions

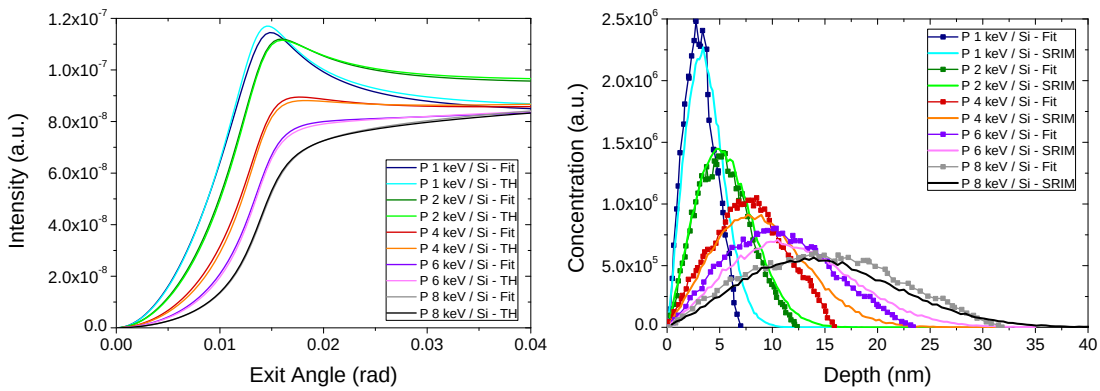

Figure VI.12: The application of the fitting approach without *a priori* provides good results for the theoretical intensity profiles of P–implanted Si wafers. The theoretical angular intensity profiles are well reproduced and the retrieved depth distributions are in a good agreement with the expected ones.

are, however, narrower than those of the theoretical one. Since the shape of the depth distribution is not fixed beforehand, this approach may be promising to detect possible dopant diffusion in thermally annealed samples compared to as–implanted samples. In Fig. VI.13 it can be seen that at present this approach

can not be used for all types of samples: the theoretical angular intensity profiles could not be well fitted for P–implanted Ge wafers and In– and Sb–implanted Si wafers. Consequently the dopant depth depth distribution is different from the

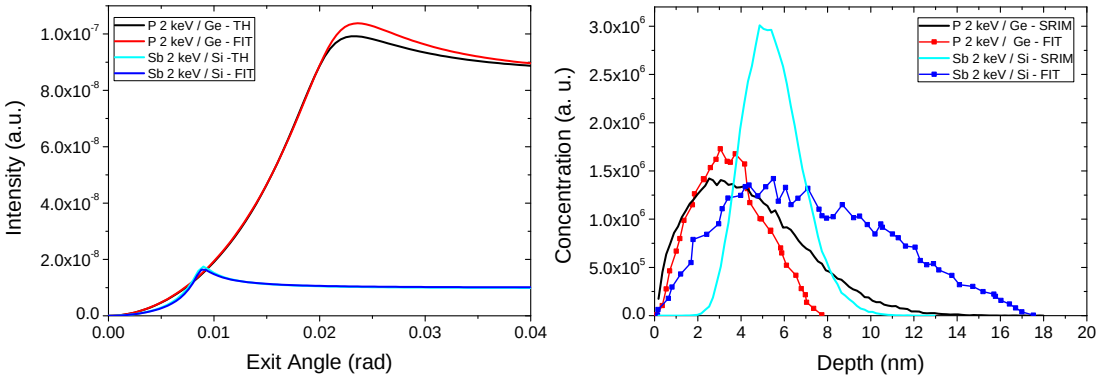

Figure VI.13: Examples where the fitting approach without *a priori* knowledge still needs to be refined to provide satisfactory results.

distribution returned by the SRIM code. The reasons are probably either the asymmetric dopant distribution of the P dopants implanted in Ge or the fact that the In dopant distribution does not span from the surface to a maximum peak concentration (indeed the concentration values start to increase further away from the surface). For these samples a pronounced refinement of the initial triangular dopant distribution is necessary in order to apply the fitting procedure to experimental angular intensity profiles. This would also allow to consider bimodal implantation profiles since up to now only monomodal distributions realized at a single implantation energy have been considered.

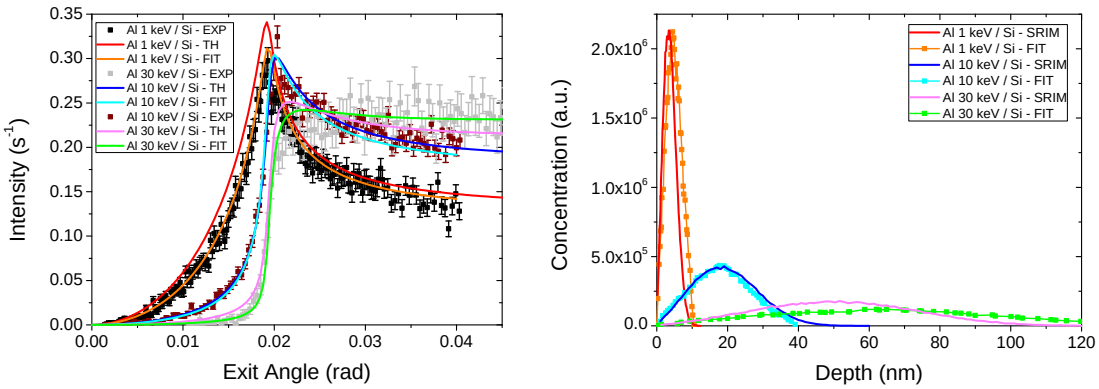

Figure VI.14: Examples of Al–implanted Si wafers where the approach without *a priori* knowledge returns results comparable to the ones obtained with other approaches.

Thus, the approach without *a priori* knowledge has still to be refined in order to

be applicable in general to theoretical examples. Only then valid results for experimental data can be obtained. For Al–implanted Si wafers this was the case. For Si wafers implanted at 1, 10 or 30 keV, the fitted angular profiles corresponding to the final distribution obtained from the iteration procedure are depicted in Fig. VI.14 (right side). For comparison, the experimental data and the results of the SRIM calculations are also plotted. As shown on the left side in Fig. VI.14, a quite good agreement is observed with the SRIM calculations as it was expected given the results when fitting with a simple or half–joined Gaussian distributions (sections VI.3 and VI.4).

VI.6 Quantification and scan of the implantation homogeneity

Concerning the quantification, it was found that for all the Al–implanted Si wafers (with the exception of the sample implanted with 1 keV), the amount of implanted ions varied within ±10%. In the present GEXRF setup the comparison of the intensity at an exit angle well above the critical angle allows to compare how the number of implanted ions varies from one sample to another, but does not give the absolute number of implanted ions. From the known depth distribution shape, only the absorption of the Al Kα X–rays in the Si matrix needs to be corrected for. Calculations of the angular intensity profile should yield a constant ratio between the experimental and the calculated intensity curves. This was the case within the indicated ±10%. Since none of our samples were certificated to be implanted with exactly 10^{16} atoms/cm^2 a reliable reference sample would be needed in order to give an absolute quantification in terms of number of atoms.

For the samples measured using the polycapillary optics to focus the primary X–ray beam, only a preliminary comparison has been realized so far. The In– and Sb– implanted samples which were implanted at the lowest fluence present also the lowest fluorescence intensity. However, the intensity ratios between different samples do not compare well to the expected, theoretical intensity ratios. Possible errors in the quantification could be due to the use of a polycapillary optics (not in terms of temporal variation but in terms of alignment to which the transmission is very sensitive; see Fig. IV.15). This may also explain the larger fluctuations observed for the P–implanted samples.

However, the polycapillary optics allowed to assess the lateral implantation homogeneity with micrometer resolution (Fig. VI.15). Such scans were realized for two P–implanted samples. For both samples the retrieved implantation fluence was identical within the error bars, the fluorescence intensity varying by not more than 10%.

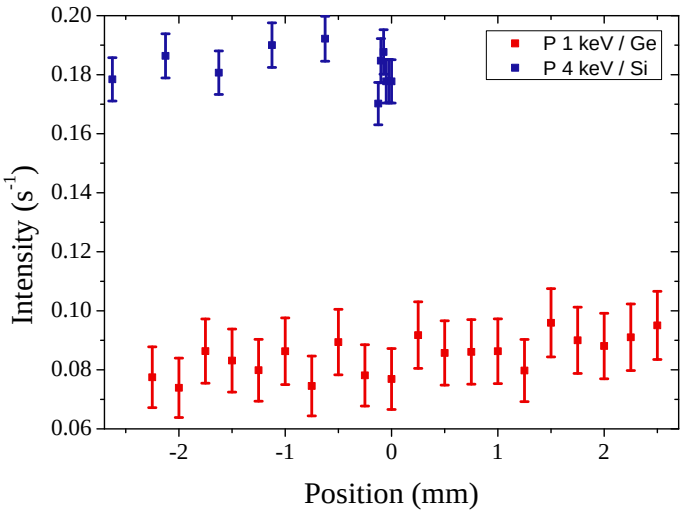

Figure VI.15: Lateral surface scans to assess the homogeneity of the implanted number of ions.

VI.7 Comparison to AES measurements

The Al–implanted Si wafers with energies of 5 and 20 keV, were also analyzed at the J. Stefan institute in Ljubljana, Slovenia, by means of AES (electron energy 3 keV, current 1 μA, beam diameter 40 μm) combined with sputtering by two symmetrically inclined Ar ion beams (energy 1 keV, incidence angle 47°, estimated sputter rate 1.8 nm per minute).

In the AES spectra for both samples no direct evidence of Al could however be found, only Si and trace amounts of C, N, O and Ar were detected. The Ar signal was probably due to the sputtering ion beams and was thus not considered in the quantification of the AES spectra. An overlap of the Al and Si LMM (68 eV fo Al and 92 eV for Si) or KLL (1396 eV for Al and 1619 eV for Si) transitions was in principle not expected, so that the main conclusion was that the setup was not sensitive enough to directly detect Al. This is somewhat surprising since the setup

was supposed to have a sensitivity of 0.1% at. which should have been sufficient to detect the Al ions which have peak concentrations of some percent.

Besides the absence of Al–peaks in the spectra, it was noted that the Si LMM intensity varied with time, and thus also the depth, instead of being constant. The source of this time variation is not certain, it could be due to instabilities in the setup or to a change of the electrical properties of a part of the Si atoms, maybe because of the presence of Al atoms. If the latter hypothesis could be verified, this would offer the possibility for an indirect detection of Al and thus an indirect way of depth–profiling. The intensity variation plotted against the depth (obtained from the sputtering rate) would thus reveal the depth distribution of the implanted Al ions. However, the shape of the intensity variation was not in agreement with depth concentration profiles retrieved with GEXRF or calculated with SRIM.

VI.8 Comparison to GIXRF and SIMS measurements

Depth–profiling measurements for five different Al–implanted wafers (implantation energies 1, 5, 10, 15 and 50 keV) were also realized by means of GIXRF (section II.6) at the PTB. The physical equivalence between GIXRF and GEXRF was demonstrated in [113] by means of the principle of microscopic reversibility (section III.1), the experimental difference being that in GIXRF the X–ray fluorescence intensity is measured as a function of the grazing incidence angle θ_i (section II.2), whereas in GEXRF it is measured as a function of the grazing emission angle θ_e (sections III.2 and IV.2.3).

The GIXRF measurements were conducted at the plane grating monochromator beam line at the Berliner Elektronenspeicherring–Gesellschaft für Synchrotronstrahlung (BESSY) [226]. The grazing incidence angular intensity profiles $I(\theta_i)$ of the Al Kα–line and Si Lα–line were recorded for a primary beam energy of 1622 eV in an angular range spanning from 0° to 4.25° and a step of 0.025°. The acquisition time per point was 20 seconds. The X–ray fluorescence signals of Al and Si were excited and detected by means of a fully calibrated setup in terms of the incident photon flux and detection efficiency for the different X–ray energies [102].

A completely reference–free quantification is thus ensured if the relevant atomic parameters are well–known. With the presented GEXRF setup a reference–free quantification is not possible.

In contrast to the presented GEXRF measurements for the Al–implanted samples, the measured GIXRF X–ray spectra had first to be corrected for background events (mainly RRS and Bremsstrahlung). The critical angle in the angular intensity profile $I(\theta_i)$ of the Si Lα–line permitted to determine the offset of the GIXRF setup and thus to calibrate precisely the incidence angle θ_i for each Al–implanted Si wafer individually. This procedure is analogue to the calibration of the exit angles θ_e in the case of GEXRF (section V.3.1), the difference being the energy of interest. Like for the GEXRF measurements where the optical properties of the Al–implanted Si wafers were considered to be identical to the ones of pure bulk Si wafers for the energy of the Si Kα–line, it was assumed that the refractive index for the beam energy of 1622 eV of the bulk Si wafer was not altered by the Al–implantation: the critical angles for the present Al–implanted Si wafers and a pure Si wafer are identical. This assumption was confirmed by X–ray reflectometry (XRR) measurements for both energies of interest. Since the value of the critical angle of bulk Si for both energies of interest are well known, the angular scales could be well calibrated in GIXRF and GEXRF. The latter aspect is crucial for depth–profiling applications of GIXRF and GEXRF, the precision on the incidence, respectively emission angle, affecting directly the accuracy on the retrieved depth profiles $f(z)$. The extinction depths as a function of the incidence, respectively emission angle are compared in Fig. VI.16.

The depth concentration distributions $f(z)$ for the different Al–implanted samples were extracted from the grazing incidence angular intensity profiles $I_{\mathrm{exp}}(\theta_i)$ by forward calculations with a modeled angular intensity profile $I_{\mathrm{model}}(\theta_i)$ and a χ^2 minimization [102]: the assumed model for $f(z)$ was similar to the case of As–implants in Si in the mentioned paper, i.e., joined half–Gaussian distributions were assumed. The used model for the angular intensity profile $I_{\mathrm{model}}(\theta_i)$ is comparable to Eq. III.21 with the difference that the fluorescence power needs to account for the grazing incidence conditions (creation of an X–ray standing wavefield for $\theta_i < \theta_c$ and an increased absorption in the depth direction due to the shallow incidence angles), whereas the emission angle θ_e in the surface transmission factor $|t_0^{\downarrow}|^2$ and the absorption factor of the X–ray fluorescence radiation is set close

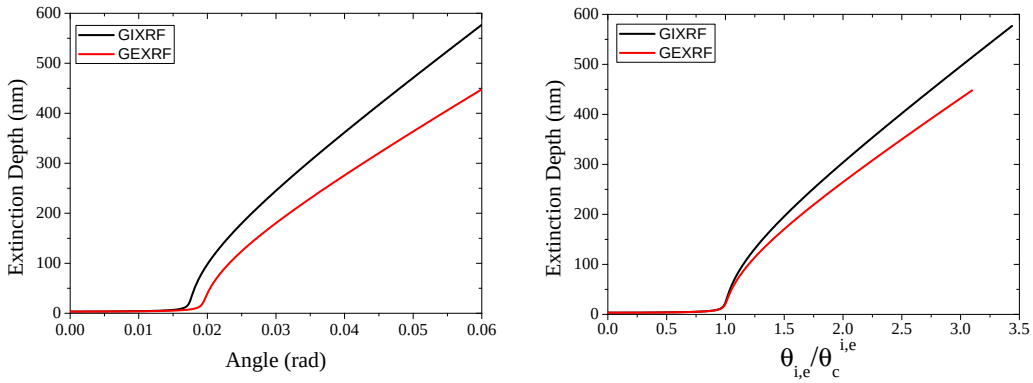

Figure VI.16: Extinction depth for Si wafers in the grazing incidence and the grazing emission geometry for the energies of interest, i.e., 1622.0 eV (the incidence beam energy) and the energy of the Al Kα–line. Since the latter one is smaller, the critical angle is larger and the extinction depth smaller for the grazing emission setup. On the right side, the plot of the extinction depth on a dimensionless (by dividing the angular scale by the relevant critical angle) scale reveals that in the grazing emission geometry the absorption of X–rays is more pronounced because of the lower energy of interest.

to $\frac{\pi}{2}$. For comparison,the angular intensity profiles of two samples for GIXRF and GEXRF are shown in Fig.VI.17 (left panel) on a dimensionless scale which permits to compare directly the refraction of X–rays of different energies. The corresponding retrieved depth distributions $f(z)$, where for the shape of $f(z)$ joined half–Gaussian distributions were assumed, are plotted on the right side of Fig. VI.17. In general the dopant concentration profiles retrieved by means of GIXRF

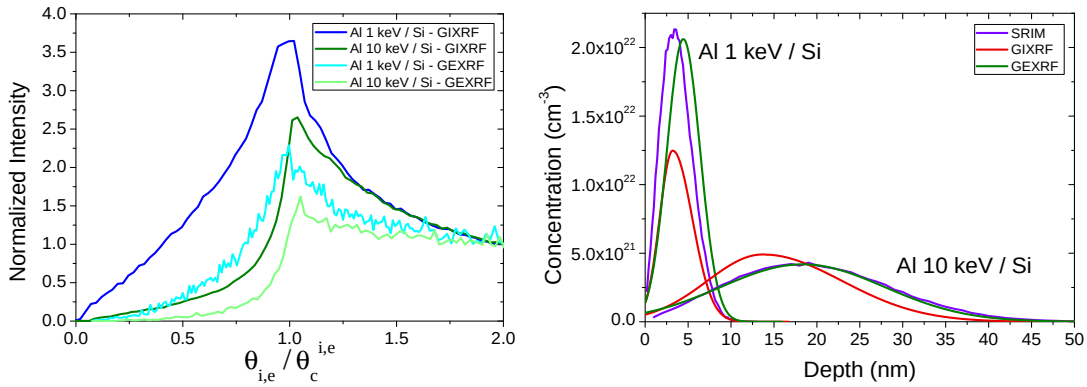

Figure VI.17: Angular intensity profiles in the grazing incidence and the grazing emission geometry and the retrieved Al concentration distribution.

are slightly distorted towards the surface, compared to the profiles obtained by GEXRF and returned by SRIM calculations. This feature becomes more apparent with increasing implantation energies. regarding the angular intensity profiles, the

peak intensity with respect to larger angles ($\theta/\theta_c = 2$) of the grazing incidence profiles is two times more pronounced than the peak intensity of the grazing emission profiles indicating that the difference between the geometries is more than the refraction of X–rays of different energies (Fig. VI.17).

In addition, the Al–implanted Si samples with implantation energies of 15 and 50 keV were analyzed with SIMS at the RTG Mikroanalysis GmbH in Berlin, Germany. The SIMS measurements were realized by means of a CAMECA IMS4F spectrometer, the sputtering ions being O_2^+ of 8 keV. The depth scale was established from the sputtering rate which was obtained by a linear interpolation of the sputtered crater depth at the end of the experiment and the measurement time. The obtained depth profile for one of the samples is compared in Fig. VI.18 to the results obtained with GIXRF and GEXRF, as well as SRIM calculations.

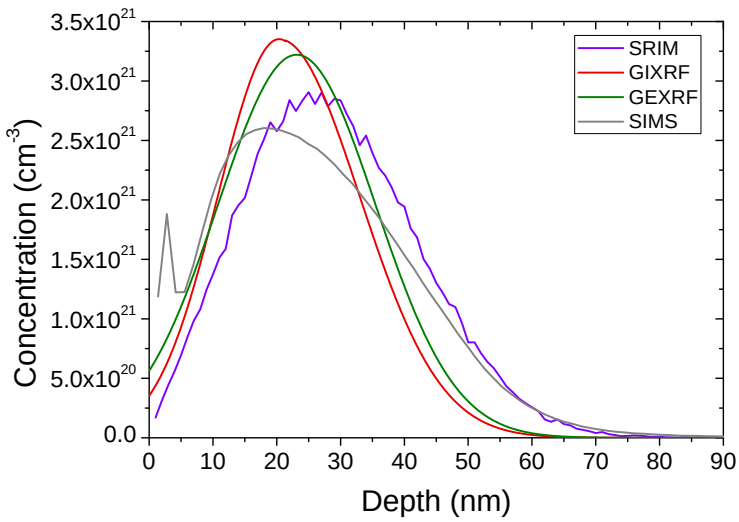

Figure VI.18: Comparison of the Al dopant concentration distribution obtained with 3 different depth–profiling techniques. Only the profile obtained by GIXRF is quantified experimentally, the concentration values of the other profiles were chosen to agree with the implantation dose of 10^{16} atoms/cm^2.

For the 15 keV implant (Fig. VI.18), the experimental curves show a maximum concentration at comparable depths below the maximum concentration depth returned by SRIM. The surface concentrations obtained with GIXRF and GEXRF are comparable, the shapes differing slightly in the sense of a broader distribution in the region between the sample surface and the maximum concentration depth for the GEXRF measurement. In this depth region, SIMS returns the steepest profile and the effect of the transient region is clearly visible. Implants realized

with lower implantation energies would thus be more difficult to be fully characterize with SIMS. For depth regions above the maximum concentration depths, the Al–concentration profiles retrieved by GIXRF and GEXRF are found to overlap, while for SIMS and SRIM larger profiles and longer tails extending into the bulk are observed.

The characterization of the 50 keV implant by the different depth–profiling techniques resulted in comparable shapes from a qualitative point of view, but the extension in the depth region are different. GIXRF returned the shallowest depth profile, while SIMS showed the broadest depth distribution of the implanted Al ions. The Al concentration profile measured with GEXRF agrees closely with the theoretical SRIM curve, both matching the SIMS profile for the largest depths.

The results presented in this section are preliminary and a more thorough discussion and interpretation of the results and the observed differences will be submitted for publication in the near future.

Chapter VII

Conclusion

In conclusion, a versatile setup for micro–focused high–resolution GEXRF measurements at X–ray synchrotron facilities and its application to non–destructive depth–profiling measurements of ion–implanted samples were presented. The experimental setup was based on the high–resolution von Hámos Bragg crystal X–ray spectrometer of the University of Fribourg which was installed for the discussed measurements at the ESRF ID21 beam line. The setup, the spectrometer, as well as the beam line were presented in detail. Further, the many advantages of the von Hámos spectrometer such as the possibility to perform reliable elemental analysis and chemical state speciation and the excellent background rejection capabilities which permit measurements with very good signal–to–background ratios, were highlighted. In particular, for the GEXRF measurements of the Al–implanted Si wafers, it was demonstrated that by selecting an appropriate primary X–ray beam energy, the high–energy resolution allows separating the Al Kα–line of interest from the elastic scattering and the Si RRS signal, and thus to achieve extremely clean background conditions.

The principles of the grazing emission geometry in which the X–ray fluorescence signal is observed under shallow angles relatively to the sample surface, as well as the calculations of the angular intensity profiles were thoroughly presented. In addition, the alternative grazing incidence geometry, which is based on shallow angle irradiation of the sample by a collimated primary X–ray beam, was described. The concepts, advantages and applications of the grazing incidence and grazing emission techniques were compared. Both geometries, grazing incidence and grazing emission, allow to enhance significantly the X–ray fluorescence from the surface relative to the bulk and thus to study the sample near–surface region with a great

sensitivity. In the grazing emission geometry, the measured dependence of the X–ray fluorescence line intensity on the emission angles around the critical angle, which depends on the fluorescence X–ray wavelength of interest and the sample matrix, allows to deduce the in–depth distribution of the emitting sources, i.e., the atoms emitting the fluorescence radiation. Indeed, the accessible depth region changes with the observation angle. These depth–profiling capabilities were demonstrated for different ion–implanted samples. Further, in order to realize laterally micro–focused measurements on the sample surface, the synchrotron radiation based high–resolution GEXRF setup was upgraded with a polycapillary optics. Polycapillary optics are quite flexible regarding the X–ray beam energy. They are used to guide X–rays by total external reflection and thus to considerably increase the local incident photon flux (i.e., gain). Thanks to the compact size, a focusing polycapillary half–lens could be installed in the von Hámos spectrometer. For the polycapillary alignment, which is quite demanding, a 5–axis positioning stage was installed.

The Al–implanted Si wafers with implantation energies differing by two orders of magnitude were investigated. From the measured angular profiles, the Al concentration distributions could be retrieved and a comparison with theoretically expected distributions showed a remarkable agreement. For some samples measurements with complementary techniques were also performed. The depth–profiles retrieved from GEXRF data were confirmed by the results obtained from GIXRF and SIMS experiments, whereas the AES experiment did not permit to draw any conclusions. The dopant depth profiles of P–, In– and Sb–implanted Si wafers as well as P–implanted Ge wafers at technologically relevant implantation fluences were also investigated. Here the focus lied especially on the low implantation energies which are relevant for the production of ultra–shallow junctions in the semiconductor industry. For these samples, the agreement with SRIM calculations was not as good as for the Al–implanted Si wafers, but the distribution and the location of the implanted ions could be quite accurately determined from the experimental angular profiles.

Several approaches for extracting the dopant depth concentration distributions from the measured angular intensity profile of a dopant X–ray fluorescence line were applied. Approaches based on purely theoretical concepts did not provide satisfactory results. Direct approaches assuming *a priori* a known distribution

function for the shape of the dopant distribution to facilitate the fitting procedure of the angular profiles allowed a quite accurate determination of the distribution and the location of the implanted ions. The employed distribution functions (Gaussian or joined half–Gaussian) were based on well–funded theoretical predictions. The approach consisting of first fitting the angular intensity profile with a given shape of the dopant distribution and subsequently verifying the retrieved results with the maximum–entropy method, needs further examination.

In addition, in an empirical approach a fitting algorithm without a priori assumptions on the shape of the dopant depth profile was developed. To start with, a bell–shaped polynomial distribution was assumed, the entered parameters being solely the bulk matrix and the energy of the X–ray fluorescence line. The evaluation of obtained theoretical angular intensity profiles (with and without statistically added Poisson noise) showed that for some cases the algorithm yields reasonable results, while for others the returned dopant depth profiles are less satisfactory even if the angular intensity profiles were quite well fitted. The encountered problems may be related to the fact that the measured angular intensity profile is not uniquely related to the depth distribution of the dopants subject to the measurement. To assess this issue the algorithm will be further developed. An application to the study of the dopant diffusion before and after annealing (necessary for the electrical activation of the dopant atoms) could then be envisaged.

To conclude the synchrotron radiation based high–resolution GEXRF method shows a great potential for characterizing narrow depth distributions of various dopants implanted in Si and Ge wafers. The sample types which can be investigated are defined by the dopant concentration which should be sufficiently above the direct detection limits and the energy of the X–ray fluorescence line. Indeed, for higher X–ray energies, the requirements on the angular accuracy increase and the angular range containing the information on the spatial distribution of the fluorescence atoms gets narrower. The requirements for successful depth–profiling measurements are, thus, more stringent. The presented setup is a unique combination of high–resolution X–ray detection and grazing emission geometry. The advantages offered by synchrotron radiation (beam intensity and energy tunability), high energy resolution X–ray detection and the grazing emission geometry, allow measurements with excellent background conditions, a good angular resolution and a reasonable X–ray fluorescence yield even considering the low solid angles of

detection inherent to high–resolution detection and the grazing emission geometry. In addition, the setup developed during this thesis permits micro–focused X–ray sample irradiation. Note that an alternative to X–ray radiation for the production of X–ray fluorescence would be electron bombardment by means of an electron gun at the University of Fribourg. Laterally micrometer–resolved studies of the sample would then also be possible. In addition, in the grazing emission region, the drawback of the short mean penetration depths of electrons would be rather an advantage since the accessible depth regions are also confined to surface–near regions.

Moreover, the laterally resolved X–ray fluorescence excitation of the sample together with nanometer–resolution depth–profiling makes an elemental 3D sample study conceivable. Indeed the necessary sensitivity and surface scanning capabilities of the setup have been demonstrated. Finally, the presented high–resolution grazing emission setup could also be used for the study of thin–layered samples or of the interfaces of stratified samples. The possible combination with X–ray absorption measurements would allow a detailed analysis of the samples (thickness, density, number of deposited atoms, elemental composition, structural evolution with increasing layer thicknesses) or the evaluation of the chemical state at the surface or interfaces (oxidation, chemical recombination).

List of Figures

List of Tables

References

[1] W. C. Röntgen, *Ueber eine neue Art von Strahlen*, Annalen der Physik, **300**, 1 – 11, 1898.

[2] J. D. Watson and F. H. C. Crick, *The transition from provirus to vegetative virus: The structure of DNA*, Cold Spring Harbor Symposia on Quantitative Biology, **18**, 123 – 131, 1953.

[3] B. W. Batterman, *Detection of foreign atom sites by their X-ray fluorescence scattering*, Phys. Rev. Lett., **22**, 703 – 705, 1969.

[4] A. H. Compton, *The total reflexion of X–rays*, Philosophical Magazine Series 6, **45**, 1121 – 1131, 1923.

[5] L. G. Parratt, *Surface studies of solids by total reflection of X-rays*, Phys. Rev., **95**, 359 – 369, 1954.

[6] R. Klockenkämper, *Total Reflection X–ray Fluorescence Analysis*, ser. Chemical analysis. Wiley-Interscience, 1996, **140**.

[7] B. L. Henke, E. M. Gullikson, and J. C. Davis, *X–ray Interactions: Photoabsorption, Scattering, Transmission, and Reflection at E = 50–30000 eV, Z = 1–92*, Atomic Data and Nuclear Data Tables, **54**, 181 – 342, 1993.

[8] P. de Bokx, C. Kok, A. Bailleul, G. Wiener, and H. Urbach, *Grazing-emission X-ray fluorescence spectrometry; principles and applications*, Spectrochimica Acta Part B: Atomic Spectroscopy, **52**, 829 – 840, 1997.

[9] M. J. Bedzyk, G. M. Bommarito, and J. S. Schildkraut, *X-ray standing waves at a reflecting mirror surface*, Phys. Rev. Lett., **62**, 1376 – 1379, 1989.

[10] P. L. Cowan, J. A. Golovchenko, and M. F. Robbins, *X–ray standing waves at crystal surfaces*, Phys. Rev. Lett., **44**, 1680 – 1683, 1980.

[11] J. A. Golovchenko, J. R. Patel, D. R. Kaplan, P. L. Cowan, and M. J. Bedzyk, *Solution to the surface registration problem using X–ray standing waves*, Phys. Rev. Lett., **49**, 560 – 563, 1982.

[12] J. R. Patel and J. A. Golovchenko, *X–ray–standing–wave atom location in heteropolar crystals and the problem of extinction*, Phys. Rev. Lett., **50**, 1858 – 1861, 1983.

[13] A. von Bohlen, *Total reflection X-ray fluorescence and grazing incidence X-ray spectrometry – Tools for micro- and surface analysis. A review*, Spectrochimica Acta Part B: Atomic Spectroscopy, **64**, 821 – 832, 2009.

[14] F. Meirer, A. Singh, P. Pianetta, G. Pepponi, F. Meirer, C. Streli, and T. Homma, *Synchrotron radiation–induced total reflection X–ray fluorescence analysis*, TrAC Trends in Analytical Chemistry, **29**, 479 – 496, 2010.

[15] N. L. Misra and K. D. S. Mudher, *Total reflection X–ray fluorescence: A technique for trace element analysis in materials*, Progress in Crystal Growth and Characterization of Materials, **45**, 65 – 74, 2002.

[16] S. Pahlke, *Quo vadis total reflection X–ray fluorescence?* Spectrochimica Acta Part B: Atomic Spectroscopy, **58**, 2025 – 2038, 2003.

[17] A. von Bohlen, M. Kramer, C. Sternemann, and M. Paulus, *The influence of X–ray coherence length on TXRF and XSW and the characterization of nanoparticles observed under grazing incidence of X–rays*, J. Anal. At. Spectrom., **24**, 792–800, 2009.

[18] R. E. A. Jiménez, *Total reflection X–ray fluorescence spectrometers for multielement analysis: Status of equipment*, Spectrochimica Acta Part B: Atomic Spectroscopy, **56**, 2331 – 2336, 2001.

[19] R. Klockenkämper, *Challenges of total reflection X–ray fluorescence for surface- and thin-layer analysis*, Spectrochimica Acta Part B: Atomic Spectroscopy, **61**, 1082 – 1090, 2006.

[20] Y. Mori, K. Uemura, and K. Shimanoe, *A depth profile fitting model for a commercial total reflection X–ray fluorescence spectrometer*, Spectrochimica Acta Part B: Atomic Spectroscopy, **52**, 823 – 828, 1997.

[21] R. Lazzari, F. Leroy, and G. Renaud, *Grazing–incidence small–angle X–ray scattering from dense packing of islands on surfaces: Development of distorted wave Born approximation and correlation between particle sizes and spacing*, Phys. Rev. B, **76**, 125411, 2007.

[22] A. Leenaers, J. Vrakking, and D. de Boer, *Glancing incidence X–ray analysis: More than just reflectivity!* Spectrochimica Acta Part B: Atomic Spectroscopy, **52**, 805 – 812, 1997.

[23] K. N. Stoev and K. Sakurai, *Recent theoretical models in grazing incidence X–ray reflectometry*, The Rigaku Journal, **14**, 22 – 37, 1997.

[24] D. K. G. de Boer, *X-ray scattering and X-ray fluorescence from materials with rough interfaces*, Phys. Rev. B, **53**, 6048–6064, 1996.

[25] D. de Boer, *X-ray reflection and transmission by rough surfaces*, Phys. Rev. B, **51**, 5297–5305, 1995.

[26] M. Rauscher, T. Salditt, and H. Spohn, *Small-angle x-ray scattering under grazing incidence: The cross section in the distorted-wave born approximation*, Phys. Rev. B, **52**, 16855 – 16863, 1995.

[27] K. Tsuji, T. Yamada, T. Utaka, and K. Hirokawa, *The effects of surface roughness on the angle–dependent total–reflection X–ray fluorescence of ultrathin films*, Journal of Applied Physics, **78**, 969 – 973, 1995.

[28] V. Holy', J. Kubeňa, I. Ohli'dal, K. Lischka, and W. Plotz, *X-ray reflection from rough layered systems*, Phys. Rev. B, **47**, 15896 – 15903, 1993.

[29] A. von Bohlen, *Total reflection X–ray fluorescence spectrometry: A versatile tool for ultra-micro analysis of objects of cultural heritage*, e-Preservation Science, **1**, 23 – 34, 2004.

[30] C. Streli, P. Wobrauschek, P. Kregsamer, G. Pepponi, P. Pianetta, S. Pahlke, and L. Fabry, *Synchrotron radiation induced total reflection X–ray fluorescence of low Z elements on Si wafer surfaces at SSRL – comparison of excitation geometries and conditions*, Spectrochimica Acta Part B: Atomic Spectroscopy, **56**, 2085 – 2094, 2001.

[31] C. Streli, G. Pepponi, P. Wobrauschek, N. Zöger, P. Pianetta, K. Baur, S. Pahlke, L. Fabry, C. Mantler, B. Kanngießer, and W. Malzer, *Analysis of low Z elements on Si wafer surfaces with synchrotron radiation induced total reflection X-ray fluorescence at SSRL, Beamline 3-3: Comparison of droplets with spin coated wafers*, Spectrochimica Acta Part B: Atomic Spectroscopy, **58**, 2105 – 2112, 2003.

[32] S. Pahlke, L. Fabry, L. Kotz, C. Mantler, and T. Ehmann, *Determination of ultra trace contaminants on silicon wafer surfaces using total-reflection X–ray fluorescence TXRF ['']state–of–the–art''*, Spectrochimica Acta Part B: Atomic Spectroscopy, **56**, 2261 – 2274, 2001.

[33] V. Egorov, E. Egorov, and M. M. Afanas'ev, *Comparative analysis of TXRF–spectroscopy efficiency under the testing target excitation by fluxes formed by the slit–cut system and waveguide-resonator*, Journal of Surface Investigation: x–ray, Synchrotron and Neutron Techniques, **2**, 904 – 912, 2008.

[34] A. Okhrimovskyy, K. Saito, and K. Tsuji, *Theoretical characterization of reflector-assisted TXRF analysis*, e-Journal of Surface Science and Nanotechnology, **4**, 579 – 583, 2006.

[35] H. J. Sanchez, C. A. Perez, R. D. Perez, and M. Rubio, *Surface analysis by total-reflection X–ray fluorescence*, Radiation Physics and Chemistry, **48**, 325 – 331, 1996.

[36] J. Yang, D. Zhao, Q. Xu, and X. Ding, *Development and application of glancing incident X–ray fluorescence spectrometry using parallel polycapillary X–ray lens*, Applied Surface Science, **255**, 6439 – 6442, 2009.

[37] K. Nakano, K. Tanaka, X. Ding, and K. Tsuji, *Development of a new total reflection X–ray fluorescence instrument using polycapillary X-ray lens*, Spectrochimica Acta Part B: Atomic Spectroscopy, **61**, 1105 – 1109, 2006.

[38] A. Iida, A. Yoshinaga, K. Sakurai, and Y. Gohshi, *Synchrotron radiation excited X–ray fluorescence analysis using total reflection of X–rays*, Analytical Chemistry, **58**, 394 – 397, 1986.

[39] R. Eller, F. Alt, G. Tölg, and H. J. Tobschall, *An efficient combined procedure for the extreme trace analysis of gold, platinum, palladium and rhodium with the aid of graphite furnace atomic absorption spectrometry and total–reflection X–ray fluorescence analysis*, Fresenius' Journal of Analytical Chemistry, **334**, 723 – 739, 1989.

[40] R. Klockenkämper and A. von Bohlen, *Total reflection X–ray fluorescence – an efficient method for micro–, trace and surface layer analysis. Invited lecture*, J. Anal. At. Spectrom., **7**, 273 – 279, 1992.

[41] R. Klockenkämper and A. von Bohlen, *Survey of sampling techniques for solids suitable for microanalysis by total–reflection X–ray fluorescence spectrometry*, J. Anal. At. Spectrom., **14**, 571 – 576, 1999.

[42] H. Stosnach and M. Mages, *Analysis of nutrition-relevant trace elements in human blood and serum by means of total reflection X–ray fluorescence (TXRF) spectroscopy*, Spectrochimica Acta Part B: Atomic Spectroscopy, **64**, 354 – 356, 2009.

[43] A. Khuder, M. Bakir, J. Karjou, and M. Sawan, *XRF and TXRF techniques for multi–element determination of trace elements in whole blood and human hair samples*, Journal of Radioanalytical and Nuclear Chemistry, **273**, 435 – 442, 2007.

[44] E. A. Hernández-Caraballo and L. M. Marcó-Parra, *Direct analysis of blood serum by total reflection X–ray fluorescence spectrometry and application of an artificial neural network approach for cancer diagnosis*, Spectrochimica Acta Part B: Atomic Spectroscopy, **58**, 2205 – 2213, 2003.

[45] L. Marcó, E. Greaves, and J. Alvarado, *Analysis of human blood serum and human brain samples by total reflection X–ray fluorescence spectrometry applying compton peak standardization*, Spectrochimica Acta Part B: Atomic Spectroscopy, **54**, 1469 – 1480, 1999.

[46] T. Magalhães, M. Carvalho, A. V. Bohlen, and M. Becker, *Study on trace elements behaviour in cancerous and healthy tissues of colon, breast and stomach: Total reflection X–ray fluorescence applications*, Spectrochimica Acta Part B: Atomic Spectroscopy, **65**, 493 – 498, 2010.

[47] T. Magalhães, M. Becker, M. Carvalho, and A. von Bohlen, *Study of Br, Zn, Cu and Fe concentrations in healthy and cancer breast tissues by TXRF*, Spectrochimica Acta Part B: Atomic Spectroscopy, **63**, 1473 – 1479, 2008.

[48] M. Carvalho, T. Magalhães, M. Becker, and A. von Bohlen, *Trace elements in human cancerous and healthy tissues: A comparative study by EDXRF, TXRF, synchrotron radiation and PIXE*, Spectrochimica Acta Part B: Atomic Spectroscopy, **62**, 1004 – 1011, 2007.

[49] T. Magalhães, A. von Bohlen, M. Carvalho, and M. Becker, *Trace elements in human cancerous and healthy tissues from the same individual: A comparative study by ZXRF and EDXRF*, Spectrochimica Acta Part B: Atomic Spectroscopy, **61**, 1185 – 1193, 2006.

[50] M. L. Carvalho, P. J. Custódio, U. Reus, and A. Prange, *Elemental analysis of human amniotic fluid and placenta by total–reflection X-ray fluorescence and energy-dispersive X–ray fluorescence: child weight and maternal age dependence*, Spectrochimica Acta Part B: Atomic Spectroscopy, **56**, 2175 – 2180, 2001.

[51] Á. Kelkó-Lévai, I. Varga, K. Zih-Perényi, and A. Lásztity, *Determination of trace elements in pharmaceutical substances by graphite furnace atomic absorption spectrometry and total reflection X–ray fluorescence after flow injection ion–exchange preconcentration*, Spectrochimica Acta Part B: Atomic Spectroscopy, **54**, 827 – 833, 1999.

[52] M. Wagner, P. Rostam-Khani, A. Wittershagen, C. Rittmeyer, B. Kolbesen, and H. Hoffmann, *Trace element determination in drugs by total–reflection X–ray fluorescence spectrometry*, Spectrochimica Acta Part B: Atomic Spectroscopy, **52**, 961 – 965, 1997.

[53] A. Cinosi, N. Andriollo, and G. P. D. Monticelli, *A novel total reflection X–ray fluorescence procedure for the directdetermination of trace elements in petrochemical products*, Analytical and Bioanalytical Chemistry, **399**, 927 – 933, 2011.

[54] F. Adebiyi, O. Asubiojo, and T. Ajayi, *Multielement analysis of nigerian bitumen by TXRF spectrometry and the physical constants characterization of its hydrocarbon component*, Fuel, **85**, 396 – 400, 2006.

[55] L. M. M. Parra, *Determination of total As in onion plants growing in contaminated substrates by total reflection X–ray fluorescence*, Journal of Radioanalytical and Nuclear Chemistry, **287**, 479 – 484, 2011.

[56] S. Pessanha, M. Carvalho, M. Becker, and A. von Bohlen, *Quantitative determination on heavy metals in different stages of wine production by total reflection X–ray fluorescence and energy dispersive x-ray fluorescence: Comparison on two vineyards*, Spectrochimica Acta Part B: Atomic Spectroscopy, **65**, 504 – 507, 2010.

[57] F. Espinoza-Quiñones, A. Módenes, S. Palácio, N. Szymanski, R. Welter, M. Rizzutto, C. Borba, and A. D. Kroumov, *Evaluation of trace element levels in muscles, liver and gonad of fish species from São Francisco river of the Paraná brazilian state by using SR–TXRF technique*, Applied Radiation and Isotopes, **68**, 2202 – 2207, 2010.

[58] J. Alvarez, L. M. Marcó, J. Arroyo, E. D. Greaves, and R. Rivas, *Determination of calcium, potassium, manganese, iron, copper and zinc levels in representative samples of two onion cultivars using total reflection X–ray fluorescence and ultrasound extraction procedure*, Spectrochimica Acta Part B: Atomic Spectroscopy, **58**, 2183 – 2189, 2003.

[59] A. Varga, R. M. G. Martinez, G. Záray, and F. Fodor, *Investigation of effects of cadmium, lead, nickel and vanadium contamination on the uptake and transport processes in cucumber plants by TXRF spectrometry*, Spectrochimica Acta Part B: Atomic Spectroscopy, **54**, 1455 – 1462, 1999.

[60] T. Capote, L. M. Marcó, J. Alvarado, and E. D. Greaves, *Determination of copper, iron and zinc in spirituous beverages by total reflection X–ray fluorescence spectrometry*, Spectrochimica Acta Part B: Atomic Spectroscopy, **54**, 1463 – 1468, 1999.

[61] N. Szoboszlai, Z. Polgári, V. G. Mihucz, and G. Záray, *Recent trends in total reflection X–ray fluorescence spectrometry for biological applications*, Analytica Chimica Acta, **633**, 1 – 18, 2009.

[62] P. Wobrauschek, *Use of total reflection X–ray fluorescence analysis in the life sciences*, Biological Trace Element Research, **43-45**, 65–71, 1994.

[63] A. Prange, U. Reds, H. Boddekker, R. Fishcer, and F.-P. Adolf, *Microanalysis in forensic sciences: Characterization of single textile fibers by total reflection X–ray fluorescence*, Analytic Sciences, **11**, 483–487, 1995.

[64] H. Hoefler, C. Streli, P. Wobrauschek, M. Óvári, and G. Záray, *Analysis of low Z elements in various environmental samples with total reflection X–ray fluorescence (TXRF) spectrometry*, Spectrochimica Acta Part B: Atomic Spectroscopy, **61**, 1135 – 1140, 2006.

[65] G. Zarazua, P. Ávila Pérez, S. Tejeda, I. Barcelo-Quintal, and T. Martínez, *Analysis of total and dissolved heavy metals in surface water of a mexican polluted river by total reflection X–ray fluorescence spectrometry*, Spectrochimica Acta Part B: Atomic Spectroscopy, **61**, 1180 – 1184, 2006.

[66] A. F. Marques, I. Queralt, M. L. Carvalho, and M. Bordalo, *Total reflection X–ray fluorescence and energy–dispersive X–ray fluorescence analysis of runoff water and vegetation from abandoned mining of Pb–Zn ores*, Spectrochimica Acta Part B: Atomic Spectroscopy, **58**, 2191 – 2198, 2003.

[67] J. Injuk and R. Van Grieken, *Optimisation of total–reflection X–ray fluorescence for aerosol analysis*, Spectrochimica Acta Part B: Atomic Spectroscopy, **50**, 1787 – 1803, 1995.

[68] G. Pepponi, P. Wobrauschek, C. Streli, N. Zöger, and F. Hegedüs, *Synchrotron radiation–induced TXRF of reactor steel samples*, X-Ray Spectrometry, **30**, 267–272, 2001.

[69] R. Fernández-Ruiz and M. García-Heras, *Study of archaeological ceramics by total-reflection X–ray fluorescence spectrometry: Semi–quantitative approach*, Spectrochimica Acta Part B: Atomic Spectroscopy, **62**, 1123 – 1129, 2007.

[70] M. L. Carvalho, A. F. Marques, M. T. Lima, and U. Reus, *Trace elements distribution and post–mortem intake in human bones from middle age by total reflection X–ray fluorescence*, Spectrochimica Acta Part B: Atomic Spectroscopy, **59**, 1251 – 1257, 2004.

[71] F. Cariati, P. Fermo, S. Gilardoni, A. Galli, and M. Milazzo, *A new approach for archaeological ceramics analysis using total reflection X–ray fluorescence spectrometry*, Spectrochimica Acta Part B: Atomic Spectroscopy, **58**, 177 – 184, 2003.

[72] M. Wegstein, H. Urban, P. Rostam-Khani, A. Wittershagen, and B. Kolbesen, *Total-reflection X–ray fluorescence spectrometry, a powerful tool for semiquantitative analysis of archaeological glass samples*, Spectrochimica Acta Part B: Atomic Spectroscopy, **52**, 1057 – 1061, 1997.

[73] C. Vázquez, G. Custo, N. Barrio, J. Burucúa, S. Boeykens, and F. Marte, *Inorganic pigment study of the San Pedro Gonzalez Telmo Sibyls using total reflection X–ray fluorescence*, Spectrochimica Acta Part B: Atomic Spectroscopy, **65**, 852 – 858, 2010.

[74] A. Guilherme, S. Pessanha, M. Carvalho, J. dos Santos, and J. Coroado, *Micro energy dispersive X–ray fluorescence analysis of polychrome lead-glazed portuguese faiences*, Spectrochimica Acta Part B: Atomic Spectroscopy, **65**, 328 – 333, 2010.

[75] C. Vázquez, A. Albornoz, A. Hajduk, D. Elkin, G. Custo, and A. Obrustky, *Total reflection X–ray fluorescence and archaeometry: Application in the Argentinean cultural heritage*, Spectrochimica Acta Part B: Atomic Spectroscopy, **63**, 1415 – 1419, 2008.

[76] K. Hühnerfu[beta], A. von Bohlen, and D. Kurth, *Characterization of pigments and colors used in ancient Egyptian boat models*, Spectrochimica Acta Part B: Atomic Spectroscopy, **61**, 1224 – 1228, 2006.

[77] D. Hellin, S. D. Gendt, N. Valckx, P. W. Mertens, and C. Vinckier, *Trends in total reflection X–ray fluorescence spectrometry for metallic contamination control in semiconductor nanotechnology*, Spectrochimica Acta Part B: Atomic Spectroscopy, **61**, 496 – 514, 2006.

[78] K. Baur, S. Brennan, P. Pianetta, and R. Opila, *Looking at trace impurities on silicon wafers with synchrotron radiation*, Analytical Chemistry, **74**, 608 A – 616 A, 2002.

[79] R. Klockenkämper and A. von Bohlen, *Total-reflection X–ray fluorescence moving towards nanoanalysis: A survey*, Spectrochimica Acta Part B: Atomic Spectroscopy, **56**, 2005 – 2018, 2001.

[80] P. Pianetta, K. Baur, A. Singh, S. Brennan, J. Kerner, D. Werho, and J. Wang, *Application of synchrotron radiation to TXRF analysis of metal contamination on silicon wafer surfaces*, Thin Solid Films, **373**, 222 – 226, 2000.

[81] B. Beckhoff, R. Fliegauf, G. Ulm, G. Pepponi, C. Streli, P. Wobrauschek, L. Fabry, and S. Pahlke, *Improvement of total reflection X–ray fluorescence analysis of low Z elements on silicon wafer surfaces at the PTB monochromator beamline for undulator radiation at the electron storage ring BESSY II*, Spectrochimica Acta Part B: Atomic Spectroscopy, **56**, 2073 – 2083, 2001.

[82] C. Streli, P. Kregsamer, P. Wobrauschek, H. Gatterbauer, P. Pianetta, S. Pahlke, L. Fabry, L. Palmetshofer, and M. Schmeling, *Low Z total reflection X–ray fluorescence analysis – Challenges and answers*, Spectrochimica Acta Part B: Atomic Spectroscopy, **54**, 1433 – 1441, 1999.

[83] C. Streli, P. Wobrauschek, V. Bauer, P. Kregsamer, R. Görgl, P. Pianetta, R. Ryon, S. Pahlke, and L. Fabry, *Total reflection X–ray fluorescence analysis of light elements with synchrotron radiation and special X–ray tubes*, Spectrochimica Acta Part B: Atomic Spectroscopy, **52**, 861 – 872, 1997.

[84] C. Streli, P. Wobrauschek, W. Ladisch, R. Rieder, and H. Aiginger, *Total reflection X–ray fluorescence analysis of light elements under various excitation conditions*, X-Ray Spectrometry, **24**, 137 – 142, 1995.

[85] J. Szlachetko, J.-C. Dousse, J. Hoszowska, M. Pajek, R. Barrett, M. Berset, K. Fennane, A. Kubala-Kukus, and M. Szlachetko, *High–resolution study of X–ray resonant Raman scattering at the K edge of silicon*, Phys. Rev. Lett., **97**, 073001, 2006.

[86] K. Baur, S. Brennan, B. Burrow, D. Werho, and P. Pianetta, *Laboratory and synchrotron radiation total–reflection X–ray fluorescence: New perspectives in detection limits and data analysis*, Spectrochimica Acta Part B: Atomic Spectroscopy, **56**, 2049 – 2056, 2001.

[87] G. Pepponi, B. Beckhoff, T. Ehmann, G. Ulm, C. Streli, L. Fabry, S. Pahlke, and P. Wobrauschek, *Analysis of organic contaminants on Si wafers with TXRF–NEXAFS*, Spectrochimica Acta Part B: Atomic Spectroscopy, **58**, 2245 – 2253, 2003.

[88] Y. Mori and K. Uemura, *Total–reflection X–ray fluorescence analysis for semiconductor process characterization*, Spectrochimica Acta Part B: Atomic Spectroscopy, **58**, 2085 – 2092, 2003.

[89] G. Buhrer, *Application of vapor phase decomposition/total reflection X–ray fluorescence in the silicon semiconductor manufacturing environment*, Spectrochimica Acta Part B: Atomic Spectroscopy, **54**, 1399 – 1407, 1999.

[90] Y. Mori, K. Uemura, H. Kohno, M. Yamagami, and Y. Iizuka, *Sweeping–TXRF: A nondestructive technique for the entire surface characterization of metal contaminations on semiconductor wafers*, Semiconductor Manufacturing, IEEE Transactions on, **18**, 569 – 574, 2005.

[91] Y. Mori, K. Uemura, H. Kohno, M. Yamagami, T. Yamada, K. Shimizu, Y. Onizuka, and Y. Iizuka, *Detection of unknown localized contamination on silicon wafer surface by sweeping–total reflection X–ray fluorescence analysis*, Spectrochimica Acta Part B: Atomic Spectroscopy, **59**, 1277 – 1282, 2004.

[92] B. Beckhoff, R. Fliegauf, M. Kolbe, M. Müller, J. Weser, and G. Ulm, *Reference–free total reflection X–ray fluorescence analysis of semiconductor surfaces with synchrotron radiation*, Analytical Chemistry, **79**, 7873 – 7882, 2007.

[93] N. S. Shin, C. H. Chang, Y. M. Koo, and H. Padmore, *Synchrotron radiation excited total reflection X–ray fluorescence quantitative analysis of Si wafer by absolute fluorescence intensity calculation*, Materials Letters, **49**, 38 – 42, 2001.

[94] R. Klockenkämper and A. von Bohlen, *A new method for depth–profiling of shallow layers in silicon wafers by repeated chemical etching and total–reflection X–ray fluorescence analysis*, Spectrochimica Acta Part B: Atomic Spectroscopy, **54**, 1385 – 1392, 1999.

[95] R. Klockenkamper and A. von Bohlen, *Depth profiling of a Co–implanted silicon wafer by total–reflection X–ray fluorescence analysis after repeated oxidation and HF–etching*, Anal. Commun., **36**, 27–29, 1999.

[96] R. Klockenkämper, A. von Bohlen, H. W. Becker, and L. Palmetshofer, *Comparison of shallow depth profiles of cobalt–implanted Si wafers determined by total reflection X–ray fluorescence analysis after repeated stratified etching and by Rutherford backscattering spectrometry*, Surface and Interface Analysis, **27**, 1003–1008, 1999.

[97] R. Klockenkämper, M. Becker, A. von Bohlen, H. W. Becker, H. Krzyzanowska, and L. Palmetshofer, *Near–surface density of ion-implanted Si studied by Rutherford backscattering and total–reflection X–ray fluorescence*, Journal of Applied Physics, **98**, 033517, 2005.

[98] R. Klockenkämper, H. Krzyzanowska, and A. von Bohlen, *Density–depth profiles of an As–implanted Si wafer studied by repeated planar sputter etching and total reflection X–ray fluorescence analysis*, Surface and Interface Analysis, **35**, 829–834, 2003.

[99] R. Klockenkämper, H. W. Becker, H. Bubert, H. Jenett, and A. von Bohlen, *Depth profiles of a shallow implanted layer in a Si wafer determined by different methods of thin–layer analysis*, Spectrochimica Acta Part B: Atomic Spectroscopy, **57**, 1593 – 1599, 2002.

[100] A. Iida, K. Sakurai, A. Yoshinaga, and Y. Gohshi, *Grazing incidence X–ray fluorescence analysis*, Nuclear Instruments and Methods in Physics Research Section A, **246**, 736 – 738, 1986.

[101] K. Iltgen, B. MacDonald, O. Brox, A. Benninghoven, C. Weiss, T. Hossain, and E. Zschech, *Ultra–shallow junction depth profile analysis using TOF–SIMS and TXRF*, AIP Conference Proceedings, **449**, 777 – 781, 1998.

[102] P. Hönicke, B. Beckhoff, M. Kolbe, D. Giubertoni, J. van den Berg, and G. Pepponi, *Depth profile characterization of ultra shallow junction implants*, Analytical and Bioanalytical Chemistry, **396**, 2825 – 2832, 2010.

[103] G. Pepponi, D. Giubertoni, M. Bersani, F. Meirer, D. Ingerle, G. Steinhauser, C. Streli, P. Hoenicke, and B. Beckhoff, *Grazing incidence X–ray fluorescence and secondary ion mass spectrometry combined approach for the characterization of ultrashallow arsenic distribution in silicon*, Journal of Vacuum Science & Technology B, **28**, C1C59 – C1C64, 2010.

[104] K. Kitts, Y. Choi, P. J. Eng, S. K. Ghose, S. R. Sutton, and B. Rout, *Application of grazing incidence X-ray fluorescence technique to discriminate and quantify implanted solar wind*, Journal of Applied Physics, **105**, 064905, 2009.

[105] S. I. Zheludeva, M. V. Kovalchuk, N. N. Novikova, I. V. Bashelhanov, N. N. Salaschenko, A. D. Akhsakhalyan, and Y. Y. Platonov, *Thickness and density determination of ultrathin solid films comprising multilayer X–ray mirrors by X–ray reflection and fluorescence study*, Review of Scientific Instruments, **63**, 1519 – 1522, 1992.

[106] U. Weisbrod, R. Gutschke, J. Knoth, and H. Schwenke, *Total reflection X–ray fluorescence spectrometry for quantitative surface and layer analysis*, Applied Physics A: Materials Science & Processing, **53**, 449 – 456, 1991.

[107] D. K. G. de Boer, *Glancing-incidence X-ray fluorescence of layered materials*, Phys. Rev. B, **44**, 498 – 511, 1991.

[108] N. Kaiser, *Review of the fundamentals of thin-film growth*, Appl. Opt., **41**, 3053–3060, 2002.

[109] H. Schwenke, J. Knoth, R. Günther, G. Wiener, and R. Bormann, *Depth profiling using total reflection X–ray fluorescence spectrometry alone and in combination with ion beam sputtering*, Spectrochimica Acta Part B: Atomic Spectroscopy, **52**, 795 – 803, 1997.

[110] R. Gunther, G. Wiener, J. Knoth, H. Schwenke, and R. Bormann, *Determination of concentration depth profiles using total-reflection X–ray fluorescence spectrometry in combination with ion–beam etching*, Review of Scientific Instruments, **67**, 2332 – 2336, 1996.

[111] W. Frank, H. J. Thomas, and A. Schindler, *Depth profiling by means of the combination of glancing incidence X–ray fluorescence spectrometry with low energy ion beam etching technique*, Spectrochimica Acta Part B: Atomic Spectroscopy, **50**, 265 – 270, 1995.

[112] G. Wiener, C. Michaelsen, J. Knoth, H. Schwenke, and R. Bormann, *Concentration–depth profiling using total–reflection X–ray fluorescence spectrometry in combination with ion–beam microsectioning techniques*, Review of Scientific Instruments, **66**, 20 – 23, 1995.

[113] R. S. Becker, J. A. Golovchenko, and J. R. Patel, *X–Ray Evanescent–Wave Absorption and Emission*, Phys. Rev. Lett., **50**, 153 – 156, 1983.

[114] H. P. Urbach and P. K. de Bokx, *Calculation of intensities in grazing–emission X–ray fluorescence*, Phys. Rev. B, **53**, 3752 – 3763, 1996.

[115] R. J. Potton, *Reciprocity in optics*, Reports on Progress in Physics, **67**, 717 – 754, 2004.

[116] K. Tsuji, *Grazing-exit electron probe X-ray microanalysis (GE–EPMA): Fundamental and applications*, Spectrochimica Acta Part B: Atomic Spectroscopy, **60**, 1381 – 1391, 2005.

[117] K. Tsuji, M. Huisman, Z. Spolnik, K. Wagatsuma, Y. Mori, R. Van Grieken, and R. D. Vis, *Comparison of grazing-exit particle-induced X-ray emission with other related methods*, Spectrochimica Acta Part B: Atomic Spectroscopy, **55**, 1009 – 1016, 2000.

[118] K. Tsuji, Z. Spolnik, K. Wagatsuma, R. Van Grieken, and R. D. Vis, *Grazing–exit particle–induced X–ray emission analysis with extremely low background*, Analytical Chemistry, **71**, 5033–5036, 1999.

[119] H. Schwenke, J. Knoth, P. A. Beaven, R. Kiehn, and J. Buhrz, *A laser plasma X–ray source for the analysis of wafer surfaces by grazing emission X–ray fluorescence spectrometry*, Spectrochimica Acta Part B: Atomic Spectroscopy, **59**, 1159 – 1164, 2004.

[120] J. Szlachetko, D. Banaś, A. Kubala-Kukuś, M. Pajek, W. Cao, J.-C. Dousse, J. Hoszowska, Y. Kayser, M. Szlachetko, M. Kavčič, M. Salome, and J. Susini, *Application of the high-resolution grazing–emission X–ray fluorescence method for impurities control in semiconductor nanotechnology*, Journal of Applied Physics, **105**, 086101, 2009.

[121] M. Claes, P. de Bokx, and R. Van Grieken, *Progress in laboratory grazing emission X–ray fluorescence spectrometry*, X-Ray Spectrometry, **28**, 224 – 229, 1999.

[122] A. Kuczumow, M. Schmeling, and R. Van Grieken, *Critical assessment and proposal for reconstruction of a grazing emission X–ray fluorescence instrument*, J. Anal. At. Spectrom., **15**, 535 – 542, 2000.

[123] R. Pérez and H. Sánchez, *New spectrometer for grazing exit X–ray fluorescence*, Review of Scientific Instruments, **68**, 2681 – 2684, 1997.

[124] K. Tsuji, S. Sato, and K. Hirokawa, *Glancing–incidence and glancing–takeoff X–ray fluorescence analysis of a Mn ultrathin film on an Au layer*, Thin Solid Films, **274**, 18 – 22, 1996.

[125] K. Tsuji and K. Hirokawa, *Takeoff angle-dependent X–ray fluorescence of layered materials using a glancing incident X–ray beam*, Journal of Applied Physics, **75**, 7189 – 7194, 1994.

[126] K. Tsuji, S. Sato, and K. Hirokawa, *Surface–sensitive X–ray fluorescence analysis at glancing incident and takeoff angles*, Journal of Applied Physics, **76**, 7860 – 7863, 1994.

[127] Y. C. Sasaki, Y. Suzuki, Y. Tomioka, and A. Fukuhara, *Observation of an interference effect for fluorescent X–rays*, Phys. Rev. B, **48**, 7724 – 7726, 1993.

[128] Y. C. Sasaki and K. Hirokawa, *New nondestructive depth profile measurement by using a refracted X–ray fluorescence method*, Applied Physics Letters, **58**, 1384–1386, 1991.

[129] S. Hasegawa, S. Ino, Y. Yamamoto, and H. Daimon, *Chemical analysis of surfaces by total–reflection-angle X–ray spectroscopy in rheed experiments (RHEED–TRAXS)*, Japanese Journal of Applied Physics, **24**, L387 – L390, 1985.

[130] Z. M. Spolnik, M. Claes, and R. Van Grieken, *Determination of trace elements in organic matrices by grazing–emission X–ray fluorescence spectrometry*, Analytica Chimica Acta, **401**, 293 – 298, 1999.

[131] M. Claes, K. V. Dyck, H. Deelstra, and R. Van Grieken, *Determination of silicon in organic matrices with grazing–emission X–ray fluorescence spectrometry*, Spectrochimica Acta Part B: Atomic Spectroscopy, **54**, 1517 – 1524, 1999.

[132] B. Holynska, M. Olko, B. Ostachowicz, J. Ostachowicz, D. Wcgrzynek, M. Claes, R. Van Grieken, P. de Bokx, P. Kump, and M. Necemer, *Performance of total reflection and grazing emission X–ray fluorescence spectrometry for the determination of trace metals in drinking water in relation to other analytical techniques*, Fresenius' Journal of Analytical Chemistry, **362**, 294 – 298, 1998.

[133] A. Kubala-Kukuś, D. Banaś, W. Cao, J.-C. Dousse, J. Hoszowska, Y. Kayser, M. Pajek, M. Salomé, J. Susini, J. Szlachetko, and M. Szlachetko, *Observation of ultralow–level Al impurities on a silicon surface by high-resolution grazing emission X–ray fluorescence excited by synchrotron radiation*, Phys. Rev. B, **80**, 113305, 2009.

[134] M. Schmeling and R. Van Grieken, *Determination of light elements in marine aerosols by grazing–emission X–ray fluorescence*, Proceedings: EUROTRAC Symposium 98, **2**, 335 – 339, 1999.

[135] P. K. de Bokx, S. J. Kidd, G. Wiener, H. P. Urbach, S. De Gendt, P. Mertens, and M. Heyns, *Grazing–emission X–ray fluorescence spectrometry: A novel tool for surface contamination analysis and thin film metrology*, Silicon Materials Science and Technology Proceedings, **98-1**, 1511 – 1523, 1998.

[136] S. de Gendt, K. Kenis, M. Baeyens, P. Mertens, M. Heyns, G. Wiener, S. Kidd, D. Knotter, and P. de Bokx, *Silicon surface metal contamination measurements using grazing–emission XRF spectrometry*, Mat. Res. Soc. Symp. Proc., **477**, 397 – 402, 1997.

[137] C. M., R. Van Ham, K. Janssens, R. Van Grieken, R. Klockenkämper, and von Bohlen A., *Micro–analysis of artists' pigments by grazing–emission X–ray fluorescence spectrometry*, Adv. X-Ray Anal., **41**, 262 – 277, 1998.

[138] F. Blockhuys, M. Claes, R. Van Grieken, and H. J. Geise, *Assessing the molecular weight of a conducting polymer by grazing emission XRF*, Analytical Chemistry, **72**, 3366 – 3368, 2000.

[139] M. Claes, P. de Bokx, N. Willard, P. Veny, and R. Van Grieken, *Optimization of sample preparation for grazing emission X–ray fluorescence in micro– and trace analysis applications*, Spectrochimica Acta Part B: Atomic Spectroscopy, **52**, 1063 – 1070, 1997.

[140] Z. M. Spolnik, M. Claes, R. E. Van Grieken, P. K. de Bokx, and H. P. Urbach, *Quantification in grazing–emission X–ray fluorescence spectrometry*, Spectrochimica Acta Part B: Atomic Spectroscopy, **54**, 1525 – 1537, 1999.

[141] A. Bekshaev and R. Van Grieken, *Substrates with a periodic surface structure in grazing–exit X–ray microanalysis*, Spectrochimica Acta Part B: Atomic Spectroscopy, **57**, 865 – 882, 2002.

[142] H. J. Sánchez, *Detection limit calculations for the total reflection techniques of X–ray fluorescence analysis*, Spectrochimica Acta Part B: Atomic Spectroscopy, **56**, 2027 – 2036, 2001.

[143] A. Kuczumow, M. Claes, M. Schmeling, R. Van Grieken, and S. de Gendt, *Quantification problems in light element determination by grazing emission X–ray fluorescence*, J. Anal. At. Spectrom., **15**, 415–421, 2000.

[144] T. Noma, H. Miyata, and S. Ino, *Grazing exit X–ray fluorescence spectroscopy for thin–film analysis*, Japanese Journal of Applied Physics, **31**, L900 – L903, 1992.

[145] H. J. Sánchez and C. A. Pérez, *Study of copper surface oxidation by grazing angle X–ray excitation*, Spectrochimica Acta Part B: Atomic Spectroscopy, **65**, 466 – 470, 2010.

[146] I. Koshelev, A. Paulikas, M. Beno, G. Jennings, J. Linton, M. Grimsditch, S. Uran, and B. Veal, *Chromium–oxide growth on Fe–Ni–Cr alloy studied with grazing–emission X–ray fluorescence*, Oxidation of Metals, **68**, 37 – 51(15), 2007.

[147] I. Koshelev, A. Paulikas, S. Uran, M. Beno, G. Jennings, J. Linton, and B. Veal, *Influence of a reactive element on the growth of a thermally grown chromia scale: A grazing emission x-ray fluorescence study*, Oxidation of Metals, **59**, 469 – 481, 2003.

[148] I. Koshelev, A. Paulikas, M. Beno, G. Jennings, J. Linton, S. Uran, and B. Veal, *Characterization of the scale on oxidized Fe–Ni–Cr alloys using grazing emission X–ray fluorescence*, Physica B: Condensed Matter, **304**, 256 – 266, 2001.

[149] M. L. Monaghan, T. Nigam, M. Houssa, S. D. Gendt, H. P. Urbach, and P. K. de Bokx, *Characterization of silicon oxynitride films by grazing–emission X–ray fluorescence spectrometry*, Thin Solid Films, **359**, 197 – 202, 2000.

[150] T. Noma, K. Takada, and A. Iida, *Surface–sensitive X–ray fluorescence and diffraction analysis with grazing-exit geometry*, X-Ray Spectrometry, **28**, 433 – 439, 1999.

[151] G. Wiener, S. J. Kidd, C. A. H. Mutsaers, R. A. M. Wolters, and P. K. de Bokx, *Characterization of titanium nitride layers by grazing-emission X–ray fluorescence spectrometry*, Applied Surface Science, **125**, 129 – 136, 1998.

[152] P. Skytt, B. Gålnander, T. Nyberg, J. Nordgren, and P. Isberg, *Probe depth variation in grazing exit soft–X–ray emission spectroscopy*, Nuclear Instruments and Methods in Physics Research Section A: Accelerators, Spectrometers, Detectors and Associated Equipment, **384**, 558 – 562, 1997.

[153] T. Noma, A. Iida, and K. Sakurai, *Fluorescent–X–ray–interference effect in layered materials*, Phys. Rev. B, **48**, 17524 – 17526, 1993.

[154] K. Tsuji, H. Takenaka, K. Wagatsuma, P. K. de Bokx, and R. Van Grieken, *Enhancement of X–ray fluorescence intensity from an ultra–thin sandwiched layer at grazing–emission angles*, Spectrochimica Acta Part B: Atomic Spectroscopy, **54**, 1881 – 1888, 1999.

[155] J. Yang, K. Tsuji, X. Lin, D. Han, and X. Ding, *A micro X–ray fluorescence analysis method using polycapillary –ray optics and grazing exit geometry*, Thin Solid Films, **517**, 3357 – 3361, 2009.

[156] J. Yang, X. Ding, and C. Liang, *A new film analysis method using polycapillary X–ray lens*, Applied Surface Science, **253**, 8352 – 8355, 2007.

[157] T. Emoto, Y. Sato, Y. Konishi, X. Ding, and K. Tsuji, *Development and applications of grazing exit micro X–ray fluorescence instrument using a polycapillary X–ray lens*, Spectrochimica Acta Part B: Atomic Spectroscopy, **59**, 1291 – 1294, 2004.

[158] K. Tsuji and F. Delalieux, *Feasibility study of three-dimensional XRF spectrometry using [mu]–X–ray beams under grazing–exit conditions*, Spectrochimica Acta Part B: Atomic Spectroscopy, **58**, 2233 – 2238, 2003.

[159] Y. Kayser, D. Banas, W. Cao, J.-C. Dousse, J. Hoszowska, P. Jagodzinski, M. Kavcic, A. Kubala-Kukus, S. Nowak, M. Pajek, and J. Szlachetko, *Depth profiles of Al impurities implanted in Si wafers determined by means of the high-resolution grazing emission X–ray fluorescence technique*, Spectrochimica Acta Part B: Atomic Spectroscopy, **65**, 445 – 449, 2010.

[160] K. Tsuji, K. Saito, K. Asami, K. Wagatsuma, F. Delalieux, and Z. Spolnik, *Localized thin–film analysis by grazing–exit electron probe microanalysis*, Spectrochimica Acta Part B: Atomic Spectroscopy, **57**, 897 – 906, 2002.

[161] Z. Spolnik, J. Zhang, K. Wagatsuma, and K. Tsuji, *Grazing–exit electron probe X–ray microanalysis of ultra–thin films and single particles with high–angle resolution*, Analytica Chimica Acta, **455**, 245 – 252, 2002.

[162] A. Bekshaev, J. de Hoog, and R. Van Grieken, *Grazing–emission electron probe microanalysis of particles near the substrate edge*, Spectrochimica Acta Part B: Atomic Spectroscopy, **56**, 2385 – 2395, 2001.

[163] A. Bekshaev and R. Van Grieken, *Interference technique in grazing–emission electron probe microanalysis of submicrometer particles*, Spectrochimica Acta Part B: Atomic Spectroscopy, **56**, 503 – 515, 2001.

[164] K. Tsuji, Z. Spolnik, K. Wagatsuma, J. Zhang, and R. E. V. Grieken, *Enhancement of electron–induced X–ray intensity for single particles under grazing–exit conditions*, Spectrochimica Acta Part B: Atomic Spectroscopy, **54**, 1243 – 1251, 1999.

[165] C. Maurizio, M. Rovezzi, F. Bardelli, H. G. Pais, and F. D'Acapito, *Setup for optimized grazing incidence X–ray absorption experiments on thin films on substrates*, Review of Scientific Instruments, **80**, 063904, 2009.

[166] B. Pollakowski, B. Beckhoff, F. Reinhardt, S. Braun, and P. Gawlitza, *Speciation of deeply buried TiO_x nanolayers with grazing–incidence X–ray fluorescence combined with a near–edge X–ray absorption fine-structure investigation*, Phys. Rev. B, **77**, 235408, 2008.

[167] G. A. Waychunas, *Grazing-incidence X-ray absorption and emission spectroscopy*, Reviews in Mineralogy and Geochemistry, **49**, 267 – 315, 2002.

[168] F. Meirer, G. Pepponi, C. Streli, P. Wobrauschek, and N. Zoeger, *Grazing exit versus grazing incidence geometry for X–ray absorption near edge structure analysis of arsenic traces*, Journal of Applied Physics, **105**, 074906, 2009.

[169] K. Shinoda, S. Sato, S. Suzuki, T. Uruga, H. Tanida, H. Toyokawa, Y. Terada, and Y. Takagaki, *Nondestructive depth resolved analysis by using grazing exit fluorescence–yield X–ray absorption spectroscopy*, Journal of Surface Analysis, **15**, 295 – 298, 2009.

[170] Y. Suzuki, *Surface extended X–ray-absorption fine–structure spectroscopy measurement using the evanescent–wave effect of fluorescent X–ray*, Phys. Rev. B, **39**, 3393 – 3395, 1989.

[171] Y. Fujii, E. Yanase, and K. Nishio, *A proposal of depth profile analysis method of strain distribution in surface layer using X–ray diffraction at small glancing angles of incidence*, J. Phys.: Conf. Ser., **83**, 012008, 2007.

[172] G. H. Vineyard, *Grazing–incidence diffraction and the distorted–wave approximation for the study of surfaces*, Phys. Rev. B, **26**, 4146 – 4159, 1982.

[173] R. D. Pérez, H. Sánchez, and M. Rubio, *Efficient calculation method for glancing angle X–ray techniques*, X-Ray Spectrometry, **31**, 296 – 299, 2002.

[174] R. D. Pérez, H. J. Sánchez, and M. Rubio, *Theoretical model for the calculation of interference effects in TXRF and GEXRF*, X-Ray Spectrometry, **30**, 292 – 295, 2001.

[175] R. D. Pérez, H. Sánchez, M. Rubio, and C. A. Pérez, *Mathematical model for evaluation of surface analysis data by total reflection XRF*, X-Ray Spectrometry, **28**, 342–347, 1999.

[176] H. P. Urbach and P. K. de Bokx, *Grazing emission X–ray fluorescence from multilayers*, Phys. Rev. B, **63**, 085408, 2001.

[177] K. Tsuji, K. Tetsuoka, F. Delalieux, and S. Sato, *Calculation of electron-induced X–ray intensities under grazing exit conditions*, e-Journal of Surface Science and Nanotechnology, **1**, 111 – 115, 2003.

[178] J. F. Ziegler, *SRIM–2003*, Nuclear Instruments and Methods in Physics Research Section B: Beam Interactions with Materials and Atoms, **219 – 220**, 1027 – 1036, 2004.

[179] J. Hoszowska, J. C. Dousse, J. Kern, and C. Rhême, *High-resolution von Hamos crystal X–ray spectrometer*, Nuclear Instruments and Methods in Physics Research Section A: Accelerators, Spectrometers, Detectors and Associated Equipment, **376**, 129 – 138, 1996.

[180] J. Szlachetko, M. Cotte, J. Morse, M. Salomé, P. Jagodzinski, J.-C. Dousse, J. Hoszowska, Y. Kayser, and J. Susini, *Wavelength-dispersive spectrometer for X–ray microfluorescence analysis at the X–ray microscopy beamline ID21 (ESRF)*, Journal of Synchrotron Radiation, **17**, 400 – 408, 2010.

[181] L. von Hámos, *Röntgenspektroskopie und Abbildung mittels gekrümmter Kristallreflektoren. I. Geometrisch-optische Betrachtungen*, Annalen der Physik (Leipzig), **409**, 716 – 724, 1933.

[182] W. H. Bragg and W. L. Bragg, *The reflection of X-rays by crystals*, Proc. R. Soc. Lond. A, **88**, 428 – 438, 1913.

[183] J. Szlachetko, J.-C. Dousse, J. Hoszowska, M. Berset, W. Cao, M. Szlachetko, and M. Kavčič, *Relative detection efficiency of back– and front–illuminated charge-coupled device cameras for x-rays between 1 kev and 18 kev*, Review of Scientific Instruments, **78**, 093102, 2007.

[184] M. A. Kumakhov, *Channeling of photons and new X–ray optics*, Nuclear Instruments and Methods in Physics Research Section B: Beam Interactions with Materials and Atoms, **48**, 283 – 286, 1990.

[185] D. H. Bilderback, *Review of capillary X–ray optics from the 2nd international capillary optics meeting*, X-Ray Spectrometry, **32**, 195 – 207, 2003.

[186] P. J. Schields, D. M. Gibson, W. M. Gibson, N. Gao, H. Huang, and I. Y. Ponomarev, *Overview of polycapillary X–ray optics*, Powder Diffraction, **17**, 70 – 80, 2002.

[187] C. A. MacDonald, *Applications and measurements of polycapillary X–ray optics*, Journal of X-Ray Science and Technology, **6**, 32 – 47, 1996.

[188] T. Wolff, I. Mantouvalou, W. Malzer, J. Nissen, D. Berger, I. Zizak et al., *Performance of a polycapillary halflens as focussing and collecting optic – A comparison*, J. Anal. At. Spectrom., **24**, 669 – 675, 2009.

[189] Y. Yan and W. M. Gibson, *Polycapillary optics and X–ray analytical techniques*, Advances in X Ray Analysis, **45**, 298–304, 2002.

[190] W. Malzer and B. Kanngie[beta]er, *A model for the confocal volume of 3d micro X–ray fluorescence spectrometer*, Spectrochimica Acta Part B: Atomic Spectroscopy, **60**, 1334 – 1341, 2005.

[191] M. A. Kumakhov, *Capillary optics and their use in X–ray analysis*, X-Ray Spectrometry, **29**, 343 – 348, 2000.

[192] L. Vincze, F. Wei, K. Proost, B. Vekemans, K. Janssens, Y. He, Y. Yan, and G. Falkenberg, *Suitability of polycapillary optics for focusing of monochromatic synchrotron radiation as used in trace level micro–XANES measurements*, J. Anal. At. Spectrom., **17**, 177 – 182, 2002.

[193] J. Gormley, T. Jach, E. Steel, and Q.-F. Xiao, *Polycapillary X–ray optic spectral gain and transmission*, X-Ray Spectrometry, **28**, 115 – 120, 1999.

[194] M. A. Kumakhov and F. F. Komarov, *Multiple reflection from surface X–ray optics*, Physics Reports, **191**, 289 – 350, 1990.

[195] C. A. MacDonald, *Focusing polycapillary optics and their applications*, X-Ray Optics and Instrumentation, **2010**, 1 – 17, 2010.

[196] J. M. Poate and L. Rubin, *Ion implantation in silicon technology*, Ind. Phys., **9**, 12–15, 2003.

[197] C. B. Yarling, *History of industrial and commercial ion implantation*, J. Vac. Sci. Technol. A, **18**, 1746 – 1750, 2000.

[198] H.-J. Kang, S.-H. Ahn, J.-S. Lee, and J.-H. Lee, *Surface modification of aluminum by N–ion implantation*, International Journal of Precision Engineering and Manufacturing, **7**, 57–61, 2006.

[199] C. B. Yarling, *Progress in ion implantation technology for metal surface treatments and other related topics*, International Conference on Ion Implantation Technology Proceedings, **2**, 824 – 826, 1999.

[200] D. Ikeda, M. Ogawa, Y. Hara, Y. Nishimura, O. Odusanya, K. Azuma, S. Matsuda, M. Yatsuzuka, and A. Murakami, *Effect of nitrogen plasma-based ion implantation on joint prosthetic material*, Surface and Coatings Technology, **156**, 301 – 305, 2002.

[201] J. Rieu, A. Pichat, L.-M. Rabbe, A. Rambert, C. Chabrol, and M. Robelet, *Ion implantation effects on friction and wear of joint prosthesis materials*, Biomaterials, **12**, 139 – 143, 1991.

[202] P. K. Chu, *Semiconductor applications of plasma immersion ion implantation*, Plasma Physics and Controlled Fusion, **45**, 555, 2003.

[203] S. Heo, H. Hwang, H. T. Cho, and W. A. Krull, *Ultrashallow (< 10 nm) p/n junction formed by* $b_1 8 h_2 2$ *cluster ion implantation and excimer laser annealing*, Applied Physics Letters, **89**, 243516, 2006.

[204] G. Claudio, K. J. Kirkby, M. Bersani, R. Low, B. J. Sealy, and R. Gwilliam, *Effect of the tilt angle on antimony in silicon implanted wafers*, Journal of Applied Physics, **95**, 5471 – 5474, 2004.

[205] R. MacCrimmon, J. Hautala, M. Gwinn, and S. Sherman, *Gas cluster ion beam infusion processing of semiconductors*, Nuclear Instruments and Methods in Physics Research Section B: Beam Interactions with Materials and Atoms, **242**, 427 – 430, 2006.

[206] H.-Y. Yu, Y. Nishi, K. Saraswat, S.-L. Cheng, and P. Griffin, *Germanium in situ doped epitaxial growth on SI for high–performance n^+/p^- –junction diode*, Electron Device Letters, IEEE, **30**, 1002 – 1004, 2009.

[207] C. O. Chui, K. Gopalakrishnan, P. B. Griffin, J. D. Plummer, and K. C. Saraswat, *Activation and diffusion studies of ion-implanted p and n dopants in germanium*, Applied Physics Letters, **83**, 3275 – 3277, 2003.

[208] H. Bracht, S. Schneider, J. N. Klug, C. Y. Liao, J. L. Hansen, E. E. Haller, A. N. Larsen, D. Bougeard, M. Posselt, and C. Wündisch, *Interstitial–mediated diffusion in germanium under proton irradiation*, Phys. Rev. Lett., **103**, 255501, 2009.

[209] C. Wündisch, M. Posselt, B. Schmidt, V. Heera, T. Schumann, A. Mücklich, R. Grötzschel, W. Skorupa, T. Clarysse, E. Simoen, and H. Hortenbach, *Millisecond flash lamp annealing of shallow implanted layers in Ge*, Applied Physics Letters, **95**, 252107, 2009.

[210] P. Williams, *Secondary ion mass spectrometry*, Annual Review of Materials Science, **15**, 517 – 548, 1985.

[211] R. N. S. Sodhi, *Time–of–flight secondary ion mass spectrometry (TOF–SIMS) – Versatility in chemical and imaging surface analysis*, Analyst, **129**, 483 – 487, 2004.

[212] W. Vandervorst, *Semiconductor profiling with sub-nm resolution: Challenges and solutions*, Applied Surface Science, **255**, 805 – 812, 2008.

[213] P. Holliger, F. Laugier, and J. C. Dupuy, *Sims depth profiling of ultrashallow P, Ge and As implants in Si using MCs2+ ions*, Surface and Interface Analysis, **34**, 472 – 476, 2002.

[214] W. Chu and J. Liu, *Rutherford backscattering spectrometry: Reminiscences and progresses*, Materials Chemistry and Physics, **46**, 183 – 188, 1996.

[215] M. Copel, *Medium–energy ion scattering for analysis of microelectronic materials*, IBM Journal of Research and Development, **44**, 571 – 582, 2000.

[216] A. L. Tofterup, *Theory of elastic and inelastic scattering of electrons emitted from solids: Energy spectra and depth profiling in XPS/AES*, Surface Science, **167**, 70 – 100, 1986.

[217] J. Miranda, J. Rickards, and R. Trejo-Luna, *PIXE depth profiling using variation of detection angle*, Nuclear Instruments and Methods in Physics Research Section B: Beam Interactions with Materials and Atoms, **249**, 394 – 396, 2006.

[218] R. Klockenkämper, M. Becker, H. Bubert, P. Burba, and L. Palmetshofer, *Determination of the implantation–dose in silicon wafers by X–ray fluorescence analysis*, Analytical Chemistry, **62**, 1674 – 1676, 1990.

[219] M. Kavcic, M. Zitnik, K. Bucar, and J. Szlachetko, *Application of wavelength dispersive X–ray spectroscopy to improve detection limits in X–ray analysis*, X-Ray Spectrometry, **40**, 2 – 6, 2011.

[220] H. Zhang, M. Gao, L. Xu, M. Lin, X. Niu, and W. Lv, *United Gauss–Pearson–IV distribution model of ions implanted into silicon*, Solid State Ionics, **179**, 832 – 836, 2008.

[221] K. Suzuki, K. Ikeda, Y. Yamashita, M. Harada, N. Taoka, O. Kiso, T. Yamamoto, N. Sugiyama, and S.-I. Takagi, *Ion–implanted impurity profiles in Ge substrates and amorphous layer thickness formed by ion implantation*, IEEE Transactions on Electron Devices, **56**, 627 – 633, 2009.

[222] K. Suzuki and R. Sudo, *Analytical expression for ion–implanted impurity concentration profiles*, Solid-State Electronics, **44**, 2253 – 2257, 2000.

[223] K. Suzuki, R. Sudo, Y. Tada, M. Tomotani, T. Feudel, and W. Fichtner, *Comprehensive analytical expression for dose dependent ion–implanted impurity concentration profiles*, Solid-State Electronics, **42**, 1671 – 1678, 1998.

[224] C. Kok and H. P. Urbach, *On the regularization of the inverse Laplace transform in grazing–emission X–ray fluorescence spectroscopy*, Inverse Problems in Engineering, **7**, 433–470, 1999.

[225] S. M. P. Smolders and H. P. Urbach, *On the determination of dopant–concentration profiles by grazing emission X–ray fluorescence spectroscopy using the maximum–entropy method*, Journal of Engineering Mathematics, **43**, 115–134, 2002.

[226] F. Senf, H. Lammert, R. Follath, T. Zeschke, W. Gudat, K. Feichtinger, P. Fischer, W. Hübner, and R. Strobel, *A new UHV angle encoder for high-resolution synchrotron radiation monochromators*, Journal of Synchrotron Radiation, **5**, 584 – 586, 1998.

Acknowledgements

Je tiens à remercier ici toutes les personnes qui ont contribué, de manière quelconque, à l'élaboration et la réalisation des projets et des mesures présentées dans cette thèse.

Un très grand merci va tout naturellement à mon directeur de thèse, le Prof. Dr. Jean–Claude Dousse, qui m'a encouragé à entrer dans le monde de la recherche scientifique et m'a offert la possibilité de réaliser un travail de doctorat. De part son soutien et son expérience, il m'a guidé durant les quatre dernières années tout en me laissant beaucoup de libertés.

Je tiens également à remercier particulièrement la Dr. Joanna Hoszowska pour son expertise, ses conseils et ses encouragements.

Ein herzlicher Dank geht an Dr. Burkhard Beckhoff von der Physikalisch–Technischen Bundesanstalt für sein Interesse an und seine Bereitschaft die Begutachtung meiner Arbeit zu übernehmen.

Ma reconnaissance va aussi envers les membres actuels et anciens du groupe de recherche AXP pour des discussion scientifiques intéressantes et stimulantes qui ont créé une ambiance de travail agréable. Merci à Jakub et Monika Szlachetko, Wei Cao, Yves–Patrick Maillard et Stanislaw Nowak.

J'adresse mes remerciements chaleureux aux collaborateurs de l'atelier mécanique, notamment à Oswald Raetzo, et à ceux de l'électronique pour leur contribution au développement de l'instrumentation expérimentale, ainsi qu'au secrétaires pour leur aide dans le règlement des formalités et affaires administratives.

Cependant ma gratitude ne s'adresse pas uniquement à des personnes qui ont pu contribuer par leur avis scientifique et professionel à la réalisation de ce travail. J'exprime également mes remerciements à toute personne m'ayant soutenu et motivé de manière plus personnelle. Leur apport n'est aucunement à négliger. Merci donc à tous mes amis.

Ein besonders lieber Dank geht an Laura für ihre feinfühlige Unterstützung.

Zu gudder Lescht well ech mengen Elteren e ganz grousse Merci soen fir hier groussaarteg Ënnerstëtzung an all menge Projeten, eng Ënnerstëtzung ouni déi ech main Studium net hätt realiséieren kennen. MERCI!

Curriculum Vitae

Personal Details

First Name & Name: Yves Kayser

Place and date of birth: Luxembourg, 28th of August 1983

Nationality: Luxembourg

Marital status: single

Current Address: Rue de Lausanne 41, 1700 Fribourg

Languages: Luxembourgish (native); English, French and German (fluent)

Education & Formation

July 2007 – July 2011 Ph.D. studies at the University of Fribourg in the domain of synchrotron radiation based high-resolution grazing emission X-ray fluorescence (GEXRF).

Sep. 2009 – Feb. 2011: Post–master diploma in higher education and educational technology at the University of Fribourg; Diploma thesis "Onlinehilfen für Studieninteressierte und Studienanfänger im Bereich der Naturwissenschaften".

Oct. 2005 – June 2007: Master of Science in Physics at the University of Fribourg with Mathematics as secondary branch; Master thesis "Photoinduced K hyper–satellite X–ray lines of Ca and the first 3d transition elements: Sc, Ti, V and Cr".

Oct. 2003 – Sept. 2005: Bachelor of Science in Physics at the University of Fribourg with Mathematics as secondary branch.

Oct. 2002 – July 2003: Scientific studies at the Centre Universitaire de Luxembourg in Mathematics and Physics.

Sep. 1995 – July 2002: Secondary school diploma at the Athénée de Luxembourg; Study direction: enseignement classique, section Latin et Langues Vivantes – Mathématiques, option Sciences Physiques.

Teaching Activites

since July 2007: Assistant in the exercise lectures of the 1st year physics lecture and assessor in oral exams of 2nd and 3nd year lectures.

Oct. 2005 – June 2007: Tutor in the lecture with exercises for the 1st year physics lecture.

Sep. 2003 and Sep. 2005: Teacher of lessons organized by the "Centre Psychologique d'Orientation Scolaires" of Luxembourg for groups of students with a reexamination in mathematics at the secondary school.

List of Publications

Refereed Papers

J. Hoszowska, A.S. Kheifets, J.-Cl. Dousse, M. Berset, I. Bray, W. Cao, K. Fennane, Y. Kayser, M. Kavcic, J. Szlachetko, and M. Szlachetko, *Physical mechanisms and scaling laws of K–shell double photoionization*, Phys. Rev. Lett. **102** (2009) 073006.

J. Hoszowska, A.S. Kheifets, M. Berset, I. Bray, W. Cao, J.-Cl. Dousse, K. Fennane, M. Kavcic, Y. Kayser, J. Szlachetko, and M. Szlachetko, *Double K-shell photoionization of low-Z atoms and He-like ions*, Eur. J. Phys. Special Topics **169** (2009) 23.

J. Szlachetko, D. Banas, A. Kubala-Kukus, M. Pajek, W. Cao, J.-Cl. Dousse, J. Hoszowska, Y. Kayser, M. Szlachetko, M. Kavcic, M. Salomé, and J. Susini, *Application of the high-resolution grazing–emission x–ray fluorescence method for impurities control in semiconductor technology*, J. Appl. Phys. **105** (2009) 086101.

W. Cao, J. Hoszowska, J.-Cl. Dousse, Y. Kayser; M. Kavcic, M. Zitnik, K. Bucar, A. Mihelic, J. Szlachetko, and K. Slabkowska, *L–subshells Coster–Kronig yields of palladium determined via synchrotron radiation based high-resolution x-ray spectroscopy*, Phys. Rev. A **80** (2009) 012512.

A. Kubala-Kukus, D. Banas, W. Cao, J.-Cl. Dousse, J. Hoszowska, Y. Kayser, M. Pajek, M. Salomé, J. Susini, J. Szlachetko, and M. Szlachetko, *Observation of ultra low–level Al–impurities on silicon surface by high-resolution grazing emission x-ray fluorescence excited by synchrotron radiation*, Phys. Rev. B Brief Report **80** (2009) 113305.

J. Hoszowska, A.K. Kheifets, J.-Cl. Dousse, I. Bray, W. Cao, K. Fennane, Y. Kayser, M. Kavcic, J. Szlachetko, and M. Szlachetko, *Single–photon double K–shell ionization of low–Z atoms*, Proc. International Symposium on (e,2e) Double Photoionization and Related Topics & 15th International Symposium on Polarization and Correlation in Electronic and Atomic Collisions, J. Phys. Conf. Series **212** (2010) 01206.

J. Szlachetko, M. Cotte, J. Morse, M. Salomé, P. Jagodzinski, J.-Cl. Dousse, J. Hoszowska, Y. Kayser, and J. Susini, *Wavelength–dispersive spectrometer for x–ray micro-fluorescence analysis at the X–ray Microscopy beamline ID21 (ESRF)*, J. Synchrotron Rad. **17** (2010) 400.

Y. Kayser, D. Banas, W. Cao, J.-Cl. Dousse, J. Hoszowska, P. Jagodzinski, M. Kavcic, A. Kubala-Kukus, S. Nowak, M. Pajek, J. Szlachetko, *Depth profiles of Al impurities implanted in Si wafers determined by means of the high–resolution grazing emission x–ray fluorescence technique*, Spectrochim. Acta Part B: Atomic Spectroscopy **65** (2010) 445.

J. Hoszowska, J.-Cl. Dousse, W. Cao, K. Fennane, Y. Kayser, M. Szlachetko, J. Szlachetko, and M. Kavcic, *Double K–shell photoionization and hypersatellite x–ray transitions of 12≤Z≤23 atoms*, Phys. Rev. A **82** (2010) 063408.

W. Cao, J.-Cl. Dousse, J. Hoszowska, M. Kavcic, Y. Kayser, J.-L. Schenker, and M. Zitnik, *Double L3M ionization of Pd induced by impact with medium–energy electrons*, Phys. Rev. A **83** (2011) 022708.

Y. Kayser, D. Banas, W. Cao, J.-Cl. Dousse, J. Hoszowska, P. Jagodzinski, M. Kavcic, A. Kubala-Kukus, S. Nowak, M. Pajek, and J. Szlachetko, *Depth profiling of dopants implanted in Si using the synchrotron radiation based high resolution grazing emission x–ray fluorescence technique*, Submitted to X–Ray Spectrometry.

J. Hoszowska, J.-Cl. Dousse, J. Szlachetk, Y. Kayser, W. Cao, P. Jagodzinski, M. Kavcic, and S. H. Nowak, *First Observation of Two-Electron One-Photon Transitions in Single-Photon K-shell Double Ionization*, Submitted to Phys. Rev. Lett.

Conference Contributions

J. Szlachetko, M. Pajek, A. Kubala-Kukus, D. Banas, J.-Cl. Dousse, J. Hoszowska, M. Szlachetko, Y. Kayser, W. Cao, M. Kavcic, M. Salomé, and J. Susini, *Application of high–resolution grazing emission x–ray fluorescence for material sciences*, 18th ESRF Users' Meeting, Feb. 6, 2008, ESRF, Grenoble, France.

J. Hoszowska, J.-Cl. Dousse, M. Berset, W. Cao, K. Fennane, Y. Kayser, M. Kavcic, A. S. Kheifets, Y-P. Maillard, J. Szlachetko, and M. Szlachetko, *Hollow magnesium, aluminium and silicon :photon energy dependence of double 1s ionization*, Annual Meeting of the Swiss Physical Society, March 26–27, 2008, University of Geneva, Switzerland.

Y. Kayser, D. Banas, W. Cao, J.-Cl. Dousse, J. Hoszowska, A. Kubala-Kukus, M. Pajek, M. Salomé J. Susini, J. Szlachetko, and M. Szlachetko, *Synchrotron radiation based high–resolution grazing emission x–ray fluorescence detection of Al–impurities on Si wafers*, Annual Meeting of the Swiss Physical Society, March 26–27, 2008, University of Geneva, Switzerland.

W. Cao, M. Kavcic, K. Bucar, J.-Cl. Dousse, J. Hoszowska, Y. Kayser, A. Mihelic, J. Szlachetko and M. Zitnik, *L–Shell Coster–Kronig coefficients of Palladium determined via high–resolution x-ray spectroscopy*, International Workshop on Photoionization (IWP2008), June 15–19, 2008, Sätra Brunn/Uppsala, Sweden.

J. Hoszowska, M. Berset, W. Cao, J.-Cl. Dousse, K. Fennane, Y. Kayser, J.-L. Schenker, J. Szlachetko, M. Szlachetko and M. Kavcic, *Double 1s ionization of Al and Si by photon and electron impact*, European Conference on X–Ray Spectrometry (EXRS 2008), June 16–20, 2008, Cavtat/Dubrovnik, Croatia.

J. Szlachetko, M. Pajek, A. Kubala-Kukus, D. Banas, W. Cao, J.-Cl. Dousse, J. Hoszowska, M. Kavcic, Y. Kayser, M. Salomé, and J. Susini, *Application of high–resolution grazing emission x–ray fluorescence (GEXRF) spectroscopy for detection of low level impurities on Si–wafers*, European Conference on X–Ray Spectrometry (EXRS 2008), June 16–20, 2008, Cavtat/Dubrovnik, Croatia.

Y. Kayser, J.-Cl. Dousse, J. Hoszowska, W. Cao, J.-L. Schenker, M. Pajek, A. Kubala-Kukus, P. Jagodzinski, M. Kavcic, and J. Szlachetko, *Depth profiling of Al–implanted Si by means of synchrtron radiation based high resolution grazing emission x–ray fluorescence*, European Conference on X–Ray Spectrometry (EXRS 2008), June 16–20, 2008, Cavtat/Dubrovnik, Croatia.

D. Banas, A. Kubala-Kukus, M. Pajek, J. Szlachetko; W. Cao, J.-Cl. Dousse, J. Hoszowska, Y. Kayser, M. Szlachetko; M. Salomé, and J. Susini, *Application of high–resolution x–ray grazing emission fluorescence in material sciences*, 9th International School and Symposium on Synchrotron Radiation in Natural Science (ISSRNS), June 15–20, 2008, Kielce, Poland.

J. Szlachetko, D. Banas, W. Cao, J.-Cl. Dousse, J. Hoszowska, Y. Kayser, A. Kubala-Kukus, M. Pajek, M. Szlachetko, M. Salome and J. Susini, *"Resonant Raman scattering in synchrotron radiation based X-ray fluorescence analysis*, IInd National Conference: Polish Synchrotron – Beamlines, June 20–21, 2008, Ameliówka, Poland.

J. Hoszowska, A.S. Kheifets, M. Berset, W. Cao, J.-Cl. Dousse, K. Fennane, M. Kavcic, Y. Kayser, J. Szlachetko and M. Szlachetko, *Double K–shell photoionization of low–Z atoms and He–like ions*, 21st International Conference on X–Ray and Inner–Shell Processes (X08), June 22–27, 2008, Paris, France.

P. Jagodzinski, J. Szlachetko, M. Pajek, A. Kubala-Kukus, D. Banas, J.-Cl. Dousse, J. Hoszowska, Y. Kayser, M. Salomé, and J. Susini, *Spectra simulations for polycapillary–based wavelength dispersive x–ray spectrometer for micro–fluorescence analysis*, 21st International Conference on X–Ray and Inner–Shell Processes (X08), June 22–27, 2008, Paris, France.

Y. Kayser, W. Cao, J.-Cl. Dousse, J. Hoszowska, , P. Jagodzinski, M. Kavcic, A. Kubala-Kukus, M. Pajek, , P. Jagodzinski, J.-L. Schenker, J. Szlachetko , *Characterization of Al–implanted Si wafers by using high resolution grazing emission x–ray fluorescence combined with synchrotron radiation*, 19th ESRF Users' Meeting, Feb. 4, 2009, ESRF, Grenoble, France.

S. Nowak, Y. Kayser, L.T. Baczewski, D. Banas, W. Cao, J.-Cl. Dousse, J. Hoszowska, M. Pajek, A. Petroutchik, J. Szlachetko, and A. Wawro, *SR–Based High–Resolution GEXRF Investigation of the Morphology of Surface Nanostructures*, Hercules Specialized Courses (HSC10), *Synchrotron radiation techniques contribution to nanoscience*, May 18–22, 2009, ESRF Grenoble, France.

Y. Kayser, W. Cao, J.-Cl. Dousse, J. Hoszowska, P. Jagodzinski, M. Kavcic, A. Kubala-Kukus, S. Nowak, M. Pajek, and J. Szlachetko, *Depth profiles of Al impurities implanted in Si wafers determined by means of the high–resolution GEXRF technique*, 13th Conference on Total Reflection X–Ray Fluorescence Analysis and Related Methods (TXRF 2009), June 15–19, 2009, Gothenburg, Sweden.

S. Nowak, Y. Kayser, L.T. Baczewski, D. Banas, W. Cao, K. Deja, J.-Cl. Dousse, J. Hoszowska, M. Pajek, A. Petroutchik, J. Szlachetko, and A. Wawro, *Investigation of the morphology of surface nanostructures by means of the synchrotron radiation based high–resolution GEXRF technique*, XXVIII International School and Conference on the Physics of Semiconductors Jaszowiec 2009, June 19–26, 2009, Krynica–Zdroj, Poland.

J. Hoszowska, A.K. Kheifets, J.-Cl. Dousse, M. Berset, J. Bray, W. Cao, K. Fennane, Y. Kayser, M. Kavcic, J. Szlachetko and M. Szlachetko, *Double K–shell photoionization and universal scaling laws*, XXVI International Conference on Photonic, Electronic and Atomic Collisions (ICPEAC), July 22–28, 2009, Kalamazoo, USA.

J. Szlachetko, M. Cotte, J. Morse, M. Salomé, J. Susini, P. Jogodzinski, J.-Cl. Dousse, J. Hoszowska, and Y. Kayser, *A Wavelength–Dispersive Spectrometer for X–ray Micro–fluorescence Analysis at the ESRF ID21 beamline*, 20th International Congress on X–ray Optics and Microanalysis (ICXOM 2009), Sept. 14–18, 2009, Karlsruhe, Germany.

M. Pajek, D. Banas, W. Cao, J.-Cl. Dousse, J. Hoszowska, Y. Kayser, A. Kubala-Kukus, S. Nowak, J. Szlachetko,

M. Salomé, and J. Susini, *Synchrotron–radiation based high–resolution grazing emission x–ray fluorescence – applications in nanoscience*, 11th International Symposium on Radiation Physics (ISRP–11), Sept. 21–27, 2009, Melbourne, Australia.

M. Pajek, D. Banas, W. Cao, J.-Cl. Dousse, J. Hoszowska, Y. Kayser, A. Kubala-Kukus, S. Nowak, J. Szlachetko, M. Salomé, and J. Susini, *Synchrotron radiation based grazing emission x–ray fluorescence*, 11th International Symposium on Radiation Physics (ISRP–11), Sept. 21–27, 2009, Melbourne, Australia.

S. Nowak, Y. Kayser, L.T. Baczewski, D. Banas, W. Cao, J.-Cl. Dousse, J. Hoszowska, M. Pajek, A. Petroutchik, J. Szlachetko, and A. Wawro, *The synchrotron radiation based high–resolution grazing x–ray emission zechnique for surface morphology analysis*, HERCULES XX Workshop, March 25–26, 2010, Grenoble, France.

J. Szlachetko, M. Cotte, J. Morse, M. Salomé, M. Pajek, P. Jagodzinski, J.-Cl. Dousse, J. Hoszowska, Y. Kayser, and J. Susini, *Application of wavelength–dispersive spectroscopy at ID21 X–ray Microscopy beamline of ESRF: new possibilities for micro–fluorescence and micro–XANES analysis*, 10th jubilee International School and Symposium on Synchrotron Radiation in Natural Science (ISSRNS), June 6–11, 2010, Szlarska Poreba, Poland.

P. Jagodzinski, M. Pajek, D. Banas, A. Kubala-Kukus, J.-Cl. Dousse, J. Hoszowska, and Y. Kayser, *Simulations of polycapillary–based wavelength dispersive x–ray flat–crystal spectrometer*, 10th jubilee International School and Symposium on Synchrotron Radiation in Natural Science (ISSRNS), June 6–11, 2010, Szlarska Poreba, Poland.

Y. Kayser, D. Banas, W. Cao, J.-Cl. Dousse, J. Hoszowska, P. Jagodzinski, M. Kavcic, A. Kubala-Kukus, S. Nowak, M. Pajek, and J. Szlachetko, *SR–based high–resolution GEXRF, a new technique to determine the depth distribution of dopants implanted in semiconductors*, European Conference on X–Ray Spectrometry (EXRS 2010), June 20–25, 2010, Figueira da Foz, Coimbra, Portugal.

J. Szlachetko, M. Cotte, J. Morse, M. Salomé, P. Jagodzinski, J.-Cl. Dousse, J. Hoszowska, Y. Kayser, and J. Susini, *Wavelength–dispersive spectrometer for x–ray micro–fluorescence analysis at the X–ray Microscopy beamline ID21 (ESRF)*, European Conference on X–Ray Spectrometry (EXRS 2010), June 20–25, 2010, Figueira da Foz, Coimbra, Portugal.

S. Nowak, D. Banas, W. Cao , J.-Cl. Dousse, J. Hoszowska,Y. Kayser, A. Kubala-Kukus, M. Pajek and J. Szlachetko, *Synchrotron Radiation Based High–resolution Grazing Emission X–Ray Fluorescence: A Multipurpose Surface Characterization Method*, XXXIX International School and Conference on the Physics of Semiconductors Jaszowiec (ISCPS 2010), June 21–24, 2010, Krynica–Zdroj, Poland.

S. Nowak, Y. Kayser, L.T. Baczewski, D. Banas, W. Cao, K. Deka, J.-Cl. Dousse, J. Hoszowska, M. Pajek, A. Petroutchik, J. Szlachetko, and A. Wawro, *Analysis of surface nanostructures via the SR–based high-resolution GEXRF technique*, 10th European Conference on Atoms, Molecules and Photons (ECAMP 10), July 4–9, 2010, Salamanca, Spain.

J. Hoszowska, J.-Cl. Dousse, J. Szlachetko, W. Cao, P. Jagodzinski, Y. Kayser, S. Nowak, M. Kavcic, *First observation of two–electron one–photon transitions in single–photon impact*, 37th International Conference on Vacuum UltraViolet and X–Ray Physics, July 11–16, 2010, Vancouver, Canada.

J. Hoszowska, W. Cao, J.-Cl. Dousse, K. Fennane, Y. Kayser, M. Kavcic, J. Szlachetko, and M. Szlachetko, *Photoinduced K hypersatellite x–ray emission for $12 \leq Z \leq 23$ elements*, 37th International Conference on Vacuum UltraViolet and X–Ray Physics, July 11–16, 2010, Vancouver, Canada.

J. Szlachetko, M. Cotte, J. Morse, M. Salomé, J. Susini, P. Jagodzinski, J.-Cl. Dousse, J. Hoszowska, and Y. Kayser, *Wavelength–dispersive spectrometer for x–ray micro–fluorescence analysis at the ESRF ID21 beamline*, 10th International Conference on X–Ray Microscopy (XRM 2010), Aug. 15–20, 2010 Chicago, USA.

Y. Kayser, D. Banas, W. Cao, J.-Cl. Dousse, J. Hoszowska, P. Jagodzinski, M. Kavcic, A. Kubala-Kukus, S. Nowak, M. Pajek, and J. Szlachetko, *Depth profiling of dopants implanted in Si using the SR–based high–resolution grazing emission technique*, 17th International Conference on Ion Beam Modification of Materials (IBMM 2010), August 21–27, 2010, Montréal, Canada.

J. Hoszowska, J.-Cl. Dousse, J. Szlachetko, W. Cao, P. Jagodzinski, Y. Kayser, S. Nowak, and M. Kavcic, *Photon induced two–electron one–photon transitions*, 7th International Conference on Inelastic X–Ray Scattering (IXS 2010), Oct. 11–14, 2010, Grenoble, France.

P. Hoenicke, B. Beckhoff, D. Giubertoni, E. Demenev, E. Hourdakis, A. Nassiopoulou, and Y. Kayser, *Soft X–Ray Induced Characterization Of Ultra Shallow Junction Depth Profiles and Activation*, International Conference on Frontiers of Characterization and Metrology for Nanoelectronics (ICFCMN 2011), May 23–26, 2011, Grenoble, France.

P. Jagodzinski, D. Banas, W. Cao, J.-Cl. Dousse, J. Hoszowska, Y. Kayser, A. Kubala-Kukus, S. Nowak, M. Pajek, M. Salome, and J. Szlachetko, *Investigations of speleothems by x–ray fluorescence microscopy using synchrotron radiation*, 14th Conference on Total Reflection X–Ray Fluorescence Analysis and Related Methods (TXRF 2011), June 06–09, 2011, Dortmund, Germany.

P. Jagodzinski, D. Banas, A. Kubala-Kukus, M. Pajek, J. Szlachetko, W. Cao, J.-Cl. Dousse, J. Hoszowska, Y. Kayser, S. Nowak, *Simulations of X–ray Transmission in Polycapillaries*, 14th Conference on Total Reflection X–Ray Fluorescence Analysis and Related Methods (TXRF 2011), June 06–09, 2011, Dortmund, Germany.

P. Hoenicke, B. Beckhoff, D. Giubertoni, E. Demenev, Y. Kayser, and J.A. van den Berg, *Soft X–Ray Induced Characterization Of Ultra Shallow Junction Depth Profiles*, 14th Conference on Total Reflection X–Ray Fluorescence Analysis and Related Methods (TXRF 2011), June 06–09, 2011, Dortmund, Germany.

S. H. Nowak, F. Reinhardt, H. Bresch, Y. Kayser, J. Osán, and A.E. Pap, *Geometrical Optics Modelling of Grazing Incidence X–ray Fluorescence of Nanoscaled Objects*, 14th Conference on Total Reflection X–Ray Fluorescence Analysis and Related Methods (TXRF 2011), June 06–09, 2011, Dortmund, Germany.

Y. Kayser, D. Banas, W. Cao, J.-Cl. Dousse, B. Fayard, P. Hönicke, J. Hoszowska, P. Jagodzinski, A. Kubala-Kukus, S. H. Nowak, M. Pajek, and R. Unterumsberger, *Micro–focused synchrotron radiation based high–resolution GEXRF applied to the depth profiling of low energy implants of P, In and Sb in Si and Ge*, 14th Conference on Total Reflection X–Ray Fluorescence Analysis and Related Methods (TXRF 2011), June 06–09, 2011, Dortmund, Germany.

J. Hoszowska, J.-Cl. Dousse, J. Szlachetko, W. Cao, P. Jagodzinski, Y. Kayser, S.Nowak, and M. Kavcic, *Two–electron one–photon transitions of Mg, Al and Si in K–shell double photoionization*, 43rd European Group for Atomic Systems (EGAS) Conference, June 28–July 2, 2011, Fribourg, Switzerland.

S. Nowak, Y. Kayser, L.T. Baczewski, D. Banas, W. Cao, K. Deja, J.-Cl. Dousse, J. Hoszowska, M. Pajek, A. Petroutchick, J. Szlachetko, and A. Wawro, *Effects of the sample surface roughness in grazing emission x–ray fluorescence measurements*, 43rd European Group for Atomic Systems (EGAS) Conference, June 28–July 2, 2011,

Fribourg, Switzerland.

Y. Kayser, D. Banas, W. Cao, J.-Cl. Dousse, P. Hoenicke, J. Hoszowska, P. Jagodzinski, A. Kubala-Kukus, S. Nowak, M. Pajek, and R. Unterumsberger, *Depth profiling of low energy P, I and Sb implants using synchrotron radiation based high–resolution micro–GEXRF*, 43rd European Group for Atomic Systems (EGAS) Conference, June 28–July 2, 2011, Fribourg, Switzerland.

Non–refereed papers

J. Hoszowska, A.S. Kheifets, J.-Cl. Dousse, M. Berset, I. Bray, K. Fennane, Y. Kayser, M. Kavcic, J. Szlachetko, and M. Szlachetko, *Hollow K–shell atoms created via single-photon double ionization*, ESRF Highlights 2009, pp 82–83.

J. Szlachetko, M. Cotte, J. Morse, M. Salomé, P. Jagodzinski, J.-Cl. Dousse, J. Hoszowska, Y. Kayser and J. Susini, *Wavelength–dispersive spectrometer for X–ray micro-fluorescence analysis*, ESRF Highlights 2010, pp 118–119.